
PhD Thesis

2D Structure and Kinematics of a Representative Sample of Low- z Ultra-Luminous Infrared Galaxies

Universidad Autónoma de Madrid

Facultad de Ciencias

Departamento de Física Teórica

Consejo Superior de Investigaciones Científicas

Instituto de Estructura de la Materia

Departamento de Astrofísica Molecular e Infrarroja

Memoria de tesis doctoral presentada por

Dña. M. Macarena García Marín

para optar al grado de
Doctora en Ciencias Físicas

DIRECTORES

Dr. Luis Colina Robledo
Dr. Santiago Arribas Mocoroa

TUTORA

Dra. Ángeles Isabel Díaz Beltrán

Madrid, Noviembre 2007

A mis padres

Acknowledgments

Esta memoria es fruto del trabajo realizado durante los últimos cuatro años en el Departamento de Astrofísica Molecular e Infrarroja. Para ello he contado con el apoyo y colaboración de muchas personas e instituciones sin las que no hubiera sido posible sacar adelante esta tesis.

En primer lugar, quisiera agradecer a mis directores Luis Colina y Santiago Arribas la confianza, el apoyo, la dedicación, la cercanía y los consejos que me han ofrecido desde el primer momento. Sin ellos la realización de esta tesis doctoral no hubiese sido posible. Agradezco el espíritu crítico y la inquietud que me han transmitido, que creo fundamental para este trabajo. Asimismo quiero expresar mi agradecimiento a Ángeles Díaz, por su apoyo y su imprescindible labor como tutora y enlace con la UAM.

Quiero también agradecer a Almudena Alonso Herrero sus valiosos consejos, constante apoyo y amistad, que me han sido de gran ayuda a la hora de desarrollar este trabajo. Su incesante actividad y curiosidad han sido un ejemplo a seguir para mi.

Mi agradecimiento para Ana Monreal Ibero, con la que he compartido largas noches de observación. Gracias a sus consejos, y a su tesis, mi primer acercamiento a la espectroscopia de campo integral fue más fácil.

Durante este tiempo he tenido la posibilidad de asistir a congresos y de realizar estancias en centros de investigación fuera de España. Debo agradecer a los miembros del Space Telescope and Science Institute y del United Kingdom Astronomy Technology Centre su hospitalidad y buen hacer durante mis meses de estancia.

Quiero también expresar mi agradecimiento a todas esas personas que, cada día más, desarrollan programas y herramientas de trabajo y las ponen a disposición de la comunidad. Es una gran ayuda que simplifica muchos aspectos del trabajo. En particular gracias a Jesús Maíz Apellániz, cuyas rutinas de IDL han sido la herramienta que he utilizado para hacer la práctica totalidad de las figuras de esta memoria.

A los miembros del Departamento de Astrofísica Molecular e Infrarroja, gracias por el tiempo que hemos compartido. Gracias por los cafés de la mañana, las sobremesas, las conversaciones y las degustaciones de productos de la tierra y catas de Maricubas que hemos disfrutado. Un recuerdo muy especial a los miembros de la nave 408. Gracias por las discusiones impagables, las sugerencias, las correcciones, las risas y las paletas de colores.

Este proyecto ha sido subvencionado por el Ministerio de Educación y Ciencia, bajo los proyectos AYA2002–01055, PNE2005–01480 y ESP2007–65475–C02–01. En este trabajo se ha utilizado la base de datos NASA/IPAC Extragalactic Database (NED), operada por el Jet Propulsion Laboratory, en el California Institute of Technology, bajo el contrato de la National Aeronautics and Space Administration.

Finalmente, mi mayor agradecimiento va para mi familia, al completo, que nunca ha dudado en apoyar y secundar las decisiones que he tomado. Sin ellos llegar hasta aquí no hubiese sido posible. Y gracias a Miguel, por su cariño, comprensión, buen humor, apoyo y compañía en este camino que hemos decidido recorrer juntos.

Abstract

One of the most important contributions of the *IRAS* satellite was the discovery of a population of local galaxies that emit the bulk of their energy in the IR. Among them, the Ultra-Luminous Infrared Galaxies (ULIRGs) were defined as those galaxies with $10^{12}L_{\odot} \leq L_{\text{IR}}[8-1000 \mu\text{m}] \leq 10^{13}L_{\odot}$. This high IR luminosity is believed to be mainly produced by intense star formation and/or the presence of an AGN. The ultra-luminous phase appears to be an important stage in galaxy evolution, even converting spirals into elliptical galaxies. In fact, these galaxies are key for understanding the galaxy evolution scheme, as they appear to be the low- z analogs of the galaxies that give rise to the far-IR background.

The majority of ULIRGs undergo interaction/fusion processes, that lead to a morphological, ionization and kinematic structure rather complex and extended. Given this, two-dimensional studies are ideal to analyze the stellar and warm ionized gas components in ULIRGs. To that aim, optical Integral Field Spectroscopy (IFS) along with high angular resolution *Hubble Space Telescope* (*HST*) images are the ideal and complementary techniques.

This thesis work is devoted to the analysis of the two-dimensional structure and kinematics of a representative sample of ULIRGs using IFS (with the INTEGRAL instrument, located at the 4.2 m William Herschel Telescope) and *HST* images. This is the first time that such a detailed study is performed for a representative sample of ULIRGs, selected to cover the most relevant characteristics of this galaxy class (i.e., luminosity, merger phase and ionization state). The most interesting findings can be summarized as follows:

- The observed stellar and ionized gas (e.g., $\text{H}\alpha$, $[\text{O III}]\lambda 5007$) components in ULIRGs have a rather perturbed morphology determined by the merger phase. Their distribution present wavelength-dependent variations, due to the nature and spatial distribution of the ionization source and of the dust. These variations are detected as a decoupling between the ionized gas and the stellar components, and are more common in the early merger phases. This is because processes like star-formation are activated in the extra-nuclear regions (at distances of up to 10 kpc). In the later merger phases the distribution of both components tend to be more compact and centrally-concentrated. Consistent with previous findings, the dust distribution is not uniform, but patchy and concentrated towards the central kiloparsecs. The average nuclear extinction is about 3.5 visual magnitudes, as derived from the Balmer decrement.
- The isophotal analysis indicates that morphological parameters such as the isophotal shape (boxy vs. disk) and twist show small variations with the merger phase. As in previous works, the near-IR light profiles of all ULIRGs under study are well fitted by an elliptical-like $r^{1/4}$ law up to distances of 5 kpc. These results suggest that there is little evolution in the studied structural parameters with the merger phase, and thus that

the morphological analysis needs additional information (kinematical or dynamical) to characterize the galaxies.

- About 80% of the studied galaxies have H II- or LINER-like nuclear classification, with approximately the same percentage of early and late merger phases. The extra-nuclear regions of a galaxy tend to show a similar classification to the nuclei. The presence of a Seyfert nuclei (in about 20% of galaxies) may lead to the detection of ionization cones and outer highly ionized clouds, whose observed excitation level may be higher than the nuclear one.
- The radially-averaged excitation conditions of late merger ULIRGs present variations. The shock tracer [O I]/H α shows an enhancement in the excitation towards the most external regions. This indicates an increasing importance of shocks towards the most external low surface brightness regions, in agreement with previous findings. The [N II]/H α and [S II]/H α line ratios (which are more sensitive to star formation) do not show a homogeneous behavior, indicating variations in the physical conditions over the galaxy structure.
- High-velocity shocks appear to be the primary mechanism responsible for the LINER-like ionization. From comparison with the models, the shock velocity varies from 150-200 km s $^{-1}$ in the nuclei to 150-500 km s $^{-1}$ in the most external low surface brightness regions. Photo-ionization by young stars (4-6 Myr) may be a secondary mechanism producing LINER-like excitation.
- The integrated emission of ULIRGs show excitation conditions that do not resemble those of the majority of local emission line galaxies. In fact, ULIRGs populate the extreme starburst, the highly excited and the transition regions. The differences measured between the nuclear and the integrated excitation states suggest that the classification of integrated high- z ULIRGs may vary with respect to the nuclear ones. For the diagnostic based on the [O I]/H α line ratio, a systematic enhancement in the excitation from H II to LINER is detected when comparing the nuclear vs. integrated values.
- The 2D velocity fields of the warm-ionized H α gas (with velocity amplitudes of hundreds of km s $^{-1}$) are very complex, and in general not consistent with those of pure rotating systems. In fact they are tidally-driven and dominated by the merger process. However, in the early and late merger phases some galaxies present hints (i.e., large velocity amplitude, rotation-like structure, similar position of the photometric and kinematic position angle) for rotation in the global velocity fields.
- The velocity dispersion presents large nuclear values (order of 100-200 km s $^{-1}$), although in general the σ peak is not coincident with the optical photometric nucleus of the galaxy. This indicates that the high-velocity dispersion of the extra-nuclear regions is associated to tidal-flows, and does not trace in general the mass concentrations. On the other hand, the value of the V/σ parameter, derived from the ionized gas, shows that ULIRGs range from systems with a dynamically hot component dominated by random motions, to galaxies where the large merger-induced velocities dominate.

- The dynamical masses for ULIRGs as derived from the nuclear σ are $\leq m_*$ ($m_*=1.4 \times 10^{11} M_\odot$) in 75% of cases, in agreement with previous works. The mass ratio of the members of early merger systems ranges, in general, between 1:1 and 1:3.
- The mass of the parent galaxies, light profiles, isophotal shapes, dynamical indicators (such as V/σ parameter), and their location in the fundamental plane, support previous works which suggest that ULIRGs may evolve into intermediate mass disky elliptical galaxies, partially supported by rotation.

Resumen

Una de las contribuciones más relevantes del satélite IRAS fue el descubrimiento de una población de galaxias locales que emiten la mayor parte de su energía en el infrarrojo. Entre ellas, las Galaxias Infrarrojas Ultraluminosas (ULIRGs) se definen como aquéllas en las que $L_{\text{IR}}[8-1000 \mu\text{m}] \geq 10^{13} L_{\odot}$. El origen de esta elevada luminosidad en el IR está asociado a formación estelar intensa y/o a la presencia de un núcleo galáctico activo. La fase ULIRGs parece ser un estadio importante en la evolución de galaxias, ya que puede ser un paso intermedio para la formación de galaxias elípticas a partir de galaxias espirales. Además, las ULIRGs son importantes a la hora de explicar la evolución de galaxias, puesto que parecen ser los análogos locales de las galaxias responsables de la radiación de fondo del IR lejano.

La mayor parte de las ULIRGs sufren procesos de interacción/fusión, responsables de su compleja estructura morfológica, cinemática y de ionización. Debido a esto, es interesante realizar estudios bidimensionales que proporcionen la información necesaria para comprender la estructura interna de estos objetos. La espectroscopia de campo integral (IFS) y las imágenes de alta resolución del *Hubble Space Telescope* (HST) son ejemplos de técnicas ideales y complementarias con las que realizar este tipo de estudios.

Este trabajo de tesis está dedicado al estudio bidimensional de la estructura interna y cinemática de una muestra representativa de ULIRGs, utilizando IFS (con el instrumento INTEGRAL, situado en el telescopio de 4.2 m William Herschel Telescope) e imágenes de alta resolución espacial del HST. De hecho, se trata del primer análisis detallado y sistemático de una muestra representativa de ULIRGs, seleccionadas para cubrir las características más importantes de este tipo de objetos (luminosidad, fase de fusión y estado de ionización). Los resultados más relevantes se detallan a continuación:

- Las componentes estelar y del gas ionizado (p. e. $\text{H}\alpha$, $[\text{O III}]\lambda 5007$) presentan una estructura compleja, determinada por la fase de fusión en la que se encuentra la galaxia. Se miden diferencias morfológicas entre la componente estelar y la del gas ionizado, que son debidas a la naturaleza y distribución de las fuentes de ionización, y a la extinción producida por el polvo. Estas variaciones son más comunes en las fases iniciales del proceso de fusión, ya que mecanismos como la formación estelar se activan en las regiones extranucleares (a distancias de hasta 10 kpc). En los estadios finales, la distribución de las componentes mencionadas es más compacta y centrada en el núcleo. La distribución del polvo no es homogénea a lo largo de la estructura de la galaxia, sino que tiende a concentrarse en las regiones nucleares tal y como se había mostrado en otros trabajos. La extinción nuclear promedio obtenida utilizando el decremento de Balmer es aproximadamente 3.5 magnitudes visuales.
- El estudio isofotal demuestra que los parámetros morfológicos como la estructura de la isofota (“boxy” o “disky”) y la variación de su ángulo de posición no parecen cambiar

con el estadio de fusión. Además, y tal y como se describe en la literatura, los perfiles de luz en el IR cercano de todas las ULIRGs se ajustan bien a una ley $r^{1/4}$ (característica de las galaxias elípticas). Estos resultados indican estabilidad en los parámetros estructurales seleccionados para estudiar las ULIRGs con independencia del tipo morfológico, y muestran que este análisis requiere de parámetros complementarios (cinemáticos o dinámicos) que ayuden a caracterizar a las galaxias.

- Aproximadamente el 80% de las galaxias estudiadas tienen clasificaciones nucleares H II o LINER, repartidas básicamente por igual en las galaxias con fusiones tempranas y tardías. En las regiones extranucleares, su clasificación es similar al de los núcleos. No obstante, la presencia de un núcleo Seyfert (detectados en el 20% de la muestra) puede crear conos de ionización o nubes de alta excitación, cuyo nivel de excitación puede ser superior al del núcleo.
- Los promedios radiales de las condiciones de excitación muestran variaciones. El trazador de choques $[\text{O I}]/\text{H}\alpha$ presenta un incremento de su nivel de excitación a medida que aumenta la distancia al núcleo, indicando que la importancia de los choques aumenta hacia las zonas más externas con menor brillo superficial, tal y como había sido sugerido previamente. Los trazadores $[\text{S II}]/\text{H}\alpha$ y $[\text{N II}]/\text{H}\alpha$, que son más sensibles a la formación estelar, no muestran un comportamiento homogéneo, indicando con ello la presencia de variaciones en las condiciones físicas de las galaxias.
- Los choques de alta velocidad son el mecanismo primario responsable de la ionización LINER. La velocidad del choque varía de 150-200 km s^{-1} en los núcleos a 150-500 km s^{-1} en las regiones más externas. La fotoionización por estrellas jóvenes ($4-6 \times 10^6$ años) es un mecanismo secundario que produce excitación LINER.
- La emisión integrada de las ULIRGs presenta un nivel de excitación que no es el mismo que el de la mayoría de las galaxias locales con líneas de emisión. Este tipo de galaxias se distribuye en las regiones de formación estelar extrema, alta excitación y transición.
- Se miden diferencias entre las clasificaciones nucleares e integradas. Estas variaciones sugieren que las clasificaciones de ULIRGs a alto- z pueden diferir de las nucleares. Para el diagrama de diagnóstico basado en el cociente $[\text{O I}]/\text{H}\alpha$, se produce un aumento sistemático en la excitación, de H II a LINER, entre los valores nucleares e integrados.
- Los campos bidimensionales de velocidad del gas ionizado (que presentan variaciones de velocidad de cientos de km s^{-1}) son muy complejos y en general no compatibles con rotación pura. Al contrario, están dominados por los efectos de marea producidos por la fusión de dos galaxias disco. A pesar de ello, en los estadios iniciales y finales de la fusión se aprecian indicios de rotación (tales como amplitudes de velocidad grandes, estructura similar a rotación en el campo cinemático, valor similar de los ángulos de posición fotométrico y cinemático) en los campos de velocidad globales.
- La dispersión de velocidades en las zonas nucleares es grande (entre 100 y 200 km s^{-1} aproximadamente), aunque en general el máximo no coincide con el núcleo de la galaxia. Esto indica que los picos de dispersión de velocidades medidos en las regiones extranucleares están asociados a efectos de marea y no trazan la masa. Respecto al

parámetro V/σ del gas ionizado, cubre un rango de valores que va desde los sistemas con una componente dinámicamente caliente, dominados por los movimientos desordenados, a galaxias donde domina la amplitud de velocidades inducida por el proceso de fusión.

- Las masas dinámicas derivadas de la dispersión de velocidades del núcleo son $\leq m_*$ ($m_*=1.4 \times 10^{11} M_\odot$) en el 75% de los casos, valores que concuerdan con medidas anteriores realizadas en ULIRGs. La razón de masas de las galaxias individuales pertenecientes a un sistema en fase temprana de fusión varía, en general, entre 1:1 y 3:1.
- La masa de las galaxias progenitoras, los perfiles de brillo, la estructura de las isofotas, los parámetros dinámicos (como V/σ), y su posición en el plano fundamental, apoyan trabajos que sugieren que las ULIRGs evolucionarán a galaxias elípticas “disky” parcialmente sostenidas por rotación.

Table of contents

Front page	i
Acknowledgements	v
Abstract	vii
Resumen	xi
Table of contents	1
Acronyms	3
1 Ultra-Luminous Infrared Galaxies	7
1.1 Introduction	7
1.2 ULIRGs: the Brightest Objects in the Local Universe	8
1.3 The Power Source in ULIRGs	10
1.4 Evolutionary Scenarios	14
1.5 Dynamical Processes: the Role of Interactions	16
1.6 The Deep Universe: ULIRGs in the Context of High- z Galaxies	20
1.7 Thesis Project	23
2 The Sample of ULIRGs: Selection, Observing Techniques, and Data Treatment	27
2.1 Introduction	27
2.2 Sample Selection	28
2.3 The Data	30
2.4 Multiwavelength High Angular Resolution Images: the <i>HST</i> Archive Data	30
2.5 Integral Field Spectroscopy	37
2.6 Relative <i>HST</i> -INTEGRAL Astrometry	52
3 Distribution of Stars, Gas and Dust. Tracing the Evolution in ULIRGs	53
3.1 Introduction	53
3.2 Morphological Classification of the Galaxy Sample	54
3.3 Stellar and Ionized Gas Structure	56
3.4 Two-Dimensional Dust Structure	58
3.5 Testing the Evolutionary Scenarios for ULIRGs	69
3.6 Summary and Conclusions	84
4 2D-Ionization Structure and Excitation Mechanisms	87
4.1 Introduction	87
4.2 Data and Diagnostic Tools	88
4.3 Ionization Structure of the Warm Gas	90

4.4	The Origin of LINER-Like Ionization	98
4.5	Integrated Results for ULIRGs: Aperture Effects in Galaxy Classification . .	104
4.6	Summary and Conclusions	106
5	Gas Kinematics and Dynamical Mass Derivation in ULIRGs	109
5.1	Introduction	109
5.2	Rotation Curves in Galaxies	110
5.3	Kinematic Structure of the Galaxy Sample	115
5.4	Degree of Rotation	124
5.5	Mass Derivation	131
5.6	The Location of ULIRGs in the Fundamental Plane	132
5.7	Summary and Conclusions	134
6	Global Summary and Main Conclusions	137
7	Resumen General y Conclusiones	141
A	Morphological Notes on the Individual Sources	147
B	Emission Line Maps for all the Galaxies of the Sample	153
C	Two-Dimensional Distribution of the Dust	181
D	Reliability of the Classifications According to the BPT Diagrams	185
	Bibliography	189
	Figures and Tables	198
	List of figures	198
	List of tables	201

Acronyms

2D–FIS	<i>Two–Dimensional Fiber ISIS System</i>
2MASS	<i>Two Microns All Sky Survey</i>
A&A	<i>Astronomy and Astrophysics</i>
A&AS	<i>Astronomy and Astrophysics Supplement</i>
ADR	<i>Atmosferic Differential Refraction</i>
AGB	<i>Asintotic Giant Branch</i>
AGN	<i>Active Galatic Nucleus</i>
AJ	<i>Astronomical Journal</i>
ApJ	<i>Astrophysical Journal</i>
Ap&SS	<i>Astrophysics & Space Science</i>
ApJS	<i>Astrophysical Journal Supplement</i>
ApSSS	<i>Astrophysics & Space Science Supplements</i>
ARA&A	<i>Annual Review of Astronomy and Astrophysics</i>
ASCA	<i>Advanced Satellite for Cosmology and Astrophysics</i>
ASP Conf. Ser.	<i>Astronomical Society of the Pacific Conferences Series</i>
AURA	<i>Association of Universities for Research in Astronomy Inc.</i>
BeppoSAX	<i>Satellite per Astronomia X, "Beppo" in honor of Giuseppe Occhialini</i>
BGS	<i>Bright Galaxy Sample</i>
BLR	<i>Broad Line Region</i>
BPT	<i>Baldwin, J. A., Phillips, M. M., & Terlevich, R. 1981, PASP, 93, 5</i>
CAS	<i>Concentration Assimetry and Clumpiness parameters</i>
CCD	<i>Charged Coupled Device</i>
CHANDRA	<i>Chandra X-ray Observatory</i>
COBE	<i>Cosmic Background Explorer</i>
CMB	<i>Cosmic Microwave Background</i>
COMBO-17	<i>Classifying Objects by Medium-Band Observations in 17 Filters</i>
COSMOS	<i>Cosmic Evolution Survey</i>
DEEP2	<i>Deep Extragalactic Evolutionary Probe 2</i>
DRGs	<i>Distant Red Galaxies</i>
EROs	<i>Extremely Red Objects</i>
FIR	<i>Far Infrared</i>
FISICA	<i>Florida Image Slicer for Infrared Cosmology & Astrophysics</i>
FLAMES	<i>Fibre Large Array Multi Element Spectrograph</i>
FOV	<i>Field of View</i>
FP	<i>Fundamental Plane</i>
FRD	<i>Focal Ratio Degradation</i>
FRIDA	<i>InFRared Imager and Dissector for the Adaptive Optics System of the GTC</i>
FWHM	<i>Full Width Half Maximun</i>
GDDS	<i>Gemini Deep Deep Survey</i>
GEMS	<i>Galaxy Evolution From Morphology And SEDs</i>
GMOS	<i>Gemini Multiobject Spectrograph</i>
GNIRS	<i>Gemini Near InfraRed Spectrograph</i>

GOODS	<i>Great Observatory Origins Deep Survey</i>
GTC	<i>Gran Telescopio de Canarias</i>
HST	<i>Hobby–Eberly Telescope</i>
HET	<i>Hubble Space Telescope</i>
HyLIRG	<i>Hyper Luminous Infrared Galaxy</i>
IFS	<i>Integral Field Spectroscopy</i>
IAC	<i>Instituto de Astrofísica de Canarias</i>
IFU	<i>Integral Field Unit</i>
IGM	<i>Inter Galactic Medium</i>
IMF	<i>Initial Mass Function</i>
ING	<i>Isaac Newton Group</i>
IR	<i>Infrarrojo</i>
IRAF	<i>Image Reduction and Analysis Facility</i>
IRAS	<i>InfraRed Astronomical Satellite</i>
IRS	<i>Infrared Spectrograph</i>
ISM	<i>Inter Stellar Medium</i>
ISO	<i>Infrared Space Observatory</i>
JWST	<i>James Webb Space Telescope</i>
KMOS	<i>K-band Multi-Object Spectrograph</i>
KPNO	<i>Kitt Peak National Observatory</i>
LBGs	<i>Lyman Break Galaxies</i>
LBT	<i>Large Binocular Telescope</i>
LINER	<i>Low-Ionization Nuclear Emission-line Region</i>
LIRG	<i>Luminous Infrared Galaxy</i>
LUCIFER	<i>LBT NIR Spectroscopic Utility with Camera and Integral Field Unit for Extragalactic Research</i>
MAMBO	<i>Max Planck Milimeter Bolometer</i>
MIR	<i>Mid Infrared</i>
MIRI	<i>Mid Infrared Instrument</i>
MNRAS	<i>Monthly Notices of the Royal Astronomical Society</i>
MPFS	<i>Multi-Pupil Fiber/Field Spectrograph</i>
MUSE	<i>Multi Unit Spectroscopic Explorer</i>
NASA	<i>National Aeronautics and Space Administration</i>
NB03	<i>Naab, T. & Burkert, A. 2003, ApJ, 597, 893</i>
Nb06	<i>Naab, T., Jesseit, R. & Burkert, A. 2006, MNRAS, 372, 839</i>
NFIS	<i>Narrow-Field Instruments</i>
NICMOS	<i>Near Infrared Camera and Multi-Object Spectrometer</i>
NIR	<i>Near Infrared</i>
NOAO	<i>National Optical Astronomy Observatory</i>
OASIS	<i>Optically Adaptive System for Imaging Spectroscopy</i>
OSIRIS	<i>OH–Suppressing InfraRed Imaging Spectrograph</i>
PA	<i>Position Angle</i>
PAH	<i>Polycyclic Aromatic Hydrocarbon</i>
PASP	<i>Publications of the Astronomical Society of the Pacific</i>
PMAS	<i>Potsdam MultiAperture Spectrophotometer</i>
PPAK	<i>PMAS Pak</i>

PSF	<i>Point Spread Function</i>
NIRSpec	<i>Near Infrared Spectrograph</i>
QSO	<i>Quasi Stellar Object</i>
RGO	<i>Royal Greenwich Observatory</i>
ROSAT	<i>ROentgen SATellite</i>
SALT	<i>Southern African Large Telescope</i>
SAURON	<i>Spectrographic Areal Unit for Research on Optical Nebulae</i>
SB1	<i>Standard Bundle 1</i>
SB2	<i>Standard Bundle 2</i>
SB3	<i>Standard Bundle 3</i>
SB99	<i>Starburst 99</i>
SCUBA	<i>Submillimeter Common-User Bolometer Array</i>
SDSS	<i>Sloan Digital Sky Survey</i>
SED	<i>Spectral Energy Distribution</i>
SFE	<i>Star Formation Efficiency</i>
SFR	<i>Star Formation Rate</i>
SINFONI	<i>Spectrograph for INtegral Field Observations in the Near Infrared</i>
S/N	<i>Signal to Noise</i>
SPIFFI	<i>SPectrometer for Infrared Faint Field Imaging</i>
SWIFT	<i>Short Wavelength Integral Field Spectrograph</i>
TDGs	<i>Tidal Dwarf Galaxies</i>
TIGER	<i>Traitement Intégral des Galaxies par l'Etude de leurs Raies</i>
UDF	<i>Ultra Deep Field</i>
UIST	<i>UKIRT Imaging Spectrometer</i>
ULIRG	<i>Ultraluminous Infrared Galaxy</i>
UV	<i>UltraViolet</i>
VIMOS	<i>VISible MultiObject Spectrograph</i>
VLT	<i>Very Large Telescope</i>
VIRUS	<i>Visible IFU Replicable Ultra-cheap Spectrograph</i>
WFPC2	<i>Wide Field and Planetary Camera 2</i>
WHT	<i>William Herschel Telescope</i>
WYFFOS	<i>Wide Field Fibre Optical Spectrograph</i>
XMM	<i>X-ray Multi-mirror Mission</i>

Chapter 1

Ultra-Luminous Infrared Galaxies

Ultra-Luminous Infrared Galaxies (ULIRGs, $10^{12}L_{\odot} \leq L_{IR}[8 - 1000\mu\text{m}] \leq 10^{13}L_{\odot}$) are among the brightest objects of the local Universe. Their high infrared (IR) luminosity along with their dusty nature, high molecular gas content, and high merging rate, make them one of the most interesting galaxy class to be studied. In fact, several investigations have emphasized the importance of ULIRGs in the grand scheme of galaxy evolution, showing that they are not a local Universe curiosity, but much more numerous at high-z. In this Chapter we will present a brief review of the most important topics in the study of ULIRGs, starting with their discovery and emphasizing their main power source, the role of merging, the dynamical processes, and their importance at high-z. Finally we will describe the structure and main goals of this thesis work.

1.1 Introduction

The first mid-IR¹ observations of extragalactic sources (Seyfert galaxies, Quasistellar Sources, and Planetary Nebulae) were made by Low & Kleinmann (1968), who found for some galaxies that “*one of their most extraordinary characteristics is their enormously bright infrared continuum*”. A few years later, Rieke & Low (1972) reinforced the evidence for strong infrared emission in several extragalactic objects by performing the photometry of a large number of sources. Among their findings, they pointed out the presence of some galaxies with “*extraordinarily high infrared luminosities*”, that rivaled with the bolometric luminosity of a Quasi Stellar Object (QSO) and could be “*the most luminous objects in the Universe*”. From the very early investigations, the observed mid- and far-IR emission in these galaxies was interpreted as re-radiated by the dust present in molecular clouds. The dust was believed to be heated by early-type stars, although the contribution of heavily obscured luminosity sources (e.g., Active Galactic Nuclei, AGN) was not ruled out (Harper & Low 1973; Rieke & Lebofsky 1979; Telesco & Harper 1980). Also, the interaction process was considered key to explain the nuclear activity and the starbursts (Toomre & Toomre 1972; Larson & Tinsley 1978). The importance of merger in this type of galaxies was confirmed by Gehrz et al. (1983) with the study of the interacting system Arp 299.

The real revolution came with the launch of the InfraRed Astronomical Satellite (*IRAS*, Neugebauer et al. 1984) in January 1983. During 10 months, *IRAS* scanned almost

¹The infrared (IR) spectral range covers from about 0.75 μm to 350 μm , and it is normally divided into three regions: the near-IR (from 0.75 to 5 μm), the mid-IR (from 5 to 25 μm), and the far-IR (from 25 to 350 μm) (Glass 1999).

all the sky in the thermal infrared without the influence of the atmosphere (see atmospheric windows in Fig. 1.1). It used four bands centered at 12, 25, 60, and 100 μm , with the spatial resolution defined by the detectors (e.g., $0''.5$ at $12\mu\text{m}$, $2'$ at $100\mu\text{m}$). The *IRAS* observations were an important advance for the IR astronomy, and increased the number of cataloged sources by about 70%.

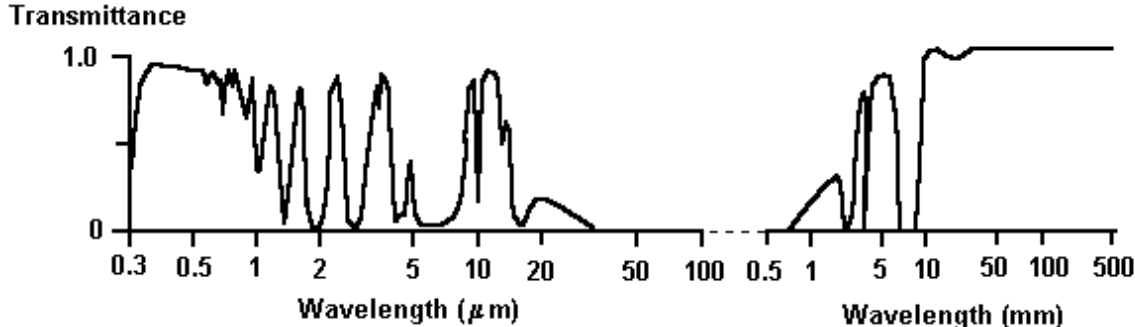


Figure 1.1: Atmospheric transmission windows. Image from <http://www.crisp.nus.edu.sg/~research/tutorial/atmoseff.htm>.

1.2 ULIRGs: the Brightest Objects in the Local Universe

Among the luminous, ultra-luminous, and hyper-luminous galaxies detected by *IRAS*, those with high IR emission ($L_{bol} \sim L_{IR}$) were classified using the definitions shown in Table 1.1. Ultra-luminous Infrared Galaxies (ULIRGs) were defined as those objects with infrared luminosity of $10^{12} \leq L_{IR}/L_{\odot} \leq 10^{13}$ (see reviews by Sanders & Mirabel 1996 and Lonsdale et al. 2006). With such luminosities, ULIRGs are the brightest objects in the local Universe, although not very common. Locally their space density is several orders of magnitude lower than that of the normal galaxies. However, they are twice as numerous as QSO and with comparable bolometric luminosity (see Fig. 1.2 *Left*). In addition, ULIRGs tend to show peculiar morphologies as the result of different stages of ongoing merger processes (e.g., Borne et al. 2000 using Hubble Space Telescope *HST* images).

According to their *IRAS* colors, there are two classifications (Sanders et al. 1988):

- Cold ULIRGs: systems with $f_{25}/f_{60} < 0.2$. This group comprises about 75% of ULIRGs. They normally are at early merger stages and show a nuclear spectral type of H II or Low Ionization Nuclear Emission-line Region (LINER).
- Warm ULIRGs: systems with $f_{25}/f_{60} > 0.2$. About 25% of ULIRGs fall into this group. Most of these galaxies show Seyfert-like spectra (Sanders et al. 1988b).

Sanders & Mirabel (1996) showed that the shape of the spectral energy distribution (SED) of ULIRGs changes with increasing total L_{IR} . Moreover, systematic variations are detected in the mid-IR colors: the higher the L_{IR} , the higher the f_{60}/f_{100} and the lower the f_{12}/f_{25} . In addition, the IR selected galaxies present different behavior depending on the wavelength range. Luminosity variations of a factor 3 or 4 in the optical are accompanied by variations of up to 3 orders of magnitude in the IR (Fig. 1.2 *Right*).

Table 1.1: Acronyms and definitions used by the *IRAS* catalog

F_{FIR}	$1.26 \times 10^{-14} \cdot (2.58f_{60} + f_{100}) [Wm^{-2}]$
L_{FIR}	$L(40 - 500\mu m) = 4\pi D_L^2 C F_{FIR} [L_\odot]$
F_{IR}	$1.8 \times 10^{-14} (13.48f_{12} + 5.16f_{25} + 2.58f_{60} + f_{100}) [Wm^{-2}]$
L_{IR}	$L(8 - 1000\mu m) = 4\pi D_L^2 F_{IR} [L_\odot]$
L_{IR}/L_B	$F_{IR}/\nu f_\nu(0.44\mu m)$
<i>LIRG</i>	Luminous IR Galaxy, $L_{IR} \geq 10^{11} L_\odot$
<i>ULIRG</i>	Ultra-Luminous IR Galaxy, $L_{IR} \geq 10^{12} L_\odot$
<i>HyLIRG</i>	Hyper-Luminous IR Galaxy, $L_{IR} \geq 10^{13} L_\odot$

Note: The quantities f_{12} , f_{25} , f_{60} , and f_{100} are the *IRAS* flux densities in Jy at 12, 25, 60 and 100 μm . The scale factor C (typically in the range 1.4-1.8) is the correction factor required to account mainly for the extrapolated flux long-ward of the *IRAS* 100 μm filter. D_L is the luminosity distance. Table adapted from Sanders & Mirabel 1996.

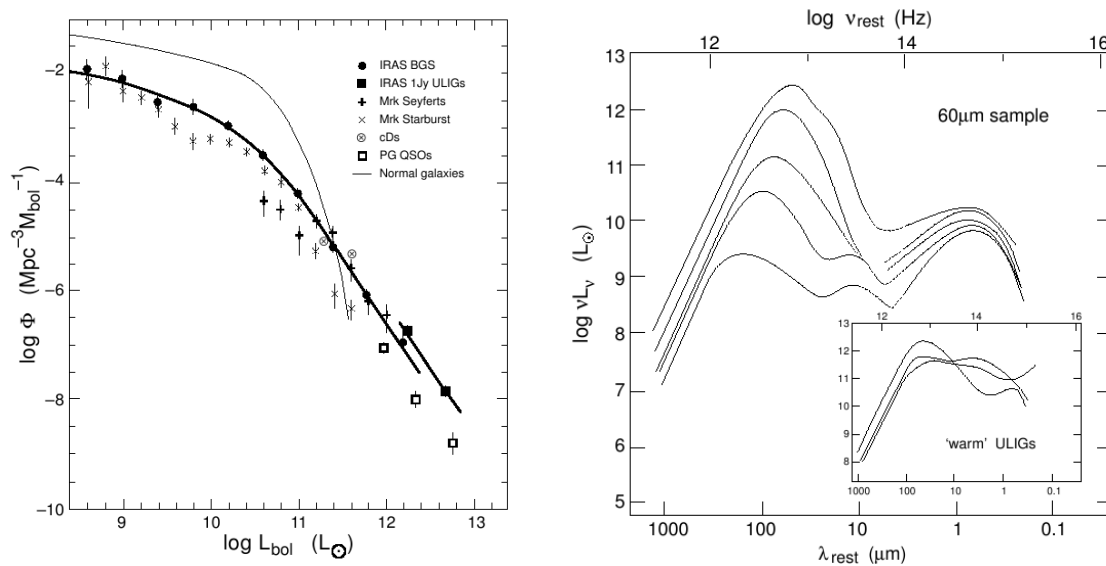


Figure 1.2: **Left:** The luminosity function for infrared galaxies compared with other extragalactic sources (Sanders & Mirabel 1996). **Right:** Variation of the mean SEDs (from sub-millimeter to UV wavelengths) with increasing L_{IR} for the 60 μm sample of infrared galaxies. (Insert) Examples of the subset ($\sim 15\%$ for the current sample) of ULIRGs with *warm* infrared colors (Sanders & Mirabel 1996).

Despite intense studies over the past decade, there are fundamental questions that are still open, and deserve further investigation. Some of these questions are:

- What is the main power source responsible for such a large luminosity in ULIRGs?
- What is the dynamical history of these objects? and What is their role in the grand scheme of galaxy evolution?
- What is the relation between ULIRGs and the population of IR bright galaxies detected at high- z ?

In what follows the most relevant results regarding these questions will be presented.

1.3 The Power Source in ULIRGs

Since the very first detections of IR-bright galaxies, the nature of their dominant power source has been one of the key questions to resolve. Today it is widely accepted that their main energy source is strong starburst activity (e.g., Arp 220 with at least $240 M_{\odot} \text{ yr}^{-1}$, Anantharamaiah et al. 2000) possibly triggered by the merger (ISO observations, Genzel et al. 1998). The presence and importance of an AGN, highly obscured by dust, is still under debate, although it appears to be more relevant in warm galaxies with high luminosity (Veilleux, Kim & Sanders 1999).

The nature of the ionization source has been the topic of several studies at different wavelength ranges. Some of the most relevant results are summarized here:

- **Optical and Near-IR Spectroscopy:**

Although ULIRGs are objects affected by the presence of dust, with extinctions of up to $A_V \sim 10$ mag depending on the observation (Lonsdale et al. 2006), optical spectroscopy is a valuable tool to classify the excitation mechanism that dominates the galaxy. Baldwin, Phillips & Terlevich (1981, hereafter BPT) were pioneers in this field, and proposed several optical diagnostic diagrams to discriminate the ionization mechanisms present in emission-line objects (see Fig. 1.3 Left). These canonical classifications separate the physical processes responsible for the gas excitation into three big groups: (a) H II-like ionization, that indicates photo-ionization by O and B stars, (b) Seyfert-like ionization, that identifies the presence of an AGN, (c) LINER-like activity, which can be produced by a variety of processes: the presence of a low-luminosity AGN (Ho, Filippenko & Sargent 1993; Grooves et al. 2004), the trigger of starbursts (Barth & Shields 2000), and large scale fast shocks (Dopita & Sutherland 1995).

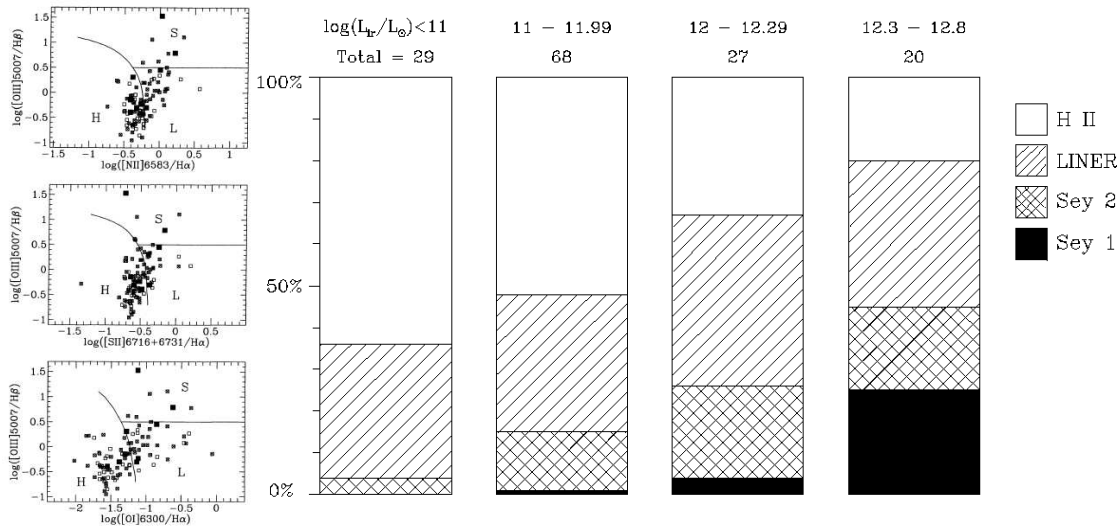


Figure 1.3: **Left:** BPT diagrams for single nucleus systems in the Bright Galaxy Sample (BGS). The H indicates H II-like, L indicates LINER-like, and S Seyfert-like excitation. Filled squares represent galaxies with $\log(L_{IR}/L_{\odot}) > 12$, Veilleux et al. 1995). **Right:** Fraction of optical spectral classification of infrared galaxies (1 Jy sample) vs. infrared luminosity (Kim et al. 1998)

Using long-slit spectroscopy of a complete sample of ULIRGs (the 1 Jy sample), Kim

et al. (1995) analyzed their nuclear ionization state, finding that the fraction of ULIRGs dominated by Seyfert activity increases in galaxies with luminosities above $L_{IR} \approx 10^{12.3} L_{\odot}$. In contrast, the proportion of H II galaxies dominated by photo-ionization by hot stars seems to decrease with luminosity. The LINER-like galaxies show a constant proportion throughout the IR luminosity range (see Fig. 1.3 Right).

- **Near-IR Spectroscopy:**

Extinction plays an important role for knowing whether or not ULIRGs present nuclear Seyfert activity. In extreme cases, if the nucleus is highly affected by dust, there would be no indication for the presence of an AGN in the optical, and the AGN emission could be completely absorbed even in hard X-rays (e.g., the recent detection of an AGN with CO(2-1) observations in Arp 220, Downes & Eckart 2007).

IR photons are less affected by dust absorption than the optical ones. For instance, using optical lines ($H\alpha/H\beta$) the eastern nucleus of the LIRG Arp 299 shows a extinction of $A_V = 2.9$ mag, whereas with the near-IR-optical lines ($Pa\alpha/H\alpha$) the extinction value rises up to $A_V \simeq 6.1$ mag (Alonso-Herrero et al. 2000; García-Marín et al. 2006). This, along with large improvement in IR technology, are some of the reasons why the interest of observing ULIRGs in the IR range has increased over the years.

The first attempts to identify features of AGNs in the near-IR were based on the detection of the coronal line $[Si\ VI]\lambda 1.96\ \mu m$ or broad IR Hydrogen recombination lines (Goldader et al. 1995; Murphy et al. 1999; Veilleux, Kim & Sanders 1999). These works plus the optical results indicate that about 20%-25% of ULIRGs present clear AGN features; this fraction rises up to 35%-50% for objects with $L_{IR} > 10^{12.3} L_{\odot}$.

More recently, a new diagnostic diagram based on the continuum slope and the equivalent width of the Polycyclic Aromatic Hydrocarbon (PAH) emission feature at $3.3\ \mu m$ (see Fig. 1.4) has been proposed (Risaliti et al. 2006). By analyzing the presence and contribution of AGNs in ULIRGs, they find that about 2/3 of ULIRGs host an AGN. However, their energetic contribution is relevant (>30% of the bolometric luminosity) in only about 20% of the 15 ULIRGs from the BGS (Risaliti et al. 2006).

- **Mid-IR Spectroscopy:**

Using observations of 15 ULIRGs with the ISO satellite, Genzel et al. (1998) proposed a new mid-IR diagnostic diagram based on the line ratios $[O\ IV]/[Ne\ II]$ or $[O\ IV]/1.7 \times [S\ III]$, and the relative strength (lines vs continuum) of the PAH at $7.7\ \mu m$ (see Fig. 1.5 Left). They concluded that 70%-80% of the galaxies of the sample are mainly powered by star formation, and 20%-30% are powered by a central AGN. In addition, in about 50% of ULIRGs observed with ISO, the starburst activity and active nucleus coexist in a circumnuclear disk/ring of about 1-2 kpc. In that sample there is no evidence of AGN dominating the final stages of the merger. The fraction of ULIRGs hosting an AGN was corroborated by Rigopoulou et al. (1999) using a large sample of ULIRGs. They found that the differences on the spectra around $8.0\ \mu m$ between starburst galaxies, AGN, and ULIRGs probes the validity of the PAH diagnostic diagram as a tool to segregate the galaxies according to their ionization source (Fig. 1.5 Right).

The launch of the *Spitzer* Space Telescope in 2003 was another landmark in the mid-IR observations of ULIRGs. For instance, Surace et al. (2006) have discovered (qualitatively) extended dust emission in the bodies and the tidal tail features of ULIRGs.

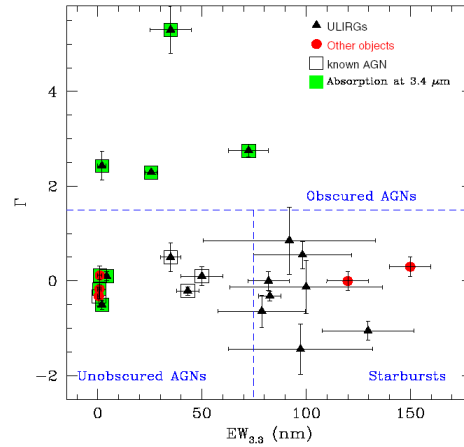


Figure 1.4: Near-IR diagnostic diagram proposed by Risaliti et al. (2006). Γ - $EW_{3.3}$ for a sample of ULIRGs and control sources. Γ represents the slope of the continuum power law, defined as $f_{\lambda} \propto \lambda^{\Gamma}$ in the L-band spectra. Γ ranges from -2 to ~ 3 . $EW_{3.3}$ is the equivalent width of the broad emission feature at $3.3 \mu\text{m}$ rest-frame. The origin of this line is believed to be the reprocessing of UV radiation by PAH molecules.

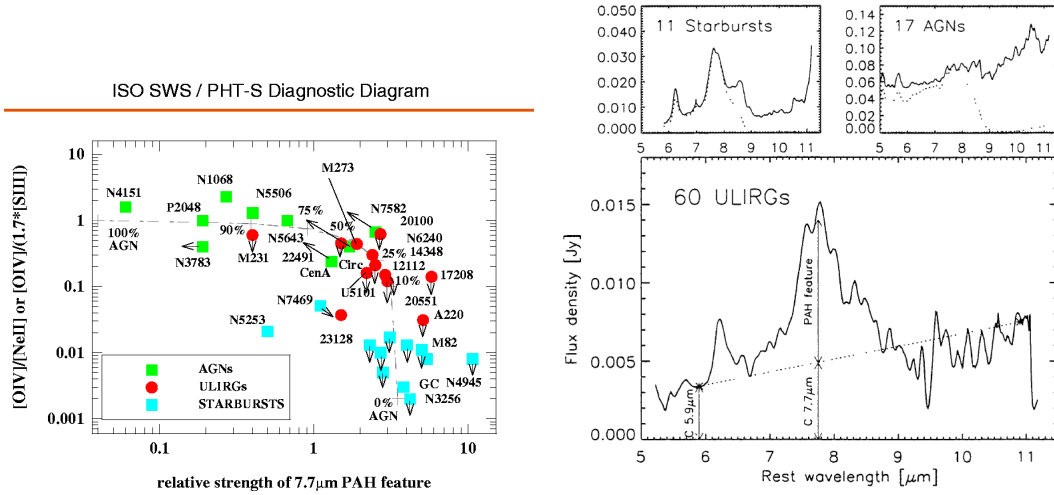


Figure 1.5: **Left:** Diagnostic diagram based on ISO data (Genzel et al. 1998). **Right:** Average ISOPHOT-S spectrum of a sample of ULIRGs, individually scaled to $S_{60}=1$ Jy. Average spectra of starburst galaxies and AGNs are shown for comparison. The dashed lines represent these spectra after applying an additional $A_V=50$ foreground extinction and re-scaling for display purposes (Lutz et al. 1998).

Elliptical galaxies do not show such emission, reflecting a bias in the optical selection or evolution in the distribution of gas with the merger. Interstellar crystalline silicates have been detected in 11 ULIRGs, pointing to massive stars as responsible for their origin (Spoon et al. 2006). With respect to the energy source, Mrk 231 (optically classified as Seyfert 1) shows strong silicate absorption (Weedman et al. 2005), but no clear indication for the presence of an AGN in the mid-IR (i.e., no high excitation lines such as $[\text{Ne VI}]$ are detected, Armus et al. 2007). More recently, using spectroscopic data, Imanishi et al. (2007) conclude that about 30% (possibly 50%) of the observed optical non-Seyfert ULIRGs can be explained with emission consisting of low energetic

modestly obscured ($A_V < 20\text{-}30$ mag) PAH-emitting normal starbursts. In addition they detect an energetically dominant, highly obscured centrally concentrated source with no-PAH emission. The latter can be interpreted as an AGN.

- **Molecular Gas Observations:**

Whether the energy source in ULIRGs is star formation and/or accretion onto a black hole, the presence of high amounts of interstellar gas for sustaining the processes involved is necessary. In the case of the starburst activity, to maintain the star formation rate, in the case of the AGN the gas will be needed for “feeding” the central engine.

The content of molecular hydrogen (H_2) can be traced using the $CO(J=1 \rightarrow 0)$ and $CO(J=2 \rightarrow 1)$ lines at millimeter wavelengths. As derived from observations of those transitions, ULIRGs (as well as LIRGs) are known to have large quantities of molecular gas, ($\gtrsim 10^9\text{-}10^{10}M_\odot$, Sanders et al. 1991; Solomon et al. 1997; Bryant & Scoville 1999; Tacconi et al. 1999; Evans et al. 2002). This reservoir of gas is concentrated in their central kpc ($r < 0.5\text{-}1$ kpc).

The Star Formation Efficiency (SFE), a parameter defined as the ratio L_{IR}/M_{H_2} , can be interpreted either as an increase of the star formation rate (SFR, i.e., higher efficiency on the star formation) or as a possible evidence for AGN contribution (Sanders & Mirabel 1996). The values of the SFE range between $10 < L_{IR}/M_{H_2} < 100 L_\odot M_\odot^{-1}$, being $\sim 100 L_\odot M_\odot^{-1}$ an empirical upper limit (Planesas et al. 1997). When the observed L_{IR}/M_{H_2} ratio ranges between 10 to $30 L_\odot M_\odot^{-1}$, the infrared luminosity is dominated by star formation alone. When L_{IR}/M_{H_2} observed ratio ranges between 30 to $100 L_\odot M_\odot^{-1}$, the infrared luminosity is increasingly dominated by the central AGN.

There are two surveys dedicated to the study of molecular gas content in separated pairs of ULIRGs, Dihn-V-Trung et al. (2001) and Evans et al. (2002). The main conclusion from these works is that about 2/3 of the molecular gas lies near the most active nucleus. On the contrary, using higher angular resolution data, Graciá-Carpio et al. (2007) found one ULIRG where the most active galaxy does not have the largest amount of molecular gas, but a large nuclear dust concentration.

- **Radio Continuum Observations:**

There is a strong correlation between the infrared flux and the radio continuum found in normal, starbursts and Seyfert galaxies (van der Kruit et al. 1971; Rieke & Low 1972; Helou et al. 1985; Sanders & Mirabel 1985; Yun, Reddy & Condon 2001). This relation allows to study compact nuclei of luminous IR galaxies in spectral regions with high optical depth using radio interferometry. One of the pioneering studies of a complete sample of luminous IR galaxies was carried out by Condon et al. (1991) (40 galaxies, 6 ULIRGs observed with the VLA at 4.85 GHz). They demonstrated that the compact IR nuclei were consistent with star formation. Further studies revealed a cluster of luminous radio supernovae in the ULIRG Arp 220 (Smith et al. 1998). This is a clear evidence for high SFR, estimated then as $100M_\odot \text{ yr}^{-1}$ (Colina & Pérez-Olea 1992; Smith, Lonsdale & Lonsdale 1998). Such star-forming rate would explain the IR luminosity by itself, without the need for an AGN. In addition, other works have pointed out the possibility of additional clusters of supernovae in other ULIRGs: *IRAS* 17208–0014, Mrk 299, and Mrk 273 (Momjian et al. 2003; Neff, Ulvestad & Teng 2004; Bondi et al. 2005). Nonetheless, there are ULIRGs where the radio emission is

dominated by an AGN (e.g., Mrk 231, Lonsdale et al. 2003). In any case, even when the AGN is dominating the radio structure, its contribution is small compared to the IR emission which is dominated by the star formation (Colina & Pérez-Olea 1995; Carilli et al. 1998; Farrah et al. 2003).

- **X-ray Observations:**

The interest of observing ULIRGs in the X-ray range arises from the fact that X-rays coming from an AGN can pass through large column densities and be detected. In fact, hard X-ray emission can penetrate heavy extinctions, with N_H as large as 10^{24} cm^{-2} . Therefore, observations at this wavelength range have been used as a diagnostic to discriminate between AGN and star formation (Rieke 1988). In the past years, observations of individual or small samples of galaxies have been carried out using ROSAT, ASCA, and BeppoSAX.

Based on the weakness of the soft X-ray emission in 10 galaxies from the BGS, Rigopoulou et al. (1996) ruled out the possibility of these objects being a quasar with a modest line of sight reddening. Additional support to the low X-ray emission in ULIRGs is obtained from a ROSAT survey. Only about 10% of 323 ULIRGs were detected in soft X-ray emission (Boller et al. 1998). However, the effect of the quasar could be diluted due to the expected column density from the CO measurements (about 5×10^{23} cm^{-2}). There are, of course, ULIRGs with confirmed AGN detections using ASCA and CHANDRA, such as Mrk 231, Mrk 273, or the case of Arp 220 whose spectra present an emitting point source. The analysis of ULIRGs as observed with the XMM satellite concludes that the nature of these sources is mixed, and that starbursts dominate over the AGN (Franceschini et al. 2003). In any case, some ULIRGs must harbor luminous X-ray AGN, but they may be hidden by large column densities. That is the case of Mrk 231, where BeppoSAX revealed a highly absorbed ($N_H \sim 2 \times 10^{24}$ cm^{-2}) power law component (Braitto et al. 2004). Nonetheless this AGN was already detected in the optical (BLRs+Fe II).

Furthermore, soft X-rays are useful to study regions of hot gas and to analyze interaction processes and galactic winds. McDowell et al. (2003) found a correlation between H α and soft X-ray emission in the ULIRG Arp 220. In addition they confirm their relation with presence of star-forming induced super-winds.

1.4 Evolutionary Scenarios

The ULIRG evolution can be understood from two different points of view: activity and morphology.

Attending to the activity, there have been several efforts to define an evolutionary scenario which explains the observable characteristics of ULIRGs:

- The first model was proposed by Sanders et al. (1988), and postulates that all ULIRGs host a QSO hidden by a cocoon of dust that will disappear with time. The proposed evolution can be summarized as:

$$\text{cold ULIRG} \longrightarrow \text{warm ULIRG} \longrightarrow \text{QSO}$$

- More recently Colina et al. (2001) have proposed an alternative scenario to that of Sanders, where the mass plays a key role. In this model cold ULIRGs would be the final product of the merger of two (or more) low mass ($0.3-0.5L_*$) disk galaxies. Warm ULIRGs and low-luminosity QSO could be explained with the merger of intermediate mass ($0.5L_* < L < L_*$) galaxies. A high luminosity QSO would be the final product of the merger of massive ($>L_*$) galaxies. In this model only warm ULIRGs are explained by a QSO with a dusty envelope.

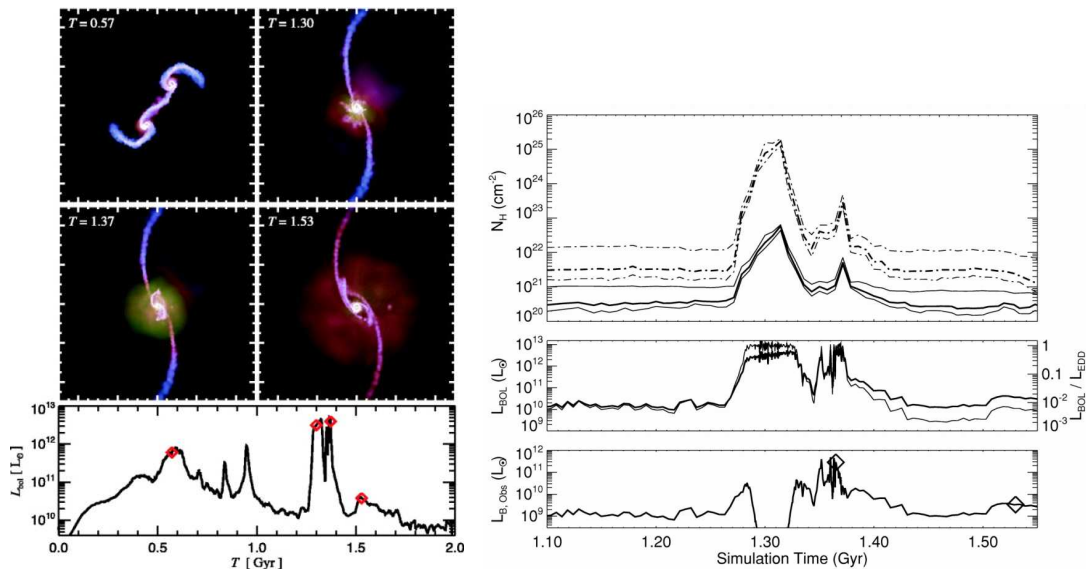


Figure 1.6: **Left Panels:** Projected gas density of the merger of two galaxies shown in boxes of 140 kpc in side, color-coded by temperature (blue to red, upper panels). The bolometric luminosity of the central black hole(s) is shown in the lower panel, with diamonds marking the times shown above. Bolometric luminosities prior to the merger are the sum of the two individual black hole luminosities. **Right Panels. Top:** Thick contours plot the median column density N_H as a function of the simulation time, with thin contours at 25% and 75% inclusion levels. Solid contours represent the density of the “hot-phase” inter stellar medium (ISM), and dashed contours represent the total simulation density. **Right Panels. Middle:** Bolometric luminosity of the black hole, $L_{bol} = \epsilon \dot{M} c^2$ (thick line) and ratio of bolometric to Eddington luminosity, $l \equiv L_{bol}/L_{Edd}$ (thin line). **Right Panels. Bottom:** Observed B-band luminosity calculated given the median hot-phase ISM density. Diamonds mark times shown in the right panel (Hopkins et al. 2005).

Concerning to the morphology observed in ULIRGs, a model where the merger of two disk galaxies evolves until it reaches relaxation, and forms an elliptical galaxy has been proposed (e.g., Kormendy & Sanders 1992; Genzel et al. 2001). Several authors have performed simulations of disk galaxy mergers for testing whether or not they can evolve into an elliptical galaxy. From the variety of simulations some of them are worth to mention. Mihos & Hernquist (1994) used numerical simulations to investigate the triggering of starburst by the merger process (see explanation below). Naab & Burkert (2003) and Naab et al. (2006) have analyzed remnants of disk galaxies mergers, with and without gas, to study their structure and dynamics². The simulations by Hopkins et al. (2005) can be useful to understand whether the central QSO hosted in the merger remnant is visible or not. Essentially, the model proposes that QSOs are originated in mergers, but they are heavily

²A comprehensive explanation of these models will be given in Chapter 3.

obscured for long periods of time by the large gas column densities that are feeding the black hole. In turn, feedback drives away the gas, creating a brief window in time where the black hole is visible as an optical quasar (see Fig. 1.6). Finally, Bekki, Shioya & Whiting (2006) modeled the relative importance of starbursts and AGN in ULIRGs (Fig 1.7). As a result of their simulations, they proposed two different evolutionary paths. For starburst dominated ULIRGs:

$$\text{merger} \longrightarrow \text{ULIRGs} \longrightarrow \text{E+A} \longrightarrow \text{E}$$

with A a post-starburst population and E an elliptical galaxy. Finally, for AGN dominated ULIRGs formed by merged, the proposed evolutionary path is:

$$\text{merger} \longrightarrow \text{ULIRGs} \longrightarrow \text{QSOs} \longrightarrow \text{QSO+A} \longrightarrow \text{E+A} \longrightarrow \text{E}$$

Additional simulations of merger of disk galaxies have been performed by DiMatteo et al. 2005 and Springer 2005. Broadly speaking their results are consistent with those of the previous models.

1.5 Dynamical Processes: the Role of Interactions

The dynamical processes in ULIRGs are dominated by the merger that almost all ULIRGs undergo (Sanders et al. 1988; Borne et al. 2000; Farrah et al. 2001; Veilleux et al. 2002). They present a large variety of morphologies with plumes, tails, one or more nuclei connected by bridges, and a number of objects with amorphous or elliptical-like morphology (§ 1.7). They contain large amounts of gas and dust ($\sim 50\%$ in mass) in their nuclear regions (Solomon et al. 1997). In fact, dust is responsible for some of the complex morphological structures seen in the optical range (Bushouse et al. 2002). Toomre & Toomre (1972) proposed for the first time that the bridges, tails and structures observed in multiple galaxies were produced by close encounters. The main consequences of these merger/fusion processes can be summarized as follows:

- **Formation of Elliptical Galaxies:**

The last phase of the encounter between two disk galaxies can be a galaxy with a mass similar to those of elliptical galaxies of intermediate mass (about $m_* = 1.4 \times 10^{11} M_\odot$; Cole et al. 2001) and a de Vaucouleurs ($r^{1/4}$) surface brightness profile (Schweizer 1982). It has been found that the surface brightness distributions of evolved mergers are well fitted with this profile (Wright et al. 1990). Furthermore, the dynamical characteristics of ULIRGs (see Fig. 1.8), along with their location in the fundamental plane (FP) are consistent with that of low-intermediate mass elliptical galaxies with moderate rotation (Genzel et al. 2001; Tacconi et al. 2002; Dasyra et al. 2006).

- **Formation of Tidal Dwarf Galaxies:**

The so-called Tidal Dwarf Galaxies (TDG) are auto-gravitating entities product of the collision between two disk galaxies (Zwicky 1956). Formally speaking, Duc et al. (2004) define TDGs as those objects whose progenitor galaxy have masses greater than $10^9 M_\odot$, were born in the tidal tails, and were formed by the debris expelled by the merger. In addition to this, Iglesias-Páramo & Vílchez (2001) established a luminosity criteria to classify TDGs candidates ($L(H\alpha) > 10^{39} \text{ erg s}^{-1}$). The formation of TDGs could

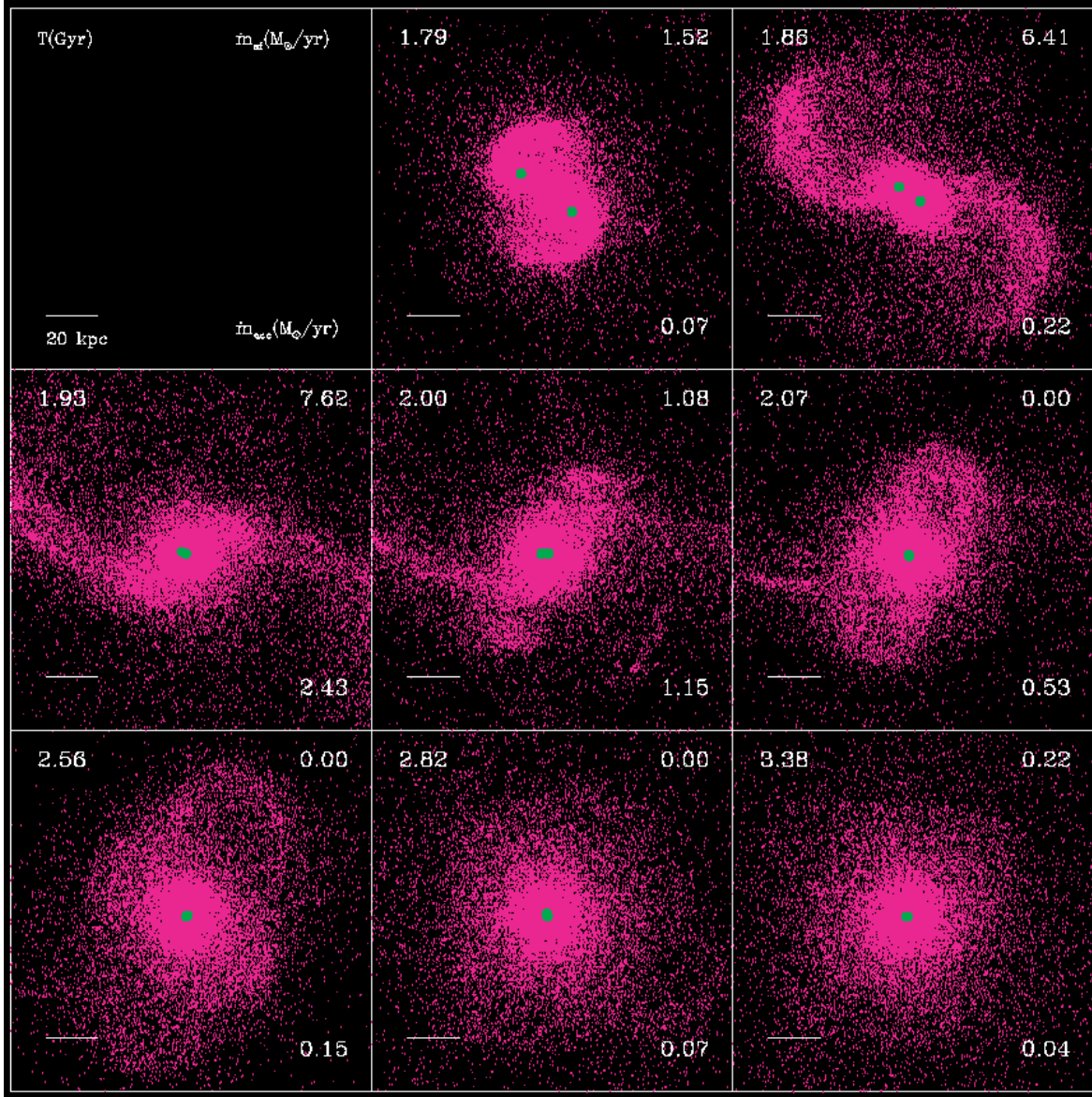


Figure 1.7: Snapshots of the mass distribution projected onto the xy plane from numerical simulations of ULIRGs (Bekki, Shioya & Whiting 2006). Stellar particles (old stars) and gaseous ones are shown in magenta (i.e. dark halo particles are not shown). Big green dots represent the location of the super-massive black holes. Time (T , Gyr), SFR (\dot{m}_{sf} in units of $M_{\odot} \text{ yr}^{-1}$), accretion rate (\dot{m}_{ac} in units of $M_{\odot} \text{ yr}^{-1}$), and the simulation scale are shown at upper left-hand panel, lower-right hand panel, and lower-left hand panel, respectively, for each frame. Time T represents the time elapsed since the simulation starts. Note that the accretion rate can become very high when the two bulges finally merge (i.e. when the two super massive black holes become very close to each other).

account for the lack of globular clusters in elliptical galaxies, despite the fact that they could contain super star clusters (Kennicutt & Chu 1988). ULIRGs have all the necessary conditions for being the ideal “nurseries” for TDGs. In fact, they have been detected in several ULIRGs using optical integral field spectroscopy (IFS, Monreal-Ibero et al. 2007).

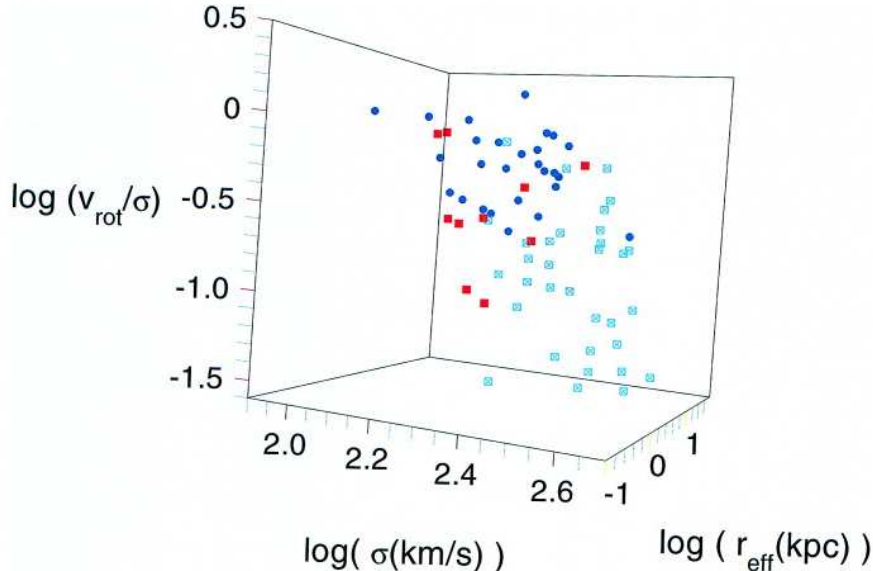


Figure 1.8: σ - r_{eff} - v_{rot} distribution of ULIRGs merger (filled red squares), boxy giant ellipticals (light blue open squares with crosses; $M(B) < -20.5$, $B-K=3.9$), and disk ellipticals/lenticulars (dark blue filled circles; $M(B) < -18.5$, $B-K=3.9$). Elliptical data from Bender et al. 1992; Faber et al. 1996. Note that because of beam smearing and inclination effects, the ULIRGs rotation velocities are lower limits (Genzel et al. 2001).

- **Bursts of Star Formation:**

Starburst activity can be triggered by the merger of two disk galaxies, which on their first passage may activate an ultra-luminous phase (i.e., fueled by star formation). Fig. 1.9 shows the relative SFR for merging disk galaxies with and without bulge, as described by the model of Mihos & Hernquist (1996). The absence of bulge implies the formation of a bar between the galaxies that transfers material from the disks towards the center, which in turn triggers star formation in the early phases of the interaction (after about 26 Myr). A SFR on average 10 times the initial one is sustained by about 150 Myr. As a result, this early conversion of gas into stars depletes the starburst, and the star formation dies out before the final merger (at about 90 Myr after the first encounter). The simulations of galaxies with bulge do not form a strong bar, and thus the initial bursts of star formation are not so intense. As a consequence, in the last phases of the encounter a large amount of material is channeled to the center. This produces a violent (about 70 times the initial) and short-lived (~ 50 Myr) starburst once the galaxies have coalesced.

A large percentage of ULIRGs, that undergo mergers processes, present strong emission lines ($H\alpha$, $P\alpha$, $Br\gamma$) useful for deriving the SFR (of about $100M_{\odot} \text{ yr}^{-1}$; Colina et al. 2000; Smith, Lonsdale & Lonsdale 1998). Direct evidence for the relevance of the

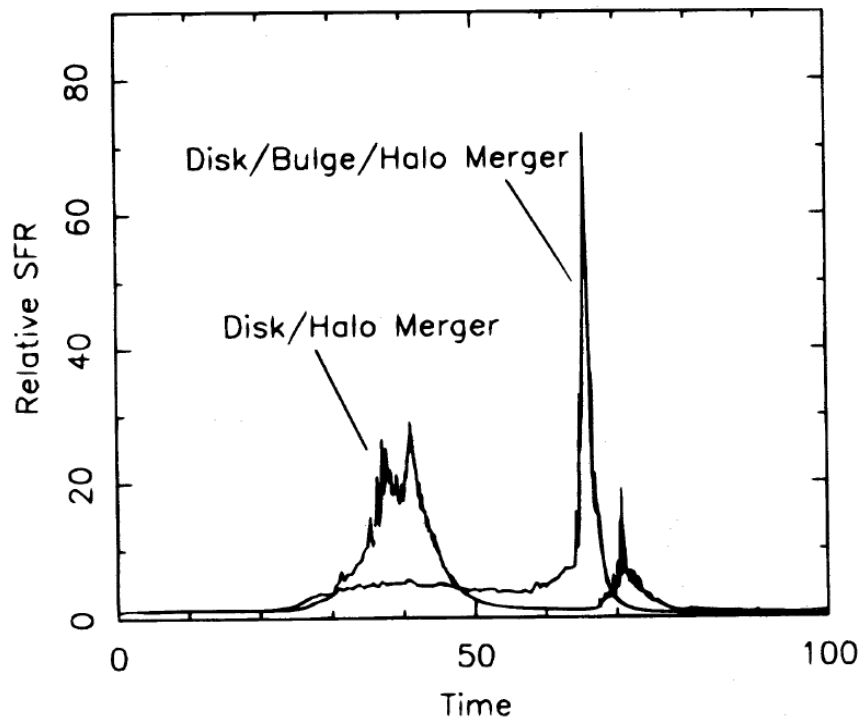


Figure 1.9: Evolution of the global star formation rate (relative to two isolated disks) for galaxies with and without bulge. The time units are in 1.3×10^6 yr (Mihos & Hernquist 1996).

starbursts comes from spectra between $0.2\text{--}3\mu\text{m}$, where strong absorption lines produced by young stars can be found (e.g., Genzel et al. 2001 and references therein). The presence of massive molecular disks associated with intense star formation gives further support to the presence of strong star formation.

- **Wind-Driven Enrichment of the Intergalactic Medium:**

There are evidences of super-winds in ULIRGs (Heckman et al. 1990, 1996; Veilleux et al. 1995) that can be detected in the spectra as kinematic multicomponents. They may reach values of several hundreds of km s^{-1} and be extended to kpc scales. One of the mechanisms that may produce the winds detected in ULIRGs is star formation (SFR of the order of $100 M_{\odot} \text{ yr}^{-1}$, Veilleux et al. 2005). In fact, some authors find that more than 75% of ULIRGs may have winds (e.g., Rupke et al. 2002, 2005b; Martin 2005). The kinetic energy produced by the supernovae combined with stellar winds induced by star formation, are responsible for outflows that extract material from the galaxy and enrich the intergalactic media (Heckman et al. 1990). Moreover, super-winds in ULIRGs could provide an explanation to the high abundances in metals of the intra-cluster medium and the enrichment of the media in clusters of galaxies (Elbaz et al. 1992).

1.6 The Deep Universe: ULIRGs in the Context of High- z Galaxies

In 1946, Gamov predicted the existence of a cosmic radiation background whose origin was associated with the beginning of the Universe. This fact was confirmed by Penzias & Wilson (1964). In 1989, NASA launched the Cosmic Background Explorer (COBE), with the mission of measuring the diffuse infrared background radiation from the early universe; in fact, it detected anisotropies in the cosmic microwave background (CMB). Later on, Puget et al. (1996) and Hauser et al. (1998) confirmed the presence of a FIR-submm background radiation. This radiation, whose origin is the combination of sub-mm galaxies and *Spitzer* sources, has about the same value than the optical background radiation.

In spite to its relatively bright detection limits, the *IRAS* satellite detected a strong evolution in the luminosity function of ULIRGs (and LIRGs) out to (at least) $z \sim 0.5$. In addition, it detected high- z lensed sources (up to $z=2.286$; Lonsdale et al. 2006 and references therein). In the last few years, and with the new generation of instruments, a population of (U)LIRGs located at cosmological distances has been detected. Furthermore, they are hundreds of times more abundant in the high- z Universe than locally.

The population of high- z bright IR galaxies are the Sub-millimeter galaxies, the (U)LIRGs detected by *Spitzer*, and the Lyman break galaxies, that will be introduced in what follows. Other cosmologically important sources, the red evolved galaxies, will also be discussed.

- **Submillimeter Galaxies:**

Submillimeter galaxies were first detected at $850 \mu\text{m}$ with the Submillimetre Common-User Bolometer Array (SCUBA, Smail, Ivison & Blain 1997, Blain et al. 1999). They represent a population of IR bright galaxies, either powered by intense starbursts ($\gg 100 M_{\odot} \text{yr}^{-1}$) or Compton-thick, dust enshrouded AGN associated with the formation of super-massive black holes (Blain et al. 2002; Ivison 2002). Submillimeter galaxies are mainly located at $z \geq 2$ (see Fig. 1.10), and their spatial density at $z \sim 2$ is about 1000 times larger than in the local Universe (Chapman et al. 2003). Furthermore, they have been imaged by *Spitzer* at $z > 2.5$. *Spitzer* spectroscopic data with IRS have shown that PAH emission of sub-mm galaxies is consistent with that of the local ULIRG population (Lutz et al. 2005). This fact, along with the similarity between the SEDs of low- z ULIRGs and sub-mm galaxies (Blain 2002), and their dusty star-forming nature are the reasons why they are thought to be ULIRGs at high- z , and therefore progenitors of the giant elliptical galaxies of the local Universe (Smail et al. 1997; Blain et al. 1999; Scott et al. 2002).

The same type of galaxies have been detected at $1200 \mu\text{m}$ with the Max-Planck Millimeter Bolometer array (MAMBO, Bertoldi et al. 2000; Eales et al. 2003). Although these sources are located at $z > 3$, the combined population of Submillimeter galaxies detected by SCUBA and MAMBO does not appear to have a significant presence at $z > 3$ (Greve et al. 2004).

- **(U)LIRGs Detected by *Spitzer*:**

The *Spitzer* space telescope, working in the $3\text{-}180 \mu\text{m}$ range, has carried out studies of the MAMBO and SCUBA sources and in galaxies at high- z (e.g., Ivison et al. 2004; Yan

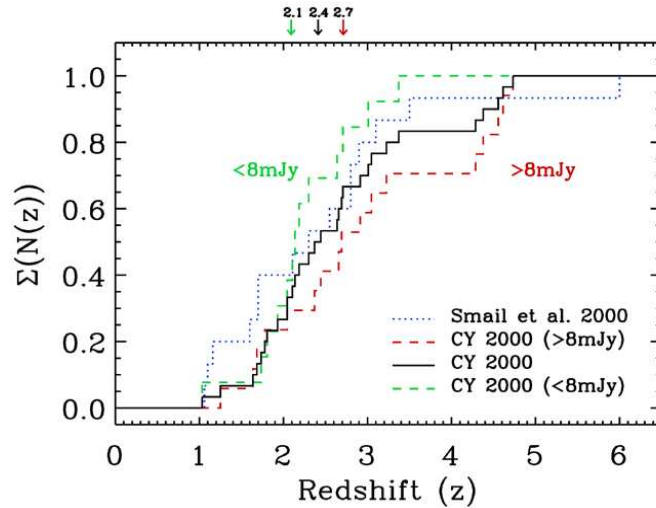


Figure 1.10: Cumulative redshift distribution, $\Sigma(N(z))$, of the 8 mJy SCUBA sample as deduced from the spectral index between 1.4 GHz and $850\mu\text{m}$ using the CY redshift estimator (Carilli & Young, 2000; solid line). For comparison, $\Sigma(N(z))$ for the complete SCUBA lens survey by Smail et al. (2000, 2002) has also been plotted (dotted line). $\Sigma(N(z))$ for ≥ 8 and ≤ 8 mJy sources are plotted as dashed lines assuming the CY model (Iverson et al. 2002).

et al. 2007), demonstrating the coincidence between the SED of the SCUBA sources and ULIRGs (Egami et al. 2004). Moreover, the analysis of deep images at $24\mu\text{m}$ revealed the existence of a population of ULIRGs at redshifts between 1 and 3 not previously detected (Le Floc’h et al. 2004; Papovich et al. 2004). From the study of more than 8000 sources detected at $24\mu\text{m}$, it is concluded that the contribution of LIRGs and ULIRGs to the total SFR density increases from $z\sim 0$ up to $z\sim 2.5$, accounting for at least half of the newly born stars by $z\sim 1.5$ (Le Floc’h et al. 2005; Pérez-González et al. 2005; see Fig. 1.11). Further confirmation to this was provided by Caputi et al. (2006) by comparing K-band selected galaxies in the GOODS field with those detected at $24\mu\text{m}$.

- **Lyman Break Galaxies:**

The Lyman-break galaxies (LBGs) were discovered as a significantly concentration of galaxies at $z\sim 3$ (Steidel et al. 1998). To look for this high- z galaxies, Giavalisco et al. (1998) defined a color criteria (Eqs. 1.1, 1.2) based on the Oke & Gunn (1983) scale magnitudes. The colors were such that they could detect the Lyman Break at $\lambda_{rest}=912\text{Å}$ for galaxies at $z\approx 3$. Further confirmation of the redshift in this galaxy class was given by Steidel et al. (2003) using ground-based spectroscopy.

$$(U_n - G) \geq 1.0 + (G - R) \quad (1.1)$$

$$(G - R) \leq 1.2 \quad (1.2)$$

The LBGs are very bright in the ultraviolet due to the starbursts triggered by the fusion processes (Sommerville et al. 2001). Furthermore, using *Spitzer* observations, Rigopoulou et al. (2006) analyzed the SED of LBGs, and established a connection

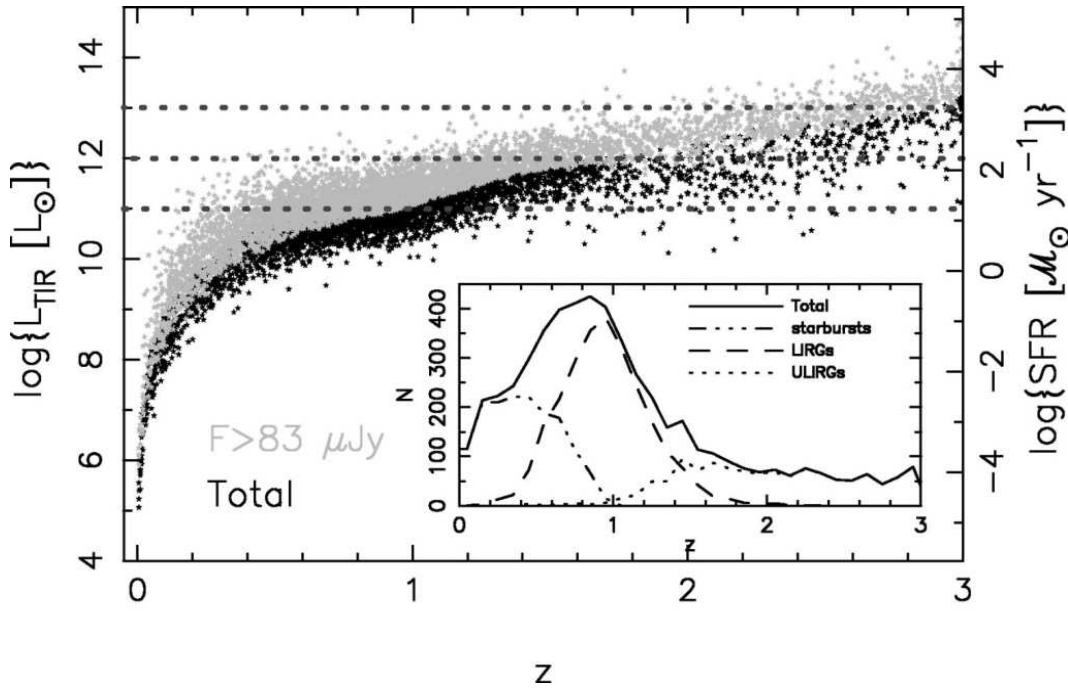


Figure 1.11: Selection effect on the total IR (TIR in plot) luminosity for the Pérez-González et al. (2005) 24 μm survey. Black stars represent the entire sample, and sources with flux above 83 μJy are represented with gray stars. The divisions for LIRGs ($10^{11} < L_{\text{IR}} < 10^{12} L_{\odot}$), ULIRGs ($10^{12} < L_{\text{IR}} < 10^{13} L_{\odot}$), and HyLIRGs ($L_{\text{IR}} > 10^{13} L_{\odot}$) are marked with horizontal lines. The inset plot shows the redshift distribution of sources with flux above 83 μJy divided into three luminosity ranges: starbursts ($L_{\text{IR}} < 10^{11} L_{\odot}$), LIRGs ($10^{11} L_{\odot} < L_{\text{IR}} < 10^{12} L_{\odot}$), and ULIRGs ($L_{\text{IR}} > 10^{12} L_{\odot}$).

between them and the Submillimeter galaxies. Nonetheless, although Lyman Break galaxies are object of much interest, it is not clear yet whether they are ULIRGs or not.

- **Red Galaxies:**

In the color magnitude relation, the galaxies are naturally segregated into two main groups (1) the late type star-forming galaxies located in the 'blue cloud', and (2) the early type quiescent galaxies located in the 'red sequence' (Fig. 1.12). These two categories are clearly separated, locally as well as at high- z . One of the key problems to solve today is how galaxies migrate from the blue cloud to the red sequence, i.e., how the strong star formation is suppressed. Mechanisms like feedback from an AGN in later phases of galaxy evolution (e.g., Springel et al. 2005; Croton et al. 2006) have been proposed for quenching star formation.

In this context, and taking into account that ULIRGs appear to be key in the formation of early type elliptical galaxies, it is interesting to describe the population of massive red galaxies located at different redshifts (McCarthy et al. 2004):

- The J-K galaxies, located at $z > 2$ and selected using a color criteria ($J-K > 2.3$). These galaxies are very rich in gas and dust, and have $\text{H}\alpha$ equivalent widths similar to those of the local LIRGs (20-30 \AA), SFR of 200-300 $M_{\odot} \text{yr}^{-1}$, and masses of between $1-5 \times 10^{11} M_{\odot}$ (van Dokkum et al. 2004).
- The red evolved galaxies from the Gemini Deep Deep Survey (GDDS), located at

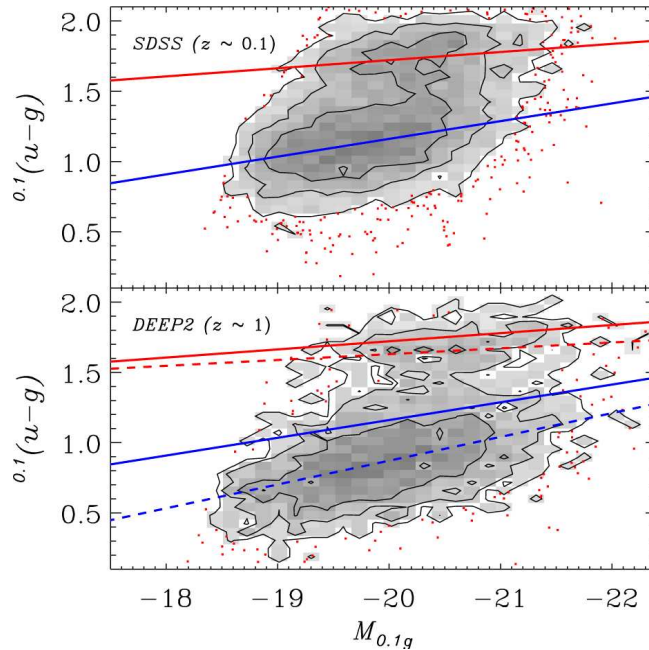


Figure 1.12: Sloan Digital Sky Survey (SDSS) predicted (top) and observed (bottom) distribution of color and absolute magnitude. The prediction assumes no change in the galaxy population between redshifts of $z=0.1$ and $z=1$. The upper solid line in each panel indicates the locus of the red sequence in the SDSS prediction. The lower solid line indicates the locus of the blue sequence in the SDSS prediction. The dashed lines in the bottom panel indicate the corresponding loci in the DEEP2 data. The red and blue sequences are both bluer at high- than at low- z (Blanton 2006).

$z \sim 1.3-2$ and whose integrated light is dominated by evolved stars (McCarthy et al. 2004).

- The extremely red objects (EROs) located between $0.9 < z < 1.3$ and detected with observing programs like the K-selected survey K20 (Cimatti et al. 2003). The identification of four old fully assembled massive ($> 10^{11} M_{\odot}$) spheroidal galaxies at $1.6 < z < 1.9$ has been reported by Cimatti et al. (2004). The existence of such old galaxies in the young Universe (when it had one quarter of its present age) shows that the build-up of massive early-type galaxies was faster in the early Universe than expected.
- Distant Red Galaxies (DRGs; $J - K_s > 2.3$) located at $z \sim 1-3$ have been observed with *Spitzer* too (Papovich et al. 2006). They have typical stellar masses $M_{\star} \gtrsim 10^{11} M_{\odot}$, and about half of these objects have SFR between $100-1000 M_{\odot} \text{ yr}^{-1}$.

ULIRGs, as candidates to be the progenitors of today’s intermediate mass elliptical galaxies, may represent the link between these two galaxy “color” stages: the “blue cloud” and the “red sequence”. This stresses the importance of studying ULIRGs at high- z as well as locally, to understand the internal processes that are undergoing.

1.7 Thesis Project

The investigation of (U)LIRGs (and galaxies in general) can be done using two different approaches: (1) Surveys of thousands of objects, useful to study global integrated

properties, and (2) detailed analysis to study the internal structure of the galaxies. In the last few years a variety of deep surveys are being carried out using state-of-the-art instrumentation (e.g., 2MASS Skrutskie et al. 2006, SDSS Alderman-McCarthy et al. 2006, 2dF Colless et al. 2001, UDF Beckwith et al. 2006, GOODS Giavalisco et al. 2004, COSMOS Capak et al. 2007, and GEMS Rix et al. 2004 among others). These studies have provided statistically significant results, and observational restrictions on the integrated properties (such as luminosity functions, stellar masses, and sizes) of galaxies. Nonetheless, an exhaustive analysis of galaxies needs from the other approach too: the detailed study of the internal properties such as the ionization state, kinematics, dust distribution, and the stellar populations. To that end it is needed to have two-dimensional spectral information over the spectral range of interest, like that provided by IFS.

The study of ULIRGs started with the observations of the IRAS satellite, whose results were key to define, select, and obtain their first IR fluxes (e.g., Soifer et al. 1984; Sanders et al. 1988). In the context of optical observations, those investigations were complemented with nuclear long-slit spectroscopy, used to determine their main energy source (e.g., Veilleux et al. 1995). From a morphological point of view, the true complexity of ULIRGs was not unveiled until the advent of the high angular resolution of the *HST* images (e.g., Borne et al. 2000; Scoville et al. 2000). In fact, the combination of these multiwavelength images with optical IFS obtained with the INTEGRAL system has been used to carry out comprehensive 2D-studies in individual or small samples of ULIRGs (e.g., Arribas, Colina & Borne 1999; Monreal-Ibero 2004).

This thesis presents, for the first time, the two-dimensional spectroscopic analysis of the internal physics, structure and kinematics of a representative (~ 20) sample of low- z (U)LIRGs. The study is based on optical IFS from the INTEGRAL instrument and high resolution *HST* images. For completeness, the analysis includes the data of the previously published ULIRGs observed with INTEGRAL (see Colina, Arribas & Monreal-Ibero 2005; García-Marín et al. 2006 and references therein). The work is divided into three main parts.

- **Stellar, ionized gas, and dust distribution:**

The first part is presented in Chapter 3, and deals with the morphological study of the galaxy sample. The aim is to characterize the galaxies, looking for structural differences related to the merger phase, and to test the elliptical-through-merger scenario. The distribution of the stellar component, the ionized gas and the dust (i.e., internal differential extinction) will be presented, along with the surface brightness distribution of the sample of galaxies. The isophotal morphological parameters derived for galaxies in evolved merger phases will be compared with theoretical models of galaxy merger remnants. In addition, the parameter V/σ will be used to analyze the dynamical stage, and to compare with the models.

- **Structure of the 2D-Ionization State:**

The second part is presented in Chapter 4, and is dedicated to study the two-dimensional distribution of the ionization state, and to investigate which mechanisms are responsible for it. We will analyze the origin of the warm gas excitation structure in the galaxies, and will establish whether or not there are behaviors that depend on the merger phase. That is, localized energy sources associated to starbursts, shocks and presence of an AGN. The origin of the LINER-like ionization will be investigated, comparing the obtained results with those of theoretical models.

The integrated excitation level of ULIRGs will be compared with that of the SDSS emission-line galaxies. Finally, the aperture effects in the determination of the ionization state, as well as the consequences for high- z galaxies classification, will be discussed.

- **2D-Kinematics and mass derivation:**

The third part is presented in Chapter 5, and analyzes the two-dimensional kinematics of the warm gas in the sample of galaxies. The degree of rotation in ULIRGs will be tested by fitting the observed velocity field with a simple thin rotating disk. The galaxy masses will be derived using two methods: the nuclear velocity dispersion and, assuming rotation, the velocity amplitude fitted with the model. Finally, the location of ULIRGs in the fundamental plane will be discussed.

This thesis deepens our knowledge about ULIRGs, and represents the first 2D study of their physical and kinematic conditions performed in a local representative sample of this galaxy type. We find that the merger basically governs the morphology, excitation state, kinematics and dynamics in this galaxy class. The results regarding the internal structure and its dependence with the merger phase will be useful too to understand the population of ULIRGs located at high- z .

Chapter 2

The Sample of ULIRGs: Selection, Observing Techniques, and Data Treatment

This Chapter is divided into three main parts. The first one addresses the description of the sample of galaxies; it includes the selection criteria and the main characteristics of the selected (U)LIRGs. In the second part the observing techniques are described, along with the set of currently available observations. Finally, the data reduction and analysis are reviewed.

2.1 Introduction

Since their discovery, ULIRGs have been the object of much scrutiny: their bright infrared luminosity and dusty nature, along with their complex morphologies and high star formation rates, have captured the interest of extragalactic astronomers. Classically, optical and infrared studies of ULIRGs have been performed using broad and narrow-band multi-filter images (e.g., Sanders et al. 1988; Scoville et al. 2000; Surace et al. 2000; Cui et al. 2001; Bushouse et al. 2002) and nuclear long-slit spectroscopy (e.g., Veilleux et al. 1994; Kim et al. 1995; Goldader et al. 1997). With these data, photometric studies of the images as well as the analysis of the ionized gas conditions (over the small area covered by the slit) can be done.

Due to the ongoing merger and to the gas and dust-rich nature of the parent galaxies, ULIRGs show a very complex two-dimensional stellar and gaseous structure. In fact, the most interesting regions of the galaxies are not always associated to the nucleus. For instance, the circumnuclear and external regions may be dominated by merger-induced star formation and/or the presence of an accreting black hole. In this context, the extrapolation of the nuclear ionizing conditions to the entire galaxy, or the simplistic view of a 1D rotation curve can be useful for certain types of analysis, but they cannot explain the complexity and consequences of the merger process, and the large scale motions taking place. Therefore, it is clear that to fully understand ULIRGs it is necessary to perform a two-dimensional spectroscopic analysis, that will allow us to study not only the nucleus, but the tails, bright knots, and low surface brightness regions as well.

The present project was conceived as the study of a representative sample of ULIRGs

using two different observational techniques:

- Optical Integral Field Spectroscopy (IFS) obtained with the INTEGRAL fiber-based system (Arribas et al. 1998).
- Multiwavelength high spatial resolution images using the Hubble Space Telescope (*HST*).

Both techniques (and instruments) are the most appropriate to reach the proposed scientific aims (see §1.7). IFS is a technique superior to long-slit spectroscopy as it allows us to perform a two-dimensional spectroscopic study, which is particularly important in non-axisymmetric objects such as ULIRGs. In addition it has other advantages like not being affected by centering errors, slit losses, and non-coverage of extra-nuclear regions of interest (see Fig. 2.1). Additionally *HST* imaging gives an unprecedented level of detail on the galaxy structure, useful for the photometric and morphological characterization.

Although some of the galaxies have been published individually and in small sub-samples (e.g., Colina et al. 2005; García-Marín et al. 2006; Monreal-Ibero et al. 2007 and references therein), the present detailed analysis of a representative sample of ULIRGs using IFS, will allow us to derive general as well as individually interesting structural properties of this type of galaxies.

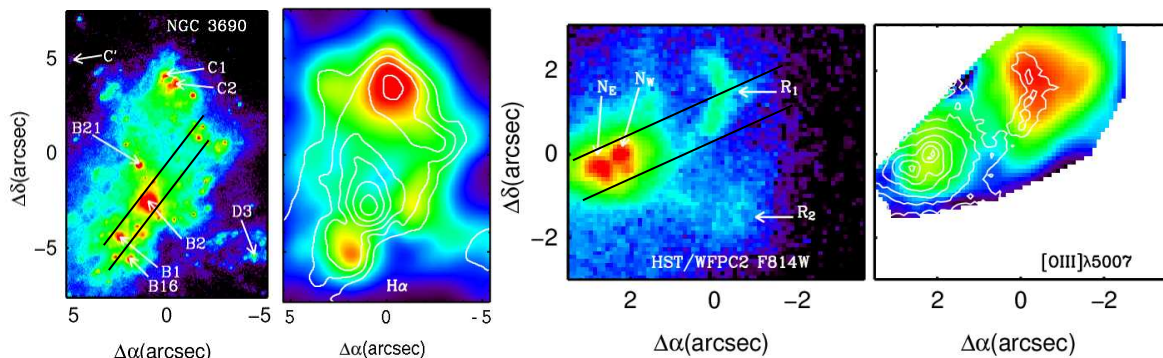


Figure 2.1: Full spatial coverage of IFS vs. longslit spectroscopy. **From left to right:** The first two images show the *HST* F814W ($\lambda_c \sim 0.8 \mu\text{m}$) image and the INTEGRAL $\text{H}\alpha$ for the galaxy NGC 3690 (García-Marín et al. 2006). The third and fourth images show the galaxy IRAS 11087+5351 as observed with *HST* WFPC2/F814W image and the $[\text{O III}]\lambda 5007$ INTEGRAL map. For both galaxies, the plausible position of a slit ($1''.0$ width) centered on the nuclear regions is shown as dark straight lines

2.2 Sample Selection

In this work, as the main goal is to derive general but detailed characteristics of ULIRGs, the decision was to design a *representative* sample of galaxies. This is because working with complete samples (that include a wide range in luminosities and morphological types) is not realistic due to the prohibitively large amount of telescope time needed. Moreover, the large amount of information provided by IFS data can make the information not manageable.

The following criteria were adopted for selecting the final galaxy sample:

- To span all the phases of the interaction process: from first approach to final merger.

Table 2.1: Properties of the Ultra-luminous Infrared Galaxies sample

Galaxy	R.A.(J2000) (hh:mm:ss)	DEC(J2000) (°:′:″)	Activity Class (Optical)	z	D_L (Mpc)	$\log(L_{IR}/L_{\odot})^{(1)}$	f_{25}/f_{60}	Scale (kpc/arcsec)
IRAS 06268+3509	06:30:12.6	+35:07:51.9	H II (C)	0.169	813	12.51 ^(†)	0.27	2.895
IRAS 06487+2208	06:51:45.7	+22:04:27.0	H II (C)	0.144	682	12.57 ^(†)	0.25	2.522
IRAS 08572+3915	09:00:25.4	+39:03:54.4	LINER (E)	0.058	259	12.17	0.23	1.130
IRAS 09427+1929	09:45:32.4	+19:15:34.9	H II (H)	0.149	708	12.10	0.30	2.600
IRAS 11087+5351	11:11:36.4	+53:35:02.0	Sey1 (G)	0.143	677	12.13	0.13	2.507
Arp 299(*)	11:28:30.4	+58:34:10.0	H II/Sey2 (D)	0.010	43	11.81	0.22	0.205
IRAS 12112+0305(*)	12:13:42.9	+02:48:29.0	LINER (E)	0.073	330	12.37	0.06	1.395
IRAS 12490-1009	12:51:40.7	-10:25:26.1	H II/LINER (G)	0.101	465	12.07	0.12	1.854
Mrk 231	12:56:14.2	+56:52:25.2	Sey1 (E)	0.042	186	12.57	0.27	0.832
IRAS 13156+0435	13:18:07.6	+04:18:59.4	H II/LINER (G)	0.113	525	12.13	0.32	2.058
IRAS 13342+3932	13:36:23.3	+39:16:41.9	Sey1 (E)	0.179	866	12.51	0.23	3.026
Mrk 273(*)	13:44:42.0	+55:53:12.1	LINER/Sey2 (B, E)	0.038	167	12.18	0.11	0.749
IRAS 13469+5833	13:48:40.3	+58:18:50.0	H II (I)	0.158	755	12.31	0.06	2.726
Mrk 463	13:56:02.8	+18:22:17.2	Sey1/Sey2 (F, G)	0.050	222	11.81	0.72	0.984
IRAS 14060+2919	14:08:18.9	+29:04:46.9	H II (E)	0.117	545	12.18	0.09	2.113
IRAS 14348-1447(*)	14:37:38.4	-15:00:22.8	LINER (E)	0.083	378	12.39	0.07	1.556
IRAS 15206+3342(*)	15:22:38.0	+33:31:35.9	H II (E)	0.124	580	12.27	0.20(T)	2.232
IRAS 15250+3609(*)	15:26:59.4	+35:58:37.5	LINER (H)	0.055	245	12.09	0.18	1.072
Arp 220(*)	15:34:57.1	+23:30:11.5	LINER (E)	0.018	78	12.20	0.08	0.368
IRAS 16007+3743(*)	16:02:36.9	+37:34:39.7	LINER (H)	0.185	898	12.11	0.18	3.100
IRAS 17208-0014(*)	17:23:21.9	-00:17:00.9	LINER (A)	0.043	190	12.43	0.05	0.844
IRAS 18580+6527	18:58:06.3	+65:31:32.2	H II/Sey2 (G)	0.176	850	12.26	0.08	2.986

Notes: The distances and luminosities were calculated using $\Omega_{\Lambda}=0.7$, $\Omega_M=0.3$, and $H_0=70 \text{ km s}^{-1} \text{ Mpc}^{-1}$. For the luminosity distances, the Wright (2006) cosmology calculator has been used. (1) $L_{IR}(8-1000 \mu\text{m})$ was derived using the recipe given by Sanders & Mirabel (1996); the IRAS fluxes used were obtained from the IRAS Faint Galaxy Sample (Moshir et al. 1993, Vizier on line catalog II/156A). (†) IRAS fluxes obtained from the IRAS point Source Catalog. (*) Galaxies with published results with INTEGRAL. (T) Galaxy with border-line classification. For the present purposes we have classified it as cold. References for the activity class: (A) Arribas & Colina 2003, (B) Colina, Arribas & Borne 1999, (C) Darling & Giovanelli 2006, (D) García-Marín et al. 2006, (E) Kim, Veilleux & Sanders 1998, (F) Miller & Goodrich 1990, (G) This work, (H) Veilleux et al. 1995, (I) Veilleux et al. 1999.

- To cover all types of nuclear activity, i.e., all the different ionization mechanisms; Seyfert-like (i.e., presence of an AGN), H II-like (i.e., star formation activity) and LINER-like (superwinds, shocks...).
- To cover the different FIR colors, using the classification based on the ratio of the IRAS fluxes at 25 and 60 μm . *Cold* is defined as $f_{25\mu\text{m}}/f_{60\mu\text{m}} < 0.2$, and *warm* as $f_{25\mu\text{m}}/f_{60\mu\text{m}} > 0.2$.
- To include only low- z objects. This criterion was introduced for having a relatively high linear resolution to detect intrinsically faint regions.
- To sample the luminosity range up to $\log(L_{IR}/L_{\odot})$ about 12.6.
- To select objects observable from La Palma (latitude +28 degrees), where the INTEGRAL instrument is located.

The final galaxy sample is presented in Table 2.1, along with some basic properties of the objects. The sample is composed of 22 systems (33 galaxies) covering the $\log(L_{IR}/L_{\odot})$ range from 11.81 to 12.57, and with warm (40%) and cold (60%) objects (see histogram in Fig. 2.2). The farthest galaxy is located at about 900 Mpc (i.e., $z \simeq 0.185$). As shown by the *HST* I-band images (Figs. 2.3 and 2.4) and the near-IR ones (Figs. 2.5 and 2.6, see the expected morphological differences due to the dust), we cover different phases of the merger: from galaxies such as IRAS 13156+0435 where the nuclei are located 36 kpc apart, to galaxies like Markarian 231, where the nucleus is no longer buried by a disk envelope and the central QSO is clearly visible.

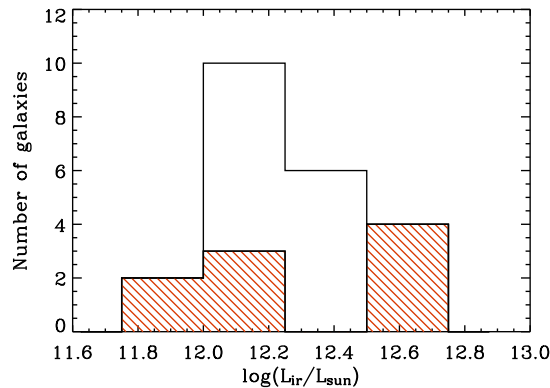


Figure 2.2: IR luminosity distribution for the sample of ULIRGs. The shaded area indicates warm galaxies.

2.3 The Data

In this section a brief description of the techniques, instruments used, and the data reduction is presented. As previously explained, the data used come from two different but complementary techniques: high angular resolution imaging as observed with the *HST* and IFS data from the fiber-based optical IFU INTEGRAL. Both methods are based on completely different concepts, and each one needs for individual and different data reduction techniques. The available dataset for each galaxy is shown in Table 2.2.

2.4 Multiwavelength High Angular Resolution Images: the *HST* Archive Data

The *HST* is a 2.4 m reflector telescope, designed between the 70's and 80's, and located in a low geocentric orbit in 1990. Compared to ground-based facilities, space observations have great advantages, mainly associated to the absence of the atmospheric veil, such as: (1) the access to spectral ranges not observable from the ground, this is particularly convenient in the UV and near-IR ranges. (2) Observations are not limited by seeing conditions; *HST* provides an angular resolution of $\sim 0''.2$ vs. the $\sim 1''.0$ ground-based ones. (3) The goodness of the calibrations due to the stability of the observing conditions.

Here we will use archive data from two instruments, the Wide Field Planetary Camera 2 (WFPC2) and the Near-Infrared and Multi Object Spectrometer (NICMOS)¹.

2.4.1 Wide Field and Planetary Camera 2 (WFPC2)

The WFPC2 is located on the center of the focal plane of the telescope and covers the spectral range from about 1150 to 10500 Å. It is composed of four cameras that operate simultaneously. Three of them (chips 2, 3, 4) have a plate scale of $0''.1 \text{ pix}^{-1}$ and a field of view (FOV) of $80'' \times 80''$, and form the Wide Field Camera. The fourth (chip 1) has a plate scale of $0''.046 \text{ pix}^{-1}$ and a FOV of $36'' \times 36''$, this is the so-called Planetary Camera.

¹Detailed information about the *HST*, its instrumentation and data reduction can be found at www.stsci.edu.

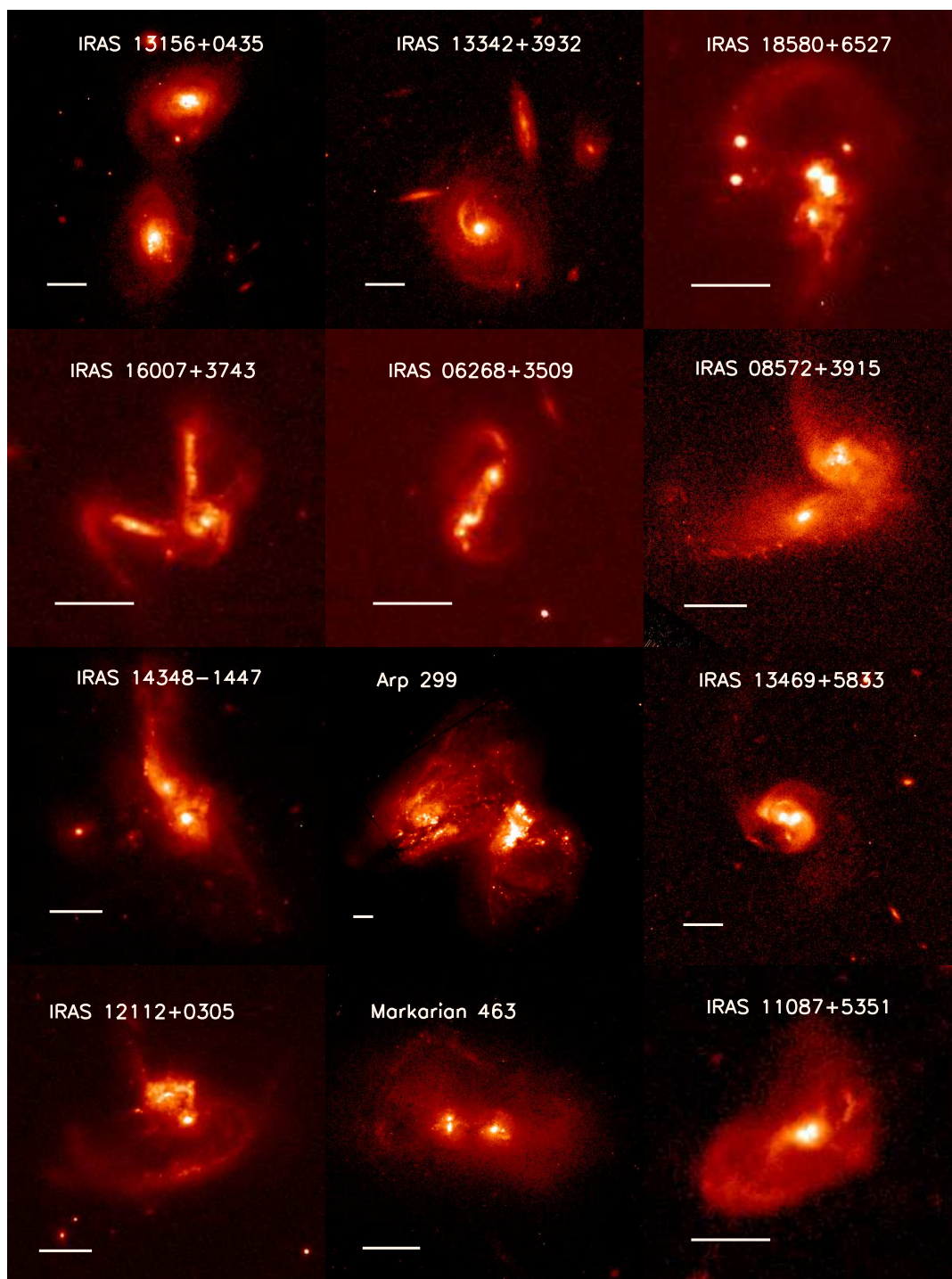


Figure 2.3: *HST* (WFPC2/F814W) images of the sample of galaxies. Orientation is North up East to the left. The horizontal bar indicates 5 arcsec.

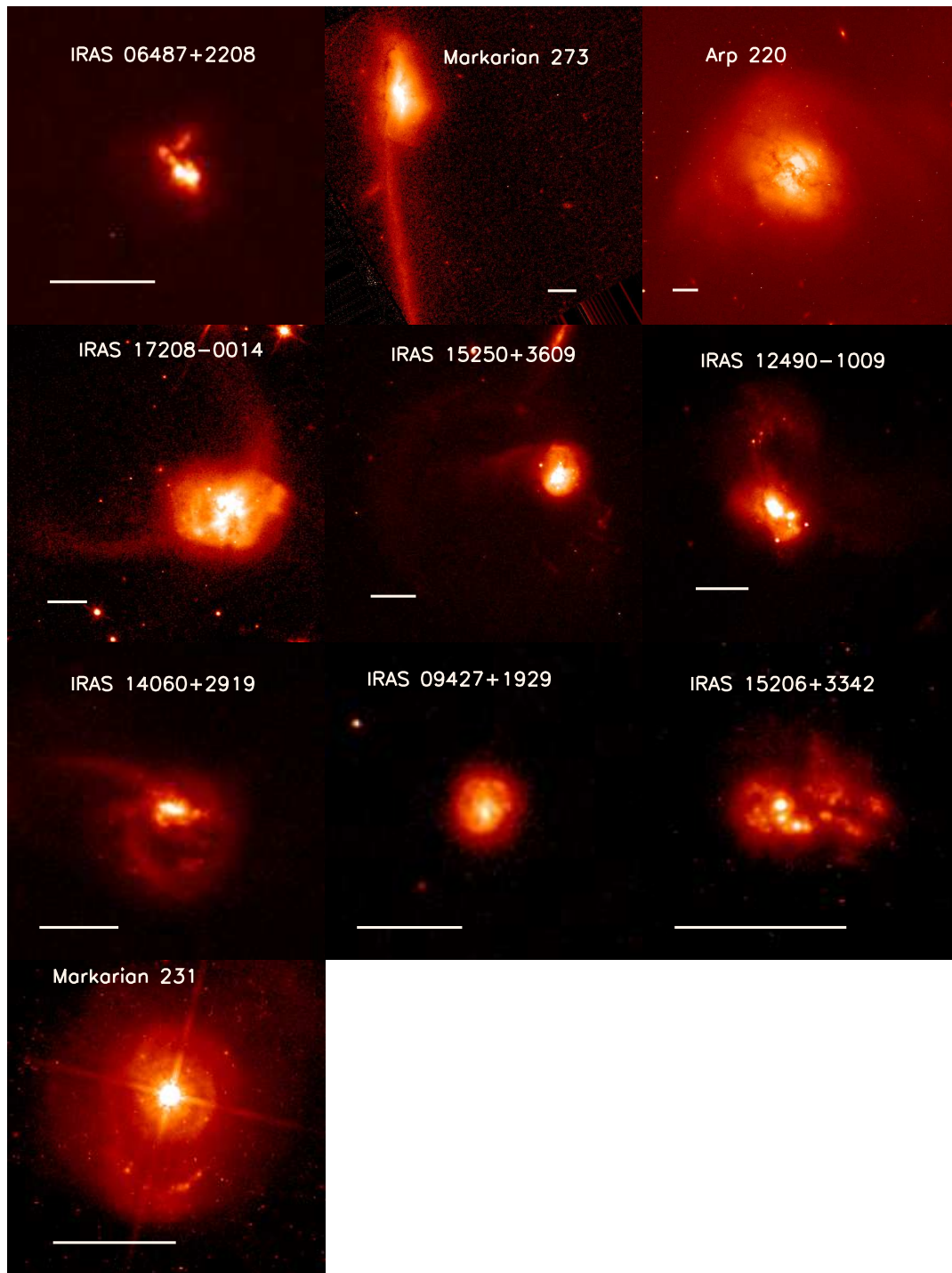


Figure 2.4: *HST* (WFPC2/F814W) images of the sample of galaxies. Orientation is North up East to the left. The horizontal bar indicates 5 arcsec.

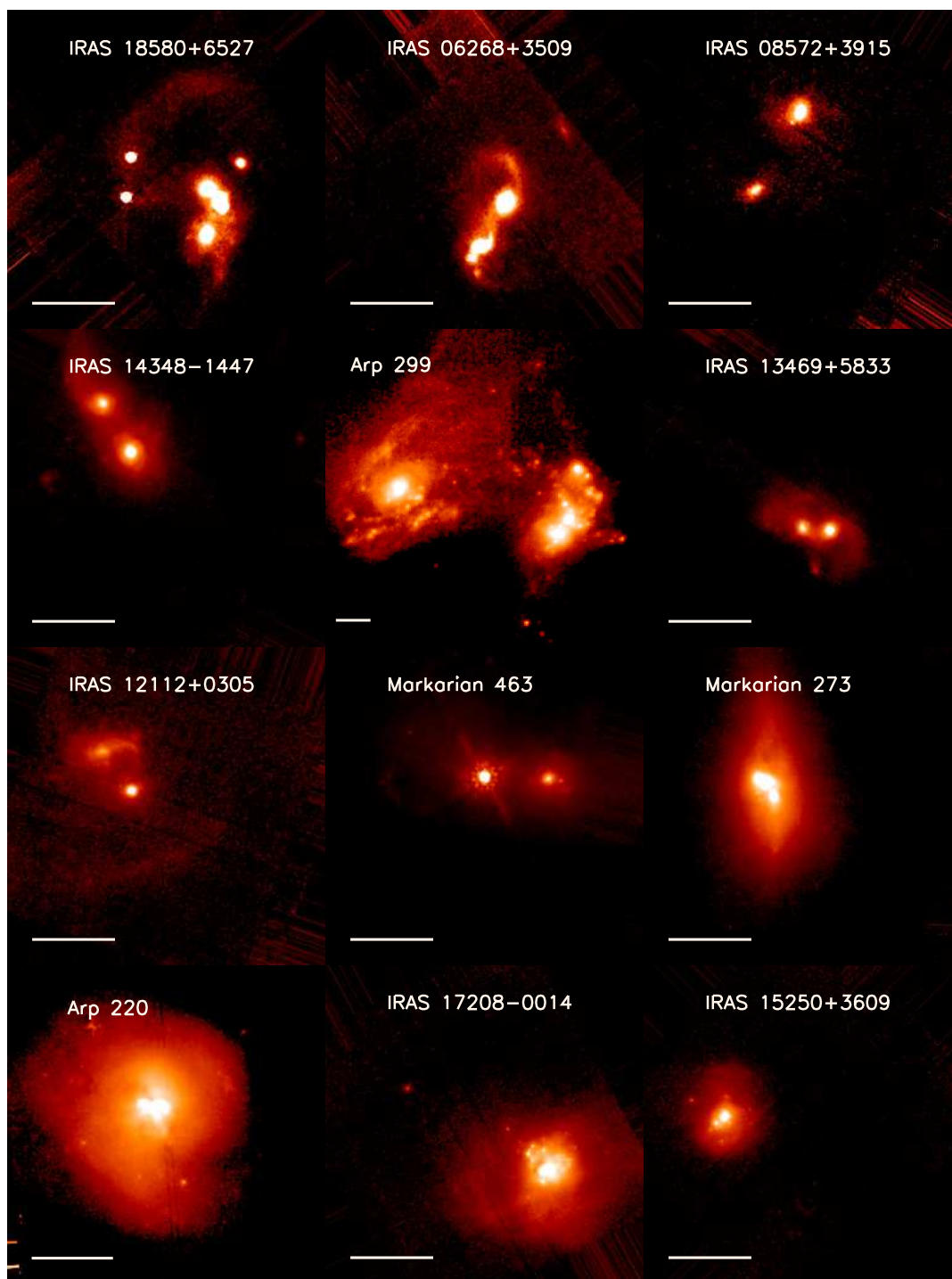


Figure 2.5: *HST* (NICMOS/F160W) images of the sample of galaxies. Orientation is North up East to the left. The horizontal bar indicates 5 arcsec.

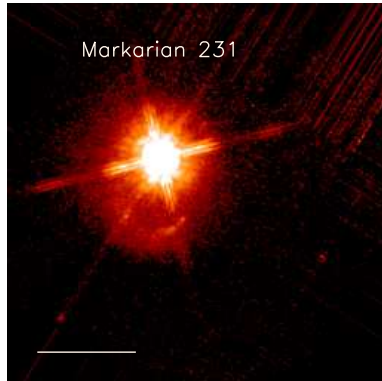


Figure 2.6: *HST* (NICMOS/F160W) image of the galaxy Mrk 231. Orientation is North up East to the left. The horizontal bar indicates 5 arcsec.

The WFPC2 is equipped with narrow (N), intermediate (M) and broad-band (W) filters; in this work we will use the F814W filter, that is similar to the ground-based Johnson-Cousin system I (Origlia & Leitherer 2000). One reason for selecting this filter is that it covers a stellar continuum very close to the red continuum observed with INTEGRAL, being thus useful to compare the structure of both set of data. In addition, the *HST*-F814W image will be used for studying the morphological properties of the galaxies, and to search for structures in the star forming regions such as sharp, bright rims of super-shells or propagating waves of star formation. All the galaxies of the sample have been observed with the F814W filter.

The archival *HST* data were calibrated *on the fly* at the time of de-archiving the images from <http://archive.eso.org>. In a nutshell, the main processing steps used by the WFPC2 pipeline are:

- Update the data quality using a bad pixel mask as reference.
- Correct the value of each pixel for the analog-to-digital correction.
- Subtract the BIAS and DARK images, and perform the flat-field correction.
- Remove shading due to finite shutter velocity.
- Photometric calibration, adding the necessary information for absolute calibration to the header.

Once processed, the derived counts can be transformed into the Vega system magnitudes using:

$$m_{F814W} = -2.5 \times \log_{10} \frac{DN}{EXPTIME} + ZEROPOINT, \quad (2.1)$$

being DN the integrated counts in the defined aperture, EXPTIME the exposure time, and ZEROPOINT a constant of value 21.639, 21.665, 21.659, and 21.641 for the chips 1, 2, 3, and 4, respectively.

2.4.2 Near Infrared Multi Object and Spectrometer (NICMOS)

NICMOS consists of three individual cameras located in one side of the *HST* FOV, and designed to operate independently. The cameras operate at different magnification scales

Table 2.2: Available data: *HST* archive data and INTEGRAL observing logs details

Galaxy	WFPC2 filters	NICMOS filters	INTEGRAL Bundle	Date	Exp-time (s)	Comment on IFU data
IRAS 06268+3509	F814W	F160W	SB2	03/02	6×1500	
IRAS 06487+2208	F814W	—	SB1	03/02	5×1500	
IRAS 08572+3915	F814W	F110W,F160W	SB2	04/99	9×1800	
IRAS 09427+1929	F814W	—	SB3	03/02	2320 ^(†)	Short non-homogeneous exp time
IRAS 11087+5351	F814W	—	SB1	03/02	6×1500	
Arp 299 (NGC 3690+IC 690)	F814W	F160W	SB2, SB3	01/04	14400 ^(‡)	
IRAS 12112+0305	F814W	F110W,F160W	SB2	04/98	5×1800	
IRAS 12490–1009	F814W	—	SB2	03/02	4×1500	
Mrk 231	F814W	F160W	SB1	03/02	4×900	H β not covered by the range Extremely wide emission lines
IRAS 13156+0435	F814W	—	SB2, SB3	03/02	18000 ^(*)	Extended [O III] non detected in N component
IRAS 13342+3932	F814W	—	SB3	03/02	6×1500	
Mrk 273	F814W	F110W,F160W	SB2	04/98	3×1500	
IRAS 13469+5833	F814W	F160W	SB1	03/02	5×1800	Sky line to H α +[N II] complex
Mrk 463	F814W	F160W,F110W	SB2	04/01	5×900	
IRAS 14060+2919	F814W	—	SB2	03/02	4×1800	
IRAS 14348–1447	F814W	F110W,F160W	SB2	04/98	4×1800	
IRAS 15206+3342	F814W	—	SB2	04/99	4×1800	
IRAS 15250+3609	F814W	F160W,F110W	SB2	04/98	5×1800	
Arp 220	F814W	F160W	SB2, SB3	05/00	48000 ^(**)	[O III] not detected
IRAS 16007+3743	F814W	—	SB2	04/01	6×1500	
IRAS 17208–0014	F814W	F110W,F160W	SB2	04/99	4×1950	
IRAS 18580+6527	F814W	F160W	SB2	04/01	7×1500	

Notes:(†)1500 s, 520 s, 300 s; (‡) 3×1200 for each individual galaxy of the system, NGC 3690 and IC 694 observed with the SB2 bundle; 3×1800 for the entire system as observed with the SB3 bundle; (*) 3×1500 for the South component with the SB2 bundle, 4×1500 for the North component with the SB2 bundle, 5×1500 for the entire system with the SB3 bundle; (**) 6×1500 for the nuclear region observed with the SB2 bundle, 26×1500 for the nucleus and extended nebula as observed with the SB3 bundle.

(Table 2.3). Its spectral coverage ranges from 0.8 to 2.5 μm . Since it works in the near infrared, the detector is cooled to cryogenic temperatures to avoid the thermal contamination coming from the environment and the instrument electronics itself.

NICMOS is equipped with narrow (N), intermediate (M) and broad (W) filters, being the most commonly-used the F110W, F160W, and F222M, that are equivalent to the ground-based Johnson-Cousin system J, H, and K (Origlia & Leitherer 2000), respectively. In this work we will mainly use the F160W data, whose interest resides in the good compromise between the capability for penetrating the dust and detect the coldest structures of the galaxy, and the low thermal IR background. This is very useful in ULIRGs, where the extinction by dust creates structures and differences in the surface brightness that do not correspond to their intrinsic morphology.

Table 2.3: Characteristics of the NICMOS cameras

Camera	Scale (arcsec/pix)	FOV (arcsec ²)	Focal Rate	Dif. Limit (μm)
NIC1	0.043	11.0×11.0	F/80.0	1.00
NIC2	0.075	19.2×19.2	F/45.7	1.75
NIC3	0.200	51.2×51.2	F/17.2	...

The archival data were calibrated *on the fly* at the time of de-archiving the images from <http://archive.eso.org>. The main steps performed for the NICMOS data reduction pipeline are.

- Subtract the Zero image and correct the bad pixels using a mask.
- Dark current subtraction and linearity correction.
- Flat field correction.
- Photometric calibration.
- Cosmic ray identification.

There is one effect that appears in the NICMOS data and that is not included in the standard pipeline: the so-called pedestal effect. This is an additive signal that appears in the NICMOS images when the amplifiers are switched on, and that have different values depending on the camera quadrant. This effect is detected as flat-field residuals in the calibrated images. In the present case no relevant residuals related to the pedestal effects were detected, and thus no additional correction was applied to the images. The only aspect that was improved with respect to the pipeline was the combination of the dithered individual exposures.

Once processed the image is given in counts per second, so it can be transformed into Vega magnitudes using:

$$m_{F160W} = -2.5 \times \log_{10}(PHOTFNU \times DN \times ZP(VEGA)^{-1}), \quad (2.2)$$

being DN the count rate per second at a given aperture, PHOTFNU a constant whose value is given in the image header in Jy s DN⁻¹, and ZP(VEGA) another constant of value 1039.3, 1040.7, and 1038.9 Jy for the cameras NIC1, NIC2, and NIC3, respectively.

2.4.3 Isophotal analysis of the HST images

One aspect that will be addressed in this work is the derivation of morphological parameters in ULIRGs, as well as their azimuthal light profiles. To that aim, the isophotal morphological parameters have been derived fitting ellipses² to the *HST* optical WFPC2/F814W and near-IR NICMOS/160W images (see available data in Table 2.2). The method applied for the ellipse fitting measures the image using an iterative technique described by Jedrzejewski (1987). The image is sampled, and a intensity distribution is obtained and analyzed by a least-square method. The best fit to the ellipses is given, along with a set of parameters for each fitted isophote. The parameters include, among others, the ellipse center (x_c, y_c), the semi-major axis (a), the ellipticity ($\epsilon = 1 - b/a$; being b the semi-minor axis, and zero the characteristic value of a circle), the position angle (P.A. measured in degrees counter-clockwise from the +y direction in the image), the total flux enclosed by the ellipse (i.e., surface brightness), and the parameter a4. This last parameter is defined as the fourth cosine coefficient of the Fourier series (Bender et al. 1998). It represents the lowest order deviation of the isophotes from pure ellipses: a positive value of a4 describes an isophote with a disk component, whereas a negative value corresponds to a boxy isophote, and zero defines an elliptical isophote. Other technical aspects worth mentioning are:

- All the images are sky (or background) subtracted.
- For the pre-coalescence systems, and in order to reduce the effect of a companion galaxy, the member of the system not involved on the fit was masked.

²Using the IRAF task `ellipse`. The software *IRAF* is distributed by the *National Optical Astronomy Observatories (NOAO)* and operated by the *Association of Universities for Research in Astronomy (AURA)*.

- Due to the variety of morphologies represented in the sample, and in order to compare the same physical regions with respect to the nucleus, a *comparison range* has been selected following the next criteria: (1) to exclude the innermost regions where the complex structure and the internal extinction occasionally do not allow to perform the fit. This restriction shall be applicable to the F814W images; (2) to avoid the residual contamination coming from the possible companion galaxy, or from the background, and (3) to obtain information from the majority of the objects. Given this, the *comparison range* covers from 3.8 to 10.5 kpc in the optical, and from 1.0 to 5.1 kpc in the near-IR.

The measured counts enclosed by each ellipse are converted into Vega magnitudes applying the transformations detailed in Eqs. 2.1 and 2.2. In this context, these azimuthal profiles promediate the structures presented in the galaxy, and therefore their local morphological features are diluted.

2.5 Integral Field Spectroscopy

The general term 3D-spectroscopy refers to those techniques that allow to obtain spatially-resolved spectra over a two dimensional field. In an extragalactic context, each point of the galaxy (α , δ) has associated a spectrum (λ), and all the information has to be stored in a two-dimensional detector. The most widely used 3D spectroscopy methods are:

- **Long-slit scanning:** It is based on the sequential mapping of an extended source using a long-slit. It allows to obtain a wide spectral range with good resolution, but needs for large amounts of observing time and, as a consequence, it is affected by a lack of homogeneity in the data (i.e., the observing conditions, such as seeing and transparency, can change during the scan).
- **Fabry-Pérot interferometry:** This technique sequentially scans the spectral range covering a wide area of the sky with the spatial resolution generally limited by the seeing. The spectral range tends to be small, but with high spectral resolution ($R > 40000$). The variations on the observing conditions and the high cost in time are among the disadvantages of this technique too.
- **Integral Field Spectroscopy (IFS):** This is a 3D-technique that *simultaneously* obtains the spectral and spatial information for a given telescope pointing (e.g., Allington-Smith 2007). The data homogeneity is one fundamental advantage of IFS, and it is a consequence of obtaining spatial and spectral information simultaneously.

Here we are mostly interested in the IFS, the technique used in the present work, which presents a good compromise between the exposure time, resolution, and homogeneity of the data. In what follows, a brief description of the different IFS techniques and instrumentation is given.

One of the first references to IFS is Vanderriest (1980), and since then several instruments have been designed using different concepts. Fig. 2.7 summarizes the different methods of IFS, and Table 2.4 gives a list of the location of the most popular present and future IFUs:

- **Lenslet Array:** This 3D technique was first proposed by Courtès (1982). The FOV of the telescope is subdivided into small sections by a lens array (Fig. 2.7, upper panel).

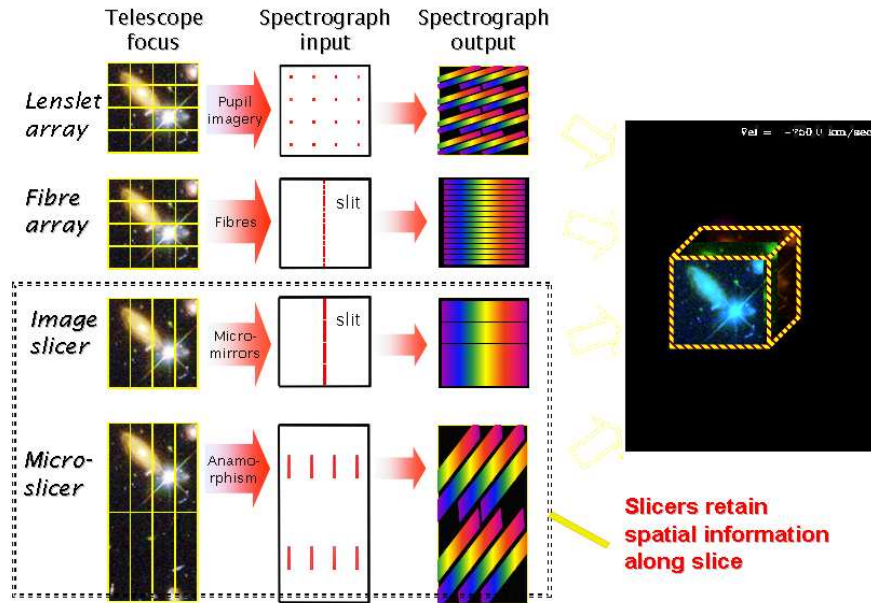


Figure 2.7: Main Integral Field Spectroscopy techniques (Allington-Smith 2007).

All these individual sections are positioned on the spectrograph input and then dispersed. It is necessary a small rotation on the dispersion direction to avoid overlaps between different spectra, and gaps between the individual spectra for preventing cross-talk contamination. This technique gives good spatial coverage and sampling, but a limited spectral information is provided (low resolution/small spectral range). The first prototype (TIGER) was developed by Bacon et al. (1995), and today instruments like OASIS, SAURON, OSIRIS and Kioto3D are based on the TIGER design (see Table 2.4).

- **Fiber Array:** A fiber array is used to subdivide the FOV in the focal plane of the telescope. The fibers are then reordered forming a pseudo-slit and the information dispersed by a conventional spectrograph (Fig. 2.7, second panel). This configuration has important advantages, being the most relevant the low cross-talk derived from the reordering of the fibers, and the large spectral coverage. There are two main disadvantages. First that round fibers cannot fill a two-dimensional region completely, and second non conservation of etendue³ known as focal ratio degradation (FRD; e.g., the light beam is widen as it travels across the fiber). The fibers, that are a good solution for working in the optical range, may be problematic for operating in the IR: (1) due to the fast focal ratio of fibers, (2) fibers should work at cryogenic temperatures, and such response has not been investigated in detail. Kapany (1958) first proposed the use of optical fibers for transforming the two-dimensional distribution of the focal plane into the one-dimensional geometry at the entrance of the spectrograph. Nonetheless he was thinking on improving the resolution rather than in 3D observations. The first fiber-based IFUs were mainly experimental, and provide the community with the

³The etendue is a characteristic of an optical system that defines the degree of spread out of the light in area and angle.

first scientific results and an idea of the potential of the technique. They were SILFID/ARGUS (Vanderriest & Lemonnier 1988), DENSEPACK (Barden & Wade 1988) and HEXAFLEX (Arribas, Mediavilla & Rasilla 1991). Today, INTEGRAL and PPAK belong to this category (see Table 2.4).

- **Lenslets+Fiber:** Some disadvantages associated to the pure fiber-based IFU (e.g., flux losses and FRD) can be avoided by coupling them to a lens array at the focal plane. In this manner the spatial coverage is optimal, and the small pupil created at the entrance of the fiber core avoid light losses and minimize the focal ratio degradation. In general these systems need for additional optical mechanisms (e.g., for converting the light to a focal ratio consistent with an existing spectrograph) that can lead to a diminishing of the system efficiency. MPFS (Afanasiev et al. 1995) was the first instrument that combined the use of fibers and microlensing. PMAS, VIMOS, FLAMES, and GMOS (see Table 2.4) are among the most popular instruments that today make use of this technique.
- **Image Slicer:** With these instruments, the light coming from the source is divided into several one dimensional slices (mirrors) which are rearranged to form a pseudo slit at the entrance of the spectrometer (Fig. 2.7, third panel) and then dispersed. The slicers were first proposed by Bowen (1938; see also Pierce 1965), and developed for infrared astronomy with the 3D spectrometer (Weitzel et al. 1996; Krabbe et al. 1997). SINFONI is an example of an IR-IFU based on this design (see Table 2.4).
- **Micro Slicers:** This new concept of transparent micro-slice IFU arises from the need for more spatial elements at a reasonable building cost. Rather than designing complex mirrors the idea is to use arrays of easily-replicable anamorphic lenslets. This is a new technique that will increase by orders of magnitude the number of spectra obtained in one pointing.

A more detailed discussion of the IFU techniques can be found in Ren & Allington-Smith (2002) and references therein.

2.5.1 INTEGRAL, the IFU at the William Herschel Telescope

INTEGRAL, the IFU used in this work, was designed and built at the Instituto de Astrofísica de Canarias (IAC), in collaboration with the Isaac Newton Group (ING) and the Royal Greenwich Observatory (RGO). It was the first IFU operating in a “common-user regime” in a telescope. A comprehensive description and characterization of the instrument can be found in Arribas et al. (1998) and del Burgo (2000).

Located at the Nasmyth focus of the 4.2m William Herschel Telescope, in the Observatorio del Roque de los Muchachos in La Palma, INTEGRAL is a fiber-based IFU (see Fig. 2.8 for a sketch of the instrument connected to the Wide Field Fibre Optical Spectrograph WYFFOS spectrograph). The instrument can work with up to six scientific bundles located in a swing plate, but the three commonly used bundles are: the Standard Bundle #1 (SB1), the Standard Bundle #2 (SB2), and the Standard Bundle #3 (SB3). Each one provides us with a different system configuration (see details in Table 2.5). The bundle is selected depending on the object (size, surface brightness), the spatial sampling needed (that will depend on the scientific case), and the observing conditions (such as the seeing) during the night.

Table 2.4: IFUs on 8-10 m telescopes

Facility	Diameter	Hemisphere	Instruments
Gemini	8 m	N	GMOS, NFIS
Gemini	8 m	S	GMOS, GNIRS
Very Large Telescope (VLT)	8.2 m	S	FLAMES, SINFONI/SPIFFI VIMOS, KMOS , SWIFT , MUSE
Hobby-Eberly Telescope (HET)	9.2 m	N	VIRUS
Keck	10 m	N	OSIRIS
Large Binocular Telescope (LBT)	~11.8 m	N	<i>LUCIFER</i>
Subaru	8.3 m	N	KYOTO-3D
Southern African Large Telescope (SALT)	11 m	S	<i>SCAM5</i>
William Herschel Telescope (<i>WHT</i>)	4.2	N	INTEGRAL, OASIS, SAURON
Calar Alto 3.5m	3.5	N	PMAS/PPAK
United Kingdom Infra-Red Telescope	3.8 m	N	UIST
Kitt Peak National Observatory (KPNO)	4.0 m	N	FISICA
Gran Telescopio de Canarias (GTC)	10 m	N	FRIDA
James Webb Space Telescope (JWST)	6.5 m	Space	NirSpec , MIRI

(*) Note: Instruments under construction are shown in bold. Instruments which have a possible integral field mode, but which is not in the baseline capability, are shown in italic. Table adapted and expanded from Sharples (2006).

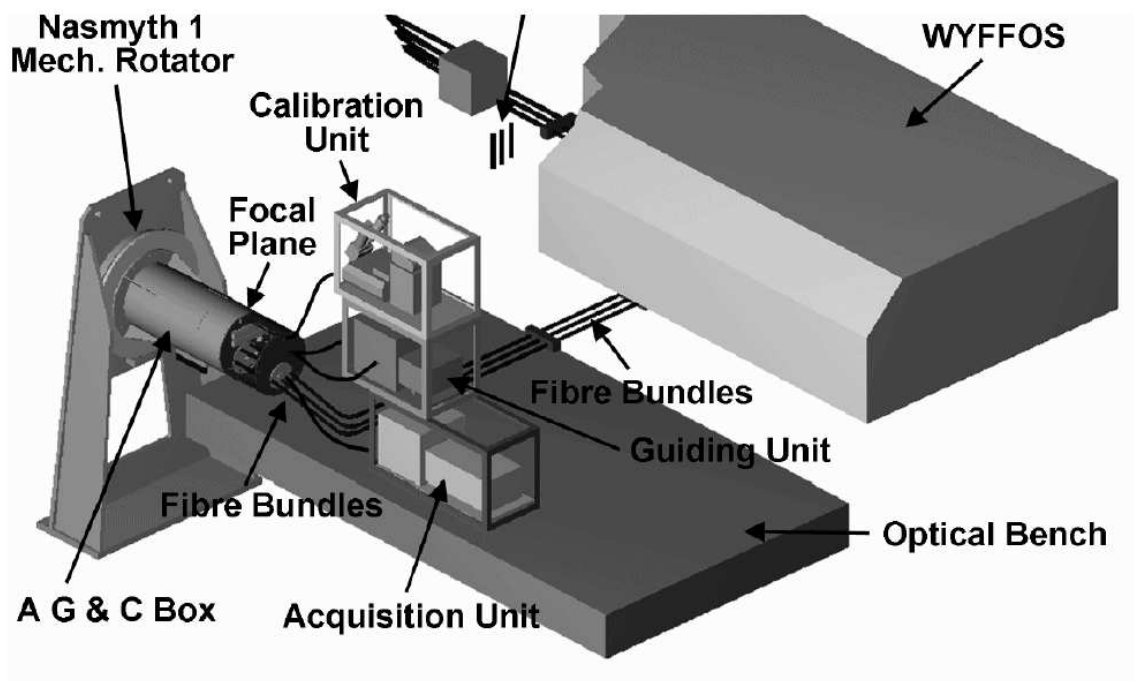


Figure 2.8: Layout of INTEGRAL connected to the WYFFOS spectrograph (see details in www.ing.iac.es).

All three bundles have a similar arrangement in the focal plane: the majority of the fibers cover a rectangular area centered in source, whereas a subset of fibers forming an outer circle of $45''$ in radius, is used for simultaneously sampling the sky (see Fig. 2.9). As the fiber geometry is circular, this configuration does not provide a full spatial coverage: the rectangular area pointing to the source presents small gaps between the fibers. The bundles can be used in two different modes: observing and calibration, for obtaining scientific

Table 2.5: Characteristics of the INTEGRAL fiber bundles

Bundle	Fiber core (\varnothing) ⁽¹⁾ (arcsec)	# Fibers ⁽²⁾	FOV ⁽³⁾ (arcsec ²)	Distance ⁽⁴⁾ (pix)	Sky-ring ⁽⁵⁾ (arcsec)
SB1	0.45	205(175+30)	7.80×6.40	variable	90
SB2	0.90	219(189+30)	16.0×12.3	4.6	90
SB3	2.70	135(115+20)	33.6×29.4	7.4	90

(1): Fiber *core* diameter (arcsec). (2): Total number of fibers (rectangle+sky ring). (3): Spatial coverage of the central rectangle. (4): Distance between spectra of adjacent fibers on the CCD. (5): Diameter of the external sky ring.

and calibration data (i.e., CuNe & CuAr lamps for arcs, and white uniform light for flats), respectively.

The bundles simultaneously feed the spectrograph forming a pseudo-slit, in such a way that only the light coming from the selected bundle (located in the center of the focal plane) enters the spectrograph. The WYFFOS spectrograph offers several gratings (see details in Table 2.6). In August 2004, a new camera for WYFFOS was commissioned (with $\sim 4000 \times 4000$ pixels vs. $\sim 1000 \times 1000$ pixels in the old one). The parameters detailed here are those corresponding to the old camera used in our observing runs.

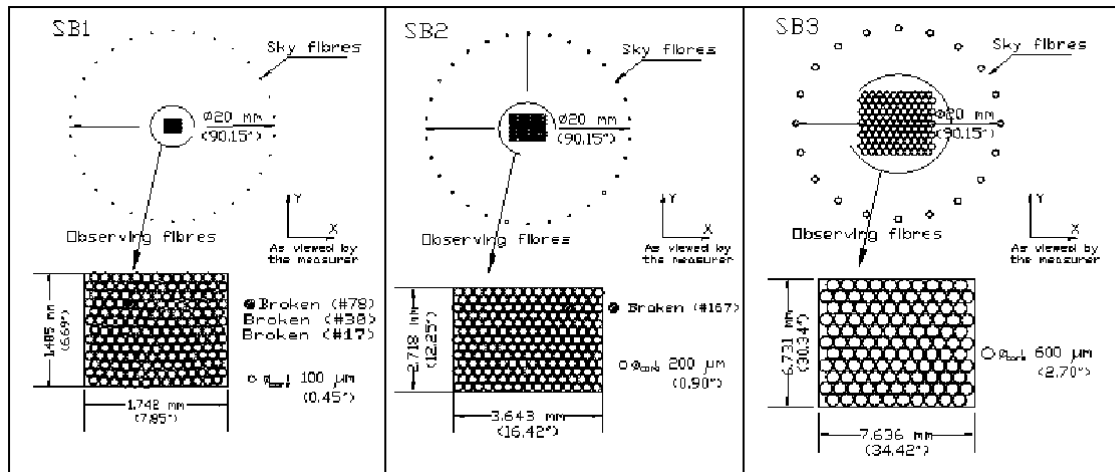


Figure 2.9: Configuration of the fibers of the INTEGRAL standard bundles at the focal plane end.

Table 2.6: WYFFOS spectral Characteristics (old camera)

Grating	1200g/mm	600g/mm	316g/mm	300g/mm
Resolution(SB1)(\AA)	2.8	6.0	11.8	11.0
Resolution(SB2)(\AA)	2.8	6.0	11.8	12.0
Resolution(SB3)(\AA)	4.8	9.8	19.4	19.6
Lineal Dispersion($\text{\AA}/\text{pix}$)	1.4	3.07	5.9	6.2
Spectral Coverage (\AA)	1445	3140	5837	6144

2.5.2 Data Reduction

A sketch of the pseudo-slit formed by the fibers at the spectrograph entrance and a raw image as those obtained at the telescope are shown in Fig. 2.10. The x-axis represents the dispersion direction, whereas the y-axis represents the spatial one. That is, the 3D information is stored in a 2D detector, where each spectrum comes from a different region of the galaxy under study.

The data reduction of the two-dimensional fiber spectra has been performed using the IRAF environment, following the standard procedures applied for this type of data (e.g., Arribas et al. 1997 and references therein; Monreal-Ibero et al. 2007). In what follows the main steps involved in the process will be briefly reviewed.

1. Image correction for BIAS, and trimming of the overscan section

The BIAS is a constant count level artificially included in the CCD during the read-out to avoid negative counts. The BIAS can be subtracted using two different techniques:

- Subtracting the mean of the overscan section (i.e., a region of the CCD not exposed to the light). Once this region is selected, it is trimmed from the image using `noao.imred.ccdred.ccdproc`. As an example, the derived value for the observing run of April 2001 was ~ 890 counts.
- Averaging zero exposure time frames (more than 10) and subtracting the entire image to the data frames. For the observing run of April 2001, the combined image gives a mean value of ~ 883 counts, with a minimum value of 880 and a maximum of 893. These differences are due to the electronic structure present in the BIAS, that in fact is not constant all over the CCD. To eliminate those local artifacts the combined image was used for the BIAS correction.

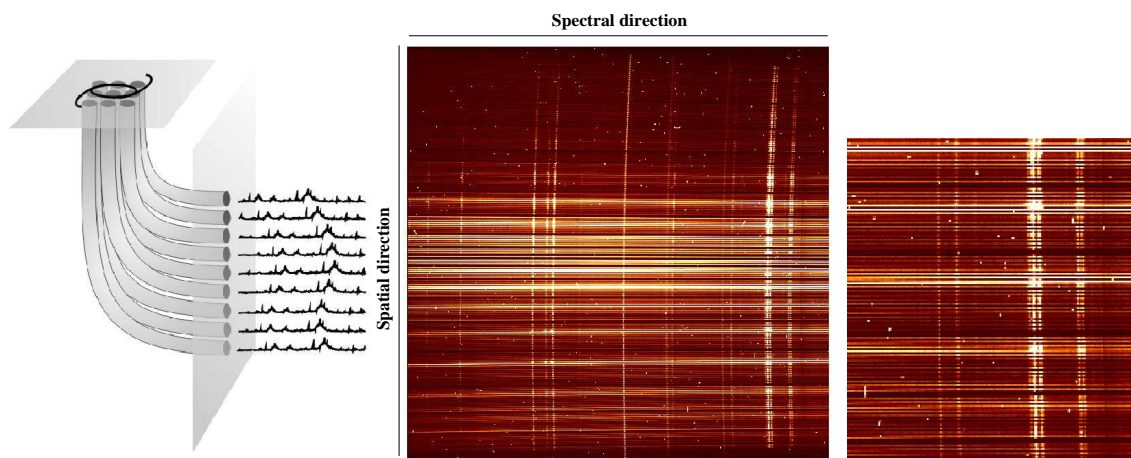


Figure 2.10: **Left:** INTEGRAL IFS concept: the galaxy light is collected in the focal plane by the fiber bundle; the fibers are reordered forming pseudo-slit and then dispersed by the spectrometer. **Center:** Raw image as obtained at the telescope. The spectral and spatial directions are indicated. **Right:** Zoom of the raw image, where the individual fibers are separated, and some emission lines are detected.

2. Defining and Tracing the Fibers

As shown in Fig. 2.10, the light coming from the astronomical source is collected by

the fibers and dispersed onto the CCD. The information coming from each fiber has to be individually identified (aperture definition) and traced (aperture trace) in order to preserve the full spatial and spectral information provided by IFS. From now on, aperture will be synonymous of fiber.

Specifically, this step has been done using a sky flat image, due to its high signal over the entire wavelength range. The first stage is to identify and consecutively number all the fibers; then the position of each fiber center is traced along the CCD using a polynomial of Legendre (order 11). This information about the “path” followed by the light is saved into a file. The location of the INTEGRAL+WYFFOS system in the Nasmyth focus of the telescope warrants its stability through one night (del Burgo 2000), thus the polynomials obtained for the sky flat can be used in all the scientific images observed during the same night. This step has to be done twice:

- To subtract the stray light and cross-talk contamination.
- To extract the spectrum corresponding to each fiber.

The IRAF task used for the aperture definition and trace is `noao.imred.specred.apall`,

3. Scattered Light Subtraction and Cross-Talk Correction

The stray light is a spurious signal in the CCD that comes from different sources, such as scattering due to the dust in the air or in the optical surfaces, or optical aberrations. The cross-talk of an aperture is defined as the amount of contaminating light that comes from other apertures. Both contaminating sources create a background that has a diluting effect on the spectra, making more difficult to measure the emission lines intensities, especially in the low surface brightness regions. The spurious light outside the defined apertures was analyzed, two-dimensionally modeled, and extracted from every image with the exception of the arc lamps, because in those cases we are only interested in the position of the peaks.

The IRAF task used in this step is `noao.imred.specred.apscatter`.

4. Fiber Extraction

The projection of the fibers into the detector is measured and added along the spatial direction to obtain a final one dimensional spectrum for every single fiber. After aperture tracing, the widths used for the extraction were 4, 4, and 6 pixels for SB1, SB2, and SB3, respectively. Once extracted, the result is a $x \times y$ image where x is the number of pixels along the dispersion axis, and y is the number of fibers/spectra (see Fig. 2.11, top panel). On the extracted image each spectrum corresponds to one region of the galaxy under study.

The IRAF task used for the aperture definition and tracing is `noao.imred.specred.apall`.

5. Wavelength Calibration

This calibration transforms the dispersion axis from pixels into wavelength units using a well characterized lamp-arc image. Once the emission lines from the arc image, and the solution is computed (using a Legendre polynomial of fourth order) the dispersion correction can be applied. For all the observations we used the R600B grating, whose spectral range covers from about 5000 to 8000 Å. Given that the arc-lamp weakly emits below $\sim 5800\text{Å}$, two arc images are combined for the calibration: short exposures of

about 1 s to cover the red range and long exposures of between 30 and 60 s to cover the blue one. Once checked the system stability, the regions of interest from each arc are attached and used as a single one; with that image the steps for the wavelength calibration are:

- To identify the emission lines in the central fiber spectrum of the arc image by using `noao.onedspec.identify`.
- To identify the emission lines of the rest of spectra of the arc image by using the central spectrum as reference with the task `noao.onedspec.reidentify`. The rms of the fits ranges from about 0.08 to 0.15 Å.
- To correct for dispersion the rest of the images using the information of the arc and the IRAF task `noao.onedspec.dispcor`.

In Fig. 2.11, second panel from the top, the result of the wavelength calibration is shown.

6. Flat-field Correction

Under a uniform illumination, the pixels present sensitivity variations, and the fibers different transmission. The goal of this step is to correct for both variations: one of low frequency (fiber to fiber) and other one of high frequency (pixel to pixel). To that aim, the average of a flat lamp along the spatial direction is taken and the profile fitted with a polynomial. The observed variations are interpreted as the pixel to pixel variations. The differences in the fiber to fiber transmission are traced by repeating the process in a sky (twilight) flat along the spectral direction. Both steps can be simultaneously done with the task `noao.imred.specred.msresp1d`. The output is a flat image with an average value of one. Dividing the science images between the flat, the variations should be corrected (Fig. 2.11, central panel).

7. Sky Subtraction

In this step, the sky contribution to the spectra of the galaxy is subtracted. Using the outer ring of fibers present in every INTEGRAL bundle, the measurements of the sky are taken simultaneously and under the same conditions that those of the galaxy under study. In all cases, the sky spectra were individually checked, paying special attention to those fibers adjacent to the nuclear ones in the spectrometer entrance (i.e., to avoid galaxy contamination). By taking the average of the outer fibers, a mean sky spectrum is calculated and subtracted from the galaxy.

The importance of the sky subtraction depends on the individual cases. It is relevant if an emission line of interest is adjacent to (or coincides with) a sky line, particularly in the low surface brightness regions where the relative importance of the sky emission is critical. The residuals of the sky subtraction are generally irrelevant in the nuclear regions, whereas in the most external/low surface brightness areas they can be almost at the same count level than detections of the weakest emission lines themselves (signal-to-noise (S/N) about 2-3).

The sky has been subtracted by using the task `noao.imred.specred.skysub` (see Fig. 2.11, fourth panel from top).

8. Relative Flux Calibration

The aim here is to transform the image counts into flux units, and to correct for the

instrumental response, using the information of a well characterized spectrophotometric standard star. The different steps for the calibration can be summarized as follows:

- Getting data from a spectrophotometric standard star during the observing run. Typically, three pointings using two or three stars were done throughout the night. To have an optimal wavelength coverage and sampling, we observed *HST* spectrophotometric standard stars (<http://www.eso.org/observing/standards/spectra/hststandards.html>).
- Once identified the fiber with highest signal from the star (the central fiber), its signal is compared to the real flux of the star and a calibration file is created (`noao.imred.specred.standard`).
- With the calibration file and the atmospheric extinction data (www.ing.iac.es), the sensitivity function of the system is derived (`noao.imred.specred.sensfunc`). This process was repeated for every observed star and the results were compared. We found variations of between 5-15% depending on the night and instrument configuration used.
- Finally, using the sensitivity function, the signal of any given galaxy can be transformed from counts to flux density ($\text{erg s}^{-1} \text{cm}^{-2} \text{\AA}^{-1}$, or alternatively f_ν) with the task `noao.imred.specred.calibrate`. If the observing conditions suffered from large variations during the night, the galaxy of interest was calibrated with the closest star in time.

This relative flux calibration shows large uncertainties with respect to the real absolute flux (errors of about 50% or larger); this is the consequence of assuming that the flux of the star is concentrated in one fiber. In any case this is not relevant for the general purpose of this thesis, where relative measurements and flux ratios are mainly used.

This is the last step on the “standard” reduction and calibration process.

9. Image Combination

Once the “standard” reduction is completed, the next step is to combine all the individual exposures (a minimum of three) using the IRAF task `imcombine`. This procedure improves the S/N of the image, and is suitable for the cosmic ray rejection. The combination has to be done taking into account the following aspects: (i) each fiber integrates information coming from a particular area of the galaxy, meaning that large variations in the seeing conditions can make one fiber to sample different regions. In the present case, the seeing conditions for each individual galaxy pointing were rather stable. As an example, the SB2 bundle (fiber diameter $0''.9$, optimal seeing about $1''.2$) has been used during all the observing runs with seeing ranging from about $0''.9$ to $1''.4$. (ii) Variations in the pointing may result in the same fiber to sample different regions of the galaxy. This may happen if there is a problem with the guiding (which is not the case) or if the instrument suffers from strong flexures. The location of INTEGRAL in the Nasmyth focus warrants its stability.

In Fig. 2.11 (fifth panel from the top) an example of a combined image is shown; the quality improvement on the data is remarkable. That image is ready for the analysis.

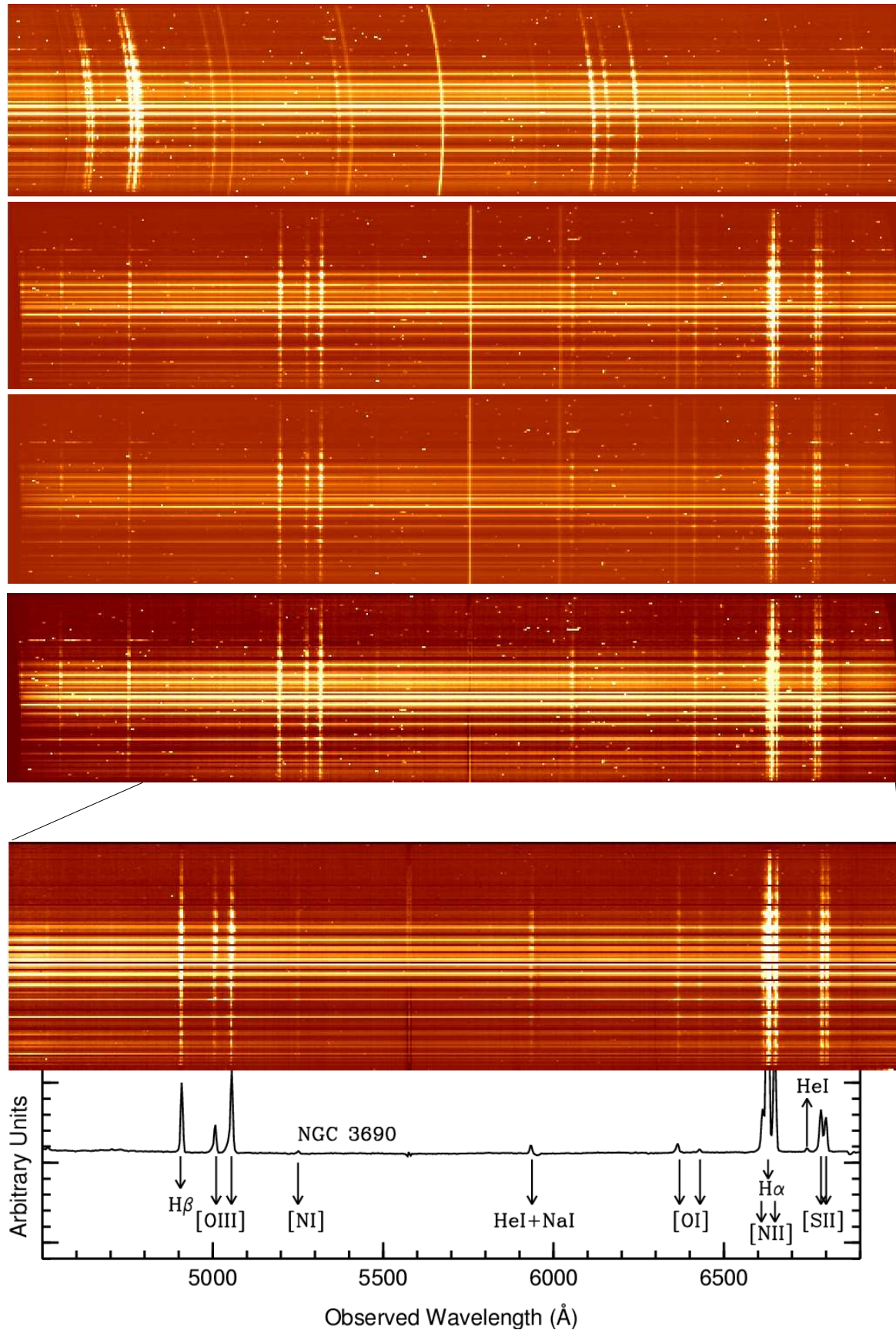


Figure 2.11: Different steps of the data reduction of the galaxy NGC 3690. **From top to bottom:** (i) Object image after the BIAS, stray light, and aperture extraction. (ii) The same image after the wavelength calibration. (iii) The same image after the flat-field correction. (iv) After the sky light subtraction. (v) NGC 3690 after the flux calibration and combination of the individual exposures. Only the spectral range of interest is shown. (vi) Identification of the emission (and absorption) lines of interest.

10. Absolute Flux Calibration

As explained above, the standard relative flux calibration presents large variations with respect to absolute measurements. For many of our measurements this is not a key aspect, but when the purpose is to derive absolute fluxes, SFRs, and mass in young stars, an absolute calibration is needed. For that reason, the process is detailed in what follows.

In the relative flux calibration, assuming that the entire stellar flux is concentrated in one single fiber leads to an overestimation of the flux. Therefore we need to calculate a contribution-to-flux conversion factor. To that aim, the total flux of the star observed with INTEGRAL is measured using an interpolated map (a defined in §2.5.3). The flux contribution from the central fiber is estimated using the same map. Then, the wavelength-dependent conversion factor f_{fiber}/f_{total} is derived for each single star. The factor is estimated in sections of 300 \AA , to obtain its variation with the wavelength range. The higher the factor, the finest the centering of the star on the fiber. The flux measured at a certain λ will be corrected by multiplying for the corresponding factor. This method corrects not only the flux values, but the atmospheric differential refraction (ADR) too. The ADR is defined as the shift of the emission peak of the star depending on the airmass and λ (see details on Filippenko 1982; Arribas et al. 1999).

This technique is not included in the standard data reduction process; once applied, the absolute flux uncertainties are about 10-15%. A comprehensive discussion of the absolute flux calibration can be found in Monreal-Ibero (2004).

2.5.3 Working with INTEGRAL Data

After the INTEGRAL data reduction, every galaxy has a set of spectra, each one associated with the region observed with the individual fibers. In the present galaxy sample, the mean spatial scale is $1.6 \text{ kpc}''$ (see individual scales in Table 2.1); the spatial resolution and the fiber bundle used will determine the physical area integrated on each spectrum. In Figs. 2.12 and 2.13 the nuclear (one or several averaged fibers, depending on the case) spectra of the systems under study are shown, indicating the INTEGRAL bundle used for each observation. The wavelength coverage is from $\lambda 4500$ to $\lambda 7000 \text{ \AA}$ rest-frame. Almost all the spectra show strong ($H\beta$, $[\text{O III}]\lambda\lambda 4959, 5007$, $H\alpha + [\text{N II}]\lambda\lambda 6548, 6484$, and $[\text{S II}]\lambda\lambda 6716, 6731$) and weak ($[\text{O I}]\lambda 6300$) optical emission lines with different ratios. In addition, some galaxies present other weak emission lines ($[\text{N I}]\lambda 5199$, $\text{He I}\lambda 5876$, and $\text{He I}\lambda 6678$) as well as interstellar absorption lines ($\text{Na I}\lambda\lambda 5890, 5896$). Aside from the differences in the relative intensity of these features, there are remarkable variations in their widths and central wavelengths. These characteristics indicate the presence of different ionization mechanisms at work, the effect of the dust and the internal kinematics of the galaxy. All these aspects will be studied in the subsequent chapters.

The spectra shown in Figs. 2.12 and 2.13 correspond to the nuclear regions, but INTEGRAL IFS provides us with much more information. In order to study the spatial structure of the stellar and ionized gas components of the galaxy, as well as other features such as the velocity field, we need to construct maps based on the two-dimensional information of each galaxy. Given that the INTEGRAL configuration does not provide a full spatial coverage of the galaxies (due to inter-fiber gaps), we will construct maps based on the interpolation

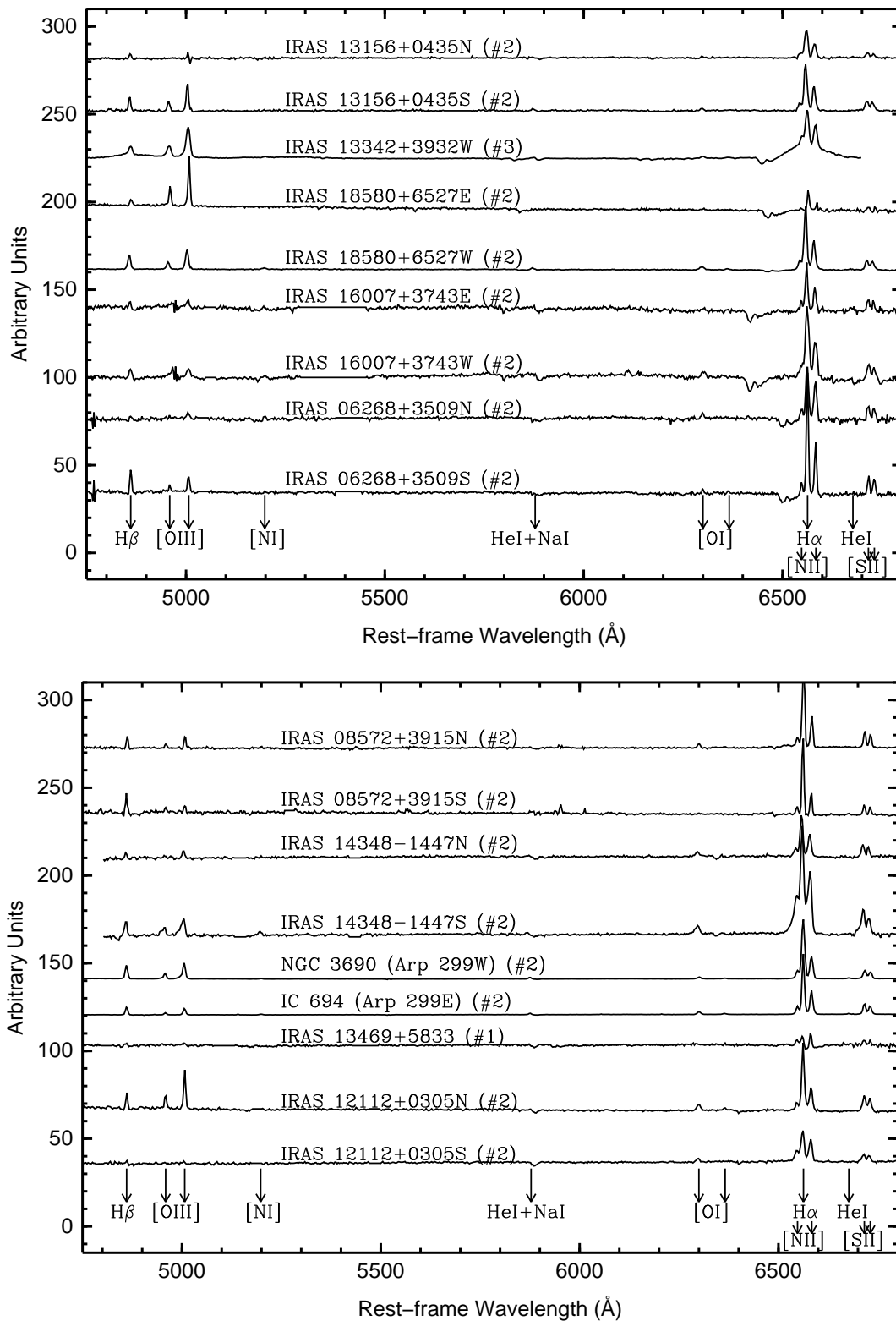


Figure 2.12: Full nuclear spectra for the sample of galaxies. The bundle used is the number indicated next to the galaxy name.

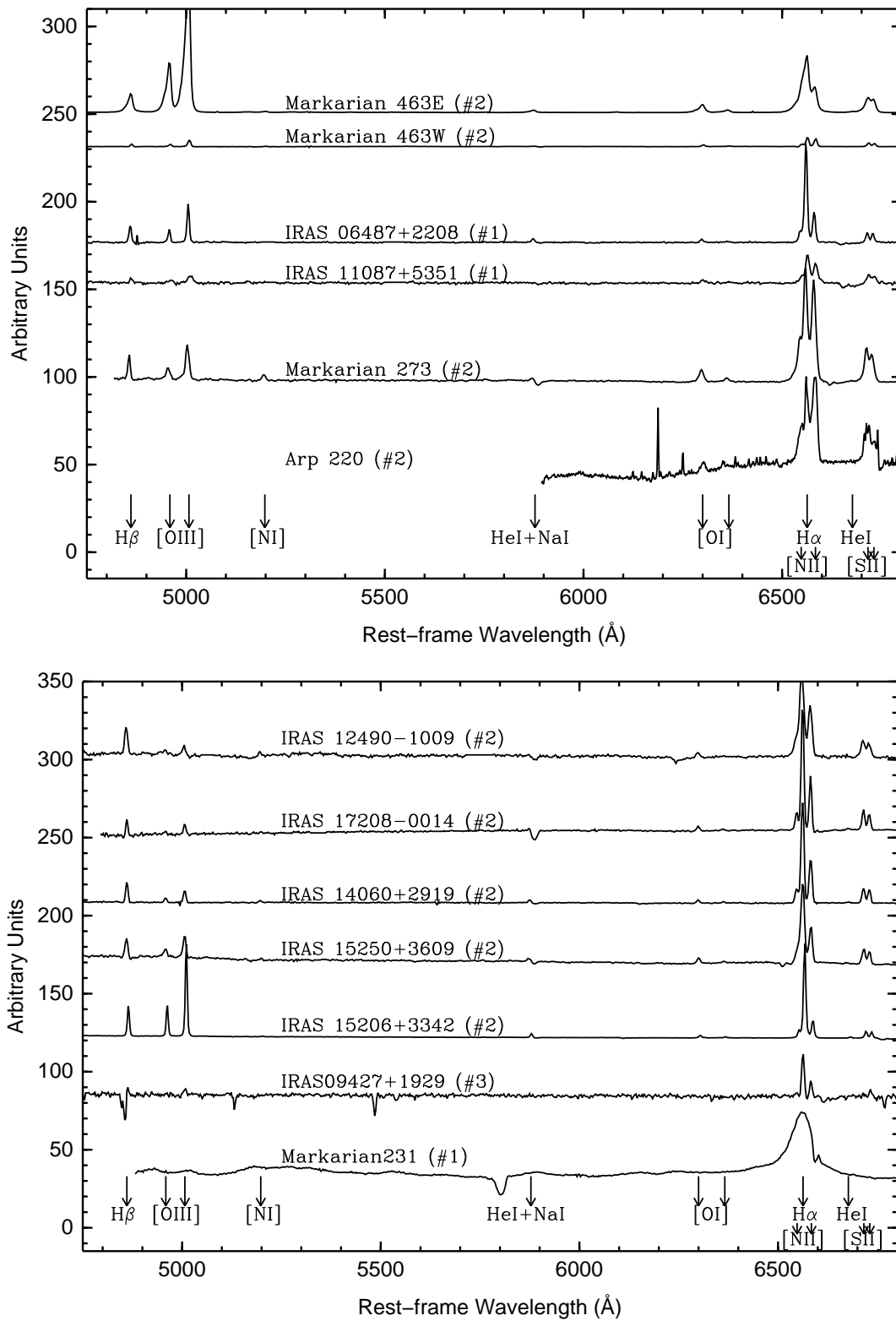


Figure 2.13: Full nuclear spectra for the sample of galaxies. The bundle used is the number indicated next to the galaxy name.

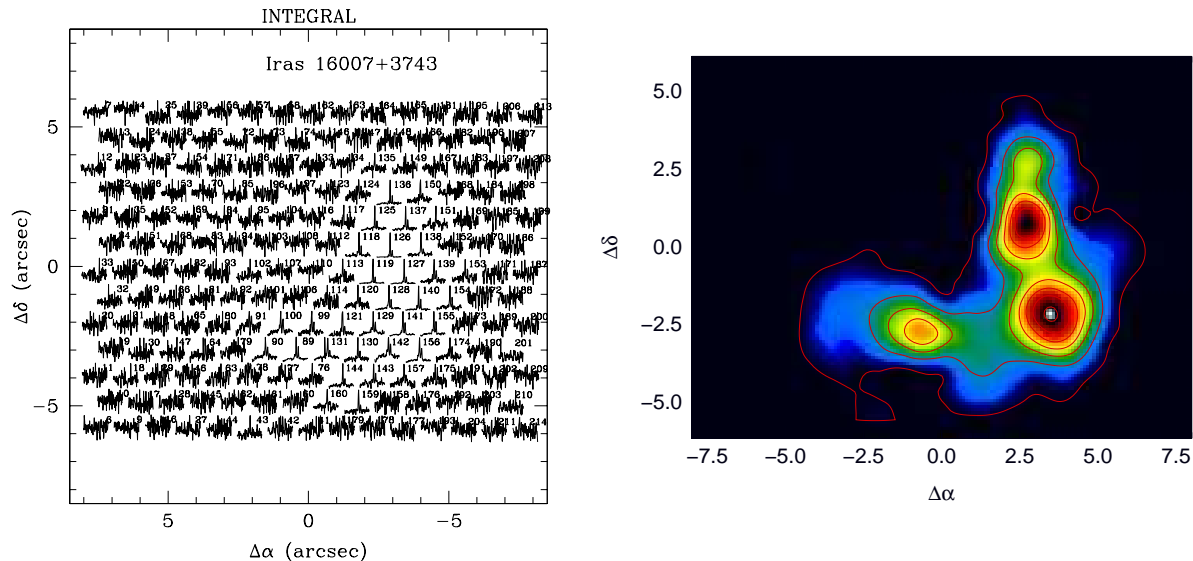


Figure 2.14: **Left:** Final calibrated $H\alpha+[N II]\lambda\lambda 6548, 6484$ complex for IRAS 16007+3743, spatially ordered as in the focal plane. The numbers on the plot indicate the number of the fiber at the entrance of the spectrograph (i.e., pseudo-slit). **Right:** Reconstructed map of the indicated spectral region using a filter over the spectra (lines+continuum).

of the observed flux or physical feature. For the generation of maps itself, a Delaunay triangulation of a planar set of points was applied using the free software IDA (García-Lorenzo et al. 2002). Broadly speaking, in the present work the maps have been derived in two different ways:

- **Filter simulations:**

Simulating a filter over the wavelength range of interest. This technique is useful to obtain continuum or isolated line maps (see Fig. 2.14). It is not recommended to use narrow filter for observing emission lines, as the relative shift in the centroid position due to the galaxy velocity field. Besides, the utility of this method diminishes in doubles or triplets of lines, as the deblending cannot be performed. On the other hand, this technique does not provides us with information about the position of the line centroid, needed for the kinematic study of the warm gas component.

- **Emission line fitting**

The individual fitting of the spectral lines of interest is the best option for analyzing the emission lines. For the present work the flux, centroid, and width of the emission lines of interest have been obtained fitting Gaussian functions to the observed emission-line profiles using the DIPSO package (Howarth & Murray 1988). The emission lines of interest, and the restrictions applied in the fits are:

- $H\beta$ ($\lambda 4861 \text{ \AA}$): Gaussian fit with no restriction.
- $[O III]$ ($\lambda\lambda 4959, 5007 \text{ \AA}$): Two Gaussian with the centroids bound, the same width, and a flux ratio of three.
- $[O I]$ ($\lambda 6300 \text{ \AA}$): Gaussian fit with no restriction.

- $\text{H}\alpha + [\text{N II}]$ ($\lambda\lambda 6548, 6563, 6584 \text{ \AA}$): Three Gaussian with the same width and the centroids bound. For the nitrogen lines a flux ratio of three has been imposed.
- $[\text{S II}]$ ($\lambda\lambda 6716, 6731 \text{ \AA}$): Two Gaussian with the centroids bound. For the flux ratio of these lines, which is an indicator of the electron density, no restriction has been applied.

The spectral features we are mainly interested on are the total flux of the line (which is given by the fit), the radial velocities, and the velocity dispersions (σ). Although in some cases there were hints of double components for certain regions, it has not been considered here due to the large uncertainties in the fits with two components.

In this work the kinematics of the warm ionized gas is traced by the $\text{H}\alpha$ emission line. The gas velocity in one region can be calculated using the equation:

$$v = \frac{\lambda_{obs} - \lambda_{lab}}{\lambda_{lab}} \times c + v_H, \quad (2.3)$$

with λ_{lab} the rest-frame wavelength of the emission line under study, λ_{obs} the observed wavelength (i.e., the centroid of the line derived with the Gaussian fit), c the speed of light and v_H is the heliocentric velocity correction⁴. An example of a two-dimensional velocity field obtained is shown in Fig. 2.15.

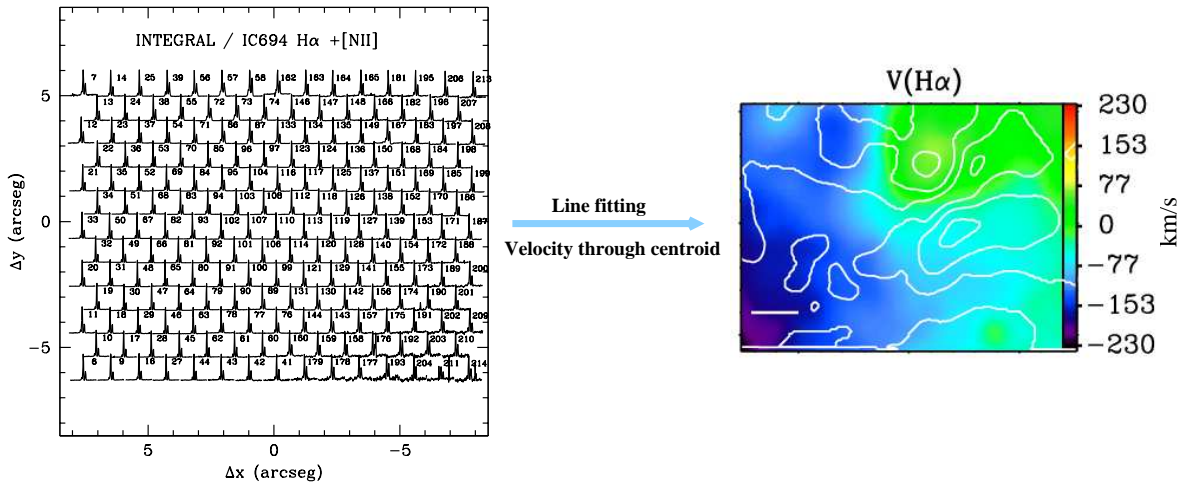


Figure 2.15: **Left:** Final calibrated $\text{H}\alpha + [\text{N II}] \lambda\lambda 6548, 6484$ complex for IC 694 (Arp 299 eastern component) spatially ordered as in the focal plane. The numbers on the plot indicate the number of the fiber. All the individual spectra are fitted using a Gaussian profile. **Right:** Two-dimensional interpolated velocity field derived from the Gaussian fits of the spectra showed on the left.

The velocity dispersion (σ) has been obtained assuming the relation:

$$\sigma_{gas} = \frac{\Delta v_{gas}}{2\sqrt{2\ln 2}}, \quad (2.4)$$

and taking into account:

⁴The heliocentric velocity correction obtained was computed with the IRAF task `noao.astutil.rvcorrect`.

$$\Delta v_{gas} = \frac{c}{\lambda_{lab}(1+z)} \times \sqrt{\Delta\lambda_{obs}^2 - \Delta\lambda_{ins}^2}, \quad (2.5)$$

$\Delta\lambda_{obs}$ is the FWHM obtained from the Gaussian fit, whereas $\Delta\lambda_{ins}$ is the instrumental FWHM. This parameter is obtained fiber-by-fiber, fitting different emission lines from an arc image, and calculating the mean value. The average measurements for the instrumental FWHM are about 2, 5, and 10 Å for the bundles SB1, SB2, and SB3 respectively. The velocity dispersion provides information about the spread on the velocity of the galaxy component traced by the observed lines.

2.6 Relative *HST*-INTEGRAL Astrometry

The final issue treated in this chapter is the alignment between the *HST* data and the INTEGRAL maps. Once the reduction process is finished and the interpolated maps of interest are derived, we have a collection of maps and *HST* images with different angular resolution. For an adequate comparison between both data sets, it is necessary to align the images to the same reference system. To that aim the high spatial resolution *HST* images have been degraded and compared with the INTEGRAL red continuum. The *HST* images have been convolved with a Gaussian of 0''5, 1''1, and 2''9 for comparing with the SB1, SB2, and SB3 bundles, respectively. Taking advantage of their morphological resemblance, we can establish the position of the INTEGRAL maps with respect to the *HST* images with an uncertainty of $\lesssim 0''.15$, $0''.30$ and $1''.5$ for the SB1, SB2, and SB3 bundles data respectively (see example in Fig. 2.16).

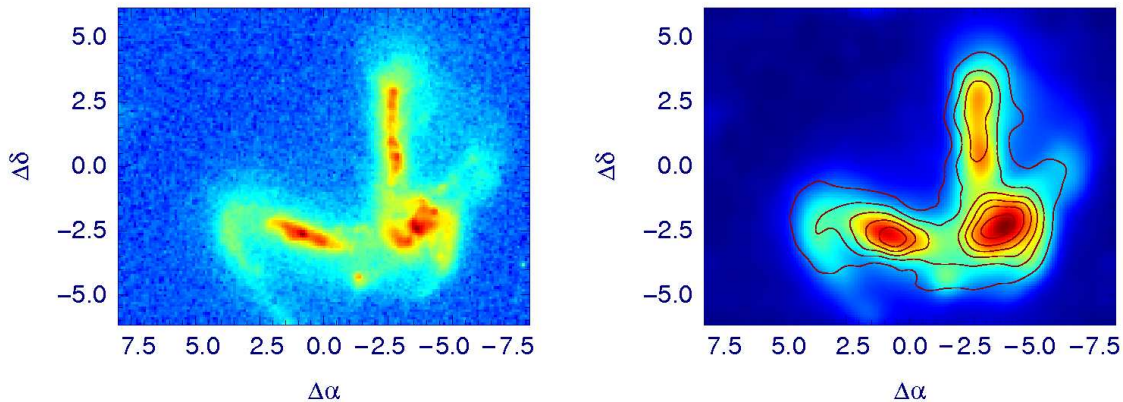


Figure 2.16: **Left:** IRAS 16007+3743 as observed with the *HST* WFPC2 F814W filter, where the structural details provided by the high spatial resolution stand out. **Right:** The previous *HST* image convolved with a PSF to simulate the atmosphere+telescope effect is shown in color. The contours are the INTEGRAL red continuum.

Chapter 3

Distribution of Stars, Gas and Dust. Tracing the Evolution in ULIRGs

In this Chapter the gaseous morphology, stellar structure, dust distribution, and evolutionary scenarios of a representative sample of ULIRGs have been studied. The stellar and ionized gas components of the sample show morphological wavelength-dependent variations. These differences are due to the combination of the nature and spatial distribution of the ionization source, and to the dust distribution. These morphological differences depend on the merger phase too, and appear to be more common in the pre-coalescence phase. The dust tends to be concentrated in the central few kiloparsecs, with the extinction in the visual ranging from 0.5 to 5 magnitudes (as derived from the Balmer decrement). The light profiles show variations with respect to a de Vaucouleurs law of up to 0.5 mag/arcsec^2 in the optical ($\sim 0.8 \mu\text{m}$). These variations are due to the presence of large amounts of dust, especially in the inner regions. However, in the near-IR band ($1.6 \mu\text{m}$), less affected by the presence of dust, the surface brightness profile in all galaxies is well fitted with an $r^{1/4}$ law. The near-IR isophotal analysis indicates that ULIRGs tend to be disk-like or to lie in the boxy-disk frontier, with the largest isophotal twists associated to the lower ellipticities. Finally, the comparison of morphological and dynamical parameters with simulations of merger remnants, and data of ellipticals and galaxy remnants, indicates that post-coalescence ULIRGs are consistent with slowly rotating disk remnants of equal (1:1) or unequal (e.g., 3:1) mergers of disk galaxies. These results support the hypothesis that the final stage of ULIRGs may be intermediate mass disk elliptical galaxies, partly supported by rotation.

3.1 Introduction

After their discovery, imaging observations of nearby ULIRGs (Sanders et al. 1988) gave the astronomers the first clues about their perturbed morphology, i.e., their interacting/merging nature. Later on, with the *HST* images, their true complex structure was unveiled (e.g., Surace & Sanders 2000; Borne et al. 2000; Scoville et al. 2000; Farrah et al. 2001; Bushouse et al. 2002). Obscured nuclear regions surrounded by tidal tails, bridges, plumes, knots, young star-forming regions star clusters and dust lanes, among other characteristics derived from the merging processes, made ULIRGs one of the most morphologically complex

extragalactic objects.

The analysis of the ionized gas component has been mainly studied using long-slit spectroscopy (e.g., Veilleux et al. 1995; Kim et al. 1995; Genzel et al. 1998), with the aim of analyze the dominant power source in ULIRGs. Nonetheless, in the last years two-dimensional studies of the ionized gas have been carried out (e.g., Mulchaey et al. 1996a; Alonso-Herrero et al. 1997, 1998; Colina et al. 2000; García-Marín et al. 2006 and references therein). This studies are useful for understanding the structure of the ionized gas, and provide an indication about the mechanisms that dominate ULIRGs.

The analysis of the stellar component in ULIRGs has lead to the conclusion that ULIRGs tend to show elliptical-like profiles (ground-based images Wright et al. 1990; *HST* images Zheng et al. 1999; Scoville et al. 2000). This fact, along with the location of ULIRGs in the fundamental plane (e.g., Kormendy & Sanders 1992; Genzel et al. 2001; Tacconi et al. 2002; Dasyra et al. 2006) and the results of numerical simulations (see Naab et al. 2006 and references therein) reinforce the idea of ULIRGs as progenitors of elliptical galaxies through dissipative collapse. These studies have been in general centered in galaxies in advanced merger phases.

This Chapter is devoted to the detailed two-dimensional analysis of the entire galaxy sample, including the stellar as well as the ionized gas component, and to test evolutionary scenarios for ULIRGs. §3.2. presents the morphological classification selected to study the sample, whose stellar and ionized gas structure will be given in §3.3. The effects of the dust will be presented in §3.4. In §3.5. we will test the evolutionary scenarios for ULIRGs, using a pure morphological and a dynamical-morphological approach, and comparing with the results of merger models. Finally, the most interesting results will be summarized in §3.6.

3.2 Morphological Classification of the Galaxy Sample

In order to analyze the structure and evolution of the sample of ULIRGs depending on the merger phase, it is important to define a solid criterion that helps us to separate the most important stages. The morphology of ULIRGs was exhaustively described by Veilleux et al. (2002) using a classification scheme first proposed by Surace (1998). Briefly, the Veilleux classification is:

- I. **First approach:** The early stages of interaction. The galaxy disks are quite unperturbed and there is no evidence for tidal tails or bridges.
- II. **First contact:** The disks overlap but strong bars or tails are not formed yet.
- III. **Pre-merger:** Two well identifiable nuclei with well developed tidal tails and bridges.
- IV. **Merger:** Apparently the nuclei have coalesced, but there still can be prominent tidal features. The galaxy core tends to be extended and crossed by dust lanes.
- V. **Old merger:** The system does not show any direct signs of tidal tails, although it presents disturbed central morphologies with knots of star formation.

Types III and IV are further divided into two subclasses. This classification is , however, extremely detailed for our purposes and occasionally non-objective; sometimes it is difficult to know whether one galaxy belongs to one category or another. In addition, to have five classes with subclasses in a sample of 22 systems can make the analysis confusing and off-focus.

Table 3.1: Characteristics of the sample of galaxies

IRAS ID	L_{IR} $\log(L_{IR}/L_{\odot})$	M(F814W)	z	Class	Morphology	IR Class
IRAS 13156+0435	12.13	-22.95	0.113	Pre-C	Interacting pair at 36.0 kpc	W
IRAS 13342+3932	12.51	-23.89	0.179	Pre-C	Interacting pair at 25.1 kpc	W
IRAS 18580+6527	12.26	-24.48	0.176	Pre-C	Interacting pair at 15.0 kpc	C
IRAS 16007+3743	12.11	-23.76	0.185	Pre-C	Interacting pair at 14.2 kpc	C
IRAS 06268+3509	12.51	-23.05	0.170	Pre-C	Interacting pair at 9.1 kpc	W
IRAS 08572+3915	12.17	-21.78	0.058	Pre-C	Interacting pair at 6.1 kpc	W
IRAS 14348-1447	12.39	-22.24	0.083	Pre-C	Interacting pair at 5.5 kpc	C
Arp 299 (NGC 3690+IC 694)	11.81	-22.46	0.010	Pre-C	Interacting pair at 5.0 kpc	W
IRAS 13469+5833	12.31	-23.06	0.158	Pre-C	Interacting pair at 4.5 kpc	C
IRAS 12112+0305	12.37	-21.57	0.073	Pre-C	Interacting pair at 4.0 kpc	C
Mrk 463	11.81	-22.90	0.050	Pre-C	Interacting pair at 3.8 kpc	W
IRAS 06487+2208	12.57	-22.54	0.144	Post-C	Double nucleus at 1.5 kpc	W
IRAS 11087+5351	12.13	-22.87	0.143	Post-C	Double nucleus at 1.5 kpc	C
Mrk 273	12.18	-21.81	0.038	Post-C	Double nucleus at 0.7 kpc	C
Arp 220	12.20	-24.05	0.018	Post-C	Double nucleus at 0.4 kpc	C
IRAS 09427+1929	12.10	-21.92	0.149	Post-C	Single nucleus	W
IRAS 12490-1009	12.07	-22.91	0.101	Post-C	Single nucleus	C
Mrk 231	12.57	-23.52	0.042	Post-C	Single nucleus	W
IRAS 14060+2919	12.18	-23.08	0.117	Post-C	Single nucleus	C
IRAS 15206+3342	12.27	-23.23	0.124	Post-C	Single nucleus	C
IRAS 15250+3609	12.09	-21.99	0.055	Post-C	Single nucleus	C
IRAS 17208-0014	12.43	-21.98	0.043	Post-C	Single nucleus	C

Note: The magnitudes have been derived using circular apertures over the sky-subtracted WFPC2/F814W image including the whole galaxy or system. The applied cosmology uses $\Omega_{\Lambda}=0.7$, $\Omega_M=0.3$, and $H_0=70 \text{ km s}^{-1} \text{ Mpc}^{-1}$. W and C mean warm and cold galaxies respectively.

The importance of mergers in ULIRGs is such that the ultra-luminous phase appears to start after the first peri-passage and lasts until the post-coalescence (Sanders & Mirabel 1996; Veilleux et al. 2002). The fusion process that ULIRGs undergo has been well reproduced by several numerical simulations (e.g., Mihos 1999; Mihos & Hernquist 1996; Bendo & Barnes 2000; Nb06). All these works suggest that by the time the two nuclei have reached a separation of $\lesssim 1 \text{ kpc}$, the stellar system has basically achieved its dynamical equilibrium. Given that, the dynamical parameters appear to be very close to their equilibrium values, although their nuclei can still be separated structures. For these reasons, in this thesis the classification scheme will be based on this dynamical criteria rather than the morphological classification detailed above. Therefore, the galaxy sample will be divided into two categories:

- **Pre-Coalescence Galaxies:** Those with a nuclear separation of $> 1.5 \text{ kpc}$.
- **Post-Coalescence Galaxies:** Those with a nuclear separation of $\leq 1.5 \text{ kpc}$.

This classification is simpler and better fitted for the present work purposes. The pre-coalescence galaxies comprise the types I, II, and III of Veilleux et al. , whereas the post-coalescence ones include types IV and V. The classification of the galaxies (11 pre- and 11 post-coalescence systems) and a brief description, among other useful parameters, are given in Table 3.1 (see in Appendix A the morphological notes for all the galaxies of the sample).

3.3 Stellar and Ionized Gas Structure

In this section the differences in the spatial distribution between the observed stellar and ionized gas components of our sample of ULIRGs are presented.

The continuum images generated with the INTEGRAL-based spectra recover the stellar structure observed in the highly angular resolution *HST* images, even in the low-surface brightness structures (see first and second panels in Fig. 3.1 to Fig. 3.6, where the galaxies are sorted by morphological type). This good behavior makes us confident that all the observed ionized gas structures are real. The stellar continuum structure in the outer low surface brightness regions is an indication of the morphological type. In the pre-coalescence galaxies they trace the bridges, plumes and tails that connect the galaxies. In the post-coalescence galaxies it tend to trace outer envelopes that bear resemblance to that of a perturbed elliptical, along with some mergers features (e.g., tails).

The structure of the warm ionized gas is traced here by the $H\alpha$ and $[O\text{ III}]\lambda 5007$ emission line maps (the rest of emission line maps can be found in Appendix B). The general morphology of the low surface brightness ionized gas maps is similar to that of the stellar component, although in some galaxies variations associated to gas in high excitation state are present (e.g., Arp 299, Mrk 463, Mrk 273 and IRAS 11087+5351). Nevertheless, the most important structural differences between the stellar and ionized gas components are observed in the high surface brightness regions (i.e., the main body of the galaxies). These variations in the distribution of the emission-line gas are not only due to the internal extinction effects, but they also reflect changes in the ionization conditions as a function of location within the galaxy. Specifically, $H\alpha$ traces preferentially the presence of young stellar populations (<5-10 Myr) including TDGs candidates, $[O\text{ III}]\lambda 5007$ traces the high excitation produced by an AGN, and $[O\text{ I}]\lambda 6300$ indicates the presence of shocks. These morphological variations dominate mostly in the pre-coalescence systems, and are present in some post-coalescence galaxies with double nuclei. The separation between the peaks of the different emission line maps and the continuum are listed in Table 3.2. The main results regarding the variations in the ionized gas structure can be summarized as follows:

- **Pre-Coalescence Galaxies:**

In this group there is a system that can be considered a particular case: IRAS 13156+0435. With a nuclear separation of 36 kpc is the only system in the sample that appears to have undergone its first peri-passage, but presents a nuclear separation still large and has the structure of the individual galaxies well preserved. It can be considered as an early pre-coalescence galaxy. For these reasons in several occasions their results will be highlighted.

The ionized gas emission for the galaxy IRAS 13156+0435 presents basically the same morphology and extension than the stellar one, with only slight variations on the position of the maximum in $[O\text{ III}]\lambda 5007$ (see Table 3.2). This indicates, for example, that in this stage of the merging process the transfer of material between the two galaxies and the shocks resulting from the fusion are not sufficient to activate extra-nuclear star formation. For the rest of pre-coalescence galaxies, the most relevant characteristics are:

- In general, one of the optical nucleus is a weak line emitter, with surface brightness

Table 3.2: Separation between the red continuum and the emission-line gas peaks.

Galaxy	Separation ^a (kpc)	[SII] λ 6716,6731 ^b (kpc)	[OI] λ 6300 ^b (kpc)	[NII] λ 6548,6584 ^b (kpc)	H α ^b (kpc)	[OIII] λ 5007 ^b (kpc)	H β ^b (kpc)
IRAS 13156+0435N	36.0	0.0 \pm 1.4	0.0 \pm 1.4	0.0 \pm 1.4	0.0 \pm 1.4	0.0 \pm 1.4	0.0 \pm 1.4
IRAS 13156+0435S	36.0	0.0 \pm 1.4	0.0 \pm 1.4	0.0 \pm 1.4	0.0 \pm 1.4	0.7 \pm 1.4	0.0 \pm 1.4
IRAS 13342+3932	25.1	0.0 \pm 5.9	2.5 \pm 5.9	0.0 \pm 5.9	0.0 \pm 5.9	1.9 \pm 5.9	0.0 \pm 5.9
IRAS 18580+6527	15.0	0.0 \pm 2.1	0.0 \pm 2.1	0.0 \pm 2.1	0.0 \pm 2.1	0.0 \pm 2.1	0.0 \pm 2.1
IRAS 16007+3743	14.2	2.4 \pm 2.2	2.9 \pm 2.2	2.2 \pm 2.2	10.0 \pm 2.2	9.3 \pm 2.2	10.0 \pm 2.2
IRAS 06268+3509	9.1	1.2 \pm 2.0	8.0 \pm 2.0	0.6 \pm 2.0	0.7 \pm 2.0	2.9 \pm 2.0	1.7 \pm 2.0
IRAS 08572+3915	6.1	6.3 \pm 0.8	0.0 \pm 0.8	6.3 \pm 0.8	6.3 \pm 0.8	4.7 \pm 0.8	0.0 \pm 0.8
IRAS 14348–1447	5.5	0.0 \pm 1.1	0.0 \pm 1.1	0.0 \pm 1.1	0.0 \pm 1.1	0.9 \pm 1.1	0.0 \pm 1.1
Arp 299/NGC 3690	5.0	1.3 \pm 0.1	0.3 \pm 0.1	1.3 \pm 0.1	1.3 \pm 0.1	1.3 \pm 0.1	1.2 \pm 0.1
Arp 299/IC 694	5.0	0.8 \pm 0.1	1.0 \pm 0.1	1.8 \pm 0.1	1.8 \pm 0.1	1.1 \pm 0.1	1.1 \pm 0.1
IRAS 13469+5833	4.5	N/A	N/A	N/A	N/A	N/A	N/A
IRAS 12112+0305	4.0	0.7 \pm 1.0	0.7 \pm 1.0	1.1 \pm 1.0	3.7 \pm 1.0	3.7 \pm 1.0	3.6 \pm 1.0
Mrk 463	3.8	3.7 \pm 0.7	3.7 \pm 0.7	3.7 \pm 0.7	3.7 \pm 0.7	3.7 \pm 0.7	3.7 \pm 0.7
IRAS 06487+2208	1.5	0.0 \pm 0.9	1.4 \pm 0.9	0.0 \pm 0.9	0.0 \pm 0.9	0.0 \pm 0.9	0.0 \pm 0.9
IRAS 11087+5351	1.5	0.9 \pm 0.9	7.0 \pm 0.9	0.6 \pm 0.9	0.7 \pm 0.9	8.1 \pm 0.9	7.6 \pm 0.9
Mrk 273	0.7	0.3 \pm 0.5	0.4 \pm 0.5	0.2 \pm 0.5	0.3 \pm 0.5	3.6 \pm 0.5	0.5 \pm 0.5
Arp220	0.4	0.3 \pm 0.2	0.3 \pm 0.2	0.5 \pm 0.2	0.4 \pm 0.2	N/A	N/A
IRAS 09427+1929	0.0	N/A	N/A	0.0 \pm 0.0	0.0 \pm 0.0	N/A	N/A
IRAS 12490–1009	0.0	0.0 \pm 1.3	0.0 \pm 1.3	0.0 \pm 1.3	0.0 \pm 1.3	0.0 \pm 1.3	0.0 \pm 1.3
Mrk 231	0.0	N/A	N/A	0.0 \pm 0.3	0.0 \pm 0.3	N/A	N/A
IRAS 14060+2919	0.0	0.0 \pm 1.5	0.9 \pm 1.5	0.0 \pm 1.5	0.0 \pm 1.5	0.0 \pm 1.5	0.0 \pm 1.5
IRAS 15206+3342	0.0	0.0 \pm 1.6	0.0 \pm 1.6	0.0 \pm 1.6	0.0 \pm 1.6	0.0 \pm 1.6	0.0 \pm 1.6
IRAS 15250+3609	0.0	0.4 \pm 0.7	0.0 \pm 0.7	0.2 \pm 0.7	0.4 \pm 0.7	0.0 \pm 0.7	0.0 \pm 0.7
IRAS 17208–0014	0.0	0.5 \pm 0.6	0.3 \pm 0.6	0.6 \pm 0.6	0.5 \pm 0.6	0.2 \pm 0.6	:

Note: (a): Nuclear separation for each system. (b): Separation between the peak of the red continuum and the ionized gas. Uncertainties have been derived taking into account the fiber diameter. Horizontal line separates pre- and post-coalescence objects.

- emission of the order of the interface between the galaxies. This is a consequence of the combined effect of different ionization mechanisms and the presence of dust.
- The observed spatial distribution of the H α recombination line is different than the continuum in 80% of the systems. The H α emission tends to be more compact, with the peak separated up to 10 kpc from the continuum. The H β distribution follows that one of H α , but with lower signal due to the extinction by dust and to the effect of the Balmer decrement (H α /H β =2.86). Also, extra-nuclear star-forming regions candidates to TDGs with H α emission are detected in 40% of systems¹.
 - There are significant shifts (up to about 8.0 kpc) between the [OI] λ 6300 and continuum peaks in 40% of systems. Furthermore, its overall morphology tends to be different than the stellar one (see Appendix B).
 - The peak of the high excitation line [OIII] λ 5007 coincides with that of H α in all cases, but IRAS 08572+3915. However, variations among the secondary peaks and in distribution of the low surface brightness regions are detected. In addition, we measure displacements of up to 9.3 kpc among the emission line and the continuum peaks. These variations are likely due to the different excitation mechanisms (e.g., presence of an obscured AGN) taking place not only in the nuclei of the systems, but in the external regions where the presence of dust is expected to be lower.
 - The [NII] λ 6548, 6584 and [SII] λ 6716, 6731, present, in 45% of cases, a behavior in general consistent with that of H α .

¹IRAS 16007+3743, IRAS 08572+3915, IRAS 14348–1447, IRAS 12112+0305.

- **Post-Coalescence Galaxies:**

For galaxies where the merger is evolved, the ionized gas tend to mimic the structure of the stellar component. In all cases, the $H\alpha$ emission is concentrated towards the optical nucleus, indicating that in the final merger stages the star formation is mainly nuclear. Nevertheless there are two galaxies with some characteristics worth mentioning: IRAS 11087+5351 and Mrk 273. Both have in common a double nucleus and clear morphological merger features (such as tidal tails and/or the presence of an outer envelope), along with a distribution of the ionized gas different to that of the continuum. The [OI] and [OIII] lines structure present remarkable differences, with peaks in extra-nuclear ionized clouds (most likely to be excited by the presence of an AGN) located up to 7-8 kpc from the nucleus respectively. In this morphologically evolved galaxies we detect extra-nuclear star-forming condensations (candidates to TDGs) only in about 10% of cases (IRAS 15250+3609).

In summary, the main structural differences between the pre- and post-coalescence systems are:

1. The two-dimensional structure of $H\alpha$ indicates that the observed extra-nuclear star formation, including the presence of TDGs candidates, is more likely to be present in the pre-coalescence systems. On the contrary in the most evolved mergers the star formation is concentrated towards the nuclei.
2. The differences in the spatial distribution of the stellar and ionized gas components are more common in the pre-coalescence systems. These variations are due to the nature and spatial distribution of the ionization sources and to the distribution of dust.
3. The disagreement observed in the structure of the continuum and the high excitation line [O III] λ 5007 in Arp 299, Mrk 273 and IRAS 11087+5351, trace the presence of ionization cones and highly-excited extra-nuclear clouds. These are indirect evidences for the presence of AGNs.

3.4 Two-Dimensional Dust Structure

There are strong evidence from multi-wavelength studies that the most active regions (starbursts or AGN) in ULIRGs are enshrouded in dust. In any case, although the dust distribution tend to be concentrated in the inner few kpc, it is very patchy, and differential extinction effects play a major role (e.g., Colina et al. 2001). For instance, the differential extinction may produce a non coincidence between the true nucleus of the galaxy and the region identified as the optical one (e.g., in IRAS 17208–0014 they are located 1.3 kpc apart Arribas & Colina 2003; in Arp 299 they are located 0.5 kpc apart García-Marín et al. 2006). In this section, the dust structure in ULIRGs will be presented. First the case of Arp 299 will be analyzed in detail, and next, the global properties derived for the entire sample will be presented.

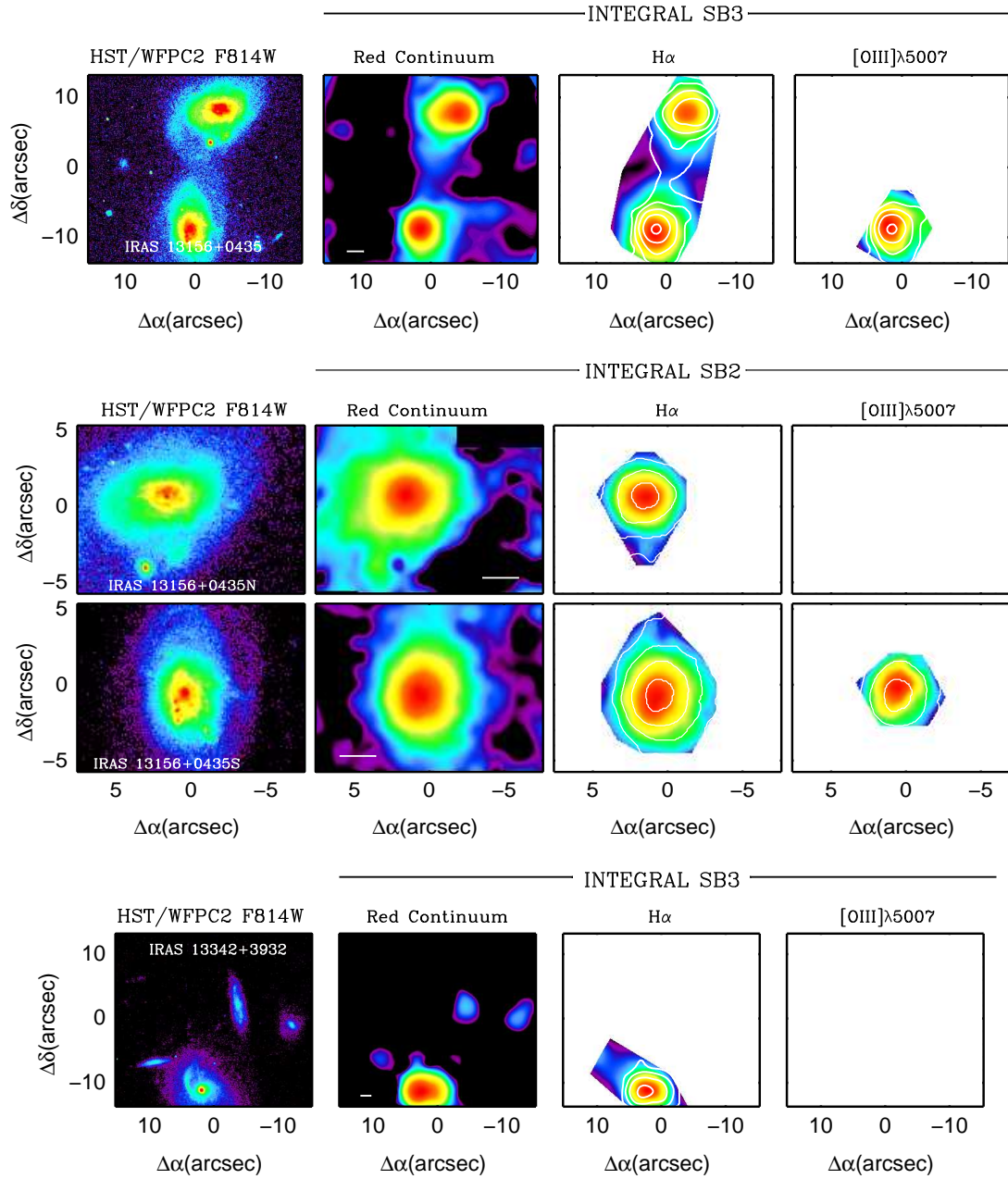


Figure 3.1: **From left to right:** *HST*/WFPC2 F814W images for IRAS 13156+0435 and IRAS 13342+3932. Emission-line free stellar continuum and emission-line images for IRAS 13156+0435 obtained with INTEGRAL SB3 and SB2 bundles (upper and middle panels) and for IRAS 13342+3932 obtained with the SB3 bundle (lower panel). The contours represent the red continuum. The maps are not corrected for extinction. The horizontal line represents 5 kpc. [O III] is detected in the N component, but not with enough information as to obtain a map.

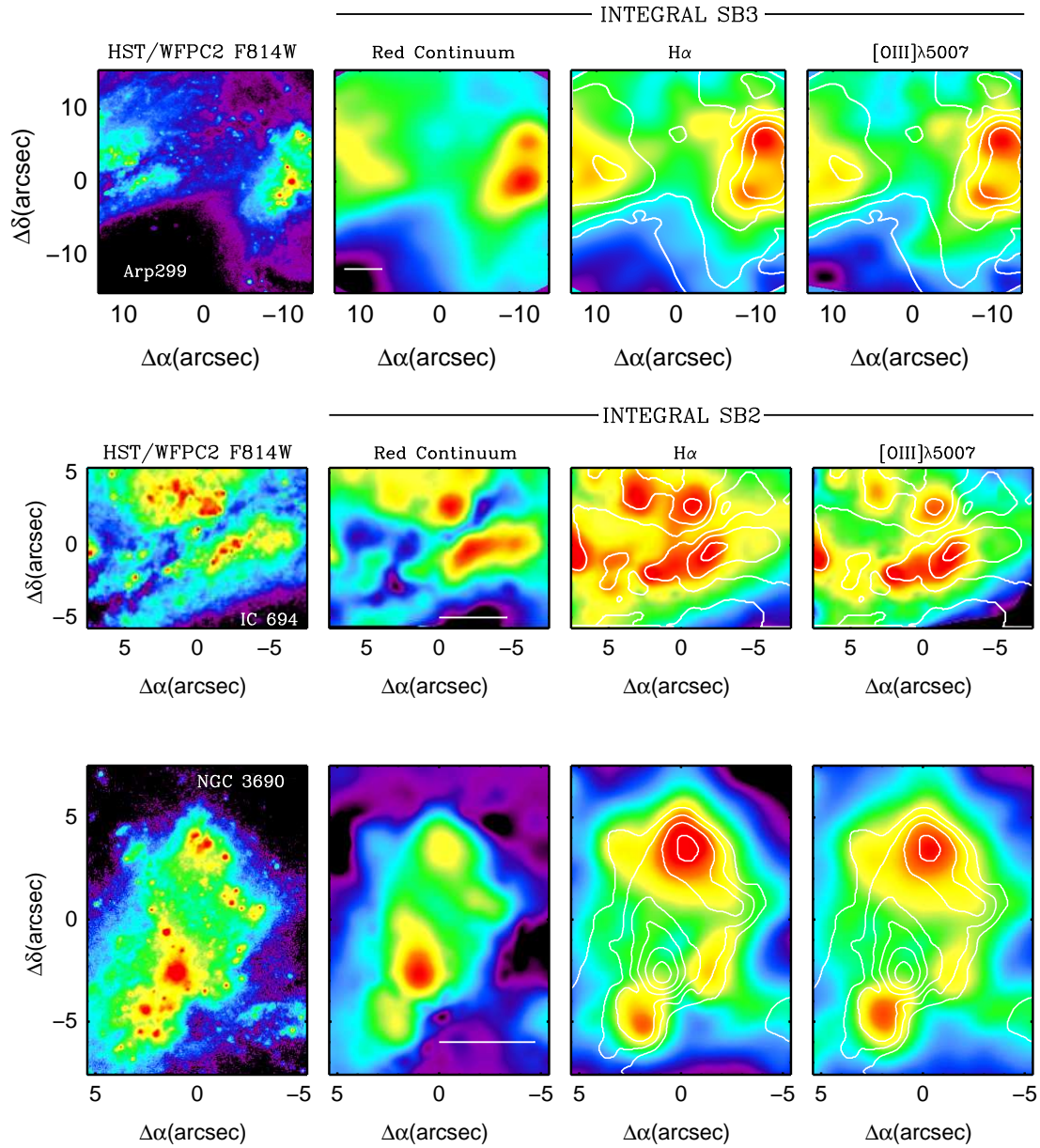


Figure 3.2: **From left to right:** *HST*/WFPC2 F814W image for the Arp 299 system. Emission-line free stellar continuum and emission-line images for the Arp 299 system obtained with INTEGRAL SB2 and SB3 bundles. The contours represent the red continuum. The maps are not corrected for extinction. The horizontal line represents 1 kpc.

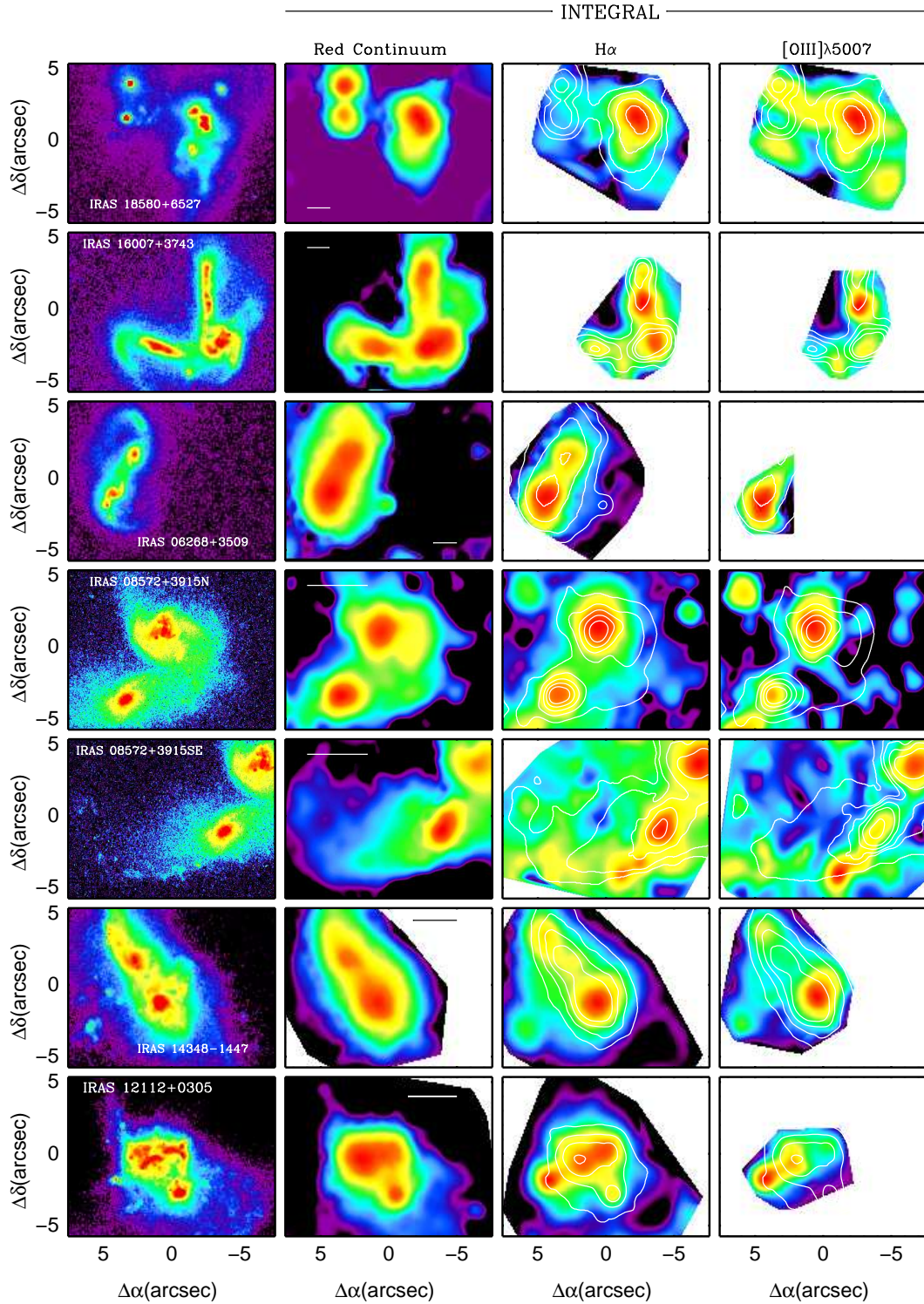


Figure 3.3: **From left to right:** *HST*/WFPC2 F814W images of the galaxies. Emission-line free stellar continuum and emission-line images for seven ULIRGs of the sample obtained with INTEGRAL SB2 bundle. The contours represent the red continuum. The maps are not corrected for extinction. The horizontal line represents 5 kpc.

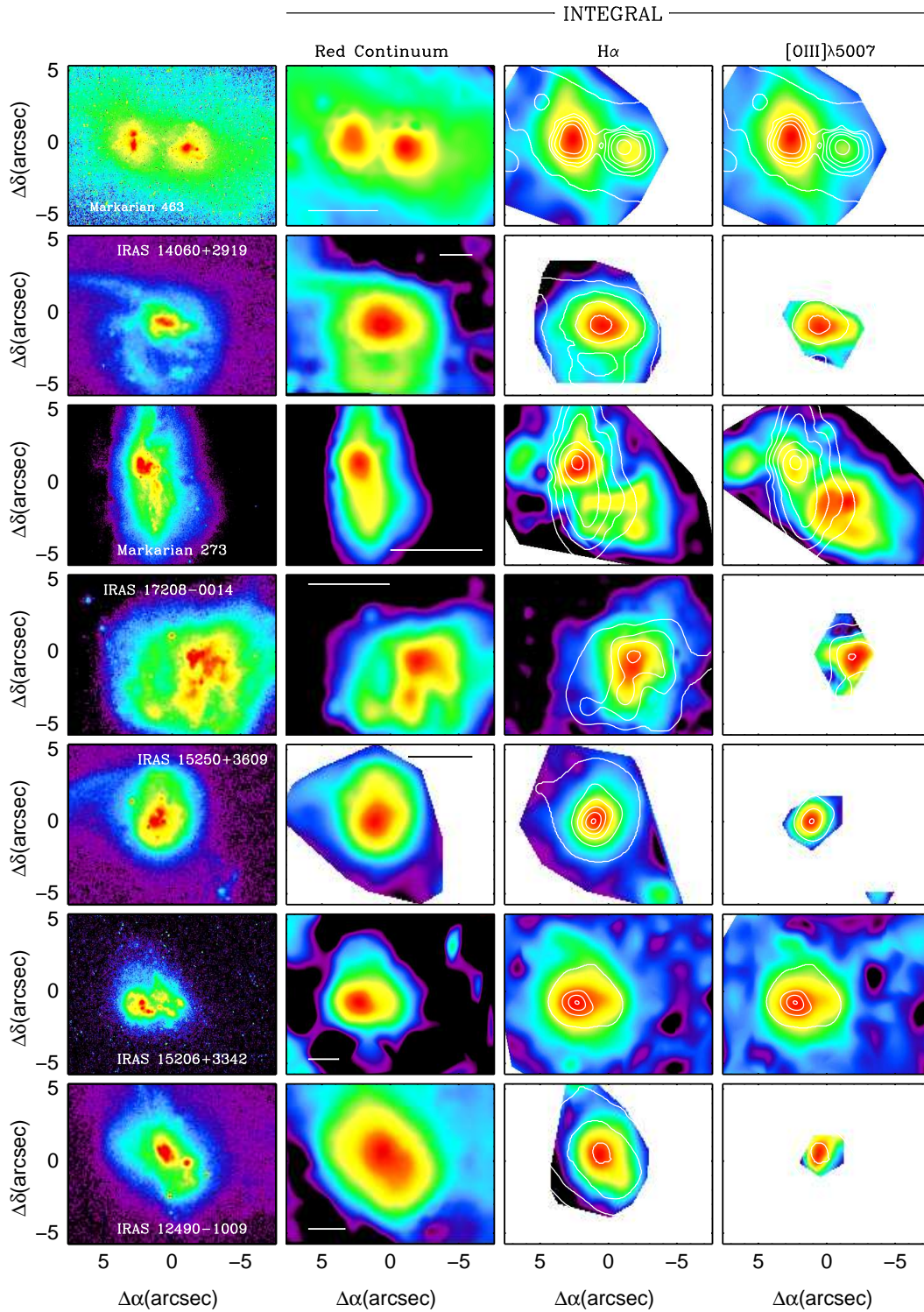


Figure 3.4: **From left to right:** *HST*/WFPC2 F814W images of the galaxies. Emission-line free stellar continuum and emission-line images for seven ULIRGs of the sample obtained with INTEGRAL SB2 bundle. The contours represent the red continuum. The maps are not corrected for extinction. The horizontal line represents 5 kpc.

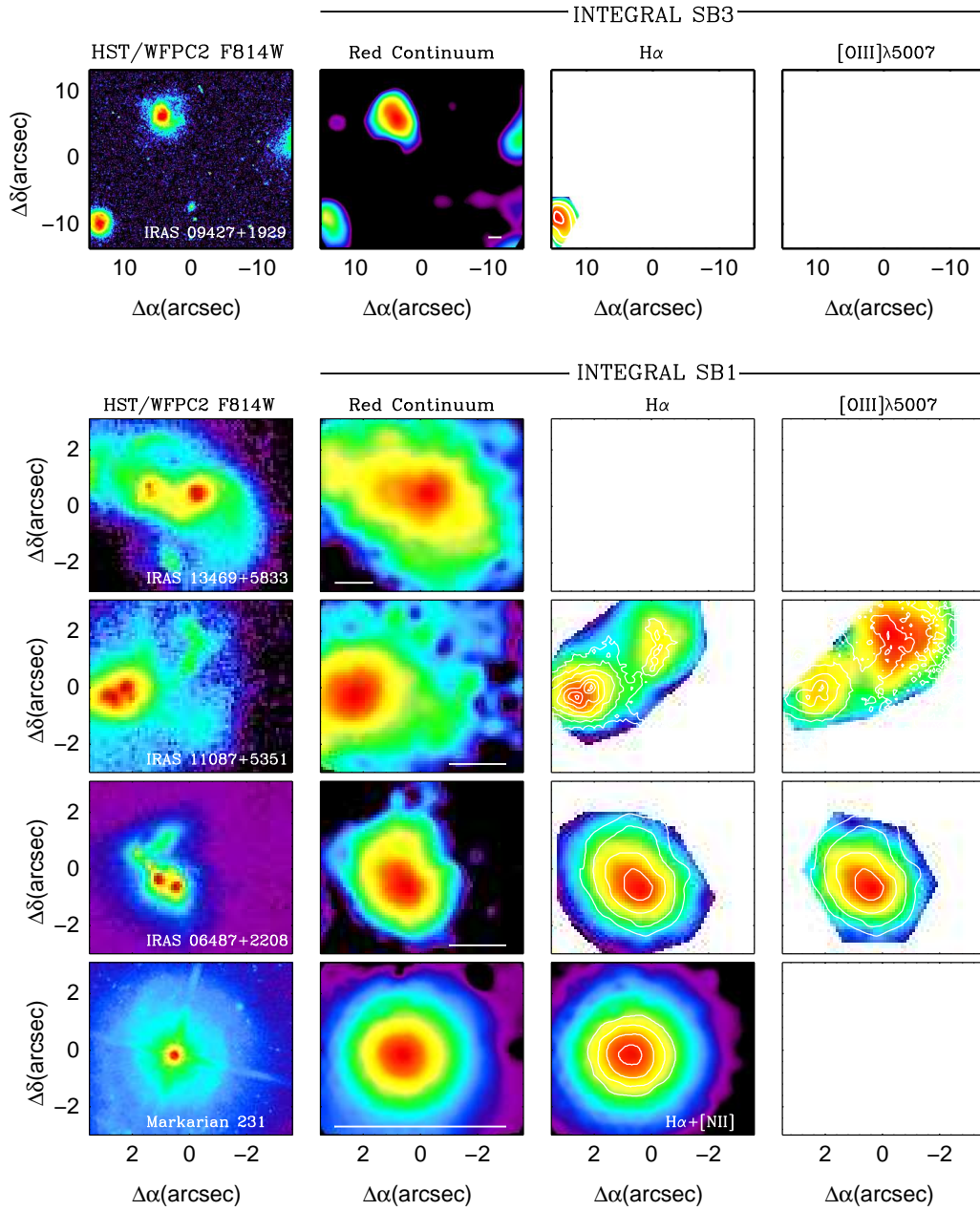


Figure 3.5: **From left to right:** *HST*/WFPC2 F814W images of the galaxies. Emission-line free stellar continuum and emission-line images for IRAS 09427+1929 as observed with the SB3 bundle (upper panel), and for four ULIRGs of the sample system obtained with INTEGRAL SB1 bundle (lower panel). The contours represent the red continuum. Due to the contamination of the AGN, in Mrk 231 the Gaussian fit of the lines was uncertain. Therefore the continuum-subtracted $H\alpha + [NII]$ map derived with a filter is presented. The white panels indicate no emission or no available data. The maps are not corrected for extinction. The horizontal line represents 5 kpc.

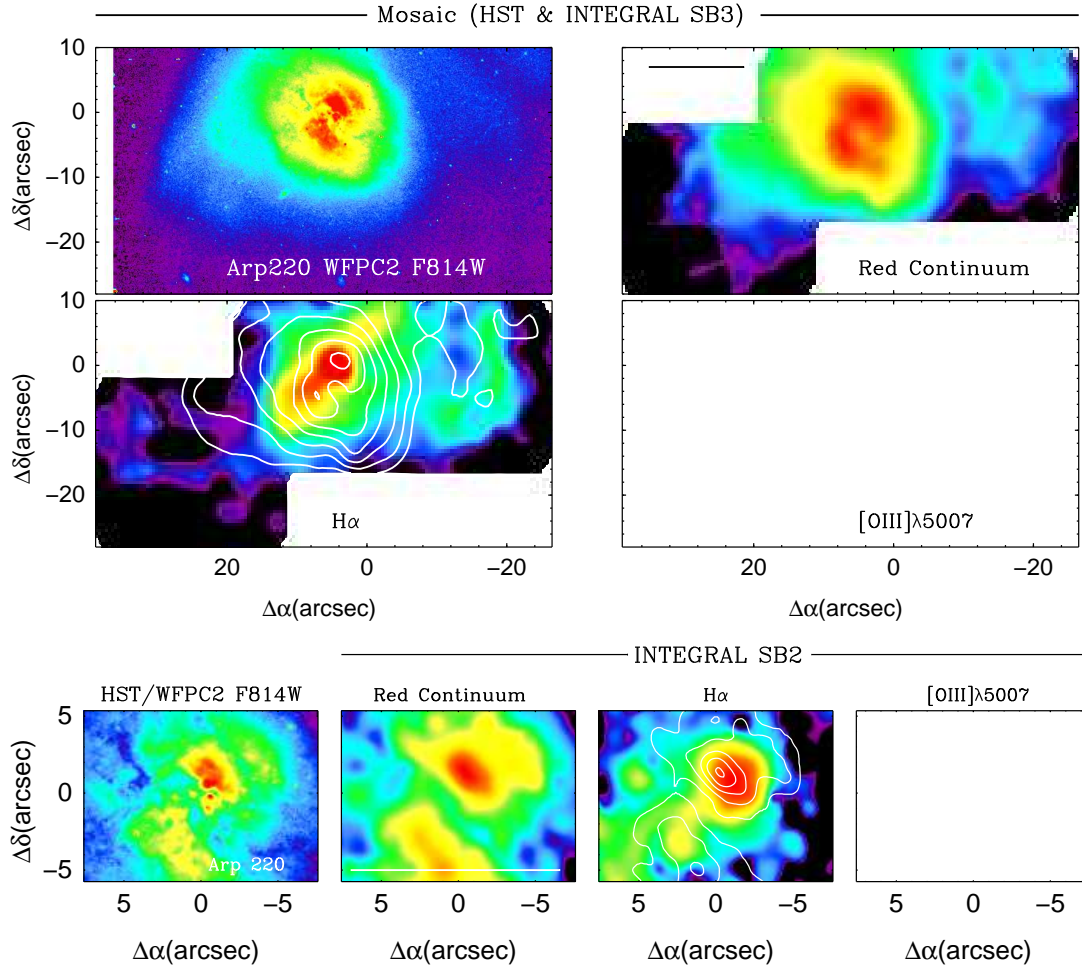


Figure 3.6: **From left to right:** *HST*/WFPC2 F814W images of Arp 220. Emission-line free stellar continuum and emission-line images for the Arp 220 obtained with INTEGRAL SB3 and SB2 bundles. The contours represent the red continuum. The white panels indicate no emission or no available data. The maps are not corrected for extinction. The [OIII] is not detected on this galaxy. The horizontal line represents 5 kpc.

In all galaxies, the extinction has been derived using the $H\alpha/H\beta$ line ratio (Balmer decrement), a foreground dust screen model and a mean interstellar extinction law based on Savage & Mathis (1979). No correction for the presence of underlying stellar hydrogen absorption lines has been applied. Assuming an equivalent width value of $EW_{abs}(H\alpha)=EW_{abs}(H\beta)\sim 2 \text{ \AA}$, the derived extinction would be overestimated by as much as $\Delta E(B-V)\sim 0.6$ for regions with extremely faint $H\beta$ emission [e.g., $EW(H\beta)\leq 20 \text{ \AA}$]. It is important to emphasize that with these optical lines it is only possible to derive the extinction up to a limit. In most occasions, and especially in dusty systems such as ULIRGs, the Balmer decrement provides only a lower limit to the extinction, specially in the central regions.

3.4.1 Internal Dust Distribution and Extinction Effects in Arp 299

Arp 299 is a nearby ($D_L\sim 43 \text{ Mpc}$) pre-coalescence LIRG (although its L_{IR} is close to the limiting value for ULIRGs) composed by two members, the eastern IC 694 and the western NGC 3690. For a long time it has been considered the prototypical LIRG, and thus has been studied in great detail in all spectral ranges. For this particular case we used three different INTEGRAL pointings: one with the SB3 bundle to cover the galaxies as well as the interface region, and two with the SB2 bundle for covering the individual galaxies (see details in Fig 3.7 and García-Marín et al. 2006).

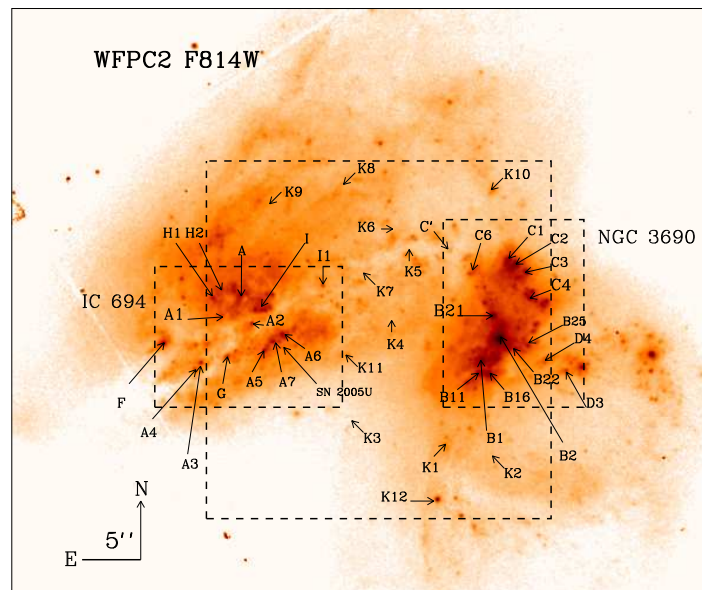


Figure 3.7: Archival HST image of the interacting system Arp 299 obtained with the WFPC2 F814W filter. The rectangular overlays indicate the effective area covered by the three pointings with the two INTEGRAL configurations used (i.e., SB2 small rectangles, SB3 large rectangle). We have marked the positions of the regions under study (see García-Marín et al. 2006). The location of a near-IR SN is marked too (Mattila et al. 2005). The image is shown on a logarithmic scale.

The two-dimensional extinction maps of the gas for the three pointings are shown in Figs. 3.8, 3.9 and 3.10. In the particular case of Arp 299 the results indicates that the highest extinguished regions are, in general, associated with the nuclei and some particular regions, whereas the external star-forming regions are less affected by the presence of dust:

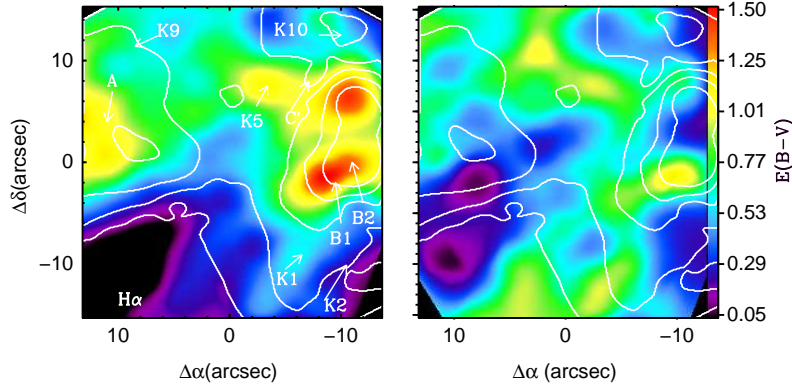


Figure 3.8: **Left:** Extinction-corrected $H\alpha$ flux distribution for the Arp 299 system (including the interface region), shown on a logarithmic scale. **Right:** Extinction map for the interface region obtained from the line ratio $H\alpha/H\beta$ shown on a linear scale. Contours represent the red continuum (García-Marín et al. 2006).

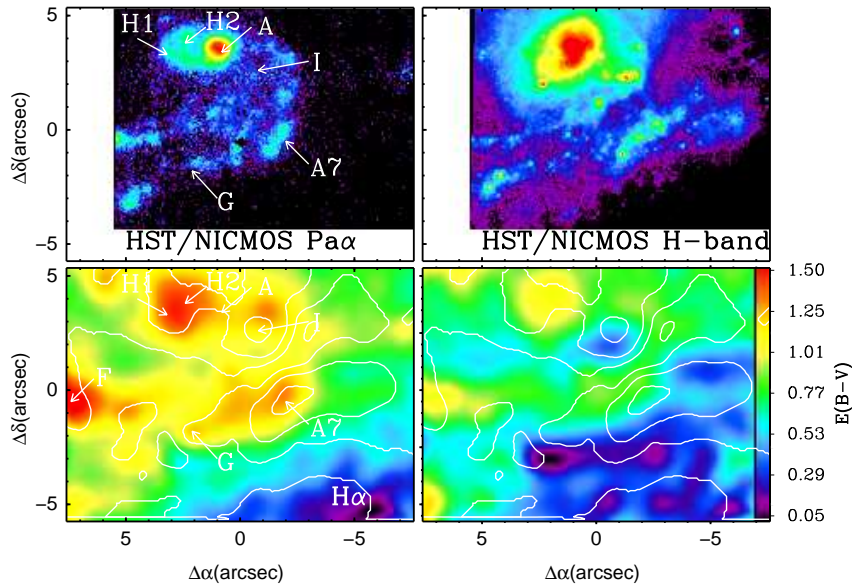


Figure 3.9: IC 694 (Arp 299E). **Top Left:** *HST/NICMOS* continuum-subtracted $Pa\alpha$ emission (F190N-F187N). **Top Right:** *HST/NICMOS* H-band continuum. **Bottom Left:** *INTEGRAL* $H\alpha$ extinction-corrected flux distribution. **Bottom Right:** Extinction map obtained with the $H\alpha/H\beta$ line ratio. As a reference several regions of interest are marked, and the red continuum contours are superimposed on the interpolated maps. The *NICMOS* images are shown covering the same FOV as the *INTEGRAL* data. All the images are represented on a logarithmic scale except for the extinction map, where a linear scale has been applied (see details in García-Marín et al. 2006 and Alonso-Herrero et al. 2000).

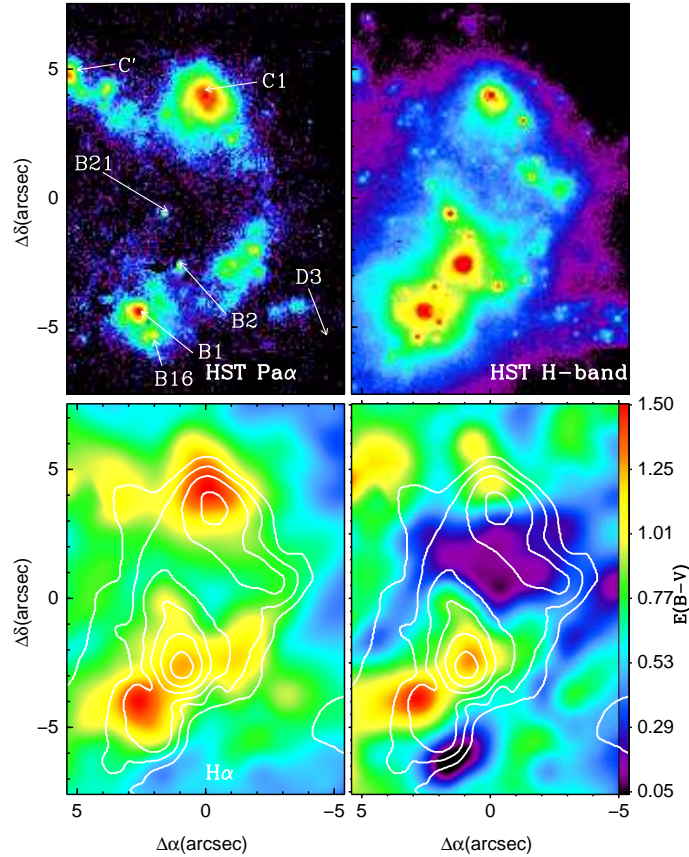


Figure 3.10: NGC 3690 (Arp 299) maps. **Top Left:** *HST*/NICMOS continuum-subtracted Pa α emission (F190N–F187N). **Top Right:** *HST*/NICMOS H-band continuum. **Bottom Left:** INTEGRAL H α extinction-corrected flux distribution. **Bottom Right:** Extinction map obtained with the H α /H β line ratio. As a reference several regions of interest are marked, and the red continuum contours are superimposed on the interpolated maps. The NICMOS images are shown covering the same FOV as the INTEGRAL data. All the images are shown on a logarithmic scale except for the extinction map, where a linear scale has been applied (see details in García-Marín et al. 2006 and Alonso-Herrero et al. 2000).

- **Interface Region:**

The extinction in the whole area covered by the SB3 bundle on scales of about 0.6 kpc is shown in Fig. 3.8. In the interface between the galaxies, it has an average value of $A_V=1.9$ mag in the regions under study (see details of the selection of the individual regions in García-Marín et al. 2006), and ranges from 0.9 ± 0.7 to 2.9 ± 0.7 .

- **IC 694:**

On scales of about 0.2 kpc, the internal extinction in the visual covers from $A_V=0.6\pm 0.5$ to 3.4 ± 0.5 mag. As can be seen in Fig. 3.9, the extinction corrected H α light distribution shows an overall morphology similar to that of the Pa α line ($\lambda_{\text{rest}}=1.875$, see Alonso-Herrero et al. 2000) except for the region associated with the peak of the emission. The nucleus of the galaxy, A, identified as the brightest near-infrared source in the *HST* images, is also the dominant Pa α line emitter. Additionally secondary H α sources are

mostly associated with star-forming regions at distances of 1-1.6 kpc from the nucleus, and tracing what seems to be a spiral-like arm previously identified in the Pa α emission-line map.

- **NGC 3690:**

This galaxy presents the widest range of extinction for the entire Arp 299 system, with values of up to $A_V=4.6\pm0.6$ mag (see Fig. 3.10). The overall H α distribution agrees well with that of the Pa α line not only in the high surface brightness region, but also in the low surface brightness ones.

Additional line ratios involving IR hydrogen recombination lines (e.g., Pa α /H α , Br γ /Pa α and Pa α /H α) can provide better estimates of the internal extinction in highly extinguished regions as those identified in Arp 299. The Pa α images of the individual galaxies (Alonso-Herrero et al. 2000) have been used for measuring the extinction in all the regions under study. The results indicate that the extinction derived using the H α /H β ratio are in general consistent with the ones derived using the Pa α /H α ratio, except in the highly absorbed regions. In that regions we measure an underestimation of a factor 2 in A_V when only the optical emission lines are used (see individual values in García-Marín et al. 2006 and Alonso-Herrero et al. 2000).

3.4.2 Internal Extinction in ULIRGs

A comprehensive analysis (similar to that carried out in Arp 299 but with lower angular resolution) can be performed for the galaxies of the sample. However, the aim here is to obtain a global view of the two-dimensional dust distribution in (U)LIRGs and not to focus on the individual details. Therefore the main results regarding the internal obscuration produced by the dust are given in what follows.

The results obtained from the analysis of the dust distribution are summarized in Table 3.3. For the pre-coalescence galaxies the mean value for the average extinction of the galaxy is $A_V=1.9\pm0.7$ mag, whereas the extinction of the optical nucleus presents a mean value of $A_V=3.2\pm2.0$ mag, one magnitude lower than the average of the region with highest extinction, $A_V=4.1\pm1.8$ mag. For the post-coalescence galaxies, the derived average values are similar: $A_V=2.3\pm1.7$ mag for the mean extinction, 2.6 ± 1.4 mag for the optical nucleus and 4.2 ± 1.8 mag for the maximum value.

As expected, the dust distribution is very patchy (see two-dimensional distribution in Appendix C), although in general its largest concentrations are located towards the nuclei. In the pre-coalescence systems the region with highest extinction is located within a distance of about 3.5 kpc from one optical nucleus. This percentage rises up to 87% in the post-coalescence galaxies. Taking into account that the mean linear scale of the sample is ~ 2.0 kpc/arcsec, and that the most common-used INTEGRAL bundle is the SB2 (0'9 per fiber), in the majority of ULIRGs (pre- and post-coalescence galaxies) the dust is concentrated towards the central kpc. The values derived for the extinction are of the order of those obtained for LIRGs (Alonso-Herrero et al. 2006), with the caveat that they may not be detecting the most obscured regions in H α . Given all this we can assert that some of the structural differences found between the stellar and the ionized gas components are partly due to the obscuration by dust. However, those spatial differences are indeed tracing variations in the ionization conditions and the state of the gas, as it will be addressed in the next

Table 3.3: Extinction information for the sample of galaxies

Galaxy (IRAS Name)	$A_{V\,mean}^1$ (mag)	$A_{V\,nuc}^2$ (mag)	$A_{V\,max}^3$ (mag)	Sep (kpc)
IRAS 13156+0435N	2.6±0.3	3.4	3.8	3.9±1.0
IRAS 13156+0435S	0.8±0.5	1.5	1.8	2.2±1.0
IRAS 13342+3932W	2.4±0.6	1.8	3.1	9.4±4.1
IRAS 13342+3932E	2.4±0.6	—	—	—
IRAS 18580+6527E	1.2±0.9	0.5	3.1	20.3±1.5
IRAS 18580+6527W	1.2±0.9	0.8	3.1	8.7±1.5
IRAS 16007+3743E	2.2±1.3	4.5	4.9	12.7±1.5
IRAS 16007+3743W	2.2±1.3	4.7	4.9	1.4±1.5
IRAS 06268+3509N	2.2±1.7	5.6	6.5	3.2±1.4
IRAS 06268+3509S	2.2±1.7	2.2	6.5	10.5±1.4
IRAS 08572+3915N	1.7±1.4	2.8:	2.8:	0.0±0.6
IRAS 08572+3915S	1.7±1.4	N/A	N/A	N/A
IRAS 14348–1447N	2.9±1.3	5.4	5.7	5.6±0.8
IRAS 14348–1447S	2.9±1.3	5.0	5.7	0.8±0.8
Mrk 463-E	0.9±0.6	0.7	2.7	4.7±0.5
Mrk 463-W	0.9±0.6	1.5	2.7	8.4±0.5
Arp 299/NGC 3690	1.9±0.8	3.7	3.9	0.5±0.1
Arp 299/IC 694	1.9±0.7	2.9	3.4	0.3±0.1
IRAS 12112+0305N	2.0±1.7	2.3	7.9:	5.5±0.7
IRAS 12112+0305S	2.0±1.7	7.9	7.9	0.0±0.7
IRAS 06487+2208	2.1±0.7	2.4	4.4	4.3±0.6
IRAS 11087+5351	1.4±1.2	3.2	3.2	0.0±0.6
Mrk 273	1.9±0.4	2.9	4.8	2.1±0.4
Arp 220	N/A	N/A	N/A	N/A
IRAS 09427+1929	N/A	N/A	N/A	N/A
IRAS 12490–1009	1.5±1.0	1.1	3.1	3.6±0.9
IRAS 14060+2919	1.5±0.6	2.2	2.6	2.3±1.0
IRAS 15206+3342	0.7±0.5	1.0	2.0	2.4±1.0
IRAS 15250+3609	3.0±2.3	2.5	7.7	2.4±0.5
IRAS 17208–0014	6.1±2.2	5.5	5.5	0.0±0.4

Notes: (1) Average extinction of the entire system \pm the standard deviation. (2) Nuclear extinction of the galaxy. The uncertainties are about 20% (3) Maximum extinction of the system. (4) Separation between the nucleus and the position of the extinction peak.

Chapter.

3.5 Testing the Evolutionary Scenarios for ULIRGs

One characteristic feature shown by ULIRGs is the interaction/merger process that they undergo, which plays a major role in their formation, evolution and fate. Although observationally it is not clear whether mergers can account for the formation of the elliptical galaxies (e.g., Floyd et al. 2004; Lotz et al. 2006), today it is widely accepted that they actually play a major role. As it has been shown by numerical simulations, dry mergers between early-type galaxies would form pressure supported massive ($\gtrsim 10^{11} M_{\odot}$) boxy ellipticals (Bender et al. 1992; Naab, Burkert & Hernquist 1999; Naab, Khochfar & Burkert 2006b; Hopkins et al. 2007). In contrast, intermediate mass disk elliptical galaxies with significant rotational support may be the result of relatively recent mergers of dissipative gas-rich galaxies (e.g Kormendy 1979; Nieto et al. 1991; Bekki et al. 1997; Naab & Burkert 2003; Naab et al.

2006).

In the case of ULIRGs, numerical simulations of gas rich galaxy mergers can reproduce their characteristics. In this context, the mass and the bulge-to-disk ratio are key parameters for determining their main power source and evolution to elliptical galaxies (Bekki et al. 2006). Observational evidence point towards ULIRGs as mergers of intermediate mass ($0.5 < L < L_*$) disk galaxies (Colina et al. 2001). Therefore, and according to the “ellipticals through mergers” scenario (first proposed by Toomre & Toomre 1972), if ULIRGs are one phase of this evolutionary sequence they should resemble ellipticals at some level; whether in their morphology and/or dynamics. In fact, the location of ULIRGs in the fundamental plane (they resemble intermediate mass [$\sim L_*$] moderately rotating elliptical galaxies, Genzel et al. 2001) has contributed to understand their evolution.

The objective of this section is to test this proposed evolutionary scenario with our sample of ULIRGs. To that aim, two different approaches will be used:

- **Purely morphological approach:** To analyze the surface brightness distribution of the galaxies testing whether or not they follow an $r^{1/4}$ profile. If they do, this would support the elliptical in formation theory. Several works (ground-based Wright et al. 1991; space-based Scoville et al. 2000) found that, qualitatively, the near-IR surface brightness profiles of some ULIRGs are consistent with those of ellipticals. Furthermore, Zheng et al. (1999) using optical space-based images of ULIRGs, conclude quantitatively that mergers of disk galaxies produces elliptical or S0 galaxies. Still these are not conclusive evidence, as even in the near-IR the azimuthal combination of tails, bright star-forming regions and deeply buried AGN could emulate qualitatively a de Vaucouleurs profile (Genzel et al. 2001).
- **Morphological and dynamical approach:** To compare R_{eff} (i.e., the effective radius, defined as the radius that encloses half the luminosity), morphological parameters (such as the ellipticity and the isophotal shape boxy/disky) and dynamical indicators (such as the velocity dispersion σ and the velocity amplitude) with the results of merger models. In general these models predict that the characteristics of equal mass (1:1) and 2:1 dissipationless mergers remnants agrees with those of the population of ellipticals in the intermediate regime between low-mass fast rotating disk and bright, massive boxy giant ellipticals. The characteristics of the unequal-mass (3:1 and 4:1) dissipationless merger remnants reproduce well the properties of low luminosity, fast rotating elliptical galaxies (Naab & Burkert 2003). The addition of 10% of gas in the parent galaxies rules out the 1:1 merger as responsible for the formation of massive boxy giant ellipticals. Previous comparisons between observations and these models suggest that the end product of local Ultra-luminous mergers remnants are moderate-mass ellipticals (Dasyra et al. 2006).

3.5.1 Pure Morphological Approach: Analysis of the Light Profiles

The azimuthal profiles for all the galaxies under study are shown in Fig. 3.11, with the de Vaucouleurs $r^{1/4}$ law ($\mu = b - aR^{1/4}$, a straight line in this plot) fitted² over the *comparison range* (i.e., 3.8-10.5 kpc in the optical and 1.0-5.1 kpc in the near-IR).

²The least squares fits were performed using the IDL-based routine `mpfitexpr` by Craig B. Markwardt, <http://www.astro.washington.edu/deutsch/idl/htmlhelp/library26.html>.

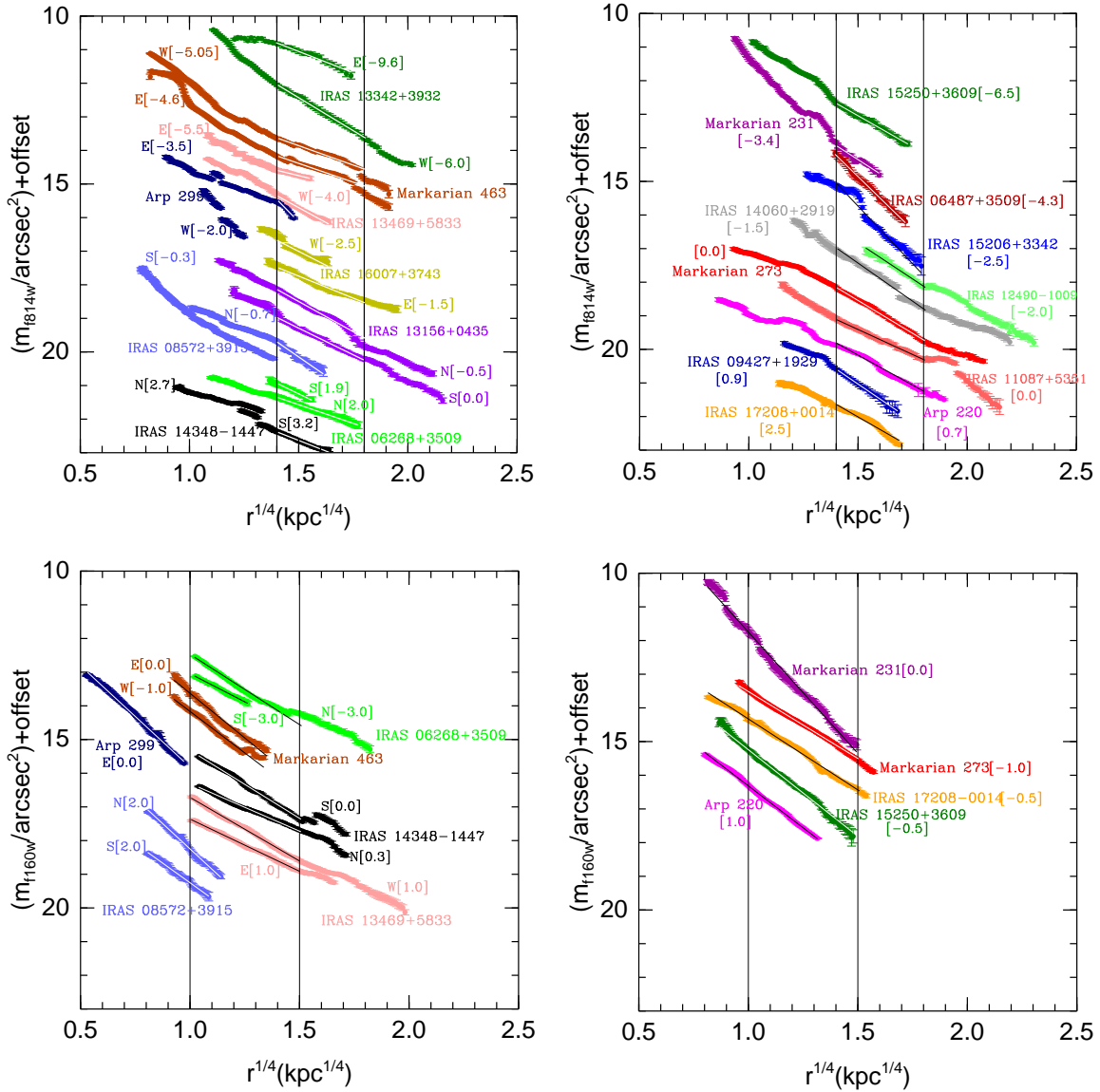


Figure 3.11: **Upper Panel:** F814W surface brightness (mag per arcsec²) plotted against the fourth root of the radius. Left: Pre-coalescence systems; for each one the two components are represented. Right: Post-coalescence galaxies. **Lower Panel:** F160W surface brightness (mag per arcsec²) plotted against the fourth root of the radius. Left: Pre-coalescence systems. Right: Post-coalescence galaxies. The values shown between brackets indicate the offset applied.

The analysis has been accomplished in all galaxies of the sample, except for IRAS 12112+0305 and IRAS 18580+6527, where the ellipse fitting is not appropriate due to their peculiar morphologies. In the near-IR profiles, the fit includes the innermost parts because of its consistent behavior with the *comparison range*. All galaxies show a smaller radial coverage in the F160W filter compared to that of the F814W. This is an instrumental effect derived from the different FOV of the cameras used: one chip of the WFPC2 covers $80'' \times 80''$ (or $36'' \times 36''$ if using the planetary camera), whereas the NICMOS2 camera occupies $19'.2 \times 19'.2$ on the sky.

In a qualitatively sense, the optical and near-IR light profiles present clear differences. While the optical profiles show strong (up to 1 mag/arcsec²) variations, especially in the innermost regions, the near-IR show a stable behavior in general more consistent with an $r^{1/4}$ law. These differences are a consequence of the morphological features shown by ULIRGs (see Figs. A.1 and A.2), some of whom are related to the presence of dust and are therefore wavelength-dependent. The innermost regions of the optical profiles (up to 3.8 kpc) are characterized by small structures and variations (up to about 0.5 mag/arcsec²), produced by the morphological features caused by the internal differential extinction. In near-IR wavelength range the largest departures (about 0.2 mag/arcsec²) from the $r^{1/4}$ law have been measured in the pre-coalescence ULIRGs, and are associated to the contribution coming from the companion galaxy. At distances of about 8 kpc and larger, the surface brightness distribution as measured in the optical present departures from a $r^{1/4}$ law by 0.3-0.5 mag/arcsec². These deviations coincide with the location of the outer limits of the galaxy (e.g., Markarian 463), with the presence of not resolved knots (e.g., IRAS 13156+0435N), tails (e.g., IRAS 12490–1009, Markarian 273, IRAS 14060+2919) or outer envelopes and low-surface brightness structures (IRAS 11087+5351).

The excesses with respect the de Vaucouleurs law have been measured as the differences between the observed and fitted profiles (see Table 3.4). In the optical light profiles, the averaged variations show no relevant differences (order of about ± 0.01 mag/arcsec²), indicating that over the studied range the sample of ULIRGs is consistent with an $r^{1/4}$ law. A similar conclusion is obtained in the near-IR band, with excess of the same order (order of about ± 0.01 mag/arcsec²) for both morphological types. Therefore, independently of their merger phase, the studied ULIRGs are consistent with an elliptical-like profile up to 10.5 kpc in the optical (although with local variations) and to 5.0 kpc in the near-IR. This result indicates that the conclusions derived from the morphology, even in the near-IR, must be taken with caution. A pure morphological approach is not enough by itself for determining the evolutionary history and fate of ULIRGs.

The second aspect that can be highlighted from this analysis are the obvious structural differences in the inner profiles between the optical and near-IR bands. These variations are believed to be a direct consequence of the observing wavelength range: the near-IR allows us to penetrate the dust (even though not at a 100% level in the most obscured regions) and thus to avoid the extinction effects produced by the most external layers of material.

The impact of the dust contribution can be evaluated by means of the F814W–F160W color. The galaxies color profiles can be divided into two groups: those with variations in color larger and smaller than 1.0 (see Fig. 3.12). The galaxies with large variations (Arp 220, IRAS 17208–0014, Mrk 273, IRAS 08572+3915N, Mrk 463E and Arp 229E) correspond to both morphological categories (pre- and post-coalescence) and some of them present

Table 3.4: Variation in magnitudes for the light profiles, and departures from the $r^{1/4}$ law

Galaxy	$\Delta\mu^{(a)}$ (F814W)	$\Delta\mu^{(b)}$ (F814W)	$\Delta\mu(r1)^{(c)}$ (F814W)	$\Delta\mu(r2)^{(d)}$ (F814W)	$\overline{\Delta\mu}^{(e)}$ (F814W)	$\Delta\mu^{(a)}$ (F160W)	$\Delta\mu^{(b)}$ (F160W)	$\Delta\mu(r1)^{(c)}$ (F160W)	$\Delta\mu(r2)^{(d)}$ (F160W)	$\overline{\Delta\mu}^{(e)}$ (F160W)
IRAS 13156+0435N	1.7	3.4	0.005	-0.251	-0.030±0.088	N/A	N/A	N/A	N/A	N/A
IRAS 13156+0435S	1.4	3.2	0.124	0.011	0.003±0.028	N/A	N/A	N/A	N/A	N/A
IRAS 13342+3932E	1.0	1.1	-0.022	-0.115	-0.004±0.051	N/A	N/A	N/A	N/A	N/A
IRAS 13342+3932W	1.6	4.0	-0.014	-0.035	0.003±0.022	N/A	N/A	N/A	N/A	N/A
IRAS 16007+3743E	1.0	1.4	0.044	0.068	0.004±0.050	N/A	N/A	N/A	N/A	N/A
IRAS 16007+3743W	0.8	1.0	0.149	0.138	0.028±0.070	N/A	N/A	N/A	N/A	N/A
IRAS 06268+3509N	0.8	1.4	0.018	-0.004	0.003±0.018	1.7	2.7	0.027	0.354	0.027±0.101
IRAS 06268+3509S	0.4	0.6	-0.037	0.028	0.001±0.021	0.8	0.8	-0.034	-0.015	-0.001±0.017
IRAS 08572+3915N	0.9	1.9	0.023	0.057	0.002±0.047	1.9	1.9	-0.069	0.025	0.002±0.044
IRAS 08572+3915S	...	2.7	1.3	1.6	-0.051	-0.012	0.003±0.027
IRAS 14348-1447N	...	0.7	1.3	2.0	0.021	0.029	0.001±0.029
IRAS 14348-1447S	0.5	1.2	0.004	0.077	0.004±0.021	1.9	2.3	-0.021	-0.035	-0.004±0.030
Arp299/NGC 3690	(*)	(*)	(*)	(*)	(*)	(*)	(*)	(*)	(*)	(*)
Arp299/IC 694	0.5	1.8	-0.058	-0.041	-0.008±0.035	2.6	2.6	-0.139	-0.056	0.005±0.054
IRAS 13469+5833E	0.2	1.2	0.006	-0.007	0.001±0.010	1.5	1.8	-0.032	0.017	0.001±0.017
IRAS 13469+5833W	0.8	1.9	0.034	0.058	0.006±0.032	3.4	1.9	0.041	0.016	0.005±0.030
Mrk 463E	1.1	3.9	-0.016	-0.231	-0.008±0.071	2.2	2.2	0.155	0.150	0.021±0.082
Mrk 463W	1.2	4.2	-0.032	-0.304	-0.010±0.072	1.8	1.8	0.093	0.295	0.038±0.088
IRAS 06487+2208	2.0	2.0	0.026	0.037	0.005±0.038	N/A	N/A	N/A	N/A	N/A
IRAS 11087+5351	1.2	3.6	0.022	-0.014	0.001±0.018	N/A	N/A	N/A	N/A	N/A
Mrk 273	1.6	3.3	-0.009	-0.038	0.003±0.023	2.3	2.7	0.121	-0.046	0.003±0.032
Arp 220	1.4	3.0	-0.067	0.0003	-0.019±0.049	2.5	2.5	-0.053	0.0129	0.004±0.032
IRAS 09427+1929	1.2	2.0	0.007	-0.005	-0.005±0.025	N/A	N/A	N/A	N/A	N/A
IRAS 12490-1009	1.1	2.7	-0.078	-0.009	-0.008±0.031	N/A	N/A	N/A	N/A	N/A
IRAS 14060+2919	1.7	3.6	-0.091	0.057	-0.007±0.071	N/A	N/A	N/A	N/A	N/A
IRAS 15206+3342	2.3	2.7	-0.084	0.207	0.085±0.147	N/A	N/A	N/A	N/A	N/A
IRAS 15250+3609	1.2	3.0	0.002	-0.002	0.001±0.028	3.4	3.4	0.108	-0.115	0.001±0.028
IRAS 17208-0014	1.1	1.8	-0.070	-0.125	0.002±0.071	2.8	2.9	-0.130	-0.023	0.002±0.07
Mrk 231	0.9	4.1	0.077	-0.061	-0.012±0.050	3.4	4.8	0.136	0.214	-0.012±0.050

Note: (a): Range of magnitudes covered by the section defined for the fit. (b): Total range of magnitudes covered by the profile. (c) Variations (i.e. model–measurement) with respect to the de Vaucouleurs law in the inner radius of the fit. (d) Variations (i.e. model–measurement) with respect to the de Vaucouleurs law in the outer radius of the fit. (e) Average variation with respect to the de Vaucouleurs law in the *comparison range*. ... means that the fit does not cover the marked limits. (*) Galaxy not well covered by the chip. Colon indicates large uncertainties due to the small range covered by the fit. Horizontal line separates the pre- and post-coalescence galaxies.

strong nuclear dust features when observed with the F814W filter (see Figs. 2.3 and 2.4, and Table 3.3). Moreover they tend to show large structural differences between the light profiles in both filters, especially in the innermost parts of the galaxies. For the remaining objects the changes through the galaxy are not so strong.

These strong color variations can be produced by two different effects, either internal extinction or change in the intrinsic colors of the stellar populations. The H-band is dominated by old stars, therefore the analysis of an old stellar population will give us an upper limit to the color contribution. This contribution can be estimated using the results of stellar evolutionary models such as Starburst99³ (SB99, Leitherer et al. 1999), and the Bruzual & Charlot models⁴ (Bruzual & Charlot 1993). SB99 predicts an I–H color of about 0.85 using an instantaneous burst of 1 Gyr ; the Bruzual & Charlot models predicts a color of 1.6 produced by an instantaneous burst of 10 Gyr. These results cannot account, in general, for the measured colors (see 3.12 Left), but establish an upper limit to the contribution of the stellar populations. In fact, assuming an average color value of 3 and a theoretical color

³The SB99 results shown include a nebular component, and have been derived for an instantaneous burst with $Z=Z_{\odot}$, Salpeter IMF and total mass of $10^6 M_{\odot}$.

⁴The BC results shown have been derived for an instantaneous burst of star formation with $Z=Z_{\odot}$, Salpeter IMF and total mass of $10^6 M_{\odot}$.

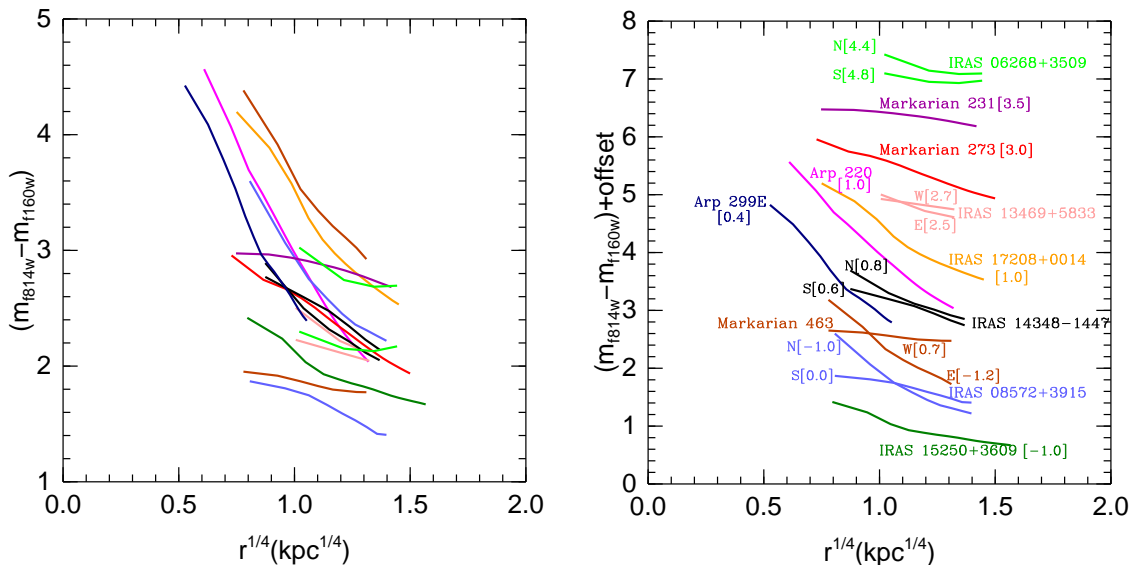


Figure 3.12: **Left:** F814W-F160W color for the galaxy sample plotted vs. the distance to the nucleus. For deriving the colors a new photometry was done, using in both images growing circular apertures of equivalent size (i.e., taking into account the different pixel scale of the WFPC2 and NICMOS cameras). **Right:** Same than left but with several offsets (indicated into brackets) applied for clarity, and the name of the galaxies indicated.

of 1.6, A_V is 4.6 mag, consistent with the average nuclear extinction derived from the Balmer decrement $A_V=3.0\pm 1.8$ mag. Therefore, we confirm that the most likely explanation for the cases with large differences in the color profile (and hence structural variations in the light profile) is that the differences are mostly due to the presence of dust.

3.5.2 Morphological and Dynamical Approach: Comparison with Models

The set of morphological and kinematic parameters derived for the sample of ULIRGs can be compared with the properties of the simulated remnants of mergers of disk galaxies produced by NB03 and Nb06. In order to understand the scope of the model the simulations will be described in what follows.

The disk galaxies simulated in NB03 were constructed in dynamical equilibrium (following Hernquist et al. 1993); each galaxy is formed by an exponential disk, a spherical non-rotating bulge and an halo composed by particles (no gas was added). Four mass relations were selected for modeling the progenitor disk galaxies: 1:1, 2:1, 3:1, and 4:1. In total 112 simulations were done using different orientations. In all cases, and once the merger was complete, the remnants were allowed to evolve and settle in equilibrium approximately 8-10 dynamical times ($\sim 10^8$ years). In that stage the photometric and kinematical properties of the remnants were measured and analyzed. After analyzing the stability of the parameters under study, they were defined in such a way that are characteristics of the remnant:

- The characteristic ellipticity ϵ_{eff} is defined as the isophotal ellipticity at $1.5r_e$, with r_e being the projected spherical half mass radius. In the present work, r_e will be identified with the effective radius R_{eff} . The latter is measured from the ellipse that encloses half

the light in the F814W and F160W bands for all galaxies.

- The coefficient $a_{4\text{eff}}$, is the mean value of a_4 between $0.25r_e$ and $1.0r_e$.
- The isophotal twist, is determined as the relative position angle $\Delta\phi$ between $0.5r_e$ and $1.5r_e$.
- The kinematical parameters used are σ , the central velocity dispersion, and V defined as the maximum velocity. For the present purposes, this velocity is defined as the largest velocity amplitude measured in the two-dimensional velocity field.

The set of simulations of Nb06 include a gaseous component. The full set of 1:1 and 3:1 mergers was simulated again replacing a 10% of the stellar disk by gas. In this case an isothermal equation of state is assumed as an approximation to the interstellar medium in disk galaxies (Naab & Burkert 2001; Barnes 2002; Li et al. 2005). As a consequence additional heat created by shocks, adiabatic compression and feedback processes is radiated away. Besides, the heating prevent the gas from cooling below its effective temperature. No star formation is included in the simulations. To guarantee the stability of the measured properties, the merger remnants were allowed to stabilize into dynamical equilibrium for about 30 dynamical times after the complexation of the merger was finished.

Given that the amount of gas in ULIRGs is about 50% of the total mass, at least in the central regions, the small amount of gas included can be one of the caveats of the simulations. As it has been shown by Barnes & Hernquist (1996), the presence of gas influences the stellar component of the merging galaxies. Therefore the present analysis may be useful for testing the goodness of the models, and determine how the results are affected by the lack of gas.

One parameter needed for the comparison is the effective radius (R_{eff}), calculated here as the radius of the fitted ellipse that encloses half of the flux for all galaxies except IRAS 12112+0305 and IRAS 18580+6257, where growing circular apertures were used. The R_{eff} is a parameter sensitive to the internal extinction of the galaxy. In the case of ULIRGs, the large amounts of dust highly obscure the central regions and therefore may lead to an overestimation of the effective radius when using optical bands. Although the use of near-IR images minimize the effect of the dust, it may be overestimated too if a two-dimensional extinction correction has not been applied over the image. This uncertainties are about 15%, as demonstrated by Monreal-Ibero 2004 with detailed two-dimensional H-band extinction corrections. On the other hand the near-IR continuum light traces not only old stellar populations, but AGN contribution and young stars; in this case the radius could be underestimated due to the unknown amount of AGN and young stars contribution. Given all this, and comparing our measurements with those obtained from different groups (see Table 5.6), the uncertainty of the value of the effective radius can be establish in about 25%.

The empirical kinematic parameters that will be compared with the models, velocity and σ , will be those of the ionized gas ($\text{H}\alpha$ recombination line), as we do not have stellar information at our disposal. The comparison between our measured values of the central σ (that traces the dynamical mass if the system is virialized) with those derived for the stellar component by several investigation groups (see Table 3.6), gives an average uncertainty of about 16%, making us confident in the use of the ionized gas kinematics. The differences between the stellar and warm gas velocities will be addressed later.

Table 3.5: Comparison of R_{eff} values

Galaxy	$R_{\text{eff}}(\text{F814W})$ (kpc)	$R_{\text{eff}}(\text{F160W})$ (kpc)	$R_{\text{eff}}^{(a)}$ (kpc)	$R_{\text{eff}}^{(b)}$ (kpc)	$R_{\text{eff}}^{(c)}$ (kpc)	$R_{\text{eff}}^{(d)}$ (kpc)	$R_{\text{eff}}^{(e)}$ (kpc)	$R_{\text{eff}}^{(f)}$ Dispersion (kpc)
IRAS 13156+0435N	5.9	—	—	—	—	—	—	0.9
IRAS 13156+0435S	4.9	—	—	—	—	—	—	0.7
IRAS 13342+3932E	4.5	—	—	—	—	—	—	0.7
IRAS 13342+3932W	2.5	—	6.67, 5.78	—	—	—	—	2.0
IRAS 18580+6527E(†)	6.5	—	—	—	—	—	—	1.0
IRAS 18580+6527W(†)	4.3	—	—	—	—	—	—	0.6
IRAS 16007+3743E	4.0	—	—	—	—	—	—	0.6
IRAS 16007+3743W	4.2	—	—	—	—	—	—	0.6
IRAS 06268+3509N	2.0	2.1	—	—	—	—	—	0.1
IRAS 06268+3509S	1.5	1.1	—	—	—	—	—	0.3
IRAS 08572+3915N	2.8	0.6	—	—	—	0.15, 0.74	0.91	1.0
IRAS 08572+3915S	1.4	0.6	—	—	—	—	1.00	0.4
IRAS 14348–1447N	1.4	1.5	—	—	3.0	—	1.70	0.2
IRAS 14348–1447S	3.0	1.3	—	—	—	0.72, 1.15	1.30	0.9
Arp 299W (NGC 3690)	1.2	Edge	—	—	—	—	—	0.2
Arp 299E (IC 694)	2.0	0.4	—	—	—	—	—	1.1
IRAS 13469+5833E	1.9	—	—	—	—	—	—	0.3
IRAS 13469+5833W	3.0	—	—	—	—	—	—	0.4
IRAS 12112+0305N(†)	2.0	1.7	—	1.67	—	—	1.89	0.2
IRAS 12112+0305S(†)	1.5	1.1	—	0.81	—	0.48, 0.85	0.75	0.3
Mrk 463E	1.0	0.2	—	—	—	—	—	0.8
Mrk 463W	1.0	1.0	—	—	—	—	—	0.2
IRAS 06487+2208	1.5	—	—	—	—	—	—	0.2
IRAS 11087+5351	8.9	—	—	—	—	—	—	1.3
Mrk 273	4.4	2.0	4.65, ...	—	2.0	0.96, 1.25	1.47	1.5
Arp 220	4.3	1.2	5.27, 2.26	—	0.55	0.62, 1.17	0.79	1.8
IRAS 14060+2919	4.8	—	6.27, ...	—	—	—	—	1.1
IRAS 15206+3342	2.9	—	3.19, ...	—	—	—	2.47	0.4
IRAS 12490–1009	7.6	—	—	—	—	—	—	1.1
IRAS 17208–0014	3.2	1.5	—	—	1.4	0.94, 1.18	1.40	0.8
IRAS 15250+3609	1.9	1.4	—	—	1.2	0.70, 1.08	1.10	0.4
Mrk 231	0.3	0.2	3.57, ...	—	0.3	—	0.20	1.5
IRAS 09427+1929	2.75	—	—	—	—	—	—	0.4

Note: (a) Veilleux, Kim & Sanders 2002. R- and K'- band ground-based seeing-deconvolve images. (b) Dasyra et al. 2006. Ellipse fitting in ground-based H-band acquisition images; (c) Tacconi et al. 2002. Derived from fit to de Vaucouleurs ($r^{1/4}$) law to K-band ground-based images. Value for IRAS 14348–1447 represents the effective radius of the entire double-nucleus system. (d) Scoville et al. 2000 K and H-band half light radii within 3 kpc diameter aperture; (e) Colina et al. 2005, space-based H-band effective radius measured from the F160W NICMOS archival images, except for IRAS 15206+3342, for which no near-IR images was available and F814W WFPC2 image was used instead. (f) Standard deviation obtained using the different R_{eff} measurements. For galaxies with only one R_{eff} (based on F814W) value a 15% of error has been assigned. (†) Galaxies not included in the comparison with models because of their morphology, that does not allow us to fit ellipses. In this case we have calculated the effective radius using growing circular apertures.

Table 3.6: Comparison of velocity dispersion values

Galaxy	$\sigma^{(a)}$ _{warm gas} (km s ⁻¹)	$\sigma^{(b)}$ _{stars} (km s ⁻¹)	$\sigma^{(c)}$ _{stars} (km s ⁻¹)	$\sigma^{(d)}$ _{stars} (km s ⁻¹)	$\sigma^{(e)}$ _{cold gas} (km s ⁻¹)	$\sigma^{(f)}$ _{stars} (km s ⁻¹)	$\sigma^{(g)}$ _{cold gas} (km s ⁻¹)
IRAS 13156+0435N	152	—	—	—	—	—	—
IRAS 13156+0435S	138	—	—	—	—	—	—
IRAS 16007+3743E	110	—	—	—	—	—	—
IRAS 16007+3743W	151	—	—	—	—	—	—
IRAS 14348–1447N	147	150	—	—	—	—	149
IRAS 14348–1447S	196	170	—	—	—	—	127
Arp 299 (NGC 3690)	172	—	—	—	—	—	—
Arp 299 (IC 694)	108	—	—	—	—	135	—
IRAS 08572+3915N	113	—	—	—	—	—	106
IRAS 08572+3915S	47	—	—	—	—	—	—
IRAS 06268+3509N	128	—	—	—	—	—	—
IRAS 06268+3509S	77	—	—	—	—	—	—
IRAS 18580+6527E	155	—	—	—	—	—	—
IRAS 18580+6527W	119	—	—	—	—	—	—
IRAS 12112+0305N	123	124	—	—	—	—	170
IRAS 12112+0305S	174	133	—	—	—	—	127
Mrk 463E	367	—	—	—	—	—	85
Mrk 463W	132	—	—	—	—	—	—
IRAS 06487+2208	163	—	—	—	—	—	—
IRAS 11087+5351	239	—	—	—	—	—	—
Mrk 273	182	—	285.0	160	200	—	—
Arp 220	185	164	166	—	212	—	—
IRAS 14060+2919	130	—	—	—	—	—	—
IRAS 15206+3342	90	—	—	—	—	—	—
IRAS 12490–1009	207	—	—	—	—	—	—
IRAS 17208–0014	191	229	229	—	130	—	—
IRAS 15250+3609	168	—	150	—	—	—	—

Note: (a) First column: warm ionized gas measurements taken from IFS data using measurements of the H α emission line (present work). σ uncertainty is about 15%. (b) Dasyra et al. 2006, measurements done using near-IR stellar CO bands; (c) Tacconi et al. 2002, near-IR emission lines measurements; (d) James et al. 1999, measurements done using the CO(2,0) near-infrared band at 2.3 μ m; (e) Downes & Solomon 1998, derived using CO interferometer data ; (f) Shier & Fischer 1998, measurements done using the CO(2,0) near-infrared band at 2.3 μ m; (g) Evans 2002, measurements from high-resolution CO(1 \rightarrow 0).

Until now, similar analysis and comparisons with models have been focused on merger remnants, i.e., ULIRGs in the so-called post-coalescence phase. Here the study will be done for the early and late phases of the merger, with the immediate aims of evaluate the differences among both morphological types. The comparison with the models will be done only in the post-coalescence galaxies, as the simulations predict results for merger remnants. The pre-coalescence systems will be treated as two individual galaxies.

3.5.2.1. Isophote Shapes

Although the boxy-disky classification is defined for elliptical galaxies, in this section the values obtained for the a4 parameter⁵, along with the ellipticity parameter ϵ_{eff} for all galaxies of the sample, will be analyzed. The motivation for doing this in the pre-coalescence ULIRGs (which are indeed believed to be disk galaxies undergoing fusion) is to test how

⁵The reader is referred to Chapter 2 for details about the derivation of the isophotal parameters.

the merger affects their morphology, and to compare with the post-coalescence ULIRGs. Furthermore, the results for the most evolved mergers will be compared with the NB03 and Nb06 sets of simulations.

IRAS 13156+0435	●	Arp 299	⊛	IRAS 06487+2208	▼	IRAS 14060+2919	△
IRAS 06268+3509	+	IRAS 13342+3932	⊛	IRAS 11087+5351	◊	IRAS 15250+3609	⊞
IRAS 08572+3915	★	Markarian 463	⊛	Arp 220	⊞	IRAS 15206+3342	⊞
IRAS 14348-1447	□	IRAS 13469+5833	⊞	IRAS 12490-1009	☾	IRAS 09427+1929	⊞
IRAS 16007+3743	◇	Markarian 273	◊	IRAS 17208-0014	♥	Markarian 231	⊛

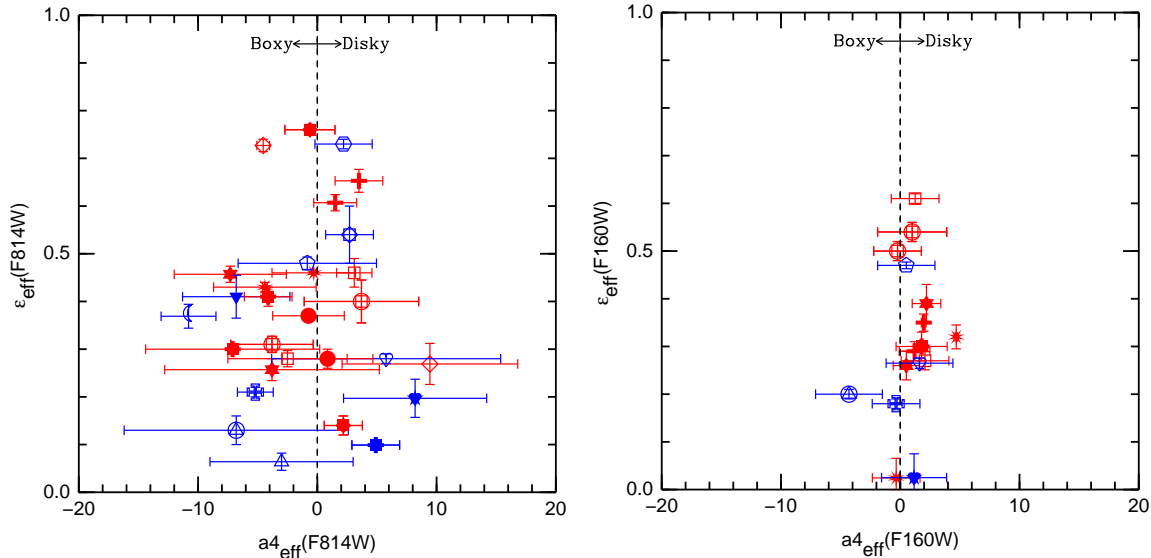


Figure 3.13: Parameter a_4 vs. ellipticity for the galaxies of the sample. In the upper panel the symbol associated to each individual galaxy is shown. Red color marks pre-coalescence objects, whereas the blue color is for the post-coalescence ones. The vertical dashed lines delineates the frontier between boxy and diskly. Error bars shown are those derived from the ellipse fitting. **Left:** Results for the F814W filter. **Right:** Results for the F160W filter.

The distribution of the objects over the $a_{4\text{eff}}-\epsilon_{\text{eff}}$ plane is shown in Fig. 3.13. From the 29 galaxies analyzed in the F814W filter, 41% fall in the diskly domain, with no clear preference for any morphological type. Nonetheless, 75% of the 16 galaxies observed in the F160W filter are classified as diskly, although as can be seen in Fig. 3.13, in several cases the uncertainties associated to the a_4 parameter makes the classification unclear. It is interesting to note that all galaxies whose classification varies from boxy (in the optical) to diskly (in the infrared), are pre-coalescence systems. This fact, along with the lower dispersion of the a_4 parameter as measured in the F160W filter, may be a consequence of the previously discussed color effect produced by the presence of dust.

In both filters we measure an effective ellipticity ≤ 0.5 , with no clear preference for any morphological phase in their distribution. In any case, there are variations (of up to 0.4) in the ellipticity of the individual galaxies as measured in the optical and near-IR. This is again a color effect produced by the presence of dust, that reinforces the idea of IR images as a major tool for unveil the true morphology of the galaxy.

The NB03 and Nb06 simulations model the behavior of the merger remnants in this plane. The models without gas predicts a clear trend in the unequal mass mergers (2:1, 3:1, 4:1) to produce diskier remnants, tendency that is enhanced as the difference in

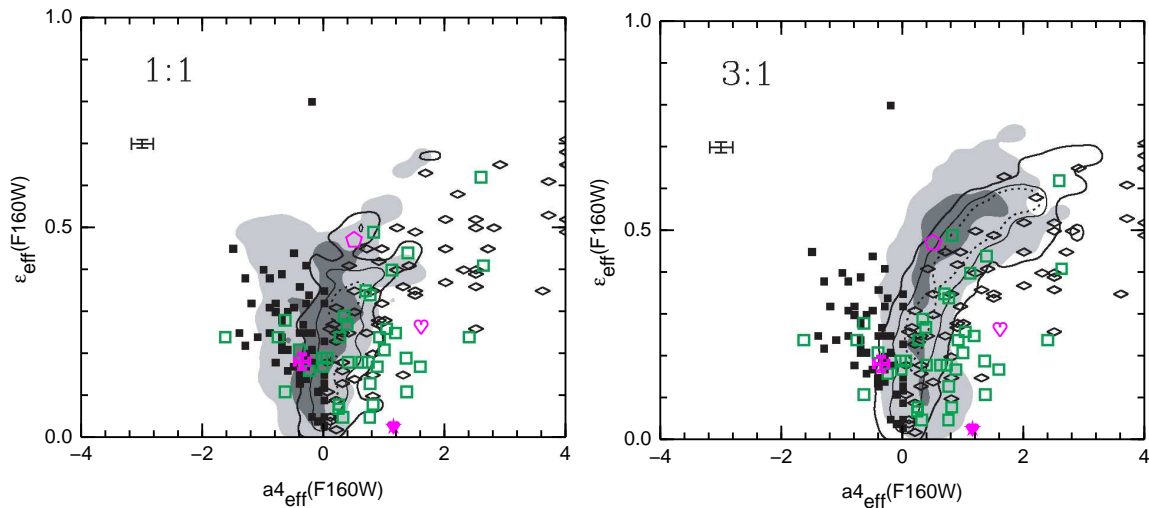


Figure 3.14: Comparison of the F160W results (points in magenta) for the post-coalescence galaxies of the sample with the NB03, Nb06 models. Ellipticity ϵ_{eff} vs. characteristic shape parameter $a4_{\text{eff}}$ for mergers with and without gas of disk galaxies with progenitor mass relations 1:1 and 3:1. The contours indicate areas of 50% (dotted line), 70% (thin line) and 90% (thick line) probability for finding a merger remnant with gas (10% gas in the parent galaxies). For comparison the shaded areas show 50% (dark grey) and 90% (light grey) probability of finding a collisionless merger remnants. Data for observed boxy (filled squares) and disky (open diamonds) ellipticals were provided by Ralph Bender to Naab et al. Data for local merger remnants (open green squares) are from Rothberg & Joseph (2006) (near-IR K-band). The background graphic has been taken from Nb06. (Symbol code for the sample of ULIRGs as in Fig. 3.13; the color code has been changed for clarity.)

mass increases. On the contrary, the major mergers (1:1) tend to form either disky or boxy ellipticals. The addition of 10% of gas in the parent galaxies makes significant variations in the results for 1:1 mergers: the stellar components do not appear boxy any more (as it was demonstrated by Bekki & Shioya 1997). As for the 3:1 mergers, the addition of the gas does not lead to such dramatic variations, but the tendency for forming disky galaxies is stronger.

Fig 3.14 shows the comparison between our post-coalescence ULIRGs (as observed in the near-IR) and the models, along with results for other galaxies obtained from the literature. From the five post-coalescence ULIRGs Arp 220 is not considered in the comparison, as its $a4_{\text{eff}}$ falls out of the models boundaries (see Fig. 3.13). For the remaining four galaxies, two of them (IRAS 15250+3609 which is boxy, and Mrk 273 which is disky) are consistent with being remnants of 1:1 or 3:1 mergers with gas. The other two (IRAS 17208–0014 and Mrk 231, both disky) show morphological characteristics not consistent with the models. In fact the location of ULIRGs in this plane is consistent with the one other galaxies (boxy and disky ellipticals, and merger remnants), demonstrating that the capability of the models to reproduce all the observations is restricted.

In conclusion, the most-reliable near-IR analysis of the isophote shapes in ULIRGs shows little variation with the merger: about 80% of the pre- and 60% of the post-coalescence ULIRGs show disky (or boxy-disky frontier) isophotes. The comparison between the F814W and F160W bands states the relevance of the color effect produced by the dust, that virtually modifies the classification from boxy (in the optical) to disky (in the near-IR) in most pre-coalescence systems. Finally, although the models of merger remnants with gas are consistent

with some post-coalescence ULIRGs, they are not able to reproduce all disk galaxies.

3.5.2.2. Isophote Twists

Another morphological characteristic that can be obtained from the isophotal analysis of the galaxies is the radial change in the relative orientation of the major axis: the isophotal twist ($\Delta\phi$)⁶. The ULIRGs of the sample show large values (of up to 150°) of the isophotal twist in both optical and near-IR filters. However, it appears to be a trend in galaxies with small ellipticities, especially in the post-coalescence ones, for showing large values of the isophotal twist. This general consensus between both filters is not extrapolable to the results on the individual galaxies: we measure large variations among the twist in both filters (e.g. up to 100° in the case of Arp 220), that are due to the wavelength-dependent morphological variations.

IRAS 13156+0435	●	Arp 299	⊠	IRAS 06487+2208	▼	IRAS 14060+2919	△
IRAS 06268+3509	+	IRAS 13342+3932	⊠	IRAS 11087+5351	◊	IRAS 15250+3609	⊠
IRAS 08572+3915	★	Markarian 463	★	Arp 220	⊠	IRAS 15206+3342	⊠
IRAS 14348-1447	□	IRAS 13469+5833	◊	IRAS 12490-1009	◊	IRAS 09427+1929	⊠
IRAS 16007+3743	◇	Markarian 273	◊	IRAS 17208-0014	♥	Markarian 231	★

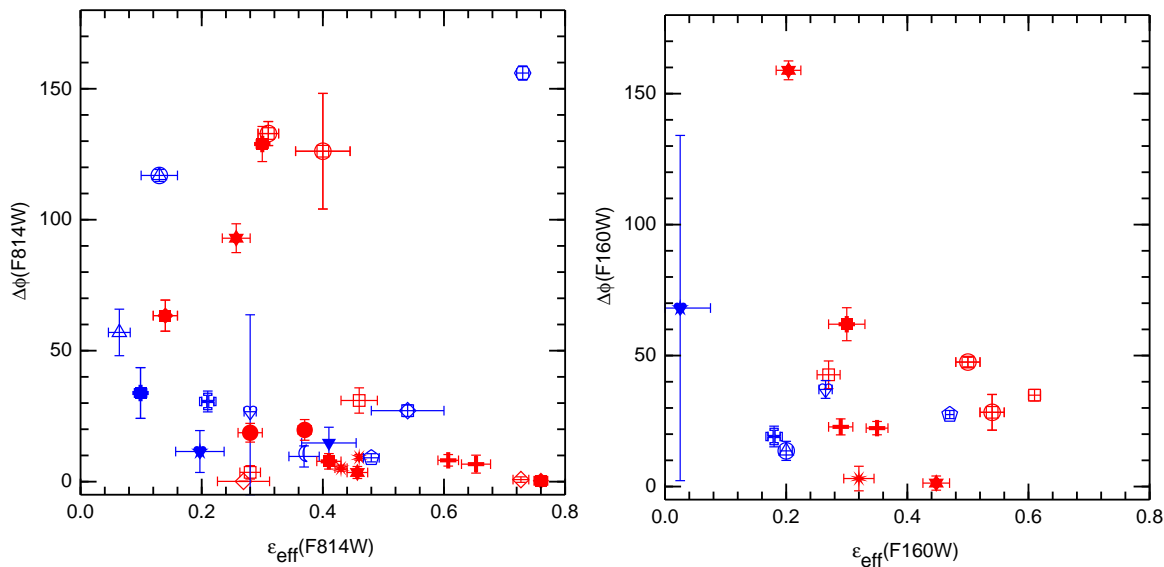


Figure 3.15: Isophotal twist $\Delta\phi$ vs. ellipticity for the studied galaxies. In the upper panel the symbol associated to each individual galaxy is shown. Red color marks pre-coalescence objects, whereas the blue color is for the post-coalescence ones. The twist units are degrees. **Left:** F814W filter. **Right:** F160W filter.

The NB03 set of simulations predict large values of $\Delta\phi$ for projections that appear nearly round (as observed in our data), and values of $\Delta\phi \leq 20^\circ$ for ellipticities $\gtrsim 0.4$. The amount of twisting in the simulations is weakly dependent of the mass ratio of the progenitor galaxies, whereas the ellipticity appears to have larger values in the unequal mass mergers. In 60% of cases observations of post-coalescence ULIRGs are well explained by the models (Fig. 3.16), although as predicted by the simulations, no conclusion about the mass of the progenitor galaxies can be obtained. The growing of $\Delta\phi$ at lower ellipticities may be

⁶As it has been explained, it is determined as the relative position angle $\Delta\phi$ between $0.5r_e$ and $1.5r_e$.

associated to the difficulty for assigning the axis in nearly round objects, fact that may lead to large variations of the position angle at different radius. The galaxies not consistent with the models, presents an excess of about 15° , this may be indicating that their dynamical stage it is not so evolved as in the other galaxies.

3.5.2.3. V/σ Parameter

In the paradigm of dynamical evolution in ULIRGs, it is important to know whether these galaxies are anisotropic or rotationally supported. In this context, the parameter V/σ (Binney 1978) measures the ratio between the maximum rotational velocity V (measured as half the observed peak-to-peak velocity) vs. the nuclear velocity dispersion σ . If σ is larger than the velocity, it means that the galaxy is sustained against gravitational collapse by the pressure originated by random movements of the stars. On the other hand, if the velocity dominates, the galaxy is sustained by rotation. In elliptical galaxies V/σ ranges between 0.1-1.5, depending on the boxy/diskyness. In spiral galaxies (which are dominated by rotation) the values are typically larger, about 3-4.

The location of the ULIRGs of the sample in the $V/\sigma-\epsilon_{\text{eff}}$ (as measured by the warm ionized gas and the F814W filter) is shown in Fig. 3.17 (Left). The dashed line in the graphic is a model for an isotropically rotating oblate spheroid (Binney 1978), and represents objects flattened by rotation. The equation that describes the line is (Kormendy et al. 1982):

$$V/\sigma \simeq \sqrt{\frac{\epsilon}{1-\epsilon}}, \quad (3.1)$$

and is considered a good approximation for ellipticities among 0 and 0.95. ULIRGs are distributed between $V/\sigma \simeq 0.4-2.5$, values that may be associated with galaxies where the warm gas is dominated by anisotropy and with some level of rotation. It is important to highlight here two aspects: (1) that the velocity amplitude of the warm ionized gas ($\text{H}\alpha$) does not trace, in general, rotation (as obtained in Colina et al. 2001). (2) That there are large differences between the velocity amplitudes of the stellar and gas components (e.g., the extreme case of Mrk 463 with 110 and $\sim 400 \text{ km s}^{-1}$, respectively). Therefore, the largest V/σ values (see Fig. 3.17) may be due to the presence of flows, superwinds or other merger-induced processes. The average values are 1.0 ± 0.6 and 1.0 ± 0.3 for the pre- and post-coalescence galaxies, meaning that the ionized gas in ULIRGs is distributed over the frontier between being dominated by velocity dispersion or velocity amplitude. No signs of relation between the ellipticity and the V/σ parameter are detected. In general, the V/σ parameter is calculated for the stars rather than the gas. The differences among both measurements can be estimated by comparison with the results from Dasyra et al. 2006 for five galaxies of our sample (see Fig. 3.17 Right). In all cases, the values for the ionized gas present an excess (from 1.2 to 2.8 times, 1.8 on average) with respect of the stellar ones, differences that are due to the intrinsic variations between the kinematics of both the stars and gas. In ULIRGs the warm gas is very sensitive to the violent merging processes at work; high velocity gradients, outflows and super-winds are not rare, and may lead to a decoupling between the gas and star phases. This point clearly needs further investigation, but at the moment is out of the scope of this work; we will only take it into account in order to perform the following comparison with the models.

The NB03 simulations (i.e., only with the stellar component in the parent galaxies),

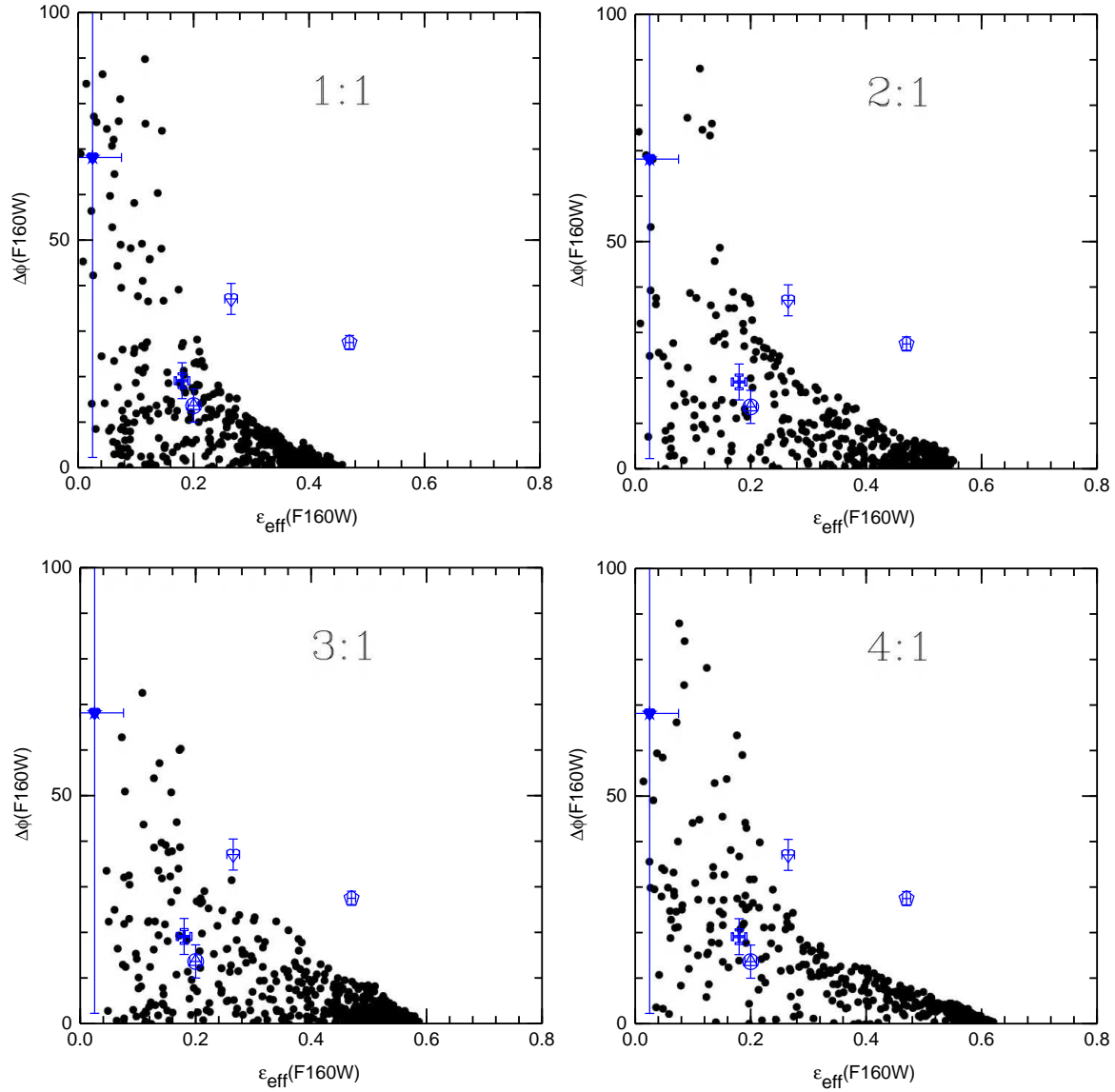


Figure 3.16: Isophotal twist $\Delta\phi$ vs. ellipticity for characteristic 1:1 and 4:1 merger remnants (NB03) compared with the post-coalescence ULIRGs observed with the F160W filter. Symbols as in Fig. 3.15.

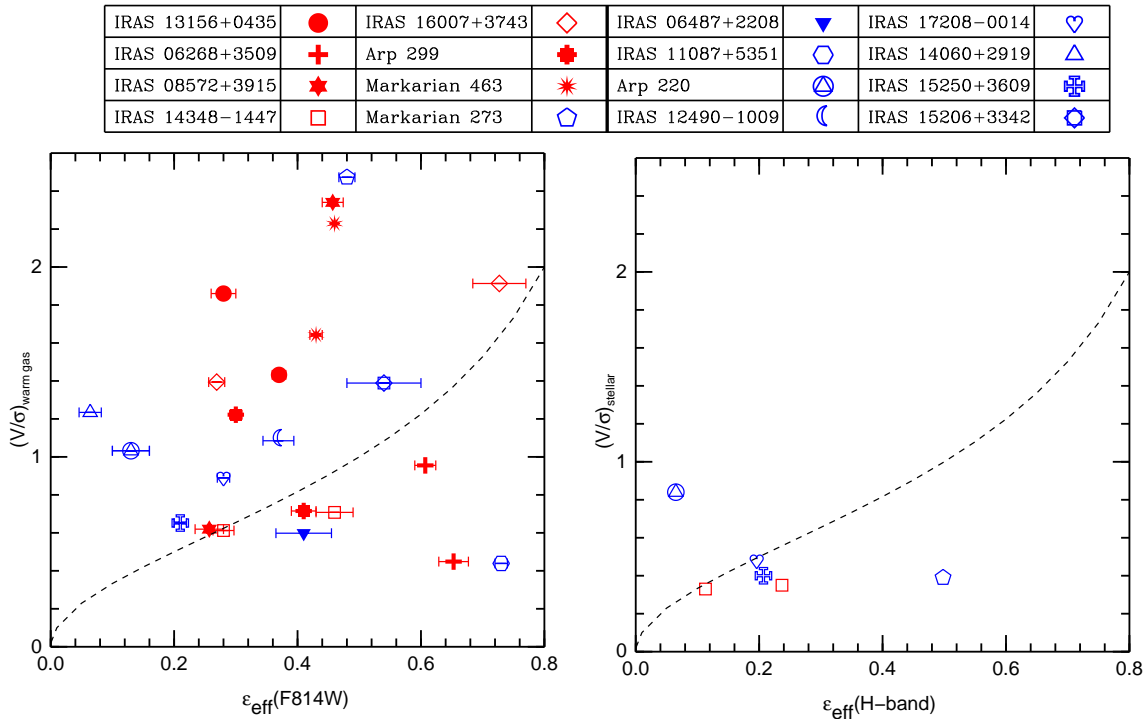


Figure 3.17: Ratio of the observed velocity and velocity dispersion vs. ellipticity. Red color marks pre-coalescence objects, whereas the blue color is for the post-coalescence ones. **Left:** Warm ionized gas values. The velocity correspond to half velocity of the differences found in the two-dimensional velocity field. **Right:** Stellar values taken from Dasyra et al. 2006.

conclude that slowly rotating boxy ellipticals are consistent with 1:1 mergers, whereas the 2:1 mergers have rotational properties that correspond to more rapidly rotating boxy and slowly rotating disk ellipticals. With respect to the 3:1 and 4:1 remnants, they can be associated to rapidly rotating disk ellipticals. The inclusion of a gas component in N06 simulations doesn't add significant variations to the analysis (see models and comparison with observed elliptical galaxies in Fig. 3.18).

The comparison between the observed post-coalescence ULIRGs and the models for 1:1 and 3:1 mergers is shown in Fig. 3.18. In general their distribution is consistent with that of disk elliptical galaxies and merger remnants (diamonds and green squares respectively in Fig. 3.18), being the ellipticity range covered almost the same. Taking into account the observed V/σ , 7 out of 9 galaxies lie above the isotropic rotating oblate spheroid, and only few appear to be consistent with the 3:1 merger remnant. Although almost all objects are located in regions populated by disk ellipticals and merger remnants (except Mrk 273 where the V/σ parameter is about 2.5). However, we are comparing ionized gas and stellar kinematics values. Therefore, the question that arises here is how the use of ionized gas is conditioning the results for our sample of ULIRGs. To evaluate this, the shifts corresponding to the stellar kinematics (from Nb06) have been plotted as blue arrows in Fig. 3.18. When these offsets are taken into consideration, at least 4 out of 9 galaxies falls above the oblate isotropic rotator line and the agreement with the models improves: three galaxies are consistent with the 1:1 merger remnants. Furthermore, some objects are in agreement with both mass ratios. The

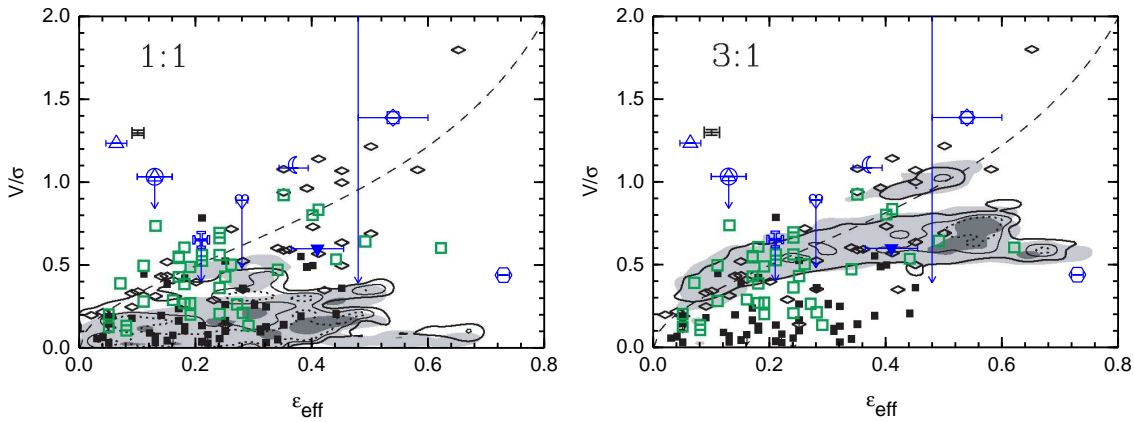


Figure 3.18: Ratio of the observed velocity and velocity dispersion of the post-coalescence galaxies vs. ellipticity compared with NB03, Nb06) models for mergers with and without gas of disk galaxies with progenitor mass relations 1:1 and 3:1. Blue arrows indicate the position for the stellar V/σ as given by Dasyra et al. 2006. The contours indicate areas of 50% (dotted line), 70% (thin line) and 90% (thick line) probability for finding a merger remnant with gas (10% gas in the parent galaxies). For comparison the shaded areas show 50% (dark grey) and 90% (light grey) probability of finding a collisionless merger remnants. Data for observed boxy (filled squares) and disk (open diamonds) ellipticals were provided by Ralph Bender to Naab et al. Data for local merger remnants (open green squares) are from Rothberg & Joseph (2006) (near-IR K-band). The background graphic has been taken from Nb06. The dashed line shows the theoretical values for an oblate isotropic rotator; the line represent objects flattened by rotation. Symbols as in Fig. 3.17

galaxies IRAS 12490–1009, IRAS 15206+3342 and IRAS 06487+2208 do not have available stellar kinematic values, but even a small shift would make them consistent with 1:1 or 1:3 merger remnants. From the galaxies not covered by the models, those more striking are Arp 220 and IRAS 14060+2919, that with another merger remnants lie in a region of nearly round galaxies, either boxy or disk, with significant rotation that are not explained by the models.

3.6 Summary and Conclusions

In this Chapter a comprehensive analysis of the stellar and ionized gas structure of the sample of ULIRGs has been presented. The main objectives of the study can be summarized in two points: (1) To fully characterize the morphology in ULIRGs attending to their merger phase. This can be done studying the stellar (morphology and light profiles), ionized gas components and dust distribution. (2) To use isophotal parameters, along with kinematic information derived from IFS, to test the proposed scenarios of elliptical-through-merger that ULIRGs appear to undergo. The main conclusions are:

- The analysis of the F814W light profiles show that they are highly affected by dust, especially in the innermost regions. This is why only the near-IR results are presented here. In that band all galaxies are well fitted by a $r^{1/4}$ law up to distances of 5 kpc. It is remarkable the fact that even in the pre-coalescence galaxies, when the outer regions are not taken into account to avoid contamination from the companion galaxy, ULIRGs show elliptical-like profiles. This result agrees with the idea of ULIRGs as transition

objects between disk and elliptical galaxies, and point towards little evolution on the light profiles once the merger starts.

- The morphology of the warm ionized gas can be significantly decoupled with respect to that of the stellar continuum (peak separated by up to 10 kpc). This observational evidence, more common in the pre-coalescence phase, is due to the combination of the different excitation mechanisms and the presence of dust.

Our results are consistent with the scenario where two interacting disk galaxies start the ULIRG phase due to the interaction process itself. The data show extra-nuclear star formation when the nuclei of the pre-coalescence systems are separated by $\lesssim 15$ kpc (as shown by the differences between the stellar continuum and $H\alpha$). The detection of decoupled $[O\text{I}]\lambda 6300$ is an indication of merger-induced shocks, whereas the ionization cones of the AGN hosted by one galaxy may be detected with the structure of the $[O\text{III}]\lambda 5007$. In the more evolved post-coalescence ULIRGs the starbursts are concentrated towards the nuclear region, where the simulations predict that the material is falling in. The shocks and AGNs can be detected, the latter either directly or via their ionization cones.

- The pure morphological parameters derived from the isophotal analysis show little or no variation with the merger phase. When observed with the F814W filter, about 40% of the pre- and 45% of the post-coalescence ULIRGs are disky (although the uncertainties tend to be large). In contrast, the analysis of the more reliable F160W band suggest that ULIRGs, with independence of the merger phase, tend to be disky or to lie in the boxy-disky frontier. The galaxies with the smallest ellipticities have the large isophotal twist values (up to 150°).
- The V/σ parameter, as traced by the $H\alpha$ emission line in all galaxies of the sample, ranges from 0.4 to 2.5. The lowest values indicate galaxies supported by velocity dispersion; the largest point towards an increasing importance of the velocity amplitude. Nonetheless it is important to bear in mind that in ULIRGs the velocity amplitude does not necessarily indicates rotation; in fact we may be tracing more tidally-induced process.
- The warm gas dynamical parameters (V/σ) and the ellipticity of post-coalescence ULIRGs are in general non consistent with the results of the merger models defined for the stellar component (NB03, Nb06). This is because the velocity amplitude of the gas tend to be larger than that of the stars. Therefore, we applied stellar values from the literature, and derive a better agreement. In particular the studied post-coalescence ULIRGs are consistent with slowly rotating disky remnants of equal (1:1) or unequal (3:1) mass merger remnants, and with the location of observed disky ellipticals and merger remnants. In spite of this, one third of the analyzed galaxies fall in regions not covered by the models (although close to the 3:1 remnants). This not only happens with the galaxies of our sample, but there are other ellipticals and merger remnants that are neither explained. At first sight this may appear to be a direct consequence of the lack of gas in the simulations, and most likely to the fact that the simulations are not allowed to form stars. In any case this is a question that is out of the scope of the present work.

To sum up, our results supports previous ideas of ULIRGs as transition objects undergoing violent fusion processes that strongly drive their morphology, gas distribution and evolution. The results obtained from the surface brightness profiles, the isophotal analysis, the dynamical indicators, and the comparison with the models, support the hypothesis that the final stage of ULIRGs may be disky elliptical galaxies, partly supported by rotation.

Chapter 4

2D-Ionization Structure and Excitation Mechanisms

In this Chapter, the internal structure of the ionization conditions of a sample of ULIRGs has been investigated. About 20% of the studied nuclei show evidences for an AGN, whereas the HII- and LINER-like activities are almost equally distributed. In addition, the two-dimensional study of the ionization sources reveals that the classification of the different regions is consistent with the nuclear ones. Variations in the value of the radially averaged excitation conditions of ULIRGs have been detected. In fact, the shock tracer $[O\text{I}]/H\alpha$ presents a systematic enhancement in the excitation towards the most external regions of post-coalescence ULIRGs (up to 0.6 dex). This highlights the importance of shocks in the low-density outer regions. Comparatively, the line ratios $[S\text{II}]/H\alpha$ and $[N\text{II}]/H\alpha$, which are more sensitive to star formation, present different behaviors (increasing and variable, respectively). The LINER-like activity appears to be primarily produced by shocks whose velocity range changes with the distance to the nucleus. They vary from 150-200 km s⁻¹ in the nuclei to 150-500 km s⁻¹ in the most external low surface brightness regions. Photo-ionization by a young (4-6 Myr) stellar population may be a secondary mechanism responsible for the LINER-like activity. The excitation conditions of the integrated emission in ULIRGs do not follow the same distribution than that found for the majority of local emission line galaxies; they populate regions of high excitation and extreme starbursts. Finally, there are differences measured between the nuclear and the integrated excitation states. This suggests that the activity classification based on the integrated emission of high-z ULIRGs might vary with respect to the local nuclear ones due to aperture effects. In particular, when the $[O\text{I}]/H\alpha$ ratio is used, we find a systematic shift from HII- to LINER-like activity when comparing nuclear vs. integrated values, respectively. This is probably due to the presence of large-scale merger-induced shocks.

4.1 Introduction

Until now the main efforts for discriminating the excitation mechanisms giving rise to the excitation in local ULIRGs have been dedicated to study their nuclear regions (e.g., Kim et al. 1998; Veilleux et al. 1999; Genzel et al. 1998). Nonetheless, several works have made use of optical-IFS for characterizing the ionization of individual regions in selected (U)LIRGs (e.g., Colina & Arribas 1999; García-Marín et al. 2006 and references therein).

In spite of this, there appears to be a lack of a systematic analysis of the two-dimensional variation in the ionization condition across the galaxies.

This Chapter presents the first systematic two-dimensional study of the ionization conditions in a sample of ULIRGs (18 systems, 27 galaxies) at different merger phases and ionization levels. Specifically, the Chapter is organized as follows. §4.2 is dedicated to the description of the data and diagnostic tools. In §4.3 the two dimensional distribution and variations of the ionization state in ULIRGs will be presented, whereas §4.4 discusses the origin of the LINER-like ionization. §4.5 compares the integrated classification of ULIRGs with that of SDSS galaxies with emission lines. Besides, it analyzes the nuclear vs. integrated classification of ULIRGs, and the implications for high- z observations of this galaxy class. Finally §4.6 gives a brief summary of the most relevant findings and conclusions.

4.2 Data and Diagnostic Tools

The ionization conditions have been studied in 9 pre- and 8 post-coalescence galaxies (see Table 4.1), the majority of which have been observed with the standard INTEGRAL SB2 configuration. Some galaxies of the sample are not present in the analysis for a variety of reasons, such as the lack of $H\beta$ detection (Arp 220), low S/N which precludes the detection of emission lines (IRAS 13469+5833), limited spatial resolution to clearly separate the ionization state in different regions (IRAS 13342+3932 and IRAS 09427+1929) and severe AGN contamination that makes it impossible to distinguish the ionized gas component (Mrk 231). The reader is referred to Chapter 2 for further details in the observations and data reduction.

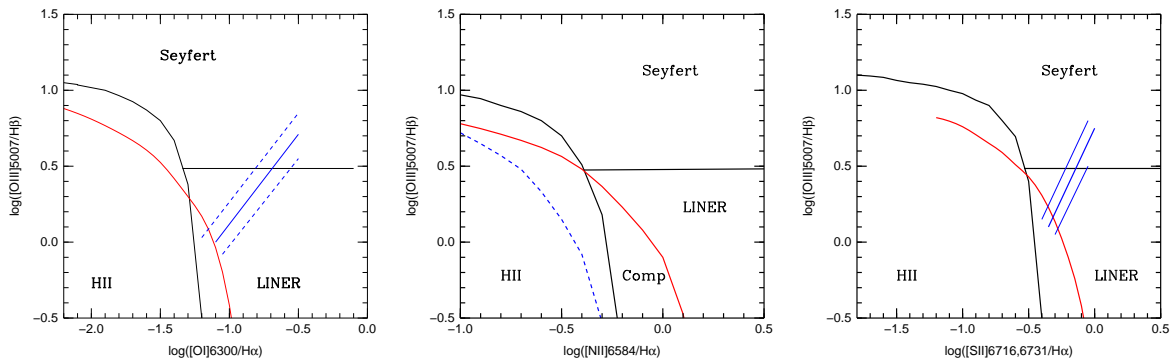


Figure 4.1: The BPT optical emission lines diagnostic diagrams, where the different empirical frontiers for classifying galaxies are shown. The Veilleux & Osterbrock (1987) classification scheme (black solid lines), the Kewley et al. (2001a) extreme starburst line (red solid), the Kauffmann et al. (2003) pure star formation line (blue dashed) and the Kewley et al. (2006) Seyfert-LINER line (solid blue) are shown.

The ionization level in all the regions¹ has been derived using the standard optical emission lines diagrams (BPT diagrams, Baldwin, Philips & Terlevich 1981), which allow us to differentiate between H II-like (i.e. star formation), Seyfert-like (i.e. presence of an AGN),

¹Throughout this Chapter the term region indicates area covered by an INTEGRAL fiber: SB1 bundle \odot $0''.45$; SB2 bundle \odot $0''.9$; SB3 bundle \odot $2''.7$.

and LINER-like ionization (see Fig. 4.1). Occasionally, and depending on the diagram used, some regions show changes in their classification; these variations have been interpreted as a consequence of changes in the dominant ionizing mechanism from photo-ionization to shocks (e.g., Monreal-Ibero et al. 2006 and references therein). In particular, the $[\text{O III}]\lambda 5007/\text{H}\beta$ - $[\text{O I}]\lambda 6300/\text{H}\alpha$ diagram is more sensitive, and therefore a more reliable tracer, to changes in the ionization conditions due to fast shocks than any of the other optical emission line ratios (Dopita & Sutherland 1995). Furthermore, different works have proposed empirical and semi-empirical frontiers to separate the three types of activities (Fig. 4.1) that show differences in the classifications, especially in the transition regions. Throughout this Chapter, the classical frontiers of Veilleux & Osterbrock (1987, black lines in Fig. 4.1) will be used (see Appendix D for a discussion about the reliability of the different frontiers for classifying ULIRGs).

One of the main goals of this work is the study of the two-dimensional variation of the ionization source in ULIRGs depending on the merger phase, rather than to concentrate on the individual details of each single galaxy. Furthermore, as ULIRGs present a complex internal distribution of the ionization state (e.g., Colina et al. 1999; Monreal-Ibero et al. 2006). Here we are particularly interested in tracing the possible variations in the excitation state of the low-surface brightness regions located in the outer parts of the galaxies. Therefore, to spatially separate and trace the mechanisms at work, it is convenient to define three different areas in the galaxies under study (see Fig. 4.2):

- **The nuclear regions:** represented by the fiber or fibers centered on the nucleus of the galaxy; typically the inner 1-2 kpc.
- **The circumnuclear regions:** given by the fibers located up to about about 2.5 to 3.0 kpc in radius from the nucleus (center-to-center fiber distance).
- **The external regions:** comprised by the fibers located at a radial distances larger than 2.5 to 3.0 kpc from the nucleus.

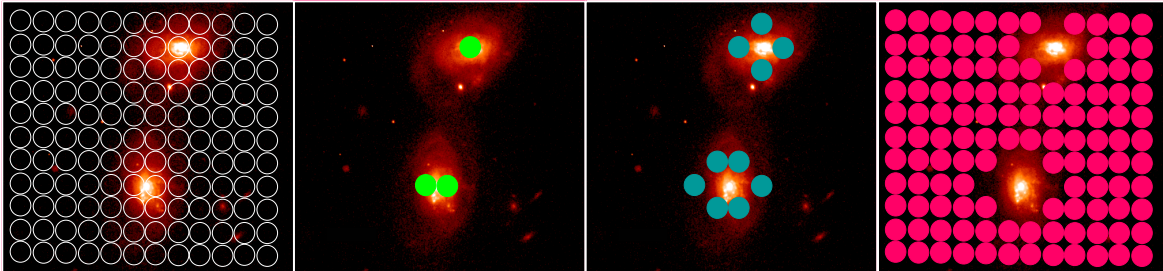


Figure 4.2: Sketch illustrating the definition of the regions under study; the fiber sizes and distribution are not realistic. **From left to right:** (1) Array of INTEGRAL fibers simulated over the galaxy IRAS 13156+0435. (2) Nuclear fibers. (3) Circumnuclear fibers, whose centers are located about 2.5-3 kpc apart from the center of the nuclear fibers. (4) External fibers, located at distances larger than 2.5-3 kpc (center-to-center) from the nucleus.

In addition to this *distance to the nucleus* criteria, two more characteristics of the galaxies have been taken into account: (i) the morphological type defined as pre- (9 systems) and post-coalescence (8 galaxies), and (ii) the *warm* (6 objects) and *cold* (12 objects) classification based on the IR colors. As indicated on every graphic below, and to make easy the

identification over the diagrams, each galaxy has its own symbol assigned. It is worth mentioning the fact that the values are not corrected for extinction. Due to the proximity of the emission lines the correction for extinction is minor for the $[\text{O I}]\lambda 6300/\text{H}\alpha$, $[\text{N II}]\lambda 6584/\text{H}\alpha$ and $[\text{S II}]\lambda 6731/\text{H}\alpha$ line ratios. For the not so close $[\text{O III}]\lambda 5007/\text{H}\beta$ the variations are less than the uncertainties. Only in the case of the galaxy Arp 299 we used extinction corrected values, for consistence with the published results (García-Marín et al. 2006). In any case this does not affects the global results presented here.

4.3 Ionization Structure of the Warm Gas

In this section, the results obtained for the spatial distribution of the ionization state in ULIRGs are presented. First, and to illustrate the flexibility and power of the IFS in studying complex systems as ULIRGs, the results regarding the ionization structure of the complex system Arp 299 will be presented. Second, we will concentrate on the analysis of the entire sample of ULIRGs.

4.3.1 Two-Dimensional Ionization in Arp 299

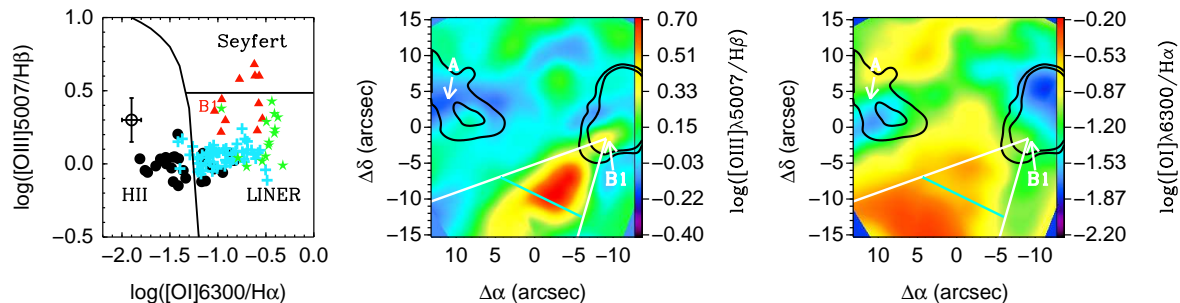


Figure 4.3: Diagnostic diagram for the system Arp 299 derived from the INTEGRAL/SB3 data. **Left Panel:** Diagnostic diagram with all the data from the SB3 bundle displayed. The symbol code is as follows: red triangles represent values within the ionization cone, and at a distance of less than 2 kpc from the nucleus B1. Green stars represent the zone within the cone at distances of 2-4 kpc from B1. Blue crosses mark the rest of the regions in the interface. Black circles represent regions in the individual galaxies IC 694 and NGC 3690 (defined as regions within the isocontours). B1 has been included in the ionization cone, and labeled as a triangle. **Center Panel:** $[\text{O III}]\lambda 5007/\text{H}\beta$ map. Nuclei A and B1 are marked. The white lines indicate the ionization cone. The transverse lines to the axis of the cone separates the inner (with Seyfert-like regions) and outer (LINER-like) sections of the cone. **Right Panel:** $[\text{O I}]\lambda 6300/\text{H}\alpha$ map. The labels and overlays are as in the middle panel.

- **Interface Region: evidence for an off-nuclear Seyfert-like ionization cone**

The $[\text{O III}]\lambda 5007/\text{H}\beta$ - $[\text{O I}]\lambda 6300/\text{H}\alpha$ line ratios have been obtained for all the INTEGRAL/SB3 individual spectra (Fig. 4.3). Although these data include the high surface brightness nuclear regions of IC 694 and NGC 3690, and their external regions, they also cover the area identified as the interface zone, i.e. the extended low surface brightness region connecting the two galaxies up to distances of about 4 kpc from their nuclei.

Changes in the ionization structure traced by the $[\text{O III}]\lambda 5007/\text{H}\beta$ and $[\text{O I}]\lambda 6300/\text{H}\alpha$ two dimensional spatial distribution line ratios are shown in Fig. 4.3.

Three different types of ionization, H II-, LINER- and Seyfert-like, are identified, and the line ratio maps clearly show that the ionization structure has a well defined spatial distribution. The majority of the regions associated with the two individual galaxies (marked with two black iso-contours in the figure) are dominated by H II-like ionization, as expected from the intense star formation taking place there (see more details in García-Marín et al. 2006). There are some exceptions; the nucleus B1 shows LINER-like activity at this angular resolution. Seyfert-like ionization is clearly resolved with a size of about $7''$ (~ 1.5 kpc) and has a conical morphology, with an opening angle of about 54° and its apex located in nucleus B1 (at a projected distance of about 1.5 kpc from the peak of the nebula) within the angular resolution (see Fig.4.3). Moreover, this highly ionized gas is not associated to any particular concentration of stellar mass according to the optical (WFPC2/F814W; see Fig. 2.3) *HST* continuum image. Off-nuclear Seyfert-like nebulae at distances of few kpc from the nucleus have already been reported in other (U)LIRGs with Seyfert nucleus (Mrk 273: Colina et al. 1999), and interpreted as photo-ionization of extranuclear interstellar gas by the AGN. Therefore, our data strongly suggest photo-ionization by a radiation cone escaping from a central dust-enshrouded AGN source located in B1. The highly ionized conical structure in Arp 299 (NGC 3690) is also detected at distances of up to 4 kpc from B1; however, the ionization associated to these outer regions of the cone is LINER-like rather than Seyfert (Fig. 4.3). Therefore, it seems that within the cone there are two ionization regimes well separated spatially. At projected distances from B1 smaller than about 2 kpc the ionization is likely due to radiation coming from the AGN located in B1, while at larger distances LINER-like ionization is dominant. This LINER-like ionization is also found in other areas of the interface region, however with a lower degree of excitation, as traced by the $[\text{O I}]\lambda 6300/\text{H}\alpha$ line ratio.

- **IC 694**

Over the area covered by the INTEGRAL SB2 bundle, H II and LINER-like ionization are present in this galaxy (Fig. 4.4). The main body of the galaxy, including the regions close to the nucleus A and the spiral arm structure (A7, G) towards the east (F), is dominated by the star-forming knots. LINER-like ionization is present elsewhere, being more prominent in diffuse low surface brightness regions located at a projected distance of about 1.8 kpc. The $[\text{N II}]\lambda 6584/\text{H}\alpha$ and the $[\text{S II}]\lambda 6725/\text{H}\alpha$ line ratio maps (not shown) also have a similar structure though, as explained above, they tend to indicate a lower ionization.

- **NGC 3690**

Three types of excitation level (H II-, LINER- and Seyfert-like) are present in this individual galaxy, as shown in the $[\text{O III}]\lambda 5007/\text{H}\beta$ - $[\text{O I}]\lambda 6300/\text{H}\alpha$ diagnostic diagram and in the two dimensional maps (Fig. 4.5). Regarding the nucleus B1, these higher resolution data give a clear Seyfert-like classification in all these line ratios, (see García-Marín 2006), and show that there is an extended zone of about $2''$ (0.4 kpc) in length associated to B1 with Seyfert characteristic. This is the inner section of the AGN-like ionization cone detected with the SB3 bundle, with its apex coincident with B1. Moreover, the region B2 presents also a high ionization state in the border line of

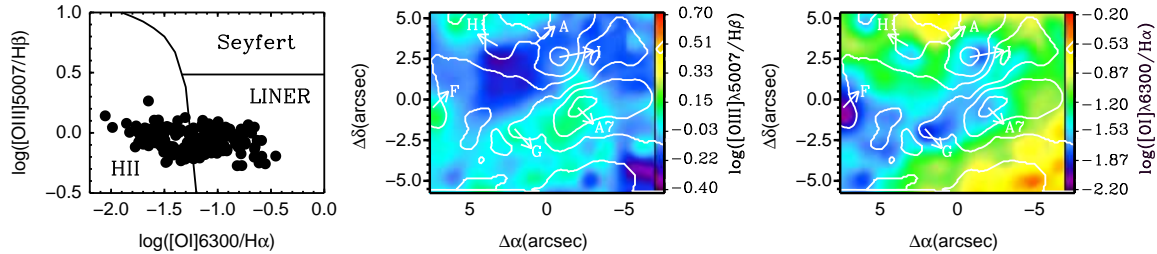


Figure 4.4: Emission line diagnostic diagram and excitation maps based on line ratios for IC 694. **Left Panel:** Diagnostic diagram obtained for the individual SB2 spectra. **Center and Right Panels:** Diagnostic maps derived from reconstructed emission line maps. As a reference we have marked several regions and superimposed red continuum contours.

Seyfert/LINER, characteristic that could indicate the presence of the counter ionization cone. The detection of Seyfert-like activity based on optical emission lines represent the first evidence in the optical for the presence of an AGN in B1, and supports the recent claim of an AGN based on X-ray (Della Ceca et al. 2002) and mid-IR (Gallais et al. 2004) data. Previous spectroscopic studies in the optical (Gehrz et al. 1983; Coziol et al. 1998; Keel 1984) did not find AGN emission, probably due to the large size of the slits ($3.6''$, $2.5''$, and $8.0''$). This is in agreement with our results, where the Seyfert nature of the B1 nucleus has been diluted in the SB3 ($\phi = 2.7''$) spectra, whereas in the higher spatial resolution SB2 ($\phi = 0.9''$) spectra the classification is clearer.

H II-like ionization dominates the rest of the main body of the galaxy (e.g. complex C), while LINER-like is present in a few outer regions. The $[O I]\lambda 6300/H\alpha$ map has its peak displaced about $0'.7$ (0.14 kpc) to the north with respect to B1. Similar displacements are observed in the $[N II]\lambda 6584/H\alpha$ and in the $[S II]\lambda 6725/H\alpha$ maps. These lines and in particular $[O I]\lambda 6300/H\alpha$ are a good tracers of shocks, thus these shifts may indicate different ionization mechanisms around B1 on scales of 200 pc. These small scale ionization changes need further investigation with high angular resolution spectroscopy.

4.3.2 Two-Dimensional Ionization in the Sample of ULIRGs

The three BPT diagnostic diagrams for all the objects and regions under study are presented in Fig. 4.6. The nuclei² of the galaxies cover the three types of ionization, with the majority of objects distributed over the H II- and LINER-like activity. Only 19% of the studied nuclei show features indicating the presence of an AGN (independent on the diagram used), with half of them being classified as warm systems. The H II- and LINER-like regions are almost equally populated, and although the distribution slightly depend on the diagram used, roughly 62% of the studied nuclei correspond to the pre-coalescence category. The nuclei dominated by star formation are preferentially warm. This result may apparently be in contradiction with Sanders et al. (1988), where a sample of 12 warm ULIRGs present Seyfert-like spectra. The fact is that our sample is not large enough as to

²In all pre-coalescence galaxies (except IRAS 12112+0305, where we have H β only in one nucleus) both nuclei have been classified.

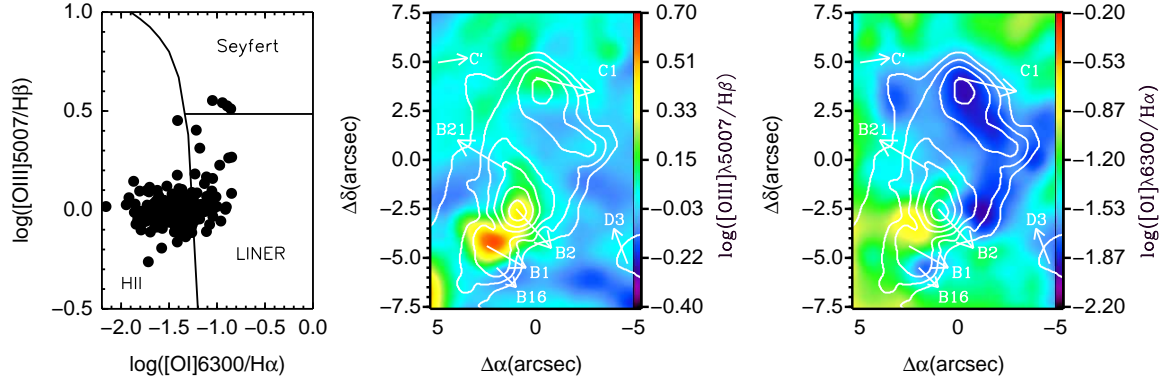


Figure 4.5: Emission line diagnostic diagram and excitation maps based on line ratios for NGC 3690. **Left Panel:** Diagnostic diagram obtained for the individual SB2 spectra. **Center and Right Panels:** Diagnostic maps derived from reconstructed emission line maps. As a reference we have marked several regions and superimposed red continuum contours.

assert that a certain percentage of warm ULIRGs do not have any indication for an AGN in the optical. Nonetheless, and taking into account the uncertainties, we can state that not all warm ULIRGs appear to have a Seyfert component.

In the circumnuclear regions, a rather continuous and consistent behavior is shown. As a rule of thumb, Seyfert nuclei are surrounded by regions that in some cases present excitation levels higher than the nucleus itself. This can be explained with the detection of narrow line regions (e.g., Arp 299 whose ionization cone has about 3.7 kpc in length García-Marín et al. 2006; and Mrk 463, with a high excitation region of about 7 kpc in length) and/or nebulae affected by the radiation coming from the AGN that may be less obscured than the nucleus itself. Special mention deserves the case of Mrk 273, where a dominant LINER-like nucleus presents an outer circumnuclear envelope of Seyfert activity of about 4.0 kpc (Colina et al. 1999). This reinforces the idea of extremely high extinction levels hiding the active nucleus in the optical range. The size of these regions is of the order of the V-shaped high excitation emission line regions measured in Seyfert galaxies (from about 0.5 to up to 27 kpc, see Mulchaey, Wilson & Tsvetanov 1996 and references therein). Regions surrounding nuclei where the star formation is the dominant mechanism are classified as star-forming or LINER-like. Consistently enough, the LINER-like nuclei (or those located in the H II-LINER border) tend to be encircled by LINER-like activity.

The most external low-surface brightness regions present about the same ionization trend than the circumnuclear ones. The pure H II and H II-LINER nuclei show external envelopes where both types of activity are detected, while the pure LINER nuclei tend to show external LINER activity. External Seyfert activity is again detected in galaxies with a Seyfert nucleus. Among those cases one worth to highlight is IRAS11087+5351. In this post-coalescence galaxy a Seyfert nucleus is detected, along with some circumnuclear activity and a strongly ionized outer nebula located at about 7 kpc from the nucleus, the furthest measured in the present sample of ULIRGs.

To obtain a global view of the spatial variations involved in the ionization state of the

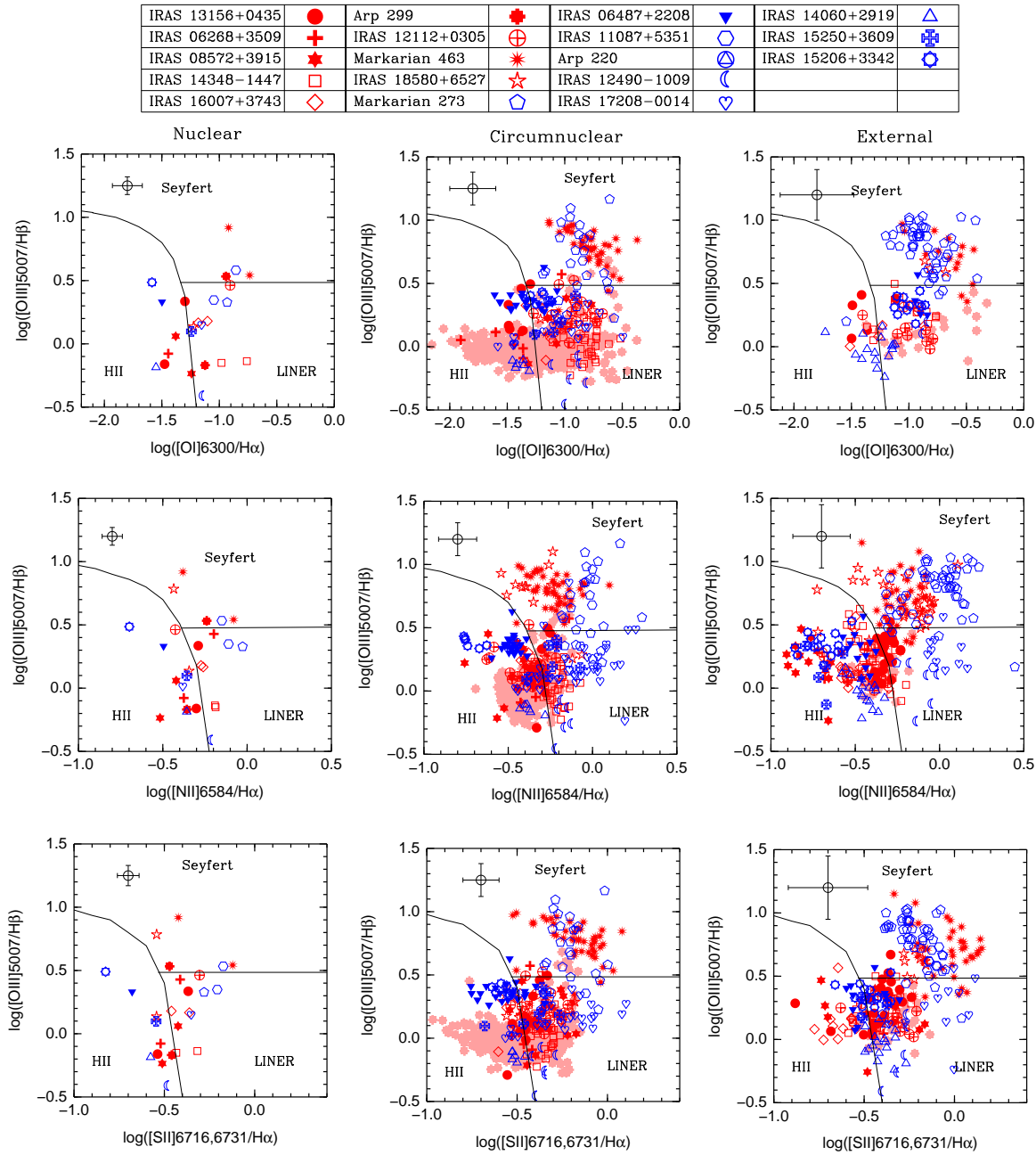


Figure 4.6: Optical emission line diagnostic diagrams, with the empirical frontiers proposed by Veilleux & Osterbrock (1987). **From left to right:** Nuclear, circumnuclear and external regions. Every point represents the spectrum obtained from one fiber. The upper panel shows the symbols associated to each galaxy. Red color indicates pre-coalescence galaxy, whereas blue color indicates post-coalescence. The color of the symbol for Arp 299 is degraded for clarity (center and right panels). Filled symbols mark warm galaxies, and empty symbols mark cold ones. The mean error bars obtained from the line fit are indicated.

galaxies, the averaged values of the regions under study have been derived (see specific values in Table 4.1). The spatially-averaged variations in the ionization state for all four optical emission line ratios are shown in Figs. 4.7 and 4.8 for the pre- and post-coalescence galaxies, respectively. In the pre-coalescence objects the circumnuclear values for each member of

Table 4.1: Average emission line ratios for the galaxies

Galaxy	$\log([\text{O I}]\lambda 6300/\text{H}\alpha)$	$\log([\text{N II}]\lambda 6584/\text{H}\alpha)$	$\log([\text{S II}]\lambda 6731/\text{H}\alpha)$	$\log([\text{O III}]\lambda 5007/\text{H}\beta)$
IRAS 13156+0435N	-1.47/-1.51/-1.50	-0.30/-0.30/-0.30	-0.54/-0.49/-0.47	-0.16:/-0.05:/0.20:
IRAS 13156+0435S	-1.30/-1.41/-1.28	-0.29/-0.30/-0.32	-0.37/-0.40/-0.39	0.33/0.31/0.30
IRAS 18580+6527E	— / — /-0.78	-0.43/-0.36/-0.15	-0.54/—/-0.22	0.78/0.85/0.67
IRAS 18580+6527W	-1.22/-0.89/-0.78	-0.34/-0.23/-0.15	-0.54/-0.34/-0.22	0.14/0.23/0.67
IRAS 16007+3743E	-1.18/-1.19/-1.27	-0.26/-0.38/-0.51	-0.36/-0.49/-0.64	0.17/0.30/0.12
IRAS 16007+3743W	-1.10/-1.12/-1.27	-0.27/-0.38/-0.51	-0.46/-0.55/-0.64	0.18/0.11/0.12
IRAS 06268+3509N	—/-1.03/—	-0.20/-0.22/-0.51	-0.41/-0.45/-0.42	0.43/0.32/0.10
IRAS 06268+3509S	-1.44/-1.31/—	-0.37/-0.39/-0.51	-0.52/-0.46/-0.42	-0.08/0.02/0.10
IRAS 08572+3915N	-1.38/-0.99/—	-0.42/-0.39/-0.72	-0.42/-0.30/-0.50	0.06/0.14/0.22
IRAS 08572+3915S	-1.24/-1.32/—	-0.52/-0.60/-0.72	-0.51/-0.46/-0.50	-0.23/0.09/0.22
IRAS 14348-1447N	-0.76/-0.76/-1.00	-0.19/-0.23/-0.40	-0.32/-0.33/-0.46	-0.14/0.01/0.26
IRAS 14348-1447S	-0.98/-0.86/-1.00	-0.19/-0.22/-0.40	-0.43/-0.34/-0.46	-0.15/0.03/0.26
Arp 299 (NGC 3690)	-0.94/-1.09/-0.73	-0.24/-0.37/-0.34	-0.47/-0.43/-0.32	0.53/0.19/0.14
Arp 299 (IC 694)	-1.12/-0.96/-0.73	-0.36/-0.37/-0.34	-0.46/-0.38/-0.32	-0.17/0.10/0.14
IRAS 12112+0305N	-0.90/-0.85/-0.95	-0.43/-0.41/-0.50	-0.30/-0.36/-0.34	0.46/0.23/0.18
IRAS 12112+0305S	—/-0.77/-0.95	—/-0.34/-0.50	—/-0.29/-0.34	—/0.20/0.18
Mrk 463E	-0.92/-0.93/-0.65	-0.38/-0.33/-0.23	-0.42/-0.32/-0.06	0.92/0.88/0.70
Mrk 463W	-0.74/-0.89/-0.65	-0.08/-0.27/-0.23	-0.12/-0.25/-0.06	0.54/0.48/0.70
IRAS 06487+2208	-1.50/-1.35/-0.90	-0.49/-0.48/-0.47	-0.68/-0.59/-0.47	0.33/0.36/0.30
IRAS 11087+5351E	-1.05/ — /-0.77	-0.15/-0.14/-0.21	-0.21/-0.22/-0.15	0.35/0.16/0.63
IRAS 11087+5351W	-0.86/-0.84/-0.77	-0.11/0.04/-0.21	-0.17/-0.16/-0.15	0.53/0.51/0.63
IRAS 12490-1009	-1.15/-0.97/-0.87	-0.21/-0.18/-0.09	-0.48/-0.37/-0.30	-0.42/-0.24/0.00
Mrk 273	-0.93/-0.90/-0.93	-0.03/-0.03 /0.04	-0.28/-0.26/-0.27	0.33/0.66/0.87
IRAS 14060+2919	-1.55/-1.39/-1.28	-0.36/-0.37/-0.44	-0.58/-0.51/-0.42	-0.18/-0.14/-0.02
IRAS 15206+3342	-1.58/-1.22/-0.99	-0.70/-0.71/-0.69	-0.82/-0.58/-0.46	0.49/0.38/0.35
IRAS 15250+3609	-1.24/-1.07/ —	-0.36/-0.23/-0.68	-0.54/-0.41/-0.46	0.10/0.22/0.19
IRAS 17208-0014	-1.15/-0.98/ —	-0.38/-0.07/0.03	-0.35/-0.22/-0.05	0.01/0.12/0.28

Notes: For all set of values, the first indicates nuclear region, the second the average of the circumnuclear regions and the third the average of the external ones. Average uncertainties for the nuclear, circumnuclear and external regions respectively are: $\log([\text{O I}]\lambda 6300/\text{H}\alpha)$: ± 0.15 , ± 0.20 , and ± 0.25 dex. $\log([\text{N II}]\lambda 6584/\text{H}\alpha)$: ± 0.07 , ± 0.10 , ± 0.18 dex. $\log([\text{S II}]\lambda 6731/\text{H}\alpha)$: ± 0.07 , ± 0.10 , and ± 0.20 dex. $\log([\text{O III}]\lambda 5007/\text{H}\beta)$: ± 0.10 , ± 0.15 , and ± 0.20 dex. : means large uncertainty.

the system are the average of those regions surrounding the corresponding nucleus, and the external are the average of all external fibers (i.e., the same for each component of the galaxy). The most relevant results can be summarized as follows:

- **The shock tracer $[\text{O I}]\lambda 6300/\text{H}\alpha$**

The radially averaged variation of this ratio is shown in Figs. 4.7, 4.8, Top Left panels. For the pre-coalescence systems no systematic tendency is detected in the structure of the excitation; only in the warm galaxies the excitation does increases between the circumnuclear and the external regions. In contrast, 90% of the most evolved post-coalescence ULIRGs show a clear increasing activity from the inner to the outer parts of the galaxies, with variations of up to 0.6 dex.

- **The star formation tracers $[\text{N II}]\lambda 6584/\text{H}\alpha$ and $[\text{S II}]\lambda 6731/\text{H}\alpha$**

The radially averaged values of these low-excitation tracers are shown in Figs.4.7 and 4.8 (Top Right and Lower Left panels). Consistently with the previous findings, in the pre-coalescence galaxies the spatial variations of the ionization conditions show no

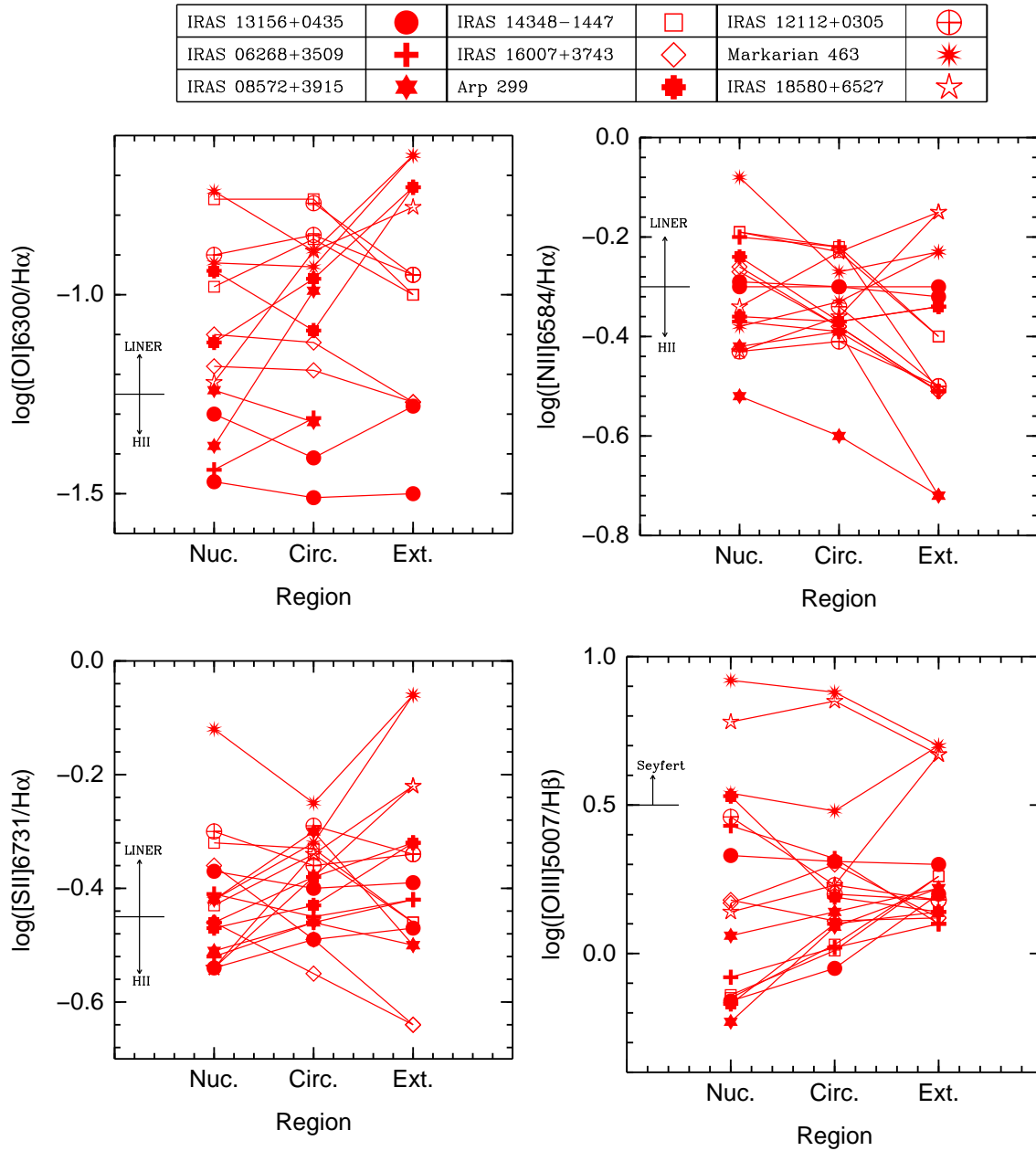


Figure 4.7: Average line ratios for the different regions (Nuclear, Circumnuclear and External) of the individual pre-coalescence galaxies. The upper panel shows the symbols associated to each galaxy. Color code as in Fig. 4.6. The approximate value for the Veilleux & Osterbrock (1987) frontier between classifications is shown. See uncertainties in Table 4.1.

systematic behavior. Contrarily to this, the post-coalescence galaxies show an increment in the excitation (of up to 0.3 dex) towards the external regions, as traced by the line ratio $\log([\text{S II}]\lambda 6731/\text{H}\alpha)$ over the galaxy radial structure in about 80% of ULIRGs. As for the $\log([\text{N II}]\lambda 6584/\text{H}\alpha)$ indicator, no clear tendency is measured.

- **The highly ionized regions tracer $[\text{O III}]\lambda 5007/\text{H}\beta$**

Figs. 4.7, 4.8 (Bottom Left panels) show the radial variations of the $[\text{O III}]\lambda 5007/\text{H}\beta$ line

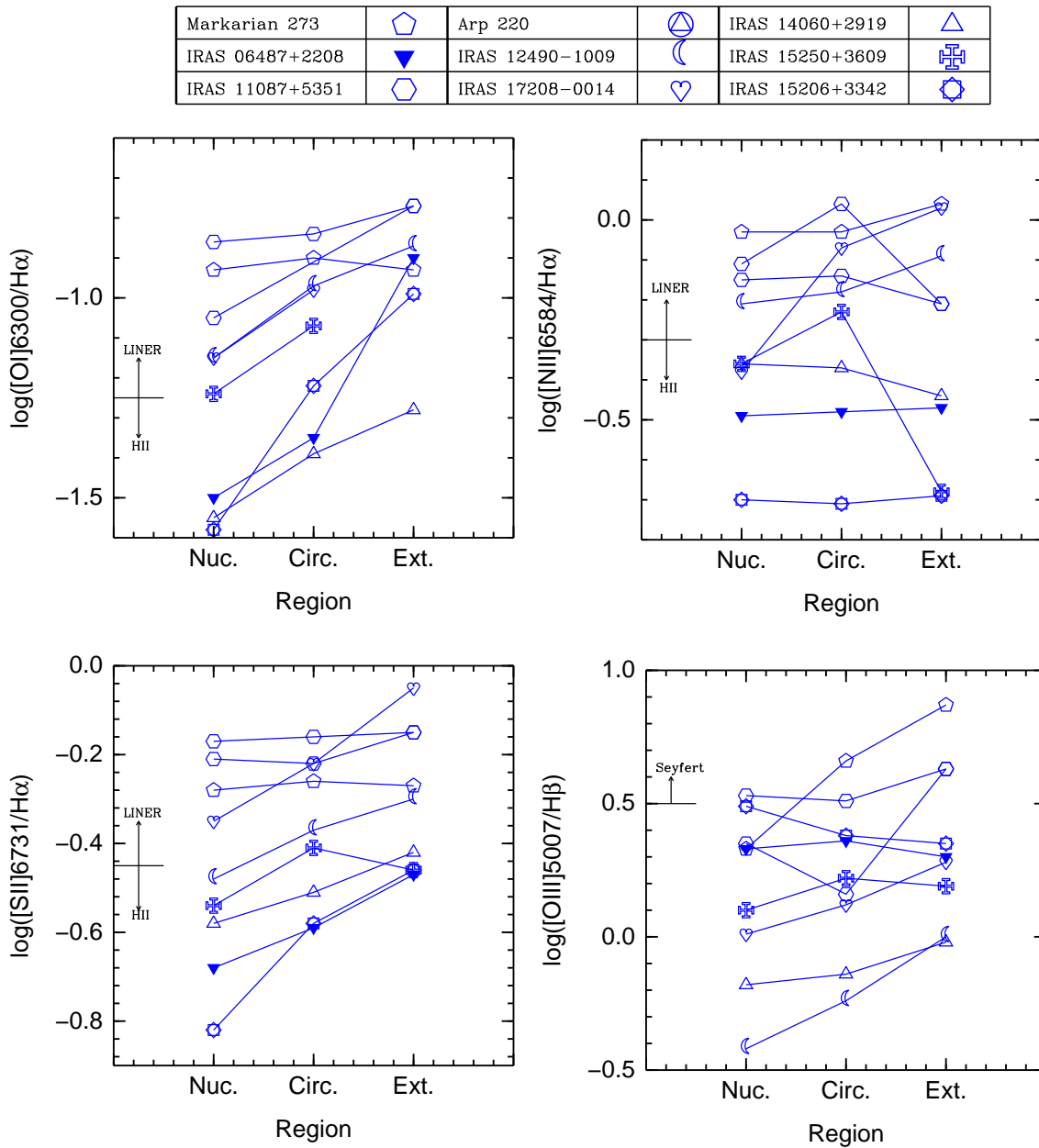


Figure 4.8: Average line ratios for the different regions (Nuclear, Circumnuclear and External) of the post-coalescence systems. The upper panel shows the symbols associated to each galaxy. Color code as in Fig. 4.6. The approximate value for the Veilleux & Osterbrock (1987) frontier between classifications is shown. See uncertainties in Table 4.1.

ratio, which is a sensitive tracer for separating the Seyfert-like from the HII- and the LINER-like ionization. The pre-coalescence ULIRGs with Seyfert nuclei show a similar degree of excitation between the nuclear and circumnuclear regions, whereas in the most external regions the ionization decreases with respect to the most excited nucleus of the system. The case of the LIRG Arp 299 is an archetype of what we call aperture effect: the outer Seyfert activity is completely diluted when the average is done. The circumnuclear and external regions that surround pre-coalescence non-Seyfert nucleus

show a systematic convergence to external ionization values of about 0.3 dex. In the post-coalescence galaxies the values of this line ratio do not show convergence to any ionization level in the most external regions. Furthermore, the radial increasing trend in the ionization is present only in about 60% of galaxies.

The most important conclusion derived from this two-dimensional analysis of the ionization state is that there are clear differences between the pre- and post-coalescence galaxies.

In the post-coalescence ULIRGs, two out of the three line ratios used for separating the H II and LINER activity tend to show an increase in the excitation towards the outer low surface brightness regions. These variations range from the nucleus to distances larger than 3 kpc. The $[\text{O I}]\lambda 6300/\text{H}\alpha$ line ratio shows a radial increase towards LINER-like excitation, that is believed to be tracing shocks. In some cases the variations are slightly lower than the uncertainties; however, the systematic trend exists. The origin of these shocks may be explained either by starburst-driven super-winds (Heckman, Armus & Miley 1990), the presence of supernovae and relatively evolved starbursts (Alonso-Herrero et al. 2000b) or the merger process (Monreal-Ibero et al. 2006)³. Also, the post-coalescence galaxies show a general increment of the ionization level towards the external regions as traced by the $[\text{S II}]/\text{H}\alpha$ line ratio. In comparison, the excitation measured with the $[\text{N II}]/\text{H}\alpha$ line ratio diminishes in half of galaxies between the circumnuclear and external regions. Given that both line ratios are tracing the same processes (i.e., star formation), they should follow the same relative trend. Due to the complexity of ULIRGs it is not straight forward to define the mechanism responsible for this differences, especially taking into account that in some cases the small variations involved and the uncertainties. Factors like the variation in the metallicity due to the differences in the stellar populations, or in the physical conditions, may produce differences between the $[\text{N II}]/\text{H}\alpha$ and $[\text{S II}]/\text{H}\alpha$ line ratios.

With respect to the pre-coalescence systems we found no clear trends in their behavior, except for the $[\text{O III}]/\text{H}\beta$ line ratio. Putting aside the galaxies with Seyfert nuclei, surrounded by highly ionized regions, the excitation level of the external regions in the pre-coalescence ULIRGs converge to a similar value (line ratio of about 0.3 ± 0.1 dex). This observational evidence may be explained taking into account that all these systems belong to the same galaxy type, have the same origin and undergo a dynamically similar pre-coalescence phase. If a Seyfert nuclei is not detected it means either that there is no such activity or that it is deeply embedded in dust (which tend to be concentrated towards the nuclear regions) and therefore invisible to the optical range. Therefore, in absence of Seyfert-like ionization, a similar ionization level traced by this line ratio in the outer low-surface brightness regions is expected.

4.4 The Origin of LINER-Like Ionization

In 1980, Heckman defined for the first time the LINER (*Low ionization Nuclear Emission-line Regions*) as those galactic nuclei where “*The spectra are dominated by lines arising from low ionization states*”. The original empirical criteria for discriminating this galaxy type was based on the ratios of oxygen forbidden lines ($[\text{O II}]/[\text{O III}] \geq 1$ and $[\text{O I}]/[\text{O III}]$

³The role of shocks in ULIRGs will be discussed in § 4.4.

$\geq 1/3$). This type of ionization (that can be nuclear or extended) is not a physical process itself; it is just an observable characteristic produced by a mechanism that needs to be determined. Generally speaking, the two main processes that have been invoked for explaining LINER process are photo-ionization and shocks. The photo-ionization can be explained in several ways:

- Photo-ionization by a non-stellar, power-law ionizing continuum coming from a low luminosity AGN (Ho, Filippenko & Sargent 1993; Grooves et al. 2004). This possibility has been proposed for explaining nuclear LINER-like ionization. It is based on the continuity between the LINERs and Seyfert galaxy spectra, along with the discovery of X-ray emission and a broad component in H α in some LINERs. In this context a LINER would be an AGN with a low ionization parameter U (Ho, Filippenko & Sargent 1993; Rupke & Veilleux 2007).
- Ionization by hot stars called *warmers* (very hot Wolf-Rayet stars of spectral type WC5, WC4 and WO) is another mechanism proposed by Terlevich & Melnick (1985) for explaining “*the missing Link between Starburst and Seyfert galaxies*”. In this scenario, the LINER nuclei are not a consequence of a non-thermal power law source, but of violent star formation activity at high metal abundance. In addition, under conditions of above solar metallicity and high density gas ($n_e \gtrsim 10^5 \text{ cm}^{-3}$), the starburst model during the Wolf-Rayet dominated phase can reproduce the spectra of some LINERs with signs of stellar activity (LINER-H II transition) (Barth & Shields 2000).
- The emission-line properties of a sample of LINER galaxies may be reproduced using an aging starburst (Alonso-Herrero et al. 2000b). The line ratios are explained by a metal-rich H II region and a supernova remnant component.
- Finally, photo-ionization by old post-AGB stars has been proposed as an alternative explanation for the ionization found in elliptical galaxies (Binette et al. 1994).

The ionization by shocks, which is the another plausible explanation for the LINER-like activity, can be explained in several ways:

- Emission-line filaments would be formed in a cooling accretion flow of the X-ray onto the dominant galaxy of the cluster, and will be a common feature of the brightest cluster members (Heckman et al. 1981; Romanishin 1986; Fabian, Nulsen & Canizares 1984; Fabian 2003). This first scenario is generally present in clusters of galaxies.
- The observed ionization in the extended extra-nuclear regions may also be explained with ionization by fast large scale shocks (Dopita & Sutherland 1995). The origin of these shocks could be galactic super-winds (Lehnert & Heckman 1996; Lutz, Veilleux & Genzel 1999; Cecil et al. 2001) detected by double-component emission lines (with differences in the velocities of between $\sim 200\text{-}600 \text{ km s}^{-1}$), starburst-drive super-winds (Heckman, Armus & Miley 1990). Furthermore, the merger process which almost all ULIRGs are experiencing, could be responsible for generating shock fronts (Monreal-Ibero et al. 2006).

So the question that arises is, which is the dominant mechanism producing LINER-like ionization in ULIRGs? Using a sub-sample of the present ULIRGs (6 galaxies) Monreal-Ibero et al. (2006) conclude that merger-induced shocks are responsible for the LINER activity detected in the outer regions of the galaxies. Although the evolution in the $[\text{O I}]/\text{H}\alpha$ line ratio found in the post-coalescence galaxies points towards an increasing importance of shocks with the evolution of the merger, the aim of the present section is to check the validity of this “shock as responsible for LINERs scenario” in the nuclear as well as circumnuclear and external regions. To achieve this purpose two different tests will be used: first the direct comparison of the line ratio with theoretical photo-ionization models; second the search for a positive correlation between the $[\text{O I}]/\text{H}\alpha$ line ratio and the $\text{H}\alpha$ velocity dispersion.

4.4.1 Comparison with Models

Fig. 4.9 shows the line ratios $[\text{S II}]\lambda 6725/\text{H}\alpha$ - $[\text{N II}]\lambda 6584/\text{H}\alpha$ derived for the nuclear (Left Column), circumnuclear (Center Column) and external (Right Column) regions of the galaxies under study compared to several photo ionization models. We chose to make the comparison with the models using those line ratios because, as we will see below, they do not depend strongly on the age of the stellar populations (Moy et al. 2001; Stasińska et al. 2003; 2006), and to perform a direct comparison with the Monreal-Ibero et al. (2006) results. The models represent: (i) photo-ionization by a power law coming from an AGN (Grooves et al. 2004, Upper row), (ii) photo-ionization produced by an instantaneous burst of star formation (Barth & Shields 2000, Middle row) and (iii) photo-ionization due to fast shocks (Dopita & Sutherland 1995, Lower row). The stellar photo-ionization models used in the comparison are for stellar populations 4 Myr old. Unlikely the $[\text{O III}]/\text{H}\beta$ line ratios, that significantly decreases after 5 Myr, the line ratios selected for the comparison are not very sensitive to variations in age (Moy et al. 2001; Stasińska et al. 2003; 2006). For example, changing from 4 to 6 Myr in the line ratio $[\text{S II}]/\text{H}\alpha$ would imply a variation (depending on parameters such as the metallicity and ionization parameter U) of about 0.1 dex towards higher values of the ionization. In any case, older ages will slightly move the models up and right in the diagrams, and no significant variations on the results will be detected. In all cases the regions classified as Seyfert have been removed from the diagrams (i.e., the origin is clear).

The comparison with the models clearly establishes that photo-ionization by an AGN cannot account for the LINER (or LINER-H II) activity in ULIRGs, either in nuclear, circumnuclear or external regions (Fig. 4.9, Upper Row). In contrast with this, photo-ionization due to instantaneous “dusty” star formation (a non-dusty model would not be realistic for ULIRGs) explains the line ratios values only partially. Specifically the region of lowest values of the $[\text{N II}]/\text{H}\alpha$ line ratios (outside the H II- area) is not accounted for by the models (Fig. 4.9, Center Row). Finally, the last set of comparisons has been done using fast velocity shocks models, which explain a large fraction of the measured ionization, including that of those regions not accounted for by star formation (Fig. 4.9, Lower Row). The ionization in the nuclear regions is consistent with shocks of between 150 and 200 km s^{-1} . Regarding the circumnuclear regions, they appear to be dominated by shocks of velocities between about 150 and 300 km s^{-1} . Finally in the most external regions of ULIRGs velocities of between 150-500 km s^{-1} would explain the observed ionization (LINER- and (LINER-H II)-like). These results are in agreement with those of Monreal-Ibero et al. (2006).

In summary, from the comparison with the three models it can be derived that fast

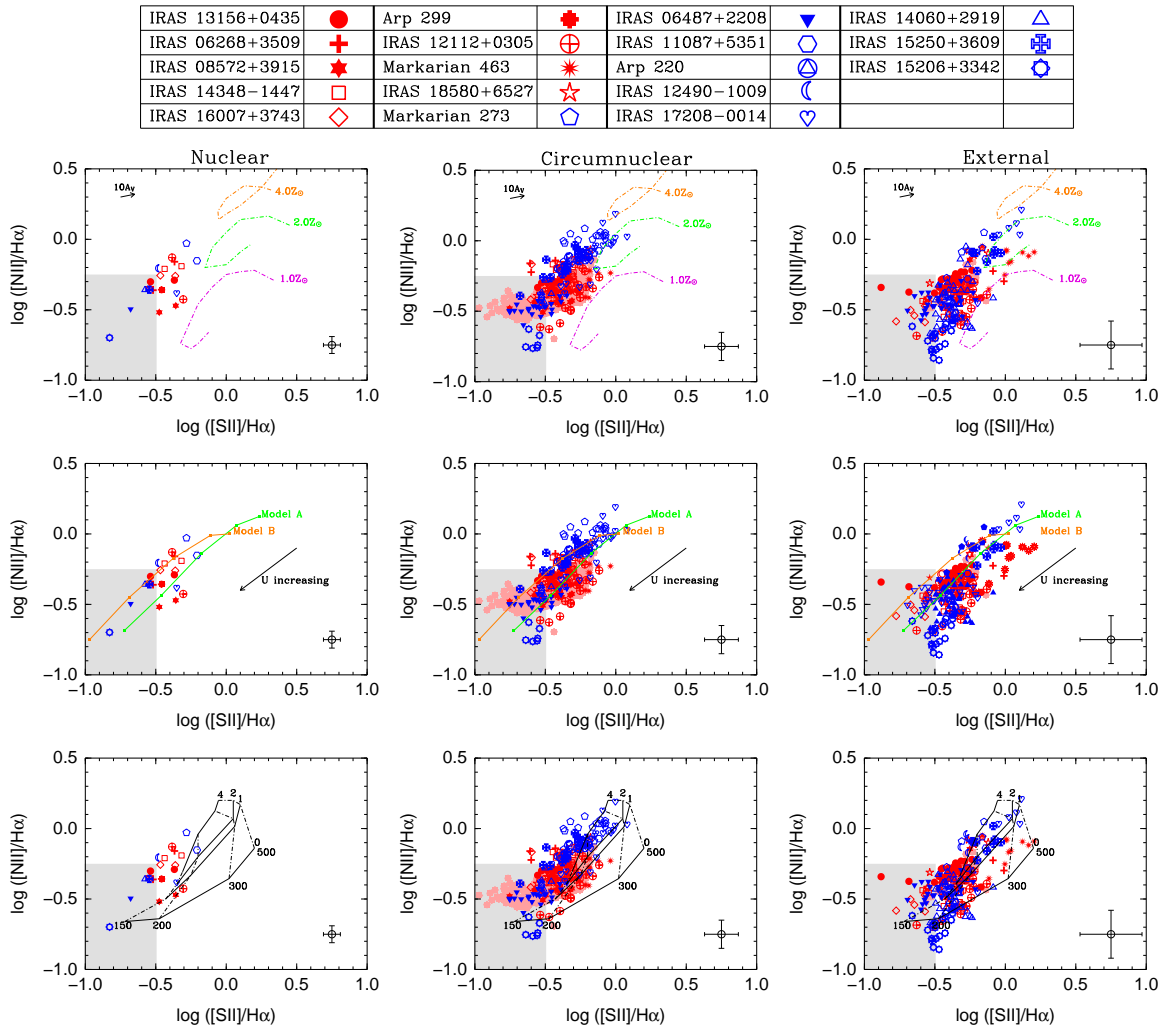


Figure 4.9: $[\text{NII}]/\text{H}\alpha$ vs. $[\text{SII}]/\text{H}\alpha$ ratios. The first column shows the information for the nuclear regions, the center column for the circumnuclear regions and the right for the external ones. In all cases the regions classified as Seyfert have been removed. The region in the lines diagrams where pure star-forming regions fall is shaded in gray. Each row shows the same information, but with different models over-plotted. **Upper row:** Predictions for AGN photo-ionization coming from a dusty cloud with $n_e=10^3\text{cm}^{-3}$ with a power law index of -1.4 (Grooves et al. 2004). Three different metallicity values are represented. **Middle row:** Instantaneous burst models of 4 Myr. with initial mass function (IMF) power law and $n_e=10^3\text{cm}^{-3}$, solar metallicity and $M_{up}=100M_\odot$. Model B includes the effect of dust, whereas model A does not include dust as a parameter. Small squares along each model correspond to the model grid points at $\log U=-4, -3.5, -3, -2.5$ and -2 , with U being the ionization parameter (Barth & Shields 2000). **Lower row:** Models for fast shock without precursor are indicated with a solid line. The value of the magnetic parameter $B/n^{1/2}(\mu\text{G cm}^{3/2})$ is indicated at the beginning of the line. Shock velocity ranges from 150 to 500 km s^{-1} (Dopita & Sutherland 1995).

shocks are the dominant mechanism responsible for the LINER-like ionization in ULIRGs. The velocity of the shocks increases radially: between 150-200 km s^{-1} in the nuclear regions, 150-300 km s^{-1} in the circumnuclear and 150-500 km s^{-1} in the external regions. In addition to this, photo-ionization due to a young stellar population (4-6 Myr) is a secondary mechanism that can contribute to the LINER excitation too.

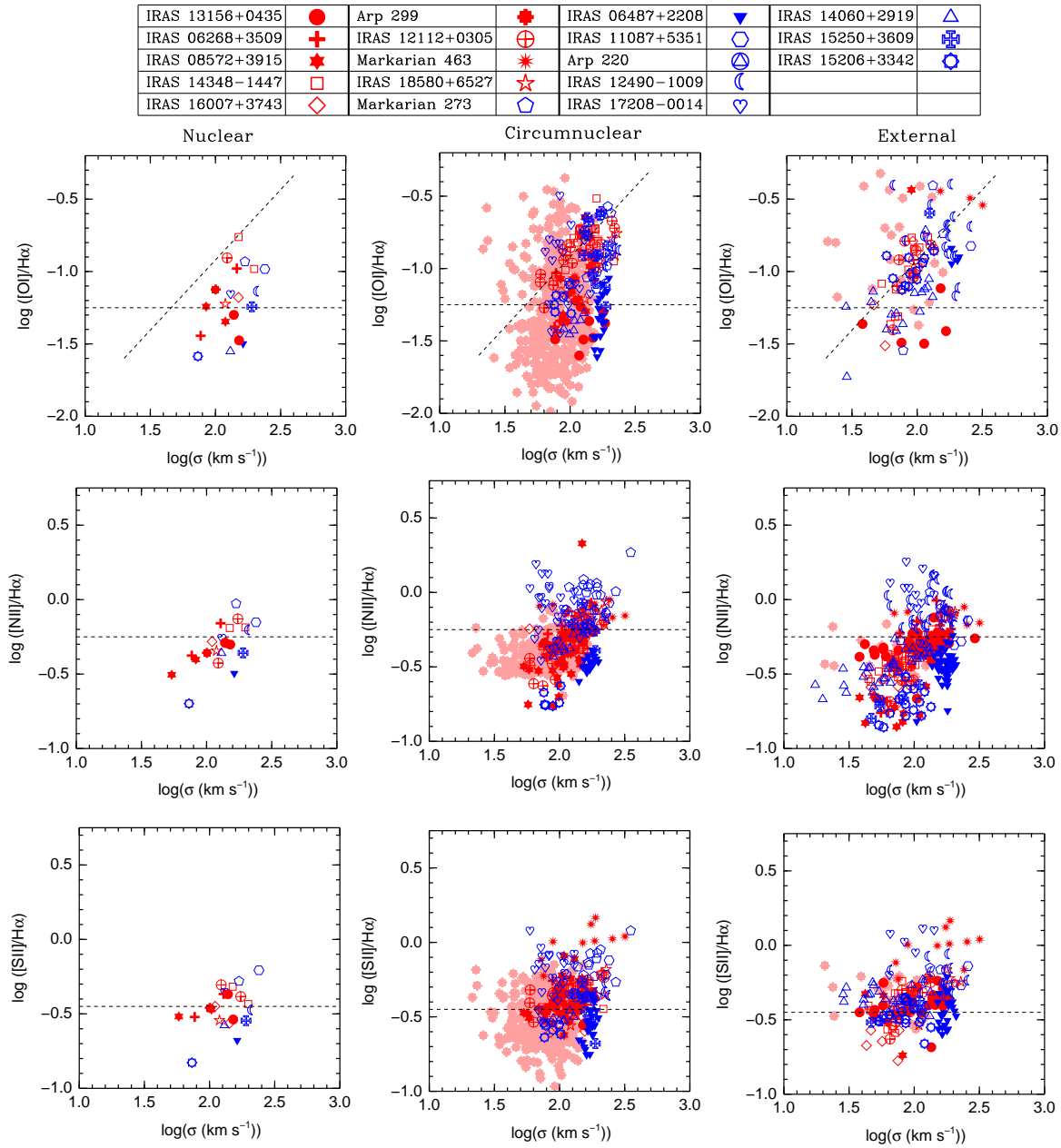


Figure 4.10: Relation between the velocity dispersion and $\log([\text{O I}]/\text{H}\alpha)$ (**Upper row**), $\log([\text{N II}]/\text{H}\alpha)$ (**Middle row**) and $\log([\text{S II}]/\text{H}\alpha)$ (**Lower row**) shown for the nuclear (**Left column**), circumnuclear (**Center column**) and external regions (**Right column**). The dashed horizontal line marks the frontier between H II regions and LINER-like activity. The relation derived by Monreal-Ibero et al. (2006) for $\log([\text{O I}]/\text{H}\alpha)$ using the external regions of a subset of ULIRGs is shown too. The uncertainty in σ is about 15%. The symbols and color code are as in Fig. 4.6.

4.4.2 Excitation vs. Velocity Dispersion σ : Additional Evidence for Ionization by Shocks

Some authors (Armus et al. 1989; Dopita & Sutherland 1995; Veilleux et al. 1995) have found a positive correlation between the velocity dispersion and the ionization, and

interpreted it as further evidence supporting the presence of shocks. This has been confirmed by Monreal-Ibero et al. (2006), who derived a positive correlation between $\log([\text{O I}]/\text{H}\alpha)$ and σ using the external regions of a small sample of ULIRGs. Here we will test the validity of these results by comparing three different line ratios ($[\text{O I}]/\text{H}\alpha$, $[\text{N II}]/\text{H}\alpha$ and $[\text{S II}]/\text{H}\alpha$) with the $\text{H}\alpha$ velocity dispersion⁴. The results obtained for the nuclear, circumnuclear and external regions are shown in Fig. 4.10. Again the regions with Seyfert-like ionization have been excluded from the diagram.

The first consistent trend between the plots is the different behavior of Arp 299, especially in terms of velocity dispersion. The reason of this variations is related to the previously discussed aperture effect: in Arp 299 each individual region (as measured with one fiber) maps a physical area about ten times smaller (in radius) than the rest of ULIRGs. Therefore, we either may be tracing different mechanisms than for the other galaxies, or the same mechanism but at different angular resolution. This fact must be taken into account if deriving a global conclusion using this correlations.

In a qualitative way, the behavior of the line ratios vs. σ is different. The $[\text{N II}]/\text{H}\alpha$ and $[\text{S II}]/\text{H}\alpha$ tend to present a more compact distribution, especially in the LINER-like individual regions (above the horizontal line in Fig. 4.10). In contrast, the shock tracer ($[\text{O I}]/\text{H}\alpha$) shows a more extended range of excitation level, even when only the LINER-like activity is considered (that is, points above the horizontal line). This indicates that there is no strong correlation between $[\text{N II}]/\text{H}\alpha$, $[\text{S II}]/\text{H}\alpha$ and σ , and that for the $[\text{O I}]/\text{H}\alpha$ line ratio there is a slight tendency in the ionization to increase with σ . In fact, the correlation parameter R is 0.68 for the circumnuclear and 0.65 for the external regions. For this line ratio, the most interesting aspect is the variation in the behavior with the distance to the nucleus (see Fig. 4.10, Upper Row).

The nuclear and circumnuclear regions show a similar (almost constant) trend non consistent with the correlation derived by Monreal-Ibero et al. (2006). In contrast, in the most external regions we find higher excitation and more dispersed σ values, that lead to a reordering around the plotted correlation. Consistently with the results of § 4.3.2, the increase of the excitation is mainly detected in the post-coalescence systems. This reinforces the previous conclusion of shocks of increasing velocity dominating the LINER-like excitation in the circumnuclear and external regions of ULIRGs (that is, at scales of 2.5-3.0 kpc and larger).

To obtain a quantitative correlation, the observed points were fitted to a linear function, but due to the large scatter of the points the derived fits (which is not shown in the graphs) were not representative of the general behavior. Therefore, the average results for the $[\text{O I}]/\text{H}\alpha$ vs. σ have been obtained for the circumnuclear and external regions of each galaxy (see Fig. 4.11). By doing this we obtain a clear general view, and confirm first the different trend among the circumnuclear and external regions. Second, the tendency of the external regions to have higher excitation levels, and to reorder around the Monreal-Ibero et al. (2006) correlation.

Summarizing, we find that the (LINER-like) ionization as traced by the $[\text{N II}]/\text{H}\alpha$ and $[\text{S II}]/\text{H}\alpha$ line ratios shows no correlation with the σ values. With respect to the relation between the $[\text{O I}]/\text{H}\alpha$ line ratio and σ , although qualitatively there appear to be a positive trend, due to the scatter it has been not possible to derive a reliable linear correlation.

⁴See details in Chapter 5.

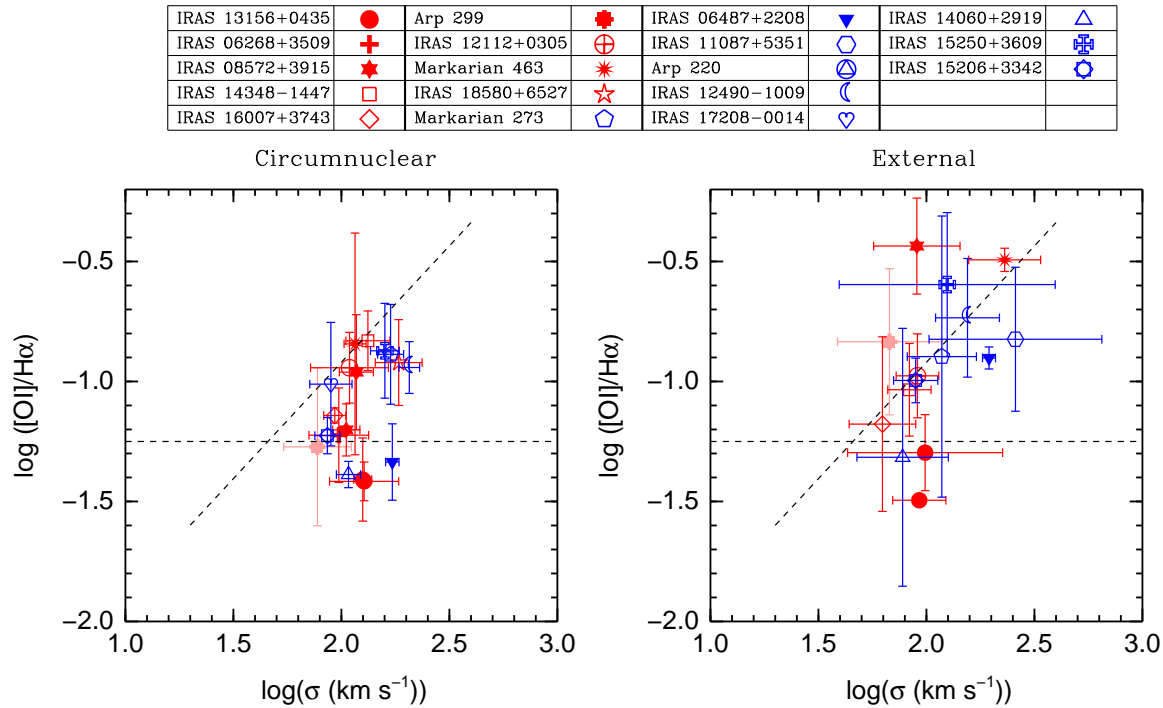


Figure 4.11: Average relation between the velocity dispersion and $\log([\text{O III}]/\text{H}\alpha)$ for the circumnuclear regions (**Left**) and external regions (**Right**). Color code as in Fig. 4.6.

Nonetheless, the behavior of the circumnuclear and external regions is rather different. The external regions present higher excitation (especially the post-coalescence galaxies) and an increase of the ionization with the velocity dispersion. These results give further support to the scenario where shocks with radially increasing velocities are responsible for the LINER-like excitation in ULIRGs.

4.5 Integrated Results for ULIRGs: Aperture Effects in Galaxy Classification

Throughout this Chapter we have introduced the so-called aperture effect, that is, how the area integrated for deriving the excitation level influences in the results. The natural questions that we can ask now are: How can we compare the integrated values of ULIRGs with the rest of emission line galaxies?, and How would the nuclear classification be influenced by the low surface brightness regions (i.e., nuclear vs. integrated activity class)?

Fig. 4.12 (Upper Row) shows the integrated classification for our sample of ULIRGs, superimposed in a sample of 85224 emission line galaxies (with redshifts between 0.04 and 0.1) from the SDSS (Kewley et al. 2006). The excitation level in ULIRGs does not coincide with that observed in the majority of emission line galaxies. As a class ULIRGs populate the higher excitation regions as traced by the $[\text{O III}]/\text{H}\beta$ line ratio, and tend to be distributed in regions of extreme starbursts and transition between H II-, LINER- and Seyfert-like excitation. This reinforces the idea of ULIRGs as galaxies of a composite nature, where in general no single excitation mechanism dominates the emission. In fact the merger, which may trigger strong

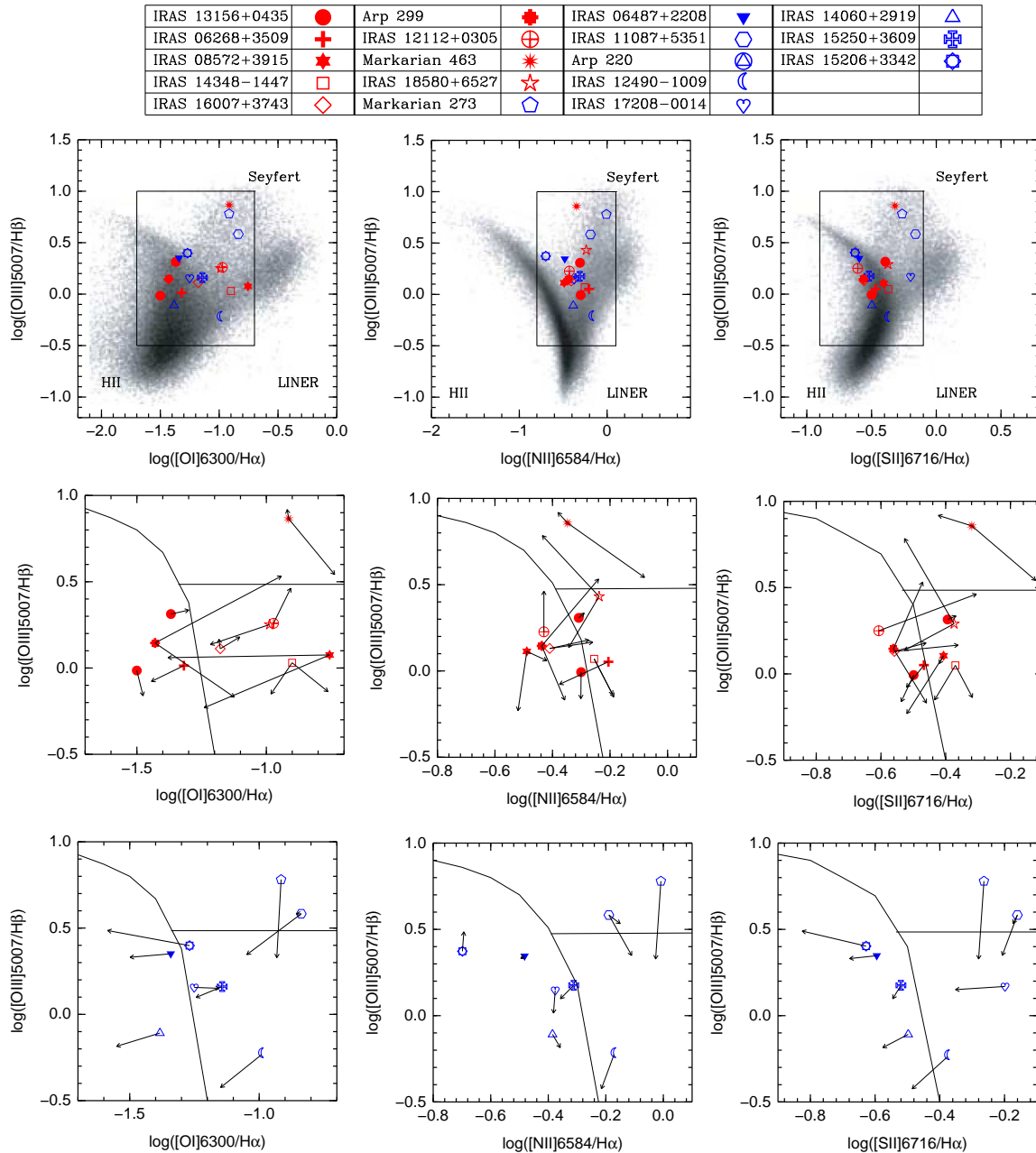


Figure 4.12: **Upper row:** The three BPT diagrams for the integrated values of ULIRGs. The gray areas mark the distribution over the diagram of 85224 emission line galaxies from the SDSS (Kewley et al. 2006). Boxes indicates the regions represented in the Middle and Lower rows. **Middle row:** Detail of the BPT diagnostic diagrams with the integrated classification of pre-coalescence ULIRGs represented as red symbols. Black arrows point to the nuclear classifications. Black lines mark the classical Veilleux & Osterbrock frontiers. **Bottom row:** As middle row, but blue symbols are post-coalescence ULIRGs.

star formation and be responsible for the shocks, is the decisive process that partly determines the excitation level in ULIRGs.

The contribution from the extra-nuclear low-surface brightness regions to the excitation level of the entire galaxy is evaluated in Fig. 4.12 (Middle and Bottom rows) for the pre- and post-coalescence ULIRGs. The nuclear vs. integrated classification of pre-coalescence

systems do not show any stable trend; nonetheless, about 50% of the systems have a different nuclear vs. integrated excitation as defined by the $[\text{N II}]/\text{H}\alpha$ and $[\text{S II}]/\text{H}\alpha$ line ratio. As for the post-coalescence ULIRGs, the integrated values show a systematic increasing in the excitation ($\text{H II} \rightarrow \text{LINER}$) compared to the nuclear ones. This is observed when using the $[\text{O I}]/\text{H}\alpha$ and $[\text{S II}]/\text{H}\alpha$ line ratios. The excitation obtained from the $[\text{N II}]/\text{H}\alpha$ line ratio does not show such a systematic response. This result is consistent with the radial increasing detected in the ionization in the post-coalescence galaxies as traced by $[\text{O I}]/\text{H}\alpha$ and $[\text{S II}]/\text{H}\alpha$. From this comparison, it is straightforward to assert that the extra-nuclear regions of ULIRGs may significantly modify the global excitation level of the galaxies. These results must be taken into account when observing high- z ULIRGs. In most occasions these high- z galaxies will be observed as integrated sources⁵, and the detailed structure observed locally will be mixed. Therefore, and due to the aperture effect, their integrated classification may not be representative of the nuclear activity. In fact, a LINER-like classification will be favored in the integrated values, meaning that the stable fraction of about 38% of LINER-like galaxies obtained from nuclear spectra by Kim et al. (1998) would increase. The Seyfert activity may be either diluted (if comes directly from the nucleus) or enhanced (if comes from highly ionize extra-nuclear nebulae as those detect in ULIRGs). This can be of particular importance for discriminating the dominant excitation mechanism in this galaxy type. In addition, high- z ULIRGs are not expected to fall in the regions most densely populated by emission-line galaxies, but to populate highly excited and transition states. This tendency of ULIRGs to favor the highly excited and extreme starburst levels (either in the nuclear and integrated activity) is consistent with the results of Veilleux et al. (1995). These characteristics does not classify ULIRGs as galaxies with an exotic ionization state, but makes them a particular category that will be actively studied at high- z .

4.6 Summary and Conclusions

The two-dimensional ionization structure of a sample of ULIRGs (17 systems, 26 galaxies) covering different merger phases and ionization states has been studied. The analysis can be divided into four main themes: (i) the analysis of the dominant ionization mechanisms (ii) the internal structure of the ionization conditions in ULIRGs, (iii) the origin of the LINER-like activity and the role of shocks, and (iv) aperture effects in ULIRGs classification, as well as predictions for high-ULIRGs. The main conclusions can be summarized as follows:

- The analysis of the line ratios shows that 19% of the studied (both pre- and post-coalescence) ULIRGs present characteristics that indicate the presence of an AGN. H II - and LINER-like nuclei are almost equally represented, with about 60% corresponding to the pre-coalescence category. The circumnuclear and external regions tend to show the same classification than the nucleus, although nuclei lying close to the H II -LINER frontier may present either activities in their extra-nuclear regions.
- We have shown that, depending on the morphological type, the averaged ionization state in ULIRGs presents radially dependent variations in scales of several kpc. In the

⁵This is straightforward taking into account the cosmological dimming and the spatial resolution at large distances (e.g., for $z=0.1 \rightarrow 1.8 \text{ kpc}''$; for $z=0.5 \rightarrow 6.1 \text{ kpc}''$; for $z=1.0 \rightarrow 8.0 \text{ kpc}''$; $z=3.0 \rightarrow 7.7 \text{ kpc}''$).

post-coalescence ULIRGs, the line ratio $[\text{O I}]/\text{H}\alpha$ increases towards the external regions with variations of up to 0.6 dex. This emphasizes the importance of shocks in the most external regions, and the fact that the lower density of material and more ordered structure in the post-coalescence systems may favor shocks. The different behavior found among the $[\text{S II}]/\text{H}\alpha$ and $[\text{N II}]/\text{H}\alpha$ line ratios may indicate a variation in the ionizing radiation or in the physical conditions. With respect to the pre-coalescence systems, their complex merger-induced excitation structure makes them not shown, as a group, any systematic trend.

- From the comparison with theoretical models we derive that LINER-like activity appears to be mainly produced by high velocity shocks, whose velocity range increases with the nuclear distance. This velocity increment in the most external regions may be due to the lower density of the media. This reinforces the idea of shocks gaining importance as the distance to the nucleus increases, and is consistent with the analysis of the radially averaged excitation conditions. A secondary mechanism responsible for the LINER-like activity may be photo-ionization by a young stellar population (4-6 Myr).
- We do not find a tight correlation between $[\text{O I}]/\text{H}\alpha$ vs. velocity dispersion, but a trend (correlation parameter R 0.68 and 0.65 for the circumnuclear and external regions) that supports the results previously reported by other works. In spite of this, this trend is different for the circumnuclear and the external regions. In the external regions the points are more ordered around the linear relation obtained from the literature, specially in the post-coalescence ULIRGs.
- As a consequence of the so-called “aperture effect”, the nuclear classification of ULIRGs does not always coincide with the integrated value. Variations in the excitation are detected in all galaxies, but only in the post-coalescence we measure a systematic increase from H II to LINER between the nuclear and integrated classifications (based in the $[\text{O I}]/\text{H}\alpha$ line ratio).
- The comparison between the integrated ULIRGs and the SDSS emission-line galaxies, demonstrates that the excitation level of ULIRGs does not coincide with the majority of SDSS galaxies. In fact, they populate the extreme starbursts, the highly excited and the transition regions. This result, and that of the previous point, need to be taken into account when interpreting the integrated observations of high- z ULIRGs.

Chapter 5

Gas Kinematics and Dynamical Mass Derivation in ULIRGs

In this Chapter the two-dimensional warm gas kinematics of 18 low- z ULIRGs has been investigated. The velocity fields are very disordered and non consistent with pure rotation, but dominated by tidally-induced forces. Nonetheless, in some cases structural indications of rotation-like velocity curves appear either in the central kpc and in the entire structure of the galaxies. The velocity fields present velocity amplitudes of up to about 400 km s^{-1} , and velocity gradients of up to about $80 \text{ km s}^{-1} \text{ kpc}^{-1}$ are measured in the tidal tails of several pre-coalescence galaxies. The velocity dispersion (σ) presents large nuclear values of the order of hundreds km s^{-1} . In about 80% of ULIRGs the location or the σ peak is not coincident with the photometric nucleus, indicating either dynamically hot regions or that σ is tracing tidally-induced flows rather than mass concentrations. For the studied ULIRGs, the V/σ parameter ranges from about 0.4 to 2.5, that is, from the pressure-supported galaxies to those where the velocity amplitude (mainly tidal-induced) dominates. To test the degree of rotation in ULIRGs, a simple kinematic model has been fitted to the data. The main conclusion is that the large scale velocity fields are dominated by tidal forces, and that the velocity amplitude does not trace, in general, rotation. In spite of this, in a few cases (such as IRAS 13156+0435 and IRAS 14060+2919) the velocity amplitude, the inclination, and the good correlation between the photometric and kinematic position angle point towards some degree of rotation in the galaxies. The dynamical masses derived from the nuclear σ are $\leq m_$ in 75% of cases, and the mass ratio of the parent galaxies is in general between 1:1 and 3:1, as it has been predicted by numerical simulations. This is in agreement with the previously proposed elliptical through merger scenario. Further confirmation to this is given by the location of ULIRGs in the fundamental plane, which in the case of post-coalescence ULIRGs is consistent with that of elliptical galaxies and other ULIRGs.*

5.1 Introduction

The kinematic of ULIRGs is determined by the interaction/merger processes that these galaxies undergo. In fact, the warm gas velocity fields are very complex, and on scales of several to few kpc not consistent with pure rotation. On the other hand, the two-dimensional velocity dispersion does not always coincide with the stellar nucleus (see Colina et al. 2005 and references therein).

Although there have been 2D kinematical studies accomplished in ULIRGs, there is a lack of systematic analysis characterizing all the merger phases. In this Chapter, the kinematics and dynamical analysis of a representative sample of (18) ULIRGs is presented. The aim is to characterize the kinematics, masses, the role of the velocity dispersion, and the distribution of ULIRGs in the fundamental plane. Furthermore, and for the first time in this type of perturbed systems, a simple kinematic model will be fitted to the data for testing the degree of rotation at different merger phases. The Chapter is organized as follows. § 5.2 reviews a few general aspects of rotation in galaxies, including the fit of the data to a rotating disk and the dynamical mass calculations. In § 5.3 the results obtained for the kinematic in ULIRGs will be presented, whereas the fitting to the model is presented in § 5.4. The masses will be calculated in § 5.5, and in § 5.6 the fundamental plane of ULIRGs will be presented. Finally a brief summary and the main conclusions of the Chapter are given in § 5.7.

5.2 Rotation Curves in Galaxies

The rotation in galaxies was detected for the first time by Slipher (1914) and Wolf (1912), who measured inclined lines in the nuclear spectra of M31 and M81 respectively. Since then rotation curves have become very useful for studying the kinematic of galaxies, for determining the distribution of mass and for inferring the role of interactions (see a review in Sofue & Rubin 2001). In this section a simple kinematic model for disk galaxies will be discussed, and the most common deviations from the circular rotation will be presented.

5.2.1 Rotation in Disk Galaxies

Let us suppose a galaxy with a well defined thin disk with an inclination angle i with respect to the plane of the sky, and assume that the system rotates about an axis that is perpendicular to the galaxy plane which makes an angle i with the line of sight.

Then it is possible to select two different polar coordinates systems: (R, θ) , associated with the plane of the galaxy, and (ρ, ϕ) associated with the plane of the sky (see Fig. 5.1). Therefore, the radial velocity as a function of the sky coordinates is given as:

$$v_R(\rho, \phi) = V_0 + \Pi(R, \theta)\sin(\theta)\sin(i) + \Theta(R, \theta)\cos(\theta)\sin(i) + Z(R, \theta)\cos(i), \quad (5.1)$$

with $R = \rho \cos(\phi - \phi_0) / \cos\theta$ and $\tan(\theta) = \tan(\phi - \phi_0) \cdot \sec(i)$, and ϕ_0 being the PA angle of the major axis.

The different terms in Equation 5.1 are:

- V_0 , the systemic velocity.
- $\Pi(R, \theta)$, the velocity associated to movements in the radial direction.
- $\Theta(R, \theta)$, the velocity due to the movements in the tangential direction.
- $Z(R, \theta)$, the velocity in the perpendicular direction with respect to the plane.

Eq. 5.1 can be simplified assuming pure rotation ($\Pi(R, \theta) = Z(R, \theta) = 0$) and axial symmetry ($\Theta = \Theta(R)$). In this ideal example the resultant rotation curve will be like the one shown

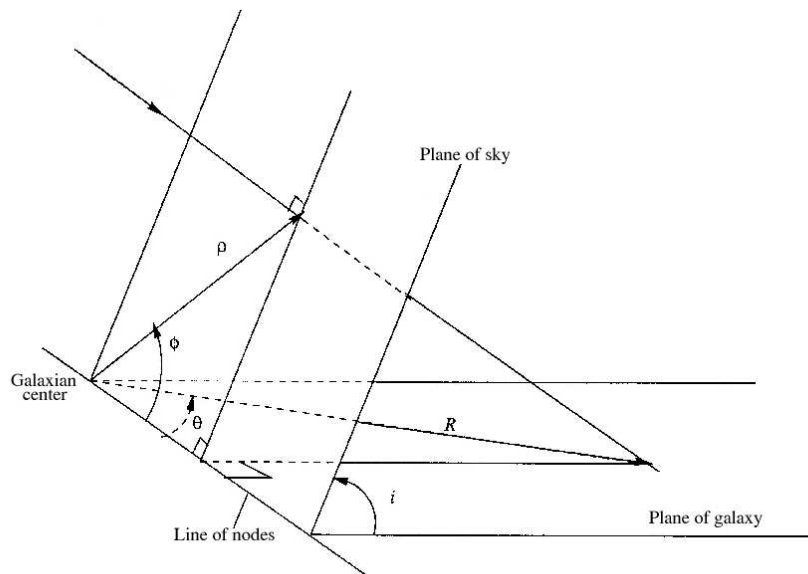


Figure 5.1: Geometric relationships of the coordinates (R, θ) in the plane of the galaxy to the coordinates (ρ, ϕ) in the plane of the sky. The galaxy is inclined at an angle i to the sky. The angles θ and ϕ are measured from the line of nodes, and the radial distances R and ρ , from the galaxy center (Mihalas & Binney 1981).

in Fig. 5.2 (*Left*), where in the inner regions the rotation velocity increases outwards. This is the so-called region of solid-body rotation, because in a spinning solid body $\Theta \propto R$. Fig. 5.2 (*Right*) shows contours of equal v_r in the plane (ρ, ϕ) for a galaxy whose rotation curve is the one in Fig. 5.2 (*Left*). In that case the major and minor axis obtained from the velocity are the same as the photometric ones. When $\Pi \neq 0 \neq Z$, it will be necessary to distinguish between the kinematic and photometric principal axes, that, in most cases, will present an offset.

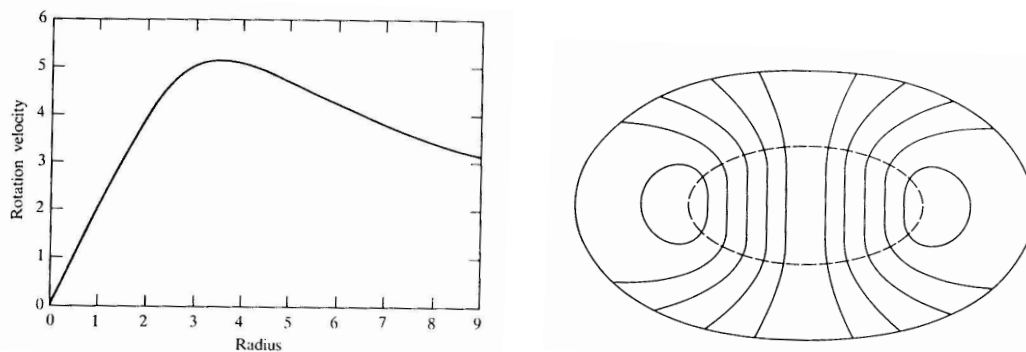


Figure 5.2: **Left:** Rotation curve model for a disk galaxy that predicts a solid rigid-like behavior for the inner parts of the galaxy. The units are arbitrary. **Right:** Isovelocity contours for a galaxy that rotates according to the model shown in the Left panel. The parallel lines are associated to the inner regions of the galaxy (Mihalas & Binney, 1981).

For further information about the rotation curves see Mihalas & Binney (1981) and the review by van der Kruit & Allen (1978).

5.2.2 Deviations from Circular Rotation

The model explained above represents an ideal situation where the material distributed in a thin disk is moving in circular orbits around the galactic center. In that configuration the kinematic axes coincide with the photometric ones. But the observed velocity fields in galaxies, even the spiral ones, tend to differ from this ideal configuration. The distortions can be divided into two categories:

- **Symmetric distortions:** They are characterized by an **s** shape in the kinematics axes. Nonetheless, the kinematic axes remain approximately perpendicular (Fig. 5.3 Left). This type of distorted velocity field may appear when the galaxy disk is warped, i.e., not plane. An approximation to this deformed disk is a galactic disc made up of tilted concentric rings (Fig. 5.3 Right). Another mechanism that leads to deviations from the ideal rotation is the presence of a bar. It may create twofold symmetric velocity fields with **s**-like isoveLOCITIES and non-symmetric kinematic axes. This is because in barred galaxies the gas follows the oval gravitational field created by the bar itself, and generate this type of distortions.

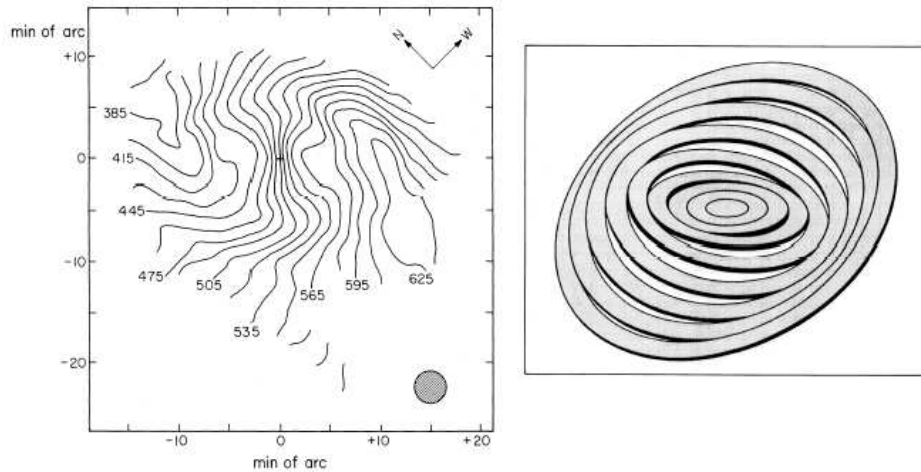


Figure 5.3: **Left:** Contours of constant H I velocity for M83. There are severe **s**-shape distortions in the kinematic principal axes, which remain approximately perpendicular. **Right:** Tilted ring model for M83. (Rogstad et al. 1974).

- **Asymmetric distortions:** Distortions without twofold rotation symmetry with respect to the galaxy center belong to this category. They can be classified in large-scale asymmetries, and small-scale disturbances and streaming motions.

Large-scale asymmetries show strong differences in the shape of the rotation curves among both extremes of the kinematics axes. Some of these asymmetries are due to tidal disturbances by interaction with a companion galaxy. This situation, that strongly evolves in time if two galaxies are merging, is characteristic of ULIRGs. Another mechanism that produces strong large scale asymmetries in the velocity field of galaxies is the presence of galactic super-winds, as proposed by Heckman, Armus & Miley (1990). The super-wind would be driven by the kinetic energy provided by supernovae and winds from massive stars in a central starburst. This energy would be released as an outflow,

heating and accelerating the gas. These outflows have been modeled with a bi-conic surface centered on the nucleus of a disk galaxy (see Fig. 5.4). In the present case this phenomena may be playing a key role, as more than 75% of ULIRGs appear to have winds (e.g., Rupke 2002, 2005; Martin 2005).

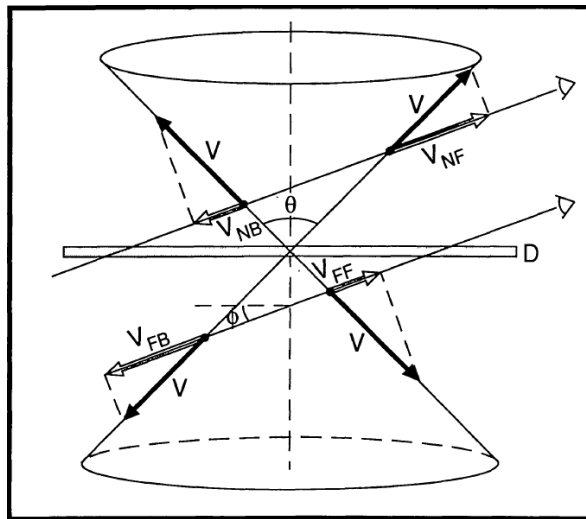


Figure 5.4: Schematic outflow along a bi-conic surface centered in the nucleus of a disk-shaped galaxy) labeled with D. The location of the observer is marked with an eyeball. The gas flows along the surface of the cone, whose opening angle is θ , with a uniform velocity v . The line of sight through the cone on the near side of the galaxy disk yields a double-peaked emission line with the gas on the front surface, producing a blue-shifted component (v_{NF}) and the gas on the back side producing a component near to the systemic velocity (v_{NB}). The line of sight through the cone on the far-side of the disk may suffer heavy obscuration by dust present in the disk. The gas on the front surface of the far-side cone will produce a component near the systemic velocity (v_{FF}), while the gas on the back surface will produce a strongly red-shifted component (v_{FB}). If the surface brightness of the gas drops rapidly as a function of distance from the nucleus, the component with velocity $v_{NB}(v_{FF})$ will be brighter than the component with $v_{NF}(v_{FB})$ (Heckman et al. 1990).

The small-scale disturbances can be detected as peculiar or even doubled valued velocity fields in some regions of the galaxy. They appear to be associated with tidal effects too. Small-scale streaming motions are produced by the gas restrain when it suffers an encounter with an spiral arm.

5.2.3 Modeling the Velocity Fields Obtained with INTEGRAL

To analyze how well a single rotating disk may reproduce the observed ionized gas ($H\alpha$ in the present case) velocity field of ULIRGs¹, the kinematic model explained in §5.2 has been fitted to the data. The process is based on iteratively fitting the model to the observed velocity field using a non-linear least-squares minimization method. It uses the robust Levenberg-Marquardt method; the main program used is the MPFIT² algorithm developed by C. Markwardt under the IDL environment.

Following the expression given by Mihalas & Binney (1981; see Eq. 5.2), and considering a pure rotating disk with axial symmetry, the expression to fit is:

¹The reader is referred to Chapter 2 for a technical explanation of two-dimensional velocity fields derived from INTEGRAL data.

²The C. Markwardt routines are available at <http://cow.physics.wics.edu/~craigm/idl/idl.htmk>.

$$v_R(\rho, \phi) = V_0 + \Theta(R)\cos(\theta)\sin(i), \quad (5.2)$$

We assume that the circular velocity at a given radius R is $\Theta(R) = \frac{2}{\pi} \cdot v_c \cdot \arctan \frac{R}{R_h}$. This empirical parametrization (Courteau 1997) has been proved to reproduce well the shape of optical rotation curves with the smallest number of free parameters (Coccatto et al. 2007). Hence the parameters that will be fitted in the program are:

- R_h : Parameter in distance that indicates the point where the rotation curves reaches its maximum.
- V_{sys} : Systemic velocity.
- i : Inclination angle, that has a global uncertainty of 180° .
- θ_0 : Position angle.
- v_c : Maximum velocity.

The rotation model has been applied to the velocity fields measured in both pre- and post-coalescence ULIRGs. Using the outputs of the fit, an ideal rotation model for the galaxy is derived and compared with the observations. In addition, the residual velocities (that is, observed-predicted velocities) will be discussed too.

5.2.4 Dynamical Mass Calculations

The difference between dynamical and stellar masses is that the first is derived taking into account the gravitational field, whereas the latter is obtained based on the integrated light assuming a mass-to-light ratio. Spiral galaxies can be modeled using a flat component for the disk and a spheroidal component for the central concentration; i.e., a de Vaucouleurs profile and a massive halo. The mass and the gravitational potential have a linear relation, therefore $M(R)$ in a spiral galaxy will have a value among the predictions of the flat and spherical models (Krumm & Salpeter 1977). Assuming a spherical distribution, the dynamical mass is given by:

$$M_{dyn} = cte \cdot \frac{RV_R^2}{G}, \quad (5.3)$$

where G is the gravitational constant, $M_{dyn}(R)$ the mass enclosed by a sphere of radius R , and cte is a value between 0.6 and 1.0, depending on the mass distribution (Lequeux 1983). Assuming $cte=1.0$, the equation with M_{dyn} in M_\odot , R in kpc and $V(R)$ in km s^{-1} is:

$$M_{dyn}(R) = 2.32 \times 10^5 RV_R^2(R), \quad (5.4)$$

If the system under analysis does not present pure rotation, this mass estimations would be a lower limit. However, in the case of ULIRGs it is not common to find pure rotation.

For spheroidal systems with none or little rotation, the mass can be derived using the virial theorem:

$$\frac{1}{2} \frac{d^2 I}{dt^2} = 2T + W, \quad (5.5)$$

where I is the inertial moment, T the kinetic energy and W the gravitational potential energy. If the system is virialized, the first member of the equation is null

$$2T = -W \longrightarrow V^2 \approx cte \frac{GM}{R} \longrightarrow M = cte \frac{V^2 R}{G}, \quad (5.6)$$

therefore, assuming that the three dimensional rms velocity V is related to the measured one-dimensional line-of-sight velocity dispersion σ by $V^2 = 3\sigma^2$, the dynamical mass of the system is given by:

$$M_{dyn} = m \cdot 10^6 R_{hm} \sigma^2 M_{\odot}, \quad (5.7)$$

where R_{hm} is the half mass radius in kpc and σ is the central velocity dispersion in km s^{-1} . The parameter m is a factor which depends on the mass distribution. Its value ranges from 1.4 for a King stellar mass distribution with a ratio tidal to core of 50, that is a good representation of elliptical galaxies (Bender et al. 1992; Tacconi et al. 2002), to 1.75 for a polytropic sphere with a density index covering a range of values (Spitzer 1987), and 2.1 for a de Vaucouleurs mass distribution (Combes et al. 1995). The parameter R_{hm} is not an observable itself, and therefore it cannot be measured directly. Thus it is inferred indirectly measuring the R_{eff} (i.e., the ratio that encloses half luminosity). When available, this has been done using the F160W-*HST* high resolution images, assuming that the near-IR continuum traces the mass. For galaxies with no near-IR F160W images available, we used the optical F814W *HST* image instead.

5.3 Kinematic Structure of the Galaxy Sample

The kinematics of the warm gas component for a sample of ULIRGs (18 systems, 9 pre- and 9 post-coalescences) is presented from Figs. 5.5 to 5.10, and summarized in Table 5.1. The velocity fields have been obtained from the $\text{H}\alpha$ emission line, except for Arp 220 whose velocity has been measured using the $[\text{N II}]\lambda 6584$ emission line, due to the complexity of the $\text{H}\alpha$ nuclear profile. In what follows, for the post-coalescence galaxies the velocity amplitude is defined as half the peak-to-peak velocity. In the case of the pre-coalescence galaxies, the velocity amplitude is defined as half the peak-to-peak velocity measured over each individual galaxy.

5.3.1 Warm Ionized Gas Velocity Fields

The overall kinematic structure of the warm gas component present large peak-to-peak velocities, of the order of hundreds of km s^{-1} , and in general is not consistent with large kpc-scale ordered motions. Only the post-coalescence galaxy IRAS 17208–0014 presents undoubted signs of rotation in a disk of about 3 kpc in size (Arribas & Colina 2003). The rest of galaxies can be separated into several categories, depending on the projected structure of their velocity fields:

- **Candidates to rotating systems**

There are structural indications for rotation in eight galaxies of the sample (4 pre- and 4 post-coalescence). The overall velocity field of the early pre-coalescence system IRAS 13156+0435 shows a high velocity merger-induced structure (of about 200 km s^{-1}) in the interface between the individual galaxies. This indicates that both galaxies are kinematically connected. Nevertheless, the velocity field of both members of

IRAS 13156+0435, along with a set of ULIRGs (IRAS 08572+3915, IRAS 18580+6527, Arp 299, Arp 220, IRAS 14060+2919, IRAS 12490–1009, and IRAS 06487+2208), show velocity gradients across the central few kpc that may be interpreted as rotation, with the photometric and kinematic axes apparently lying close in projection. This deviations from the circular rotation belongs to the asymmetric distortions category.

- **Evidence for radial flows**

Evidence for inward flows superimposed in a rotating disk has been detected in the post-coalescence galaxy IRAS 15206+3342 (Arribas & Colina 2002), along with strong outwards motions (of about 400 km s^{-1}) in the galaxies Mrk 273 and Mrk 463.

- **Galaxies with less organized structure in the velocity fields**

In some galaxies the projected velocity field is non-structured or relatively flat. This may be indicating either lack of ordered motions or high inclination angle. Galaxies with this structure are the pre-coalescence system IRAS 06268+3509, and the post-coalescence galaxies IRAS 11087+5351, and IRAS 15250+3609 (whose velocity amplitude ranges between 210 and 220 km s^{-1}).

- **Galaxies with strong tidal effects and tidal-tail stellar condensations**

Finally, and as a consequence of the tidal effects result of the ongoing merger, some post-coalescence galaxies show distorted regions, with velocity gradients of up to about $80 \text{ km s}^{-1} \text{ kpc}^{-1}$ (Arp 220, Arribas et al. 2001; Mrk 273, Colina, Arribas & Borne 1999). Furthermore, motions along extra-nuclear star-forming regions and tidal tails, including some candidates to TDGs galaxies, are detected in four pre- and one post coalescence systems (IRAS 08572+3915, IRAS 14348–1447, IRAS 16007+3743, IRAS 12112+0305, IRAS 15250+3609). Some of them present a structure in the nuclear velocity field that bear resemblance with rotation patterns. In all cases the velocity peaks ($\sim 200 \text{ km s}^{-1}$) are measured in the regions where the TDGs candidates are located (this work and Monreal-Ibero et al. 2007).

Summarizing, these results demonstrate that the merger strongly drives the kinematics. However, in a few cases large-scale (order of a few kpc) rotation-like patterns are observed. This, and the fact that they are measured in the early and late merger phases, support the results of numerical simulations. In the simulations two rotating disk galaxies interact and strongly disrupt their kinematics. Nonetheless, a reordering of the warm gas phase, and therefore rotating structures, are predicted when the disks finally coalesce (Jesseit et al. 2007).

5.3.2 Warm Ionized Gas Velocity Dispersion

The nuclear values of the velocity dispersion are shown in Table 5.1, along with the two-dimensional maps in Figs. 5.5 to 5.10. These values are large, of the order of 150 km s^{-1} . For the pre-coalescence galaxies, the nucleus with the largest σ value is the brightest near-IR (as obtained for the five systems with available *HST*/F160W image),³ or optical nucleus (as obtained from the remaining galaxies with *HST*/F814W image). However, only in three systems the σ -peak coincides with one nucleus. In the case of post-coalescence galaxies, only IRAS 17208–0014 presents spatial coincidence between the velocity dispersion

³See the light profiles in Chapter 3.

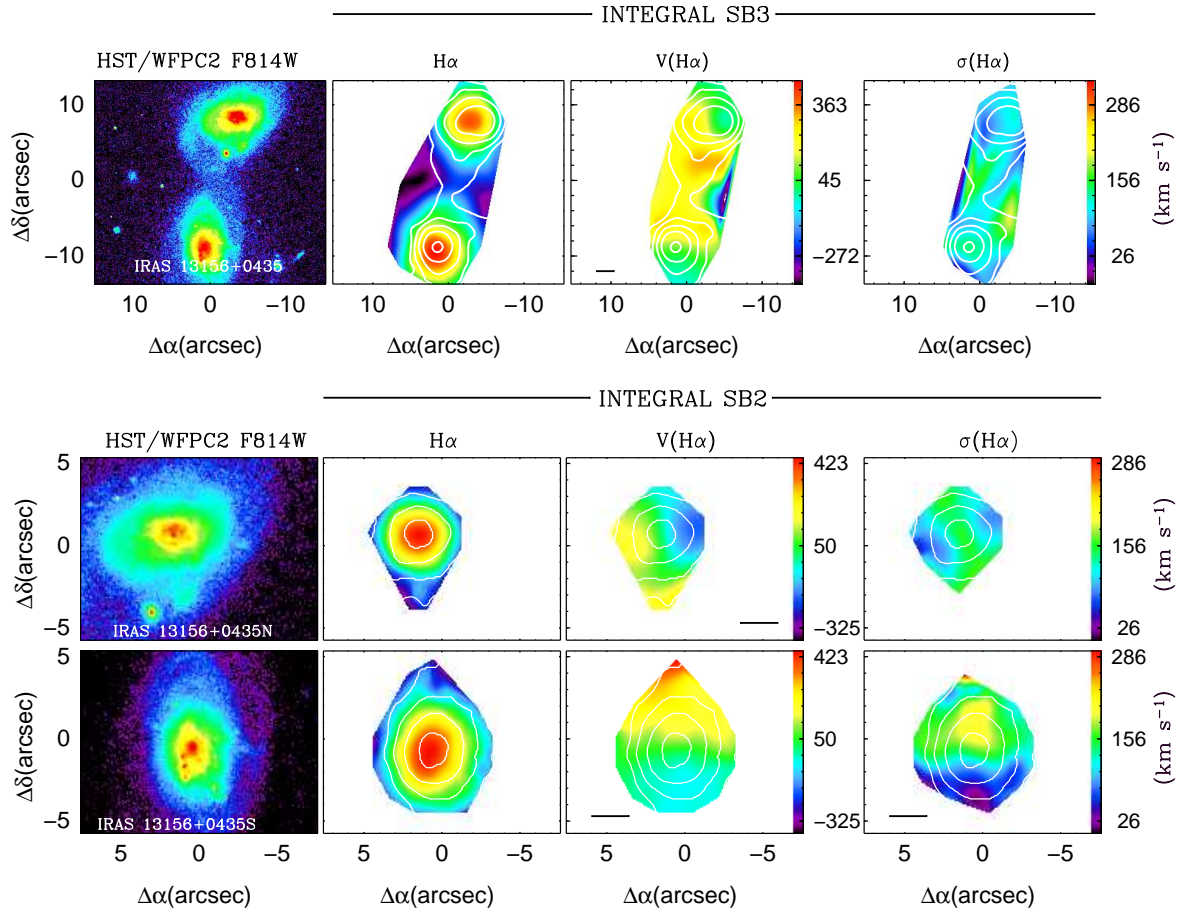


Figure 5.5: Kinematics of the pre-coalescence system IRAS 13156+0435 as observed with the SB2 and SB3 bundles. **From left to right:** The *HST* WFPC2/F814W continuum images, the morphology of the ionized gas as traced with the H α emission line, the velocity field of the ionized gas as traced with the H α line, and the velocity dispersion of the ionized gas are shown. The contours represent the red continuum. The horizontal bar indicates 5 kpc.

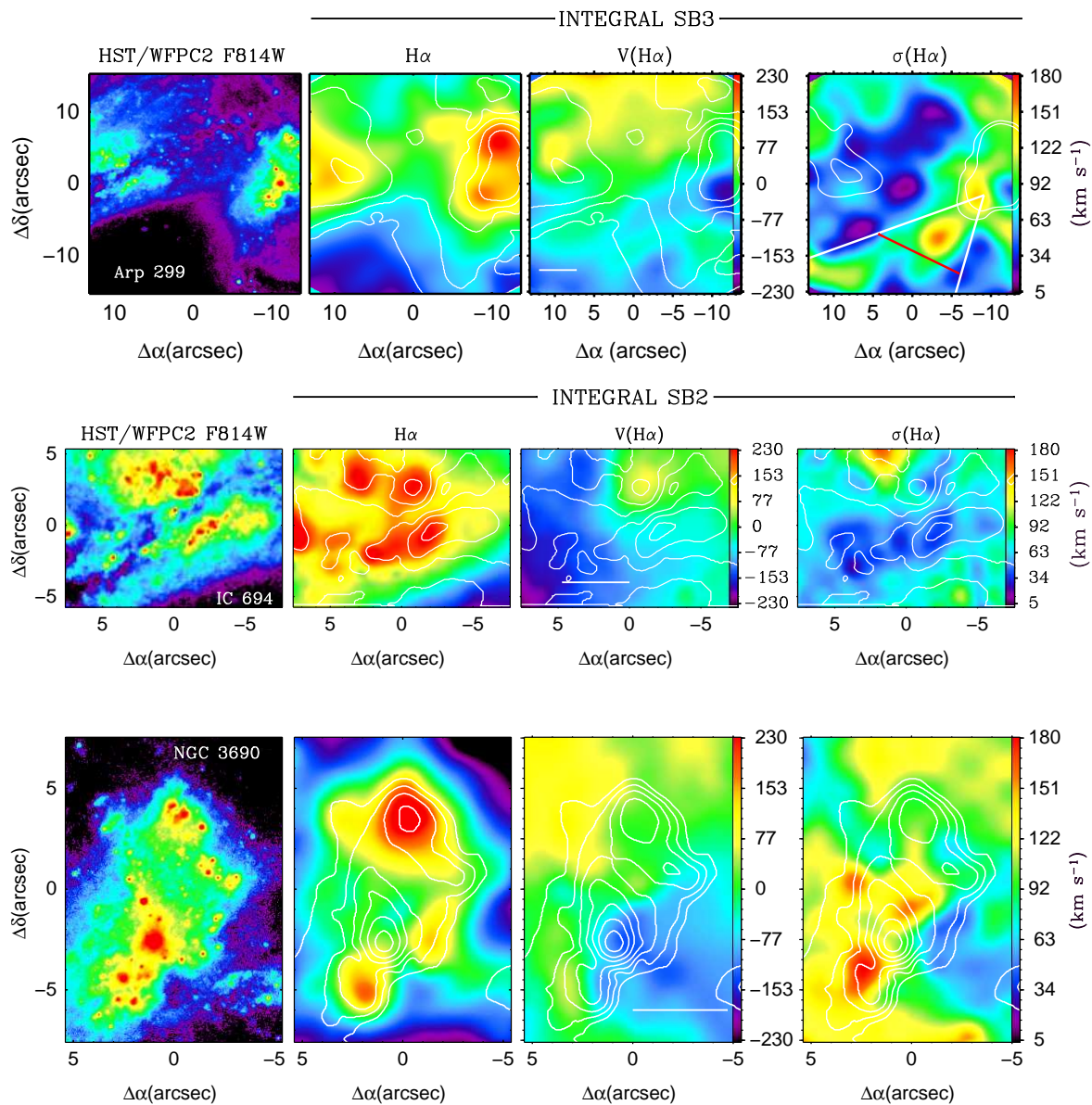


Figure 5.6: Kinematics of the pre-coalescence system Arp 299 as observed with the SB2 and SB3 bundles. **From left to right**, the *HST* WFPC2/F814W continuum images, the morphology of the ionized gas as traced with the H α emission line, the velocity field of the ionized gas as traced with the H α line and the velocity dispersion of the ionized gas are shown. The contours represent the red continuum. The horizontal bar indicates 1 kpc.

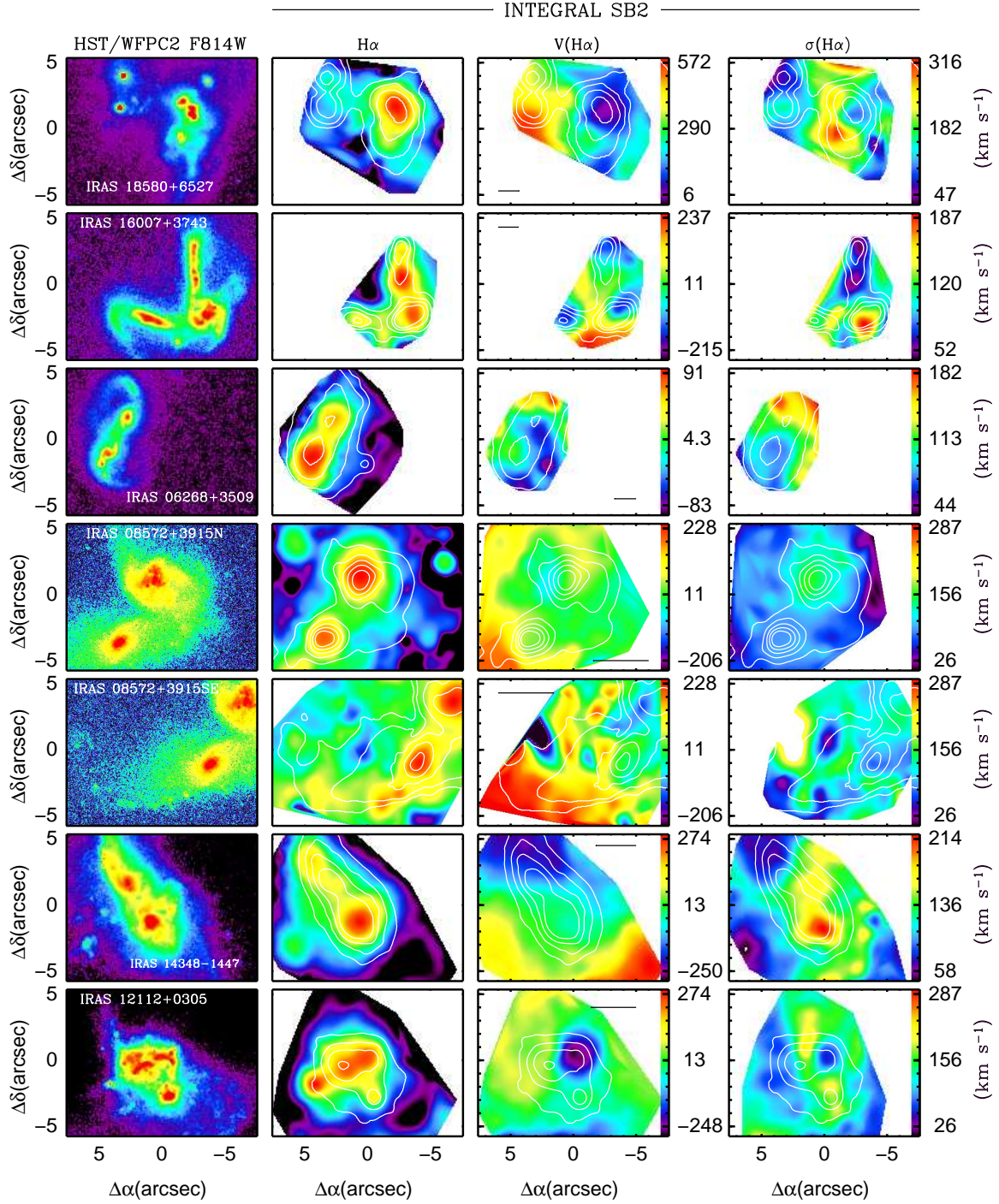


Figure 5.7: Kinematics for a set of pre-coalescence ULIRGs as observed with the SB2 bundle. **From top to bottom** the merger evolves. **From left to right** the *HST* WFPC2/F814W continuum images, the morphology of the ionized gas as traced with the H α emission line, the velocity field of the ionized gas as traced with the H α line, and the velocity dispersion of the ionized gas are shown. The horizontal bar indicates 5 kpc. The contours represent the red continuum.

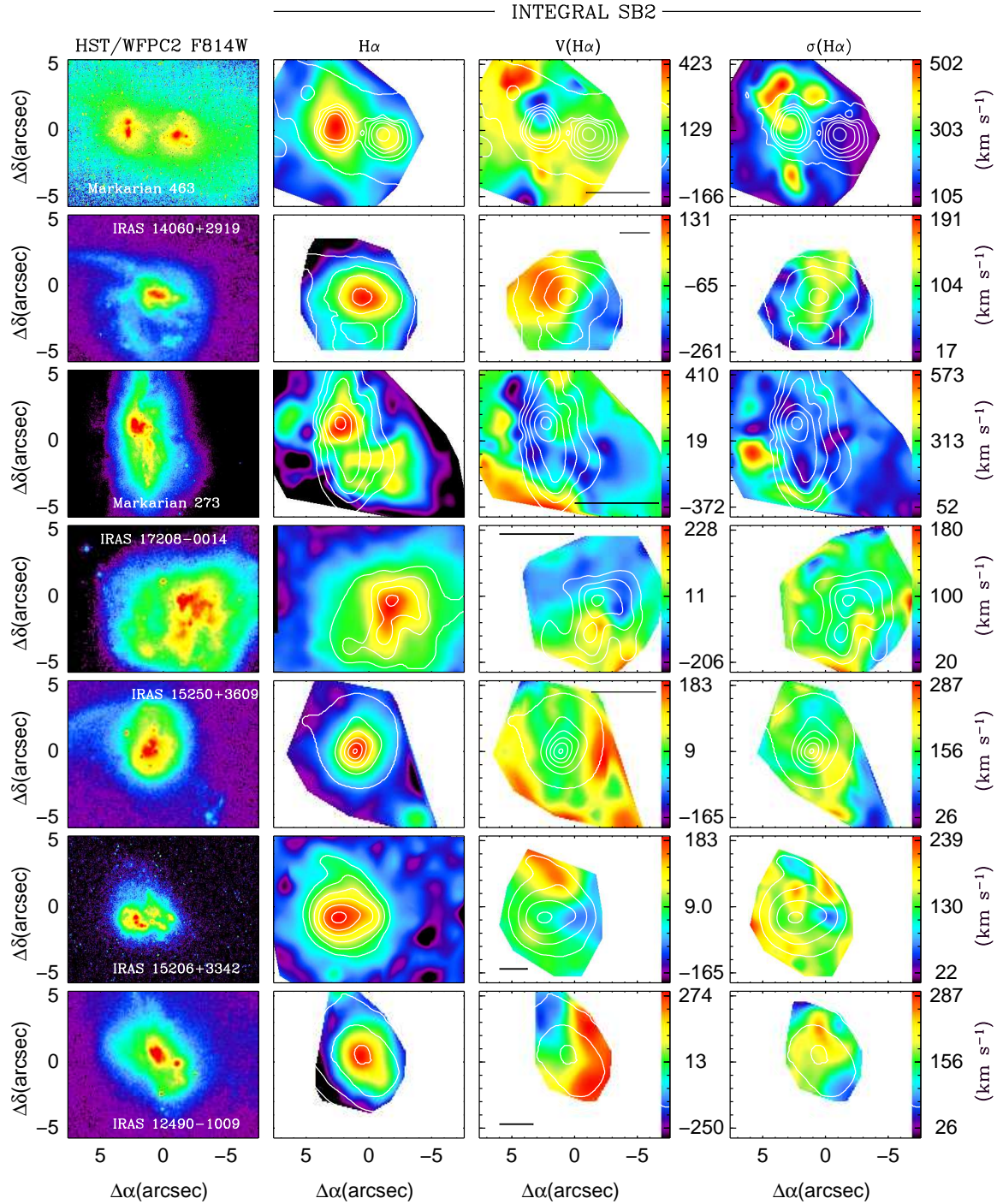


Figure 5.8: Kinematics for a set of ULIRGs as observed with the SB2 bundle. **From top to bottom**, the merger evolves. **From left to right**, the *HST* WFPC2/F814W continuum images, the morphology of the ionized gas as traced with the H α emission line, the velocity field of the ionized gas as traced with the H α line and the velocity dispersion of the ionized gas are shown. The contours represent the red continuum. The scale indicates 5 kpc. All galaxies but Mrk 463 are post-coalescence.

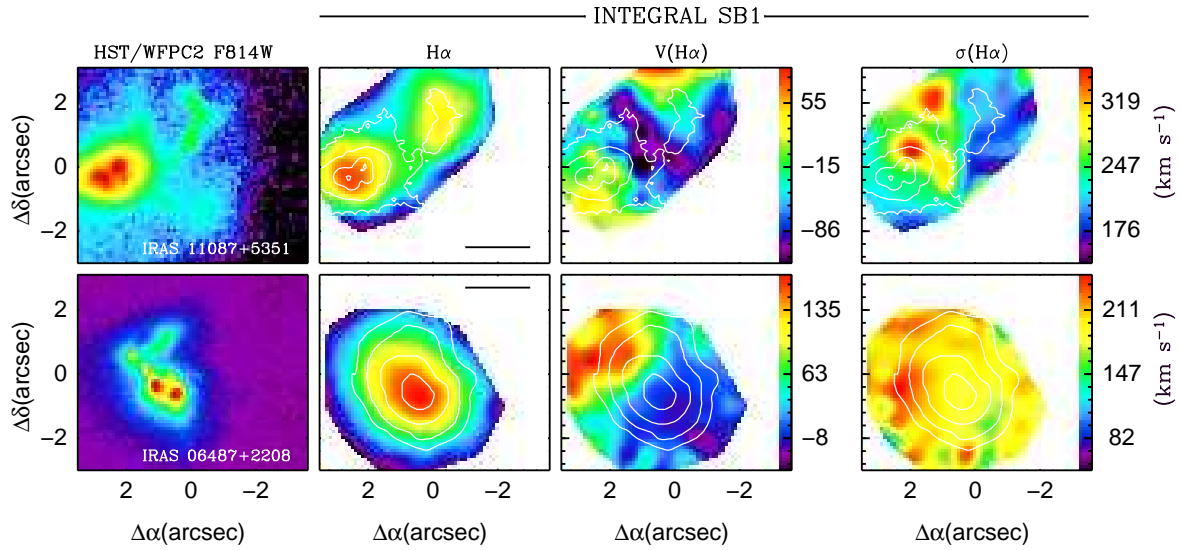


Figure 5.9: Kinematics for two post-coalescence ULIRGs as observed with the SB1 bundle. **From top to bottom**, the merger evolves. **From left to right**, the *HST* WFPC2/F814W continuum images, the morphology of the ionized gas as traced with the $H\alpha$ emission line, the velocity field of the ionized gas as traced with the $H\alpha$ line and the velocity dispersion of the ionized gas are shown. Empty boxes indicate that the information is not available. The contours represent the red continuum. The horizontal bar indicates 5 kpc.

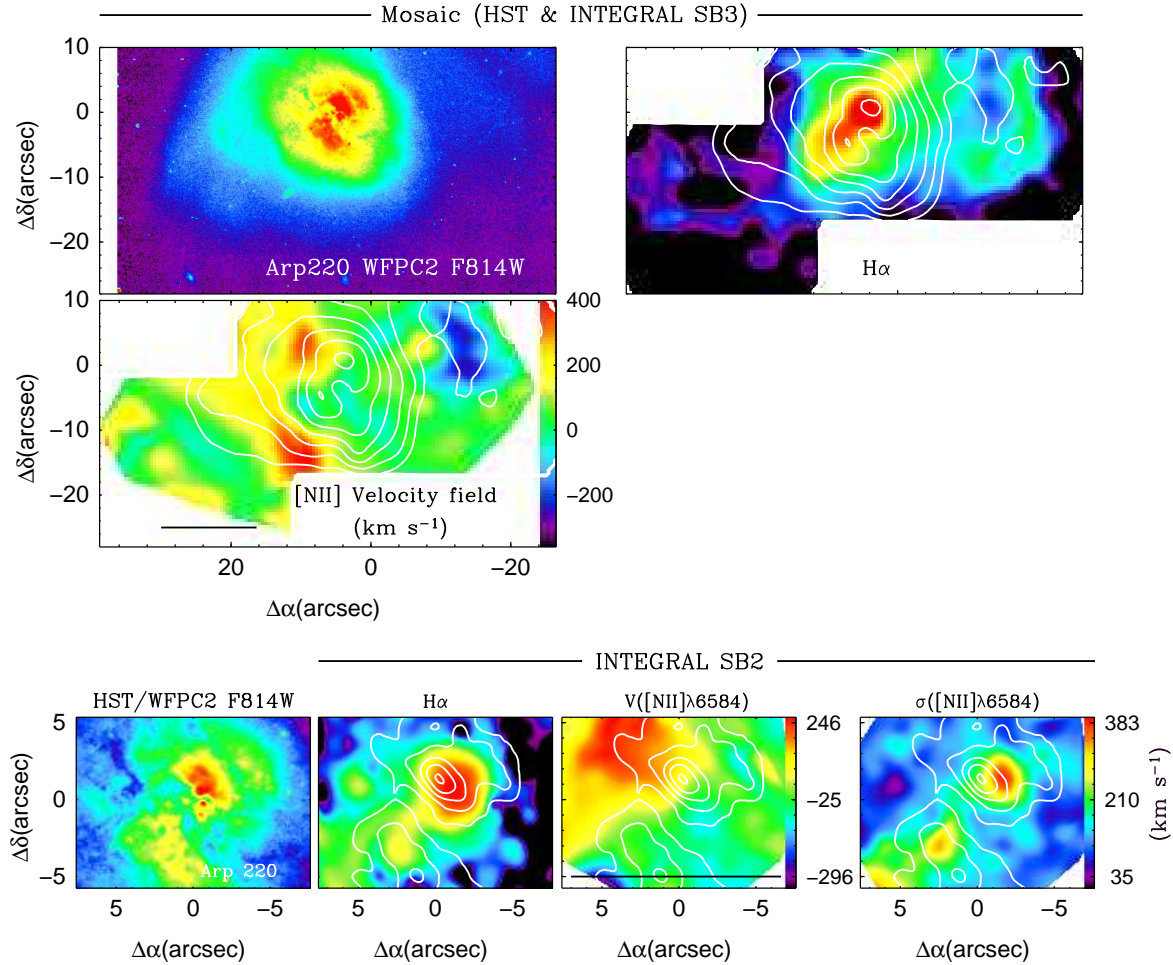


Figure 5.10: Kinematics of the post-coalescence galaxy Arp 220 as observed with the SB2 and SB3 bundles. From left to right, the *HST* WFPC2/F814W continuum images, the morphology of the ionized gas as traced with the H α emission line, the velocity field of the ionized gas as traced with the H α line and the velocity dispersion of the ionized gas are shown. The contours represent the red continuum. The horizontal bar indicates 5 kpc.

Table 5.1: Kinematic results for the sample of ULIRGs

Galaxy	v_{nuc}^{gas} (km s ⁻¹)	$\Delta(v)^{gas(1)}$ (km s ⁻¹)	σ_{nuc}^{gas} (km s ⁻¹)	$\Delta(\sigma)^{gas}$ (km s ⁻¹)	$V/\sigma^{(2)}$	σ -KC ⁽³⁾	$\Delta(\sigma$ -Nuc) ⁽⁴⁾ (kpc)	KC-Nucl ⁽⁵⁾
IRAS 13156+0435N	33875	435	152	87	1.4	No	4.9	Yes
IRAS 13156+0435S	33766	515	138	180	1.9	No	9.0	Yes
IRAS 18580+6527E	53061(†)	251	155.0	257	0.8	No	13.2	?
IRAS 18580+6527W	52614(†)	281	119.2	257	1.2	No	6.4	?
IRAS 16007+3743E	55286	422	110	151	1.9	No	11.5	?
IRAS 16007+3743W	55432	422	151	151	1.4	?	2.2	No
IRAS 06268+3509N	50854	115	128	106	0.4	No	4.1	?
IRAS 06268+3509S	50872	147	77	106	0.9	No	11.6	?
IRAS 08572+3915N	17450	140	113	100	0.6	Yes	1.2	?
IRAS 08572+3915S	17465	220	47	100	0.5	No	4.5	?
IRAS 14348-1447N	24640	208	147	176	0.7	No	7.1	?
IRAS 14348-1447S	24690	240	196	176	0.6	No	1.3	?
Arp 299 (NGC 3690)	2953	246	172	135	0.7	Yes	0.0	?
Arp 299 (IC 694)	3096	264	108	130	1.2	No	0.3	?
IRAS 12112+0305N	21930	400	130	180	1.6	No	2.4	Yes
IRAS 12112+0305S	21930	400	160	180	1.6	No	6.2	No
Mrk 463E	14956	588	179	430	1.6	No	3.4	Yes
Mrk 463W	15132	588	132	430	2.2	No	5.6	No
IRAS 06487+2208	42924	195	163	65	0.6	No	4.9	Yes
IRAS 11087+5351	42861	210	239	174	0.4	No	2.7	No
IRAS 12490-1009	30030	449	207	185	1.1	No	3.4	Yes
Mrk 273	11325	900	182	550	2.5	No	2.9	No
IRAS 14060+2919	34997	321	130	100	1.2	No	5	Yes
IRAS 15206+3342	29950	250	90	95	1.4	No	7.3	Yes
IRAS 15250+3609	16551	219	168	175	0.6	No	2.7	No
IRAS 17208-0014	12760	340	191	120	0.9	Yes	0.0	Yes
Arp 220	5400	382	185	350	1.0	?	0.5	?

Note: σ is instrumental and redshift corrected, the uncertainty is about 15%. Uncertainty in the nuclear velocity about 15 km s⁻¹ (1) Peak-to-peak velocity, (2) Velocity amplitude and nuclear velocity dispersion, (3) Do the σ peak and the kinematic center coincide?, (4) Distance between the σ peak and the nucleus, (5) Is the nucleus the kinematic center? The sign ? indicates that there are signs of rotation. All the measurements are observed values, not corrected for projection effects. The horizontal line separates pre- from post- coalescence morphological types. (†) The relative velocity between these individual galaxies (447 km s⁻¹) indicates that both galaxies may not merge.

peak and the (true) nucleus of the galaxy. For the remaining galaxies, we found spatial offsets of about 1 to 6 kpc. This general disagreement between the σ -peak and the location of the nucleus, along with the fact that in some cases σ appear to be mapping the large scales motions associated with the tidal tails, gives further confirmation to previous works. According to the literature, in general σ does not traces mass concentrations but tidal effects (e.g., Colina et al. 2005).

For the galaxies of the sample the V/σ parameter⁴ ranges from about 0.4 to 2.5. This means that ULIRGs cover a wide range of dynamical stages: from galaxies (40%) are consistent with pressure dominated galaxies with the presence of random motions (e.g., IRAS 06268+3509, IRAS 08572+3915, IRAS 11087+5351), to galaxies (60%) where the velocity amplitude appears to dominate (IRAS 13156+0435, IRAS 16007+3753, IRAS 12490-1009, and IRAS 15206+3342). The general structure of the velocity fields, and the kinematics characteristics of the gas in the extra-nuclear regions, support the idea that this velocity is mainly

⁴A discussion of this parameter can be found in Chapter 3.

merger-induced rather than associated to pure rotation.

5.4 Degree of Rotation

The analysis of the ionized gas velocity fields in §5.3.1 has shown that although in some cases we find hints for rotation, the projected velocity fields of the sample are rather complex, and in several occasions they are driven by tidal effects. That is, the two-dimensional velocity dispersion is in general unlikely to be interpreted as pure rotation. Nonetheless, it is worth to analyze whether ULIRGs show hints for rotation or not.

In this section, the degree of rotation in ULIRGs at different merger phases will be studied. To that aim, as a first order approximation, the data have been fitted to the two dimensional velocity model presented in §5.2.3. For the pre-coalescence galaxies (except for IRAS 13156+0435) the velocity fields have been divided into two sections, each one associated with one galaxy of the system. Given their complex structure, this separation is necessary for tracing the possible rotation in the central parts. The structure of the individual galaxies were separated using the surface brightness distribution. For the post-coalescence objects, the entire velocity field has been fitted. The analysis has been accomplished in all galaxies with the observed two-dimensional velocity field, except Mrk 463 and IRAS 11087+5351. In those cases the model did not converge, and the derived results were not realistic.

5.4.1 Simple Rotation Curves Modeled from the Velocity Fields

Under the considerations explained above, Eq. 5.2 is solved for each galaxy by fixing the rotating center in the photometric nucleus, except for IRAS 17208–0014 and NGC 3690 (western component of Arp 299). In those cases it has been fixed $1''.5$ and $3''.0$ away from the optical nucleus respectively.

The outputs of the models are detailed in Table 5.2. The parameter R_h indicates the distance from the kinematic center to the point where the galaxy reaches its maximum velocity. For the studied galaxies R_h ranges from 0.4 to 17.5 kpc, values which in general agree with the range covered by rotating spiral galaxies observed in the optical range (2-10 kpc Mihalas & Binney 1981). Only three galaxies show significant deviations: IRAS 18580+6527W, IRAS 12112+0305 and IRAS 17208–0014. In the first two cases (pre-coalescence galaxies) we are probably not tracing the rotation, mostly because of the influence of the low-surface tidally induced structures. For IRAS 17208–0014 the R_h value (0.4 kpc) is very small, but consistent with the size of the rotating disk that we are apparently tracing (~ 3.0 kpc; Arribas & Colina 2003).

The predicted systemic velocity has been compared with the measured nuclear one (Fig. 5.11 Left). The differences are distributed into two regimes: variations of $\pm 30 \text{ km s}^{-1}$, measured in about 40% of cases, or larger. In general, it appears that the agreement is better in the pre-coalescence systems. Another parameter that can be compared with the models is the velocity amplitude measured from IFS vs. the maximum velocity modeled (v_p , column 7 Table 5.2); this ratio has a mean value of 1.0 ± 0.5 (1.0 means agreement). Only a few galaxies deviate significantly from this trend: (i) Mrk 273, that has an extremely perturbed velocity field non-consistent with rotation (ii) IRAS 17208–0014, which has clear rotation, but restricted to the central kpc, and (iii) Arp 220, whose asymmetric distortions due to the merger are very strong.

Table 5.2: Parameters derived from the velocity field model

Galaxy	Rh (kpc)	V _{sys} (km/s)	<i>i</i> (degree)	PA (degree)	$v_p^{(1)}$ (km/s)	$(\Delta(v)^{gas}/2)/v_p^{(2)}$
IRAS 13156+0435N	8.7	33891	52.0	121	371	0.6
IRAS 13156+0435S	9.8	33782	59.0	4	256	1.0
IRAS 18580+6527E	3.1	53045	40.0	12	180	0.7
IRAS 18580+6527W	17.5	52670	80.0	176	196	0.7
IRAS 16007+3743E	3.9	55380	68.0	54	400	0.5
IRAS 16007+3743W	6.6	55414	34.0	126	164	1.3
IRAS 06268+3509N	11.6	50827	51.0	3	97	0.6
IRAS 06268+3509S	3.2	50860	31.0	59	63	1.2
IRAS 08572+3915N	10.1	17493	77.0	89	190	0.4
IRAS 08572+3915S	3.9	17536	55.0	108	112	1.0
IRAS 14348–1447N	4.4	24630	21.0	6	109	0.9
IRAS 14348–1447S	3.1	24760	13.0	144	74	1.6
Arp 299(NGC 3690)	1.5	3024	53.0	57	129	0.9
Arp 299(IC 694)	2.2	3040	61.0	88	132	1.0
IRAS 12112+0305	0.6	21925	25.0	90	65	1.5
IRAS 06487+2208	7.0	42946	74.0	51	202	0.5
IRAS 12490–1009	7.3	30071	67.0	67	460	0.5
Mrk 273	3.0	11238	8.0	83	40	11.5
IRAS 14060+2919	4.5	34952	43.0	67	168	0.95
IRAS 15206+3342	4.5	30015	18.0	89	71	1.8
IRAS 15250+3609	7.8	16606	74.0	90	180	0.6
IRAS 17208–0014	0.4	12770	9.6	148	50	3.4
Arp 220	1.2	5443	28.0	62	62	3.1

Notes: ⁽¹⁾ Projected absolute velocity value, ⁽²⁾ observed velocity amplitude compared with the modeled projected absolute velocity value. The horizontal line separates morphological types.

Another interesting parameter derived from the models is the inclination angle (*i*). It can be compared with the observed inclination angle *i*, derived using the major and minor axes derived from the fitting to ellipses⁵, and assuming a thin disk. The comparison shows, in general, no good correlation (see Fig. 5.11 Center). These differences may be due either to the intrinsic variations in the measurements of the major and minor axis in this merger systems, or to symmetric distortions that may be present in the galaxies but are not considered in this model.

Finally, the position angle (PA) of the photometric⁶ and kinematic major axes has been studied too (see Fig. 5.11 Right). We conclude that in general the photometric and kinematic PA do not coincide in ULIRGs. Nonetheless, for the galaxies classified as candidates to rotating systems, the photometric and kinematic axes are in general in good agreement (except Arp 220), that is, distributed in the range 15 ± 10 degree. IRAS 17208–0014, which shows clear central rotation, has a difference in the PA of about 50° . In spite of its nuclear ordered motion, the galaxy as a whole show no clear hints for rotation.

This results confirm that, as expected, ULIRGs are not pure rotating systems. The question to solve now is how consistent are the velocity fields with rotation (the so-called rotation degree), and whether or not rotation is mixed with more perturbed motions. To that

⁵ $i = \cos^{-1}(b/a)$, were *a* and *b* are the major and minor axis of the ellipse fitted at the same distance covered by the galaxies. See a detailed description is given in Chapter 3.

⁶Derived from the ellipses fitting described in Chapter 3.

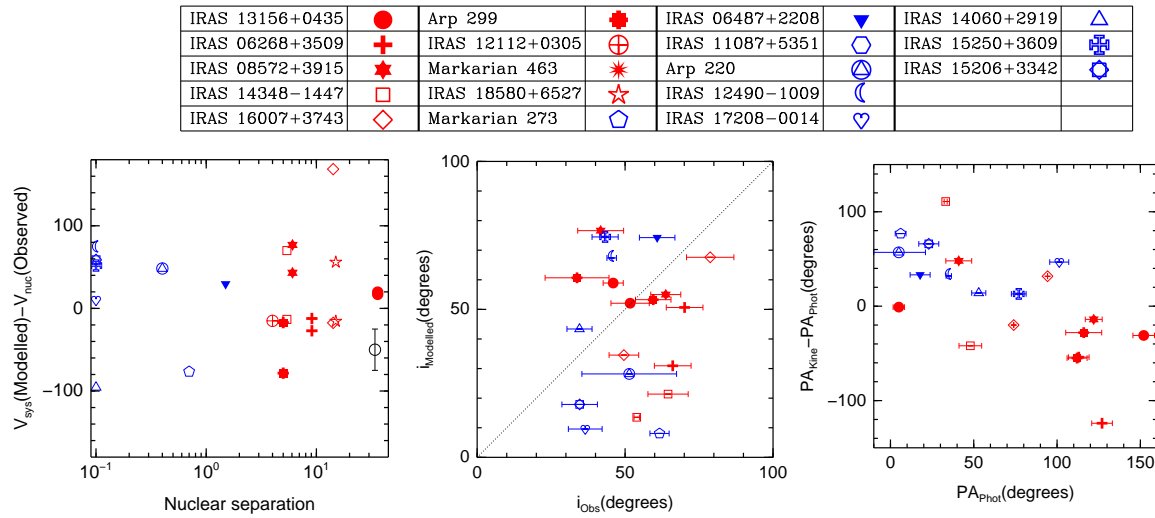


Figure 5.11: **Left:** Comparison between the observed nuclear and predicted systemic velocities. The x axis indicates, when appropriate, the nuclear separation in kpc and logarithmic scale. The single nucleus galaxies are located in 10^{-1} . **Center:** Comparison between measured and predicted inclination. **Right:** Comparison between measured and predicted PA. The photometric PA has an average uncertainty of about 10° , because of the presence of tails and disordered structures that may produce strong variations in the ellipse position.

aim the parameters derived from the fitting to the model have been used to reconstruct the two-dimensional rotation curve (from Figs. 5.13 to 5.15). The galaxies that were previously classified as candidates to rotating systems show two-dimensional velocity fields with amplitudes consistent with the observed ones. Their residual (observed-predicted) velocities tend to trace the structures created by the merger (such as bridges, interfaces or tidal tails), with values of up to 400 km s^{-1} at distances of up to 6-7 kpc from the nucleus. This demonstrates that the gas kinematics is strongly driven by the tidal effect, flows or tidal tail condensations. In spite of this, in the nuclear regions (and at distances of up to 6-7 kpc) the differences between the observed and modeled velocity fields. In some cases (like Arp 299) the residual structure actually traces the velocity field, meaning that the degree of rotation is low.

The quality of the fits can be evaluated defined the effective residual parameter, normalized to the observed peak-to-peak velocity. It is calculated measuring the two-dimensional residual velocities that are then normalized to the observed velocity amplitude. Finally, the mean value is represented using the standard deviation as the error. An effective residual equal to zero indicates a total correspondence between observation and model (see Fig 5.16 Left). The mean effective residual for the pre- and post-coalescence galaxies is about 0.4 ± 0.1 , and 0.3 ± 0.1 , respectively (when the pre-coalescence systems are treated as two individual ones). Further support to this is given by the rms of the two-dimensional velocity models (Fig. 5.16, Right). In this case, although the average rms are similar, the pre-coalescence galaxies present slightly larger values due to the strong influence of the merger that makes the low-surface brightness regions non consistent with rotation.

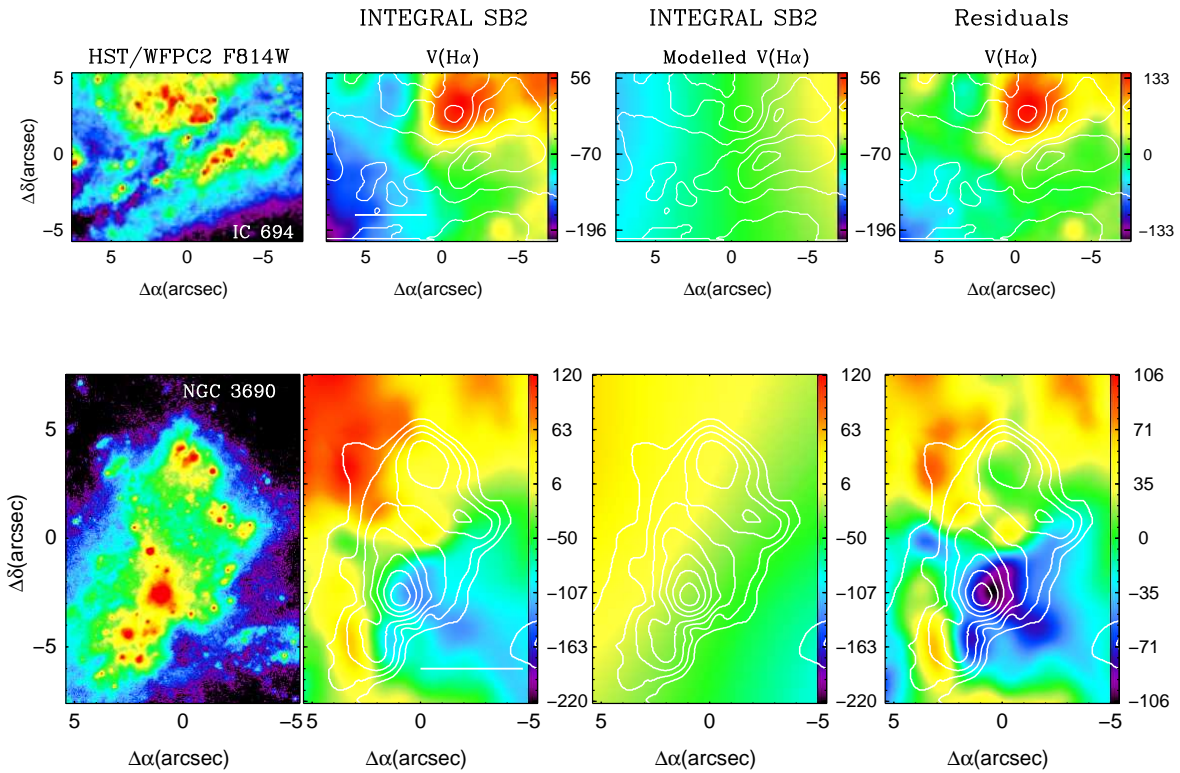


Figure 5.12: Observed and modeled velocity fields (units of km s^{-1}) for Arp 299 as observed with the SB2 bundle. **From left to right**, the *HST* WFPC2/F814W continuum images, the observed velocity field of the ionized gas as traced with the $H\alpha$ line, predicted velocity field of the ionized gas for a rotating disk, and the residual velocities (i.e., observed-predicted). The velocity is referred to the nucleus. This system is in the pre-coalescence phase. The scale indicates 1 kpc.

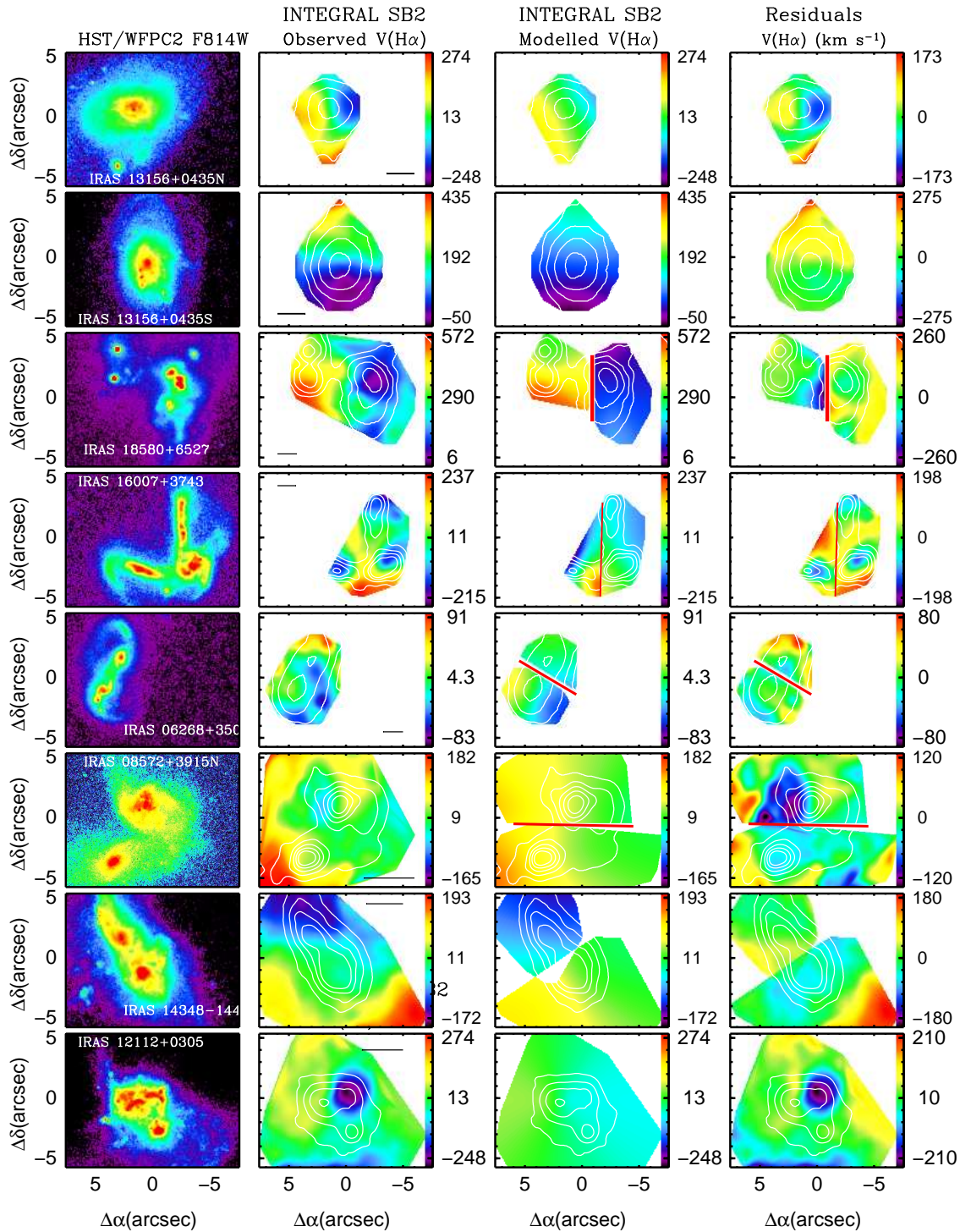


Figure 5.13: Observed and modeled velocity fields for a set of ULIRGs as observed with the SB2 bundle. **From top to bottom**, the merger evolves. **From left to right**, the *HST* WFPC2/F814W continuum images, the observed velocity field of the ionized gas as traced with the $H\alpha$ line, predicted velocity field of the ionized gas for a rotating disk, and the residual velocities (i.e., observed-predicted). The velocity is referred to the nucleus. The red line overlaid on several velocity field marks the separation done to distinguish (and independently fit) the field of each component of the system. These galaxies are in the pre-coalescence phase. The scale indicates 5 kpc.

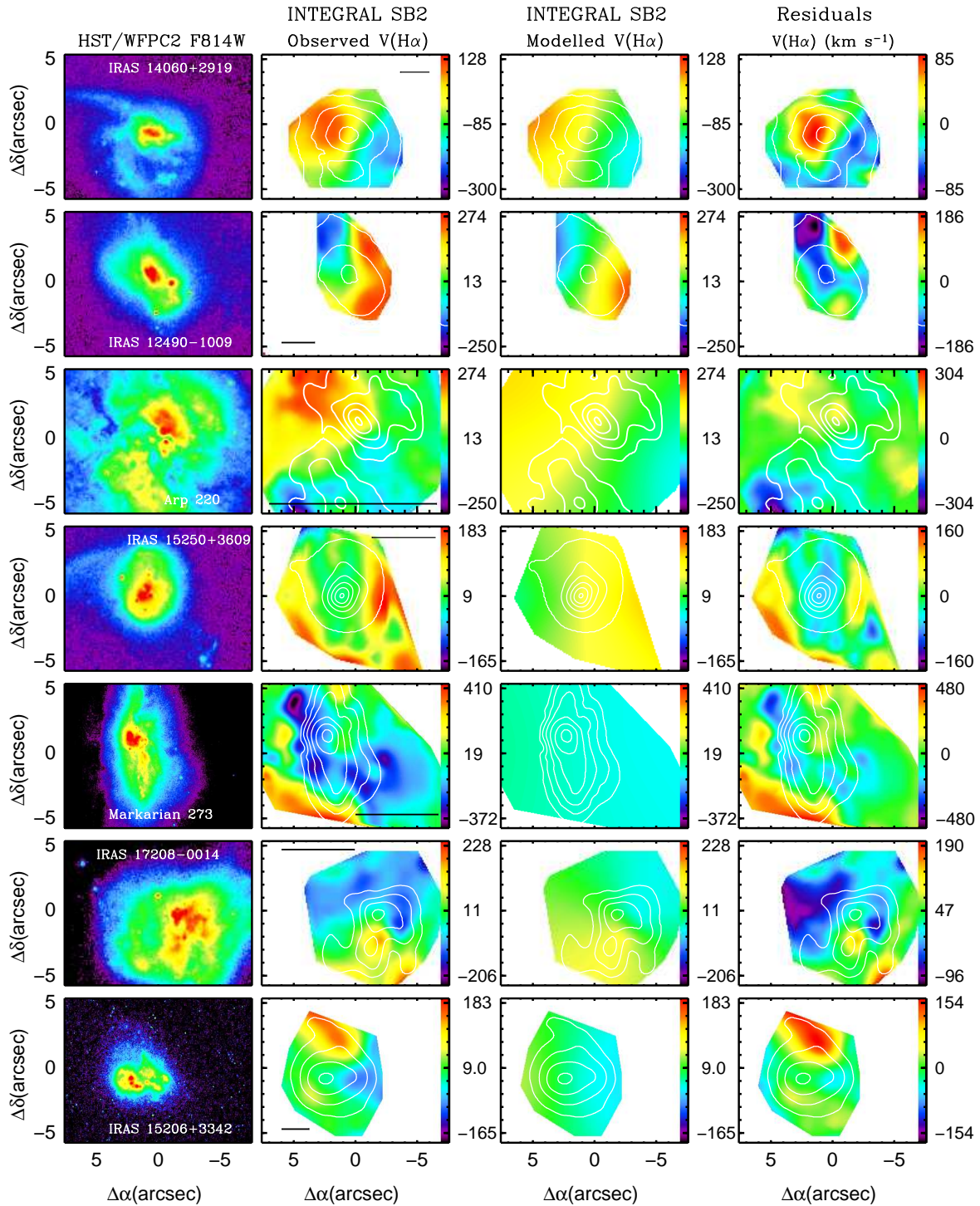


Figure 5.14: Observed and modeled velocity fields for a set of ULIRGs as observed with the SB2 bundle. **From top to bottom**, the merger evolves. **From left to right**, the *HST* WFPC2/F814W continuum images, the observed velocity field of the ionized gas as traced with the $H\alpha$ line, predicted velocity field of the ionized gas for a rotating disk, and the residual velocities (i.e., observed-predicted). The velocity is referred to the nucleus. The galaxy is in post-coalescence. The scale indicates 5 kpc.

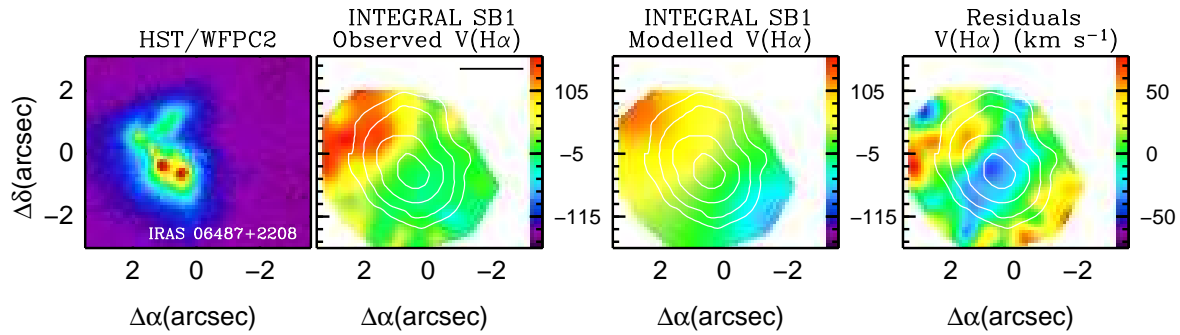


Figure 5.15: Observed and modeled velocity fields for IRAS 06487+2208 as observed with the SB1 bundle. **From left to right**, the *HST* WFPC2/F814W continuum images, the observed velocity field of the ionized gas as traced with the $H\alpha$ line, predicted velocity field of the ionized gas for a rotating disk, and the residual velocities (i.e., observed–predicted). The velocity is referred to the nucleus. Galaxies are in post-coalescence phase. The scale indicates 5 kpc.

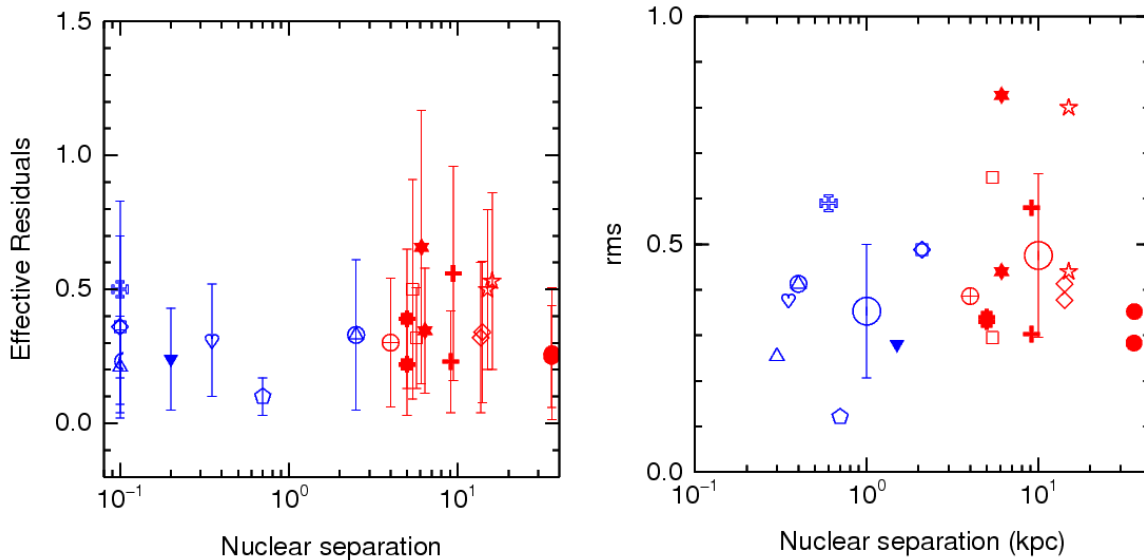


Figure 5.16: **Left:** Effective residuals represented versus the nuclear separation on the galaxies. The residuals are normalized to the velocity amplitude. Zero indicates total correspondence. **Right:** rms of the residual velocities. The large empty circles indicate average values. Galaxy symbols as in Fig. 5.11

In summary, the fit of the observed ionized gas velocity fields to a simple rotating disk demonstrates that the *global velocity field* in ULIRGs is in general not consistent with pure rotation. In any case, indications for ordered motions are detected in early pre-coalescence systems and some post-coalescence galaxies (IRAS 13156+0435, IRAS 14060+2919, IRAS 12490–1009 and IRAS 06487+2208). This is indicated by the velocity amplitude, the inclination, and the good correlation between the photometric and kinematic position angle, that point towards some degree of rotation in the galaxies. The quality of this results may improve using different strategies: (1) to observe larger FOV, that may cover all that ionized gas structures and provides a global view of the velocity field. (2) To improve the kinematic model including, for example, concentric rings to trace the symmetric distortions (i.e., warped structures), and to include rotation+flows. And (3) To analyze the stellar 2D velocity fields.

5.5 Mass Derivation

The galaxy masses have been obtained using two different approaches: (i) Provided virialization applies, to derive the dynamical mass (M_{dyn}) using the nuclear velocity dispersion, the effective radius⁷ and the polytropic sphere constant applying Eq. 5.7. To that aim the stellar kinematics is in principle preferable, but in the case of ULIRGs it has been demonstrated that the nuclear warm gas velocity dispersion is a good mass tracer (Colina et al. 2005). (ii) To derive the mass from the modeled velocity amplitude, within the radius from the pure rotating disk predicted for each single galaxy.

The dynamical mass has values of the order (or slightly lower) than m_* (see Table 5.3). The most relevant aspect of the derived masses of the individual galaxies (i.e. two galaxies for each pre-coalescence system and one for the post-coalescence) is their distribution. As shown in Fig. 5.17, 75% of the 27 analyzed galaxies have masses $\leq m_*$. This result, derived here for a representative sample of ULIRGs, is consistent with those of Colina et al. (2001; 2005) and Genzel et al. (2001). Considering the uncertainties in the assuming mass distribution (that is, a polytropic sphere), in the effective radius derivation and in σ , the dynamical mass in ULIRGs can be estimated with an uncertainty of about 40%-50%. The dynamical mass ratio of the galaxies forming pre-coalescence systems fall between about 1 and 2 (i.e. major mergers) in 78% of galaxies, whereas the system IRAS 08572+3915 appear to be a minor merger with a mass ratio of 5:1. These results are consistent with the mass relations derived in Chapter 3, and gives further support to the scenario where two intermediate mass disk galaxies are the progenitors of ULIRGs.

Assuming rotation, the velocity amplitude derived from the model can be used to derive an upper limit to the rotating mass in the sample of ULIRGs. As shown in Table 5.3 the average upper limit to the rotating mass is $1.0 \pm 1.1 \times 10^{11} M_\odot$ and $0.9 \pm 1.3 \times 10^{11} M_\odot$ for the pre- and post-coalescence ULIRGs of the sample. These upper limits tend to be of the order of M_{dyn} . The comparison between the dynamical mass and the upper mass limit obtained from the modeled velocity amplitude show that in 15% of the pre-coalescence galaxies the masses are inconsistent, 15% are in the confidence limit (establishing a factor two of confidence, taking into account the uncertainties involved), 36% are consistent, and 34%

⁷The reader is referred to Chapter 3 for a detailed discussion of σ and R_{eff} measurements, and a comparison with literature.

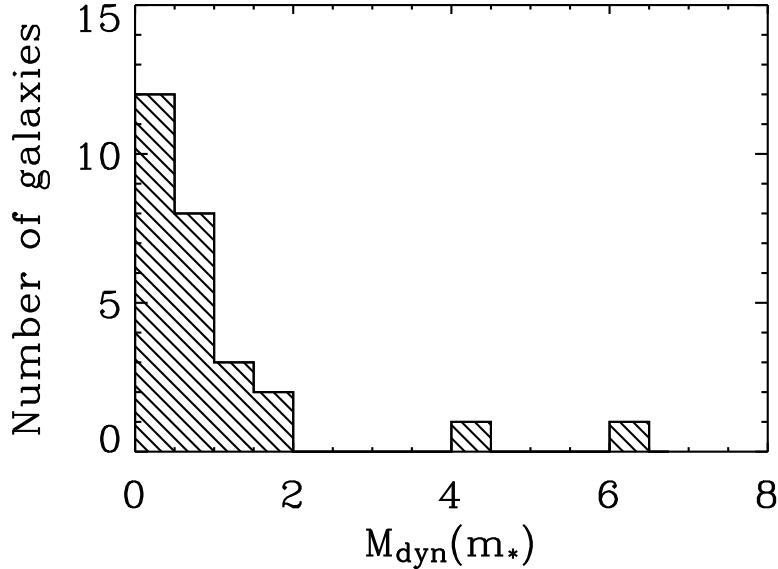


Figure 5.17: Dynamical mass histogram for ULIRGs. Here 27 individual galaxies are represented. The pre-coalescence systems are divided into two galaxies ($m_*=1.4\times 10^{11}M_{\odot}$).

present larger dynamical mass. There is one case (IRAS 12112+0305) where the difference is 16 times. This can be explained because the kinematic model is not accurate enough. On the contrary the mass ratio on the post-coalescence systems are consistent in about 90% of cases. This mass calculations point towards the idea of post-coalescence ULIRGs more consistent with rotation.

5.6 The Location of ULIRGs in the Fundamental Plane

The fundamental plane of the elliptical galaxies (FP; see Fig. 5.18) was discovered independent and simultaneously by Djorgovski & Davis (1987) and Dressler et al. (1987). It is the parameter space defined by the effective radius, the velocity dispersion, and the surface brightness, and the obtained relation is linear in a logarithmic space. Some authors give further support to the “ellipticals in formation” scenario by comparing the distribution of ULIRGs and ellipticals in the FP (e.g., Genzel et al. 2001; Dasyra et al. 2006 and references therein). The distribution of pre- and post-coalescence ULIRGs in this 3D space of parameter is presented in Fig. 5.18 (Upper Row). In a qualitative way, both morphological types populate this 3D space in a different way. The pre-coalescence systems appear to be more clustered and disordered, and the post-coalescences appear to follow a linear-like behavior. A quantitative comparison is derived using the three projections of the fundamental plane (see Fig. 5.18 Lower row) and deriving the correlation parameter R . From that analysis we conclude that in all three planes the post-coalescence ULIRGs have a better correlation, and that both morphological types undergo different dynamical phases. This makes us compare the distribution of the post-coalescence ULIRGs and elliptical galaxies in the FP. This comparison (with the H-band FP) is presented in 5.19, by overplotting our data over the Dasyra

Table 5.3: Mass calculations for the sample of ULIRGs

Galaxy	Rh (kpc)	Vc (km/s)	$M_{VelAmpl}$ ($\times 10^{11} M_{\odot}$)	$R_{eff}(F814W)$ (kpc)	$R_{eff}(F160W)$ (kpc)	M_{dyn} ($\times 10^{11} M_{\odot}$)	$M_{dyn}/M_{VelAmpl}$
IRAS 13156+0435N	8.7	471	4.5	5.9±1.2	–	2.4±0.5	0.5
IRAS 13156+0435S	9.8	299	2.0	4.9±1.0	–	1.6±0.3	0.8
IRAS 18580+6527E	3.1	279	0.6	6.5±1.0	–	2.7±0.4	–
IRAS 18580+6527W	17.5	199	1.6	4.3±1.0	–	1.1±0.2	0.7
IRAS 16007+3743E	3.9	432	1.7	4.0±0.8	–	0.8±0.2	0.5
IRAS 16007+3743W	6.6	293	1.3	4.2±0.8	–	1.7±0.3	1.3
IRAS 06268+3509N	11.6	125	0.4	2.0±0.4	2.1±0.4	0.6±0.1	1.5
IRAS 06268+3509S	3.2	122	0.1	1.5±0.5	1.1±0.5	0.11±0.05	1.0
IRAS 08572+3915N	10.1	194	0.9	2.8±2.0	0.6±2.0	0.1±0.4	0.1
IRAS 08572+3915S	3.9	137	0.2	1.4±0.9	0.6±0.9	0.02±0.03	0.1
IRAS 14348–1447N	4.4	305	0.9	1.4±0.3	1.5±0.3	0.6±0.1	0.6
IRAS 14348–1447S	3.1	331	0.8	3.0±2.0	1.3±1.5	0.8±1.0	1.0
Arp 299(NGC 3690)	1.5	162	0.1	1.2±0.2	–	0.6±0.1	6.0
Arp 299(IC 694)	2.2	151	0.1	2.0±1.5	0.4±0.1	0.4±0.3	4.0
IRAS 12112+0305N	0.6	154	0.03	2.0±0.3	1.7±0.3	0.5±0.1	16.6
IRAS 12112+0305S	–	–	–	1.5±1.0	1.1±0.5	0.5±0.1	–
Mrk 463-E	–	–	–	1.0±0.6	0.2±0.8	0.6±0.1	–
Mrk 463-W	–	–	–	1.0±0.2	1.0±0.2	0.3±0.1	–
IRAS 06487+2208	7.0	210	0.7	1.5±0.3	–	0.7±0.1	1.0
IRAS 11087+5351	–	–	–	8.9±1.8	–	8.8±1.8	–
IRAS 12490–1009	7.3	501	4.2	7.6±1.5	–	5.7±1.1	1.3
Mrk 273	3.0	287	0.6	4.4±3.0	2.0±2.6	1.1±1.5	1.8
IRAS 14060+2919	4.5	247	0.6	4.8±1.5	–	1.4±0.4	2.3
IRAS 15206+3342	4.5	229	0.5	2.9±0.5	–	0.4±0.1	0.8
IRAS 15250+3609	7.8	187	0.6	1.9±1.2	1.4±0.7	0.7±0.3	1.2
IRAS 17208–0014	0.4	300	0.1	3.2±2.0	1.5±1.7	0.9±1.0	9.0
Arp 220	1.2	345	0.3	4.3±3.5	1.2±4.1	0.7±2.4	2.3

Note: The dynamical mass has been derived using, when available, the R_{eff} for the F160W filter. For the system Arp 299 we have used R_{eff} as derived from the F814W filter, as we do not have the near-IR effective radius for both components of the system. For the system Arp 299 the optical R_{eff} has been used, as the near-IR effective radius is not available for both components of the system.

et al. (2006) graphic. This must be done taking into account the different origin of the σ value (warm ionized gas vs. stellar) and the bands used in the observations (observed optical vs. near-IR from the literature). The comparison between σ was accomplished in Table 3.6, with the conclusion that the stellar and warm gas σ as observed in the optical and near-IR are of the same order (variations of $\sim 16\%$). For the effective radius the uncertainties are about 25% (see Table and § 3.5.2). Finally, the surface brightness derived from the optical can be corrected using the F814W–F160W color derived in Chapter 3. For the galaxies with available information, the observed mean color corrections have been applied (blue empty symbols in 5.19). The remaining galaxies have been corrected using an average (2.5 magnitudes) color (blue filled symbols in 5.19). ULIRGs appear to be slightly brighter than the elliptical galaxies, but this can be explained by the starburst emission. Given all this, and the uncertainties involved, we conclude that the distribution of our post-coalescence ULIRGs in the FP is consistent to that of the elliptical and other morphologically evolved ULIRGs.

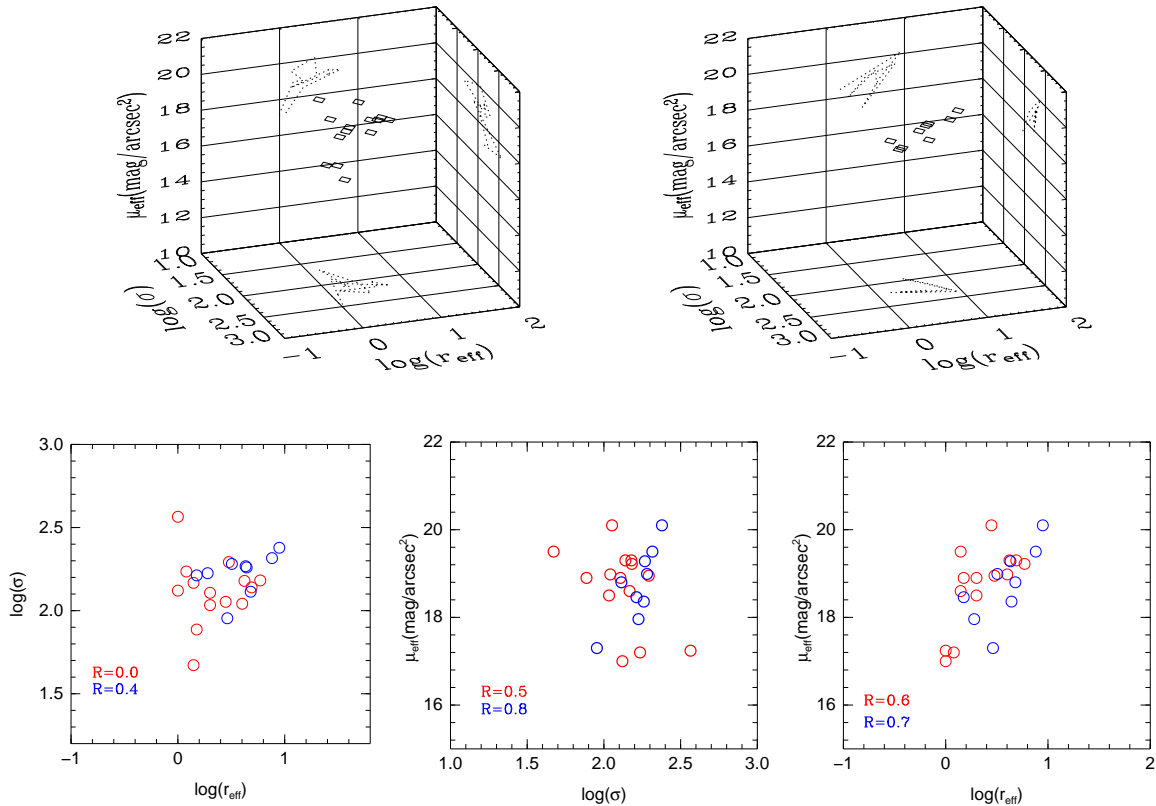


Figure 5.18: Location of ULIRGs in the fundamental plane. **Upper Row Left:** 3D view of the F814W-band fundamental plane for 14 pre-coalescence ULIRGs (7 systems) of the sample. The values are non-extinction corrected. For clarity, the projection of the galaxies on each plane is represented. **Upper Row Right:** The same than Upper Row Left, but for 9 post-coalescence ULIRGs of the sample. **Lower Row:** The three projections of the fundamental plane. Red color indicates pre-coalescence systems, whereas blue indicates the post-coalescence galaxies. The correlation parameter R (value of 1 indicates a linear relation) is detailed in all graphics, showing a better correlation in the post-coalescence galaxies in all three projections.

5.7 Summary and Conclusions

In this Chapter the kinematics of the warm gas in a sample of ULIRGs has been analyzed. For the study two different approaches have been used: (1) observational results, (2) modeled results, obtained fitting the observations to a rotating disk. In addition, the velocity dispersion, V/σ parameter and an estimation of the masses have been obtained too. The main results are summarized as follows.

- The global kinematic structure of the warm ionized gas in ULIRGs is very complex, with large velocity amplitudes of up to 400 km s^{-1} , and on first approximation not consistent with ordered rotating motions, but with motions induced by tidal forces. The merger induced forces create tidal tails, and may indeed trigger extra-nuclear star formation. In fact, these tails are the nurseries for the formation of TDGs (Duc et al. 2003; Monreal-Ibero et al. 2007). In the present sample of ULIRGs, TDGs candidates are hosted in the regions with the largest velocities. This result links the formation of TDGs to relative velocities of the order, or largest, than 200 km s^{-1} .

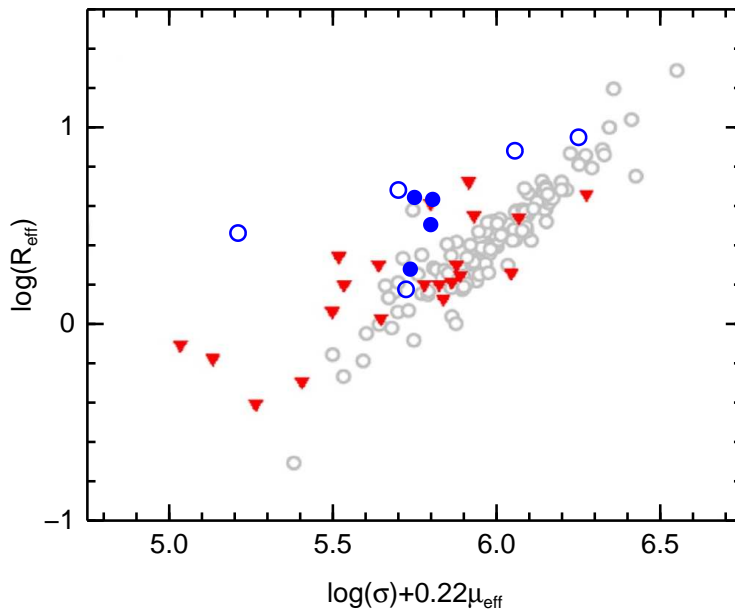


Figure 5.19: Location of ULIRGs in the H-band fundamental plane, viewed as in Pahre (1999). Local early-type galaxies (mainly from the Coma and Virgo Clusters) are plotted as open circles (Zibetti et al. 2002). Plotted as triangles are 21 ULIRGs from the literature (Dasyra et al. 2006). No extinction correction has been applied. Filled blue circles represent post-coalescence ULIRGs with an observed color (F814W-F160W) correction applied. Empty blue circles represent post-coalescence ULIRGs with an average color (F814W-F160W) correction applied.

- As demonstrated by the result of the model fitting, the global velocity field is non consistent with that of simple rotating disks. In most cases, the velocity residuals are dominated by the tidal structures and the observed and modeled kinematic parameters are in general non-consistent. Only in some ULIRGs (e.g., IRAS 131560435, IRAS 14060+2919 and IRAS 06487+2208) the velocity amplitude, the inclination and the good correlation between the photometric and kinematic position angle point towards some degree of rotation in the galaxies.
- The nuclear velocity dispersions are large, between about 150 and 200 km s⁻¹. The peak of σ and the nucleus of the galaxies do in general not coincide. Only about 10% of the pre- and 10% of the post-coalescence systems show spatial coincidence between the σ peak and the nucleus. This means that the position of the maximum σ tend to trace the large-scale motions associated to the tidal tails, rather than mass concentrations.
- The dynamical masses as derived from the nuclear σ are $\leq m_*$ in 75% of galaxies, meaning that ULIRGs as a class have masses of the order of m_* . The mass ratio of the progenitor disk galaxies correspond in general to that of a major or similar mass merger (1:1 to 1:3). These results are consistent with the predictions of Naab et al. (2006), and the results of Dasyra et al. (2006), Genzel et al. (2001), and Colina et al. (2001). In addition they give further support to the conclusions of Chapter 3. Assuming rotation, an upper limit to the rotating mass of about $1 \times 10^{11} M_\odot$ can be obtained using the modeled velocity amplitude.
- The V/σ parameter covers a range of values from 0.4 to 2.5, i.e., from the pressure

-supported dynamically warm galaxies, dominated by random motions, to those where the velocity amplitude (mainly tidal induced) dominates.

- The distribution of ULIRGs in the optical ($0.8 \mu\text{m}$) fundamental plane is different for the pre- and post-coalescence ULIRGs, with a better correlation factor for the post-coalescence galaxies in the three projections. Furthermore, the location of this post-coalescence ULIRGs in the fundamental plane is consistent with that of the ellipticals and other ULIRGs from the literature. These results indicate (1) that the dynamical stage of both morphological types is different, and (2) suggest that, as previously proposed, ULIRGs as a class may evolve into elliptical galaxies.

Chapter 6

Global Summary and Main Conclusions

The main purpose of this thesis work has been to study in detail the two-dimensional internal structure and kinematics of a representative sample of local ULIRGs ($10^{12}L_{\odot} \leq L_{\text{IR}}[8\text{-}1000 \mu\text{m}] \leq 10^{13}L_{\odot}$). The galaxies have been selected for covering different luminosity bins, morphological types and ionization states. For the first time, the analysis has been carried out in a relatively extensive (22) sample of ULIRGs, using optical IFS data obtained with the INTEGRAL system and HST high-spatial resolution images. The origin, evolution and fate of these galaxies is governed by the interaction/merger that ULIRGs undergo. They trigger the ultra-luminous phase, activate the extra-nuclear star formation, and favor the presence of high-velocity shocks. Besides, they channel material towards the nuclei, are responsible of the perturbed warm gas kinematics and, at the end, lead to the formation of intermediate mass slowly rotating elliptical galaxies. All these aspects have been studied through all the work, using the merger phase as thread, and looking for systematic behaviors in such complex objects.

In this final Chapter a summary of the most relevant conclusions are presented, including the main results for all three major subjects (i.e., morphology, ionization and kinematics).

- The observed overall two-dimensional stellar and ionized gas (e.g. $\text{H}\alpha$, $[\text{O III}]\lambda 5007$) structure differs, mainly in the pre-coalescence systems. This is due to variations in the spatial distribution of the different ionizing sources and to the internal extinction effects caused by the dust. In fact, the stellar continuum and emission-line distribution peaks are not spatially coincident in 30% of the studied objects, but separated by up to 10 kpc. Typically, in these cases the peaks of the ionized gas traced by different emission lines (e.g., hydrogen recombination, high excitation $[\text{O III}]$, and shock-tracer $[\text{O I}]$) are also not coincident. This indicates that the ionizing mechanisms may change on scales of 200 pc or less. This behavior is more likely to be present in the early merger phases, due to the interacting process which “activates” the external regions. In the most evolved mergers the stellar and ionized gas are more concentrated towards the nucleus.
- In all ULIRGs the dust is concentrated towards the nucleus (in the central kpc), leading to extinctions of between about 0.5 and 5.0 visual magnitudes (as derived from

the Balmer decrement). The obscuration is responsible for the structures detected in the F814W (I-band) light profiles, producing higher F814W-F160W colors than those predicted by the models of old stellar populations (0.85 for a population of 1.0 Gyr and 1.6 for a population of 10.0 Gyr vs. an average observed value of 3). The differences between the predicted and the average observed colors are consistent with an $A_V=4.6$, which is in agreement with those derived for the ULIRGs of the sample.

- The IR light profiles in ULIRGs are consistent with an $r^{1/4}$ law for all merger phases within the *comparison range* (i.e. 3.8 to 10.5 kpc in the optical and up to 5.1 kpc in the near-IR). The classical isophotal analysis does not reveal strong differences between the pre- and post-coalescence ULIRGs; parameters such as the isophotal shape and the isophotal twist do not show significant variations with the merger phase (e.g., all galaxies tend to show disk-like isophotes, or isophotes in the boxy-disk frontier in the near-IR). This indicates that the selected morphological parameters, by itself, are not an ideal tool for understanding the variation that ULIRGs undergo through the merger. Maybe the use of other parameters, such as the CAS (Concentration, Asymmetry and Clumpiness, Conselice et al. 2003), would help us to better characterize the different phases that galaxies undergo.
- From the studied ULIRG, 19% show nuclear features (traced by the optical line ratio) that indicate the presence of an AGN. H II- and LINER-like nuclei are almost equally distributed, with about 60% corresponding to the pre-coalescence category. The circumnuclear and external regions tend to show similar classification than the nucleus. Nuclei lying near to the H II-LINER frontier present either ionization types in their extra-nuclear regions. Not every warm ULIRG present Seyfert-like classification, in contrast with the findings of Sanders et al. 1988b for 12 warm ULIRGs.
- For the post-coalescence ULIRGs, the line ratio $[O I]/H\alpha$ present a radial increasing (of up to 0.6 dex) towards the external regions. This suggests that the importance of shocks is enhanced in the outer regions, and that may be favored by the lower density of material. This conclusion may be confirmed improving the observations, e.g., using IFUs assisted with adaptive optics. The other line ratios present different trends. As the $[S II]/H\alpha$ systematically increases in the external regions, the $[N II]/H\alpha$ present a more erratic behavior. This observational fact may be due to a variation in the ionizing radiation and/or in the physical conditions.

The complex merger-induced structure and internal processes of pre-coalescence ULIRGs makes not possible to find such clear and systematic trends, at least with the data at our disposal and at the current angular resolution.

- From the comparison with the models, it is concluded that LINER-like excitation in ULIRGs is mainly produced by the combination of two mechanisms. The primary is the presence of high-velocity shocks with radially increasing velocities: 150-200 km s⁻¹ in the nuclei, 150-300 km s⁻¹ in the circumnuclear regions and 150-500 km s⁻¹ in the most external low surface brightness regions. The general absence of superwind signatures and the kinematical properties (i.e., large velocity gradients) of the extra-nuclear regions point towards shocks induced by the merger process. The secondary mechanism is photo-ionization coming from a dusty young (4-6 Myr) stellar population. On the contrary, photo-ionization induced by the presence of an AGN is ruled out as responsible for the LINER-like activity, at least in the present sample of galaxies.

- The analysis of the “aperture effect” (i.e., changes in the classification depending on the integrated area) has been analyzed too, concluding that the excitation state of the nuclei does in general not coincide with that of the entire galaxy. For the post-coalescence ULIRGs a systematic increase in the excitation from H II to LINER between the nuclear and integrated classifications based on the shock-tracer ($[O\text{I}]/H\alpha$) is measured. No systematic trend is measured in the early mergers.
- Comparing the integrated classification of ULIRGs with that of the emission-line galaxies of the SDSS, they are not distributed over the most densely populated regions. In fact, ULIRGs represent cases of extreme starbursts, and occupy the highly excited and the transition (between the frontiers) regions. This result, and that of the previous item, must be taking into account when comparing integrated observations of high- z ULIRGs with local measurements.
- The observed tidally-induced kinematics of the warm ionized gas is rather complex. The velocity amplitudes are of hundreds of km s^{-1} , and the velocity dispersions (σ) values are large, between about 150 and 200 km s^{-1} for the nuclei. Both parameters appear to trace the large-scale motions associated with the tidal structures, including the low-surface brightness regions. In fact, the σ peak tend to be located in extra-nuclear low-surface brightness regions, rather than in with the photometric nucleus. Thus σ traces tidal effects rather than mass concentrations.
- The tidal forces responsible for the formation of the tails may trigger extra-nuclear star formation in the low-surface brightness regions. This fact links the formation of TDGs to relative velocities of the order, or largest, than 200 km s^{-1} .
- The 2D fitting to a simple rotating disk model demonstrate that the global velocity field is non consistent with pure rotation. In most cases, the residuals velocities are dominated by the tidal kinematic structures, and the observed and modeled kinematic parameters are in general non-consistent. However, in some cases the velocity amplitude, the inclination and the good correlation between the photometric and kinematic position angle point towards some degree of rotation in a few galaxies (which are in early pre- or late post-coalescence phases).
- The V/σ parameter as traced by the $H\alpha$ emission line ranges from about 0.4 to 2.5. That is, from galaxies with a dynamical hot component supported by velocity dispersion ($V/\sigma < 1$), to those where the galaxy is dominated by the merger-induced velocity amplitudes.
- The distribution of ULIRGs in the optical ($0.8\ \mu\text{m}$) fundamental plane is different for the pre- and post-coalescence ULIRGs, with a better correlation factor for the post-coalescence galaxies in the three projections. This indicates that both morphological types are in a different dynamical phase.
- Our sample of ULIRGs are intermediate mass (75% have masses $\leq m_*$) galaxies, as derived from the nuclear velocity dispersion. On the initial merger phases (1:1 to 3:1 mass relation of the parent galaxies) they conserve hints for rotation, but rapidly the velocity field is disrupted and the velocity dispersion gains importance. In the final merger phases ULIRGs appear to be consistent with slowly rotating disk ellipticals, as predicted by numerical simulations (e.g. Naab et al. 2003; 2006). This is confirmed by the distribution of the post-coalescence ULIRGs in the fundamental plane, which is consistent with that of elliptical galaxies.

All this information may be used to broadly draw an evolutionary picture for ULIRGs, consistent with the scenario where two gas- and dust-rich rotating disk galaxies suffer a close encounter that activates the star formation and triggers the ultra-luminous phase. The observation of the sample of ULIRGs at this early merger phase (galaxy nuclei separated by more than 15 kpc) show that the star formation is still concentrated in the nuclear regions. A bridge of material (with weak $H\alpha$ emission) is formed between the galaxies, establishing a kinematic link between both disks. This early connection distorts the ordered rotating velocity field towards the bridge. This is a large-scale distortion but still there are observational evidences for rotation. The maximum of the velocity dispersion may be not clearly located in the nuclear regions, and therefore does not traces the mass concentrations.

When the nuclei are closer or located at about 15 kpc, the structure of the galaxies is distorted and complex morphologies (tidal tails, plumes) are created specially in the low-surface brightness regions. That process triggers the merger-induced star formation in the external regions of the galaxies, whose location will depend on the initial geometry of the merger. In the present case extra-nuclear star formation is detected up to distances of 10 kpc from the nucleus, and not necessarily between the galaxies. Shocks may be present everywhere, but because of the complexity of the process no clear tendency is found. In some cases, extra-nuclear ionization cones may be detected, indicating the presence of an AGN. This will depend, for example, on the aperture effects, that may dilute the high excitation. Tidal tail condensations candidates to TDGs may be formed, and will be associated to the velocity peaks of the distorted merger-induced velocity field. The ionized gas velocity field is very complex, although in some nuclear regions there are still hints for rotation.

When the individual galaxies coalesce, the models predict that the material is channeled towards the nuclei, and a burst of star formation may take place. Consistently enough, the post-coalescence ULIRGs of the sample show a concentration in the star formation towards the nuclei, and a structural reordering of the galaxy. The importance of shocks increases towards the outer regions that now associated with an outer more diffuse envelope. Occasionally the material covering the nucleus may be driven away, unveiling the Seyfert nuclei; active nuclei may be detected via the ionization cones too. The warm gas kinematics may show rotation-like structures. The dynamical parameters, and the comparison with simulations, reveal that these evolved ULIRGs tend to have disk-like isophotes, masses of the order of m_* , are slightly supported by rotation and, on the fundamental plane, present an ordered distribution consistent with that of elliptical galaxies.

Chapter 7

Resumen General y Conclusiones

El objetivo principal de este trabajo de tesis ha sido el estudio detallado y bidimensional de la estructura interna y la cinemática de una muestra representativa de ULIRGs ($10^{12} L_{\odot} \leq L_{\text{IR}}[8-1000 \mu\text{m}] \leq 10^{13} L_{\odot}$). Las galaxias seleccionadas cubren diferentes luminosidades, tipos morfológicos y estados de excitación. Por primera vez, el análisis se ha realizado en una muestra de ULIRGs relativamente extensa (22). Para ello se han empleado espectroscopia de campo integral en el óptico obtenida con el instrumento INTEGRAL, e imágenes de alta resolución espacial del Hubble Space Telescope. El origen, la evolución y el destino de estas galaxias está determinado por el proceso de fusión. Éste dispara la fase ultraluminosa, activa la formación estelar extranuclear, y favorece la presencia de choques de alta velocidad. Además canaliza material hacia el núcleo, es responsable de la complejidad cinemática del gas ionizado y, en la fase final de la fusión, induce la formación de galaxias elípticas de masa intermedia en rotación lenta. Todos estos aspectos han sido abordados a lo largo del trabajo, utilizando la fase de fusión como hilo conductor, y tratando de encontrar comportamientos sistemáticos en estos objetos intrínsecamente complicados.

En este Capítulo se presenta un resumen de las conclusiones más importantes, incluyendo los resultados obtenidos para los tres grandes temas de la tesis: morfología, ionización y cinemática.

- La estructura bidimensional de la componente estelar y del gas ionizado (p. e. $\text{H}\alpha$, $[\text{O III}]\lambda 5007$) es diferente, en especial en las galaxias en pre-coalescencia. Esto se debe a la distribución espacial de las diferentes fuentes de ionización y a los efectos de oscurecimiento producidos por el polvo. En particular, el máximo del continuo estelar y del gas ionizado no coinciden espacialmente en el 30% de las ULIRGs estudiadas, midiéndose distancias entre los picos de hasta 10 kpc. En esos casos los máximos del gas ionizado trazado por las diferentes líneas de emisión (como las líneas de recombinación del hidrógeno, la línea de alta excitación de $[\text{O III}]$, y el trazador de choques $[\text{O I}]$) tampoco coinciden entre ellas. Esto indica que los mecanismos responsables de la ionización pueden variar en escalas de 200 pc o menores. Estas variaciones son más comunes en las galaxias en pre-coalescencia, como consecuencia del proceso de fusión que “activa” la zonas externas. En galaxias donde el proceso de fusión está muy avanzado, la componente estelar y la del gas ionizado tienden a concentrarse en las regiones nucleares.

- En todas las ULIRGs el polvo se concentra en las regiones nucleares (en la zonas del kpc central), y produce extinciones derivadas del decremento de Balmer de entre aproximadamente 0.5 y 5 magnitudes visuales. El oscurecimiento por polvo produce las estructuras que se observan en los perfiles de luz de la banda I, y es responsable de que se midan colores F814W–F160W mayores de los que predicen los modelos para poblaciones estelares viejas (0.85 para una población de 1.0 Gyr y 1.6 para una población de 10.0 Gyr frente a colores promedios observados de 3). Esta diferencia entre las observaciones y los modelos son consistentes con una extinción de $A_V=4.6$, que a su vez es coherente con las extinciones observadas.
- Los perfiles de brillo derivados para el rango IR se ajustan bien con una ley $r^{1/4}$ para todas las ULIRGs analizadas (incluyendo los dos tipos morfológicos) en el rango de comparación que se ha definido (de 3.8 a 10.5 kpc en el óptico y hasta 5.1 kpc en el IR). Además de esto, parámetros como la estructura isofotal (“disky” o “boxy”) y el “isophotal twist” no muestran un comportamiento que ayude a segregar los tipos morfológicos ya que, por ejemplo, todas las ULIRGs estudiadas presentan isofotas que en el IR son “disky” o se sitúan en la frontera entre “disky” y “boxy”. Esto indica que los parámetros morfológicos que se han seleccionado para analizar la muestra de galaxias no son válidos, por sí mismos, para estudiar los procesos evolutivos que las ULIRGs sufren durante la fusión. Quizás el uso de otros parámetros como los CAS (concentración, asimetría y agrupamiento, Conselice et al. 2003), podría ayudar caracterizar mejor las diferentes fases del proceso de fusión.
- El 19% de las galaxias estudiadas tienen características espectrales nucleares (derivadas de cocientes de líneas de emisión en el óptico) que indican la presencia de un AGN. En cuanto a la actividad H II y LINER están presente casi por igual en el resto de galaxias, con el 60% en fase de pre-coalescencia. Las regiones circumnucleares y externas presentan una clasificación parecida a la del núcleo. En el caso de núcleos cuya clasificación está entre la frontera H II-LINER, las dos clasificaciones están presentes en las regiones extranucleares. Sorprendentemente, y al contrario de las conclusiones derivadas por Sanders et al. 1988b para 12 ULIRGs calientes, no todas las galaxias calientes de la muestra se clasifican como Seyfert.
- Para las galaxias en estado de post-coalescencia, el cociente de líneas $[O I]/H\alpha$ crece radialmente a medida que nos alejamos del núcleo, con una variación de hasta 0.6 dex. Este resultado sugiere que la importancia de los choques incrementa hacia las regiones más externas, en donde la menor densidad de material puede hacer que el choque se vea favorecido. Esta conclusión podría verificarse optimizando las observaciones utilizando, por ejemplo, unidades de campo integral con óptica adaptativa. En cuanto a los cocientes $[S II]/H\alpha$ y $[N II]/H\alpha$, muestran un comportamiento radial creciente y variable, respectivamente. Este hecho se debe, por ejemplo, a variaciones en la radiación ionizante y/o a cambios en las condiciones físicas que afectan de manera diferente a ambos cocientes.

La complejidad estructural presente en el estado de pre-coalescencia en las ULIRGs hace que no se detecten comportamientos sistemáticos, al menos con los datos presentes y a la resolución espacial a la que trabajamos.

- La comparación con modelos indica que la excitación LINER en las ULIRGs se produce principalmente por la combinación de dos mecanismos. El mecanismo primario son los

choques de alta velocidad cuya velocidad se incrementa con la distancia radial al núcleo: 150-200 km s⁻¹ en el núcleo, 150-300 km s⁻¹ en las regiones circunucleares y 150-500 km s⁻¹ en las más externas de bajo brillo superficial. La no detección de supervientos y las características cinemáticas de las regiones extranucleares (como los gradientes de velocidad grandes), indican que los choques se producen, principalmente, por el mecanismo de fusión. El mecanismo secundario es la fotoionización procedente de una población estelar joven (4-6 Myr), con presencia de polvo. Finalmente, la fotoionización debida a la presencia de un AGN se descarta como responsable de la actividad LINER, al menos en la muestra de galaxias estudiada.

- Los efectos de apertura (es decir, cambios en la clasificación dependiendo del área integrada) son otro aspecto que se ha analizado, concluyéndose que el estado de excitación del núcleo no coincide con el integrado. De hecho en las galaxias en fase de post-coalescencia se mide una variación sistemática en la excitación de H II a LINER entre los valores nuclear e integrados (basado en el cociente [O I]/H α). En las ULIRGs en fase de pre-coalescencia también hay variaciones, pero no sistemáticas.
- Cuando se compara la clasificación integrada de las ULIRGs con las de las galaxias que presentan líneas de emisión del SDSS, éstas no se distribuyen en las regiones más densamente pobladas por las galaxias SDSS. De hecho las ULIRGs representan galaxias con brotes de formación estelar extremos, y ocupan las regiones de alta excitación y las de transición (situadas entre las fronteras de los diferentes tipos de excitación). Este resultado, y el del punto anterior, se deberán tener en cuenta cuando se realicen observaciones integradas de ULIRGs a alto z y se comparen con las locales.
- La cinemática del gas ionizado presenta estructuras complejas inducidas por el proceso de fusión. Los campos de velocidad tienen amplitudes grandes, del orden de cientos de km s⁻¹, y dispersiones de velocidades (σ) nucleares que oscilan entre 150 y 200 km s⁻¹. La posición de los picos de σ , que en general no es el núcleo de la galaxia, indica que este parámetro traza efectos de marea en lugar de concentraciones de masa. Tanto V como σ trazan los movimientos a gran escala asociados con las estructuras de marea, que afectan a las regiones de bajo brillo superficial. De hecho, los efectos de marea que forman las colas de las galaxias activan la formación estelar extranuclear en las regiones de bajo brillo superficial. Este hecho, y el que las regiones con candidatos a galaxias enanas de marea (TDGs) están en general asociadas a los picos de velocidad, establece una relación entre la formación de TDGs y velocidades relativas mayores que 200 km s⁻¹.
- Para establecer el grado de rotación en las ULIRGs de la muestra se han ajustado los datos a un modelo bidimensional de rotación simple. Los resultados demuestran que en general los campos de velocidades no son consistentes con rotación pura. El hecho de que en la mayoría de los casos la velocidad residual está dominada por las estructuras cinemáticas generadas por la interacción apoya esta tesis. No obstante, en algunos casos los valores de la amplitud de velocidades, la inclinación, y la buena correlación entre los ángulos de posición fotométrico y cinemático indican que en esas galaxias (en procesos de fusión muy tempranos o tardíos) presentan cierto grado de rotación.
- El parámetro V/σ , derivado de la línea de emisión H α , varía entre 0.4 y 2.5. Es decir, en algunas ULIRGs ($V/\sigma < 1$) se detecta la presencia de un sistema dinámicamente

caliente, dominado por los movimientos aleatorios, como los que se miden en las estrellas de las galaxias elípticas. Por otra parte hay galaxias en las que la amplitud de velocidades, dominada por el proceso que fusión, es superior a la dispersión, indicando que domina la dinámica de la galaxia.

- Las galaxias en fases de pre- y post-coalescencia presentan una distribución diferente en el plano fundamental (en el óptico, $0.8 \mu\text{m}$) de las elípticas, siendo las post-coalescentes las que tienen mejor factor de correlación. Esto indica que ambos tipos morfológicos se encuentran, efectivamente, en diferentes fases dinámicas.
- Las masas medidas en la muestra de ULIRGs utilizando la dispersión de velocidad del núcleo indican que el 75% tiene masas $\leq m_*$. En las fases iniciales del proceso de fusión se miden relaciones de masas en los sistemas de aproximadamente 1:1 y 3:1, las galaxias conservan indicios de rotación, pero en los estadios más avanzados el campo de velocidad tiene una estructura muy perturbada. De acuerdo con lo predicho por simulaciones numéricas (e.g. Naab et al. 2003; 2006), en las fases finales de la fusión las ULIRGs son compatibles con galaxias elípticas “disky” en rotación lenta. La distribución de las ULIRGs post-coalescentes en el plano fundamental, consistente con la de las elípticas, confirma este hecho observacionalmente.

Toda esta información se puede utilizar para definir, a grandes rasgos, un esquema de los procesos por los que las ULIRGs pasan a lo largo de su vida. Como veremos este escenario no contradice los modelos que predicen que dos discos rotantes ricos en gas y polvo interactúan, activando así la formación estelar y activando la fase ultra-luminosa.

Los datos obtenidos para ULIRGs en las fases iniciales de la fusión (con los núcleos separados por más de 15 kpc), indican que la formación estelar y la actividad en general, se concentran en las zonas nucleares. Entre ambas galaxias se detecta un puente de material que emite débilmente en $H\alpha$, y que establece una “ligadura” cinemática entre ambas galaxias. Esto perturba la cinemática de las galaxias a gran escala, aunque hay indicios observacionales de que existe un cierto grado de rotación. El pico de la dispersión de velocidades no se asocia claramente al núcleo de las galaxias, indicando que no está trazando concentraciones de masa.

En las galaxias en las que los núcleos están situados a 15 kpc o más cerca, la estructura morfológica está muy perturbada. Hay profusión de colas de marea, plumas, y puentes creados por el efecto de marea, que afectan especialmente a las regiones de bajo brillo superficial. Estos procesos activan la formación estelar en las regiones extranucleares, cuya distribución dependerá de la geometría inicial de la galaxia aunque no tiene que estar necesariamente localizada entre los miembros del sistema. En este caso, se mide formación estelar extranuclear a distancias de hasta 10 kpc del núcleo. La presencia de choques puede darse básicamente en cualquier lugar del sistema, pero debido a su elevada complejidad no ha sido posible encontrar un comportamiento sistemático. En ocasiones es posible detectar conos de ionización, que dan indicios indirectos de la presencia de un AGN; este tipo de detecciones dependen de factores como la apertura utilizada ya que si es muy grande la contribución del cono puede quedar diluida. En las colas de marea se detectan candidatos a TDGs, que en general se asocian a los máximos de los campos de velocidad inducidos.

Cuando finalmente las galaxias alcanzan el estado de post-coalescencia, los modelos teóricos predicen que el material se canaliza hacia la región nuclear, produciéndose un brote de formación estelar intenso. Las ULIRGs de la muestra en fase de post-coalescencia muestran

características consistentes con este escenario, como la concentración de la actividad nuclear en las regiones nucleares y una reordenación general de la galaxia. Además, se mide un aumento en la importancia de los choques a medida que la distancia al núcleo aumenta, es decir, en las regiones de bajo brillo superficial que ahora pueden formar parte de una envoltura difusa con estructura similar a la de una elíptica. En ocasiones los movimientos de material pueden desvelar la estructura del núcleo Seyfert, que también es detectable con los conos de ionización. La cinemática del gas ionizado sigue dominada por los efectos de marea, pero en algunos casos hay indicios de rotación (es decir, de reorganización del material). Los parámetros dinámicos, y la comparación con las simulaciones, indican que estas ULIRGs evolucionadas tienen isofotas “disky”, masas del orden de m_* , están parcialmente sostenidas por rotación y su distribución en el plano fundamental es bastante ordenada y compatible con la de las galaxias elípticas.

Appendix A

Morphological Notes on the Individual Sources

The high spatial resolution of the *HST* images provide us with an unprecedented level of morphological detail. Even in galaxies that observed from the ground do not show interaction features, the *HST* observations reveal merging characteristics and in some cases secondary nucleus. This subsection is dedicated to a brief description of the main morphological characteristics of the systems under study, as observed with the *HST* F814W band. The contour images (using a logarithmic scale) are shown in Figs.A.1 and A.2.

- **IRAS 13156+0435**

This is a pre-coalescence system formed by two disk-like galaxies with the nuclei located about 36 kpc apart. The entire system covers about 68 kpc in length, taking into account the low surface brightness regions. The galaxies are connected by a bridge of material that emits in $H\alpha$ and kinematically confirms the interaction.

- **IRAS 13342+3932**

This system is a rather peculiar example. It is composed by two galaxies in pre-coalescence phase, being with one of the members largest in size. The total size of the system is 51 kpc and the nuclei are separated by 25 kpc. The eastern galaxy appears to be almost edge-on, whereas the western, with a Seyfert nucleus, is almost face-on. The latter presents a well developed tail of 14.2 kpc that could be the product of a previous merger.

- **IRAS 18580+6527**

The total angular linear size of this pre-coalescence system is 52.7 kpc. It is one of the most exotic galaxies of the sample, with two well defined structures. The eastern component shows the presence of two point-like sources separated by 7.1 kpc and aligned in the North-South direction. These sources are both classified as Seyfert (see Chapter 4) with the $[NII]/H\alpha$ diagnostic diagram. The central regions of the eastern galaxy appears to have lost the majority of the surrounding material, with the arc-like structure extending out into the other galaxy being the most remarkable morphological characteristic. The western galaxy appears quite perturbed with several bright knots surrounding the nucleus. Both individual galaxies are connected by a bridge of material.

- **IRAS 16007+3743**

This pre-coalescence system has a total size of about 40.3 kpc, and is composed of

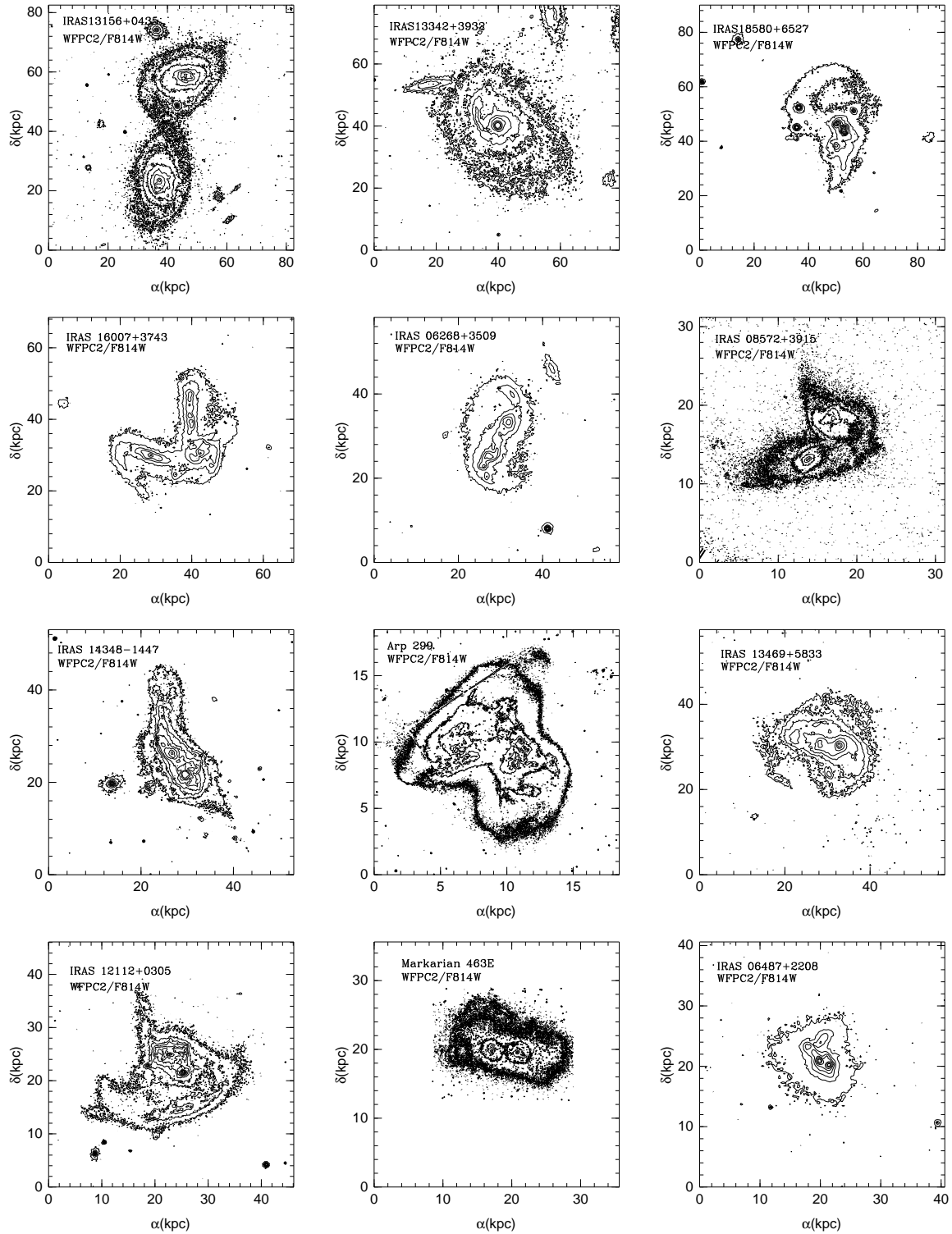


Figure A.1: Contour plot on a logarithmic scale for the WFPC2/F814W images of the ULIRGs sample (see galaxy name on labels). From top to bottom and left to right, the objects are sorted by nuclear separation. North is up, east to the left.

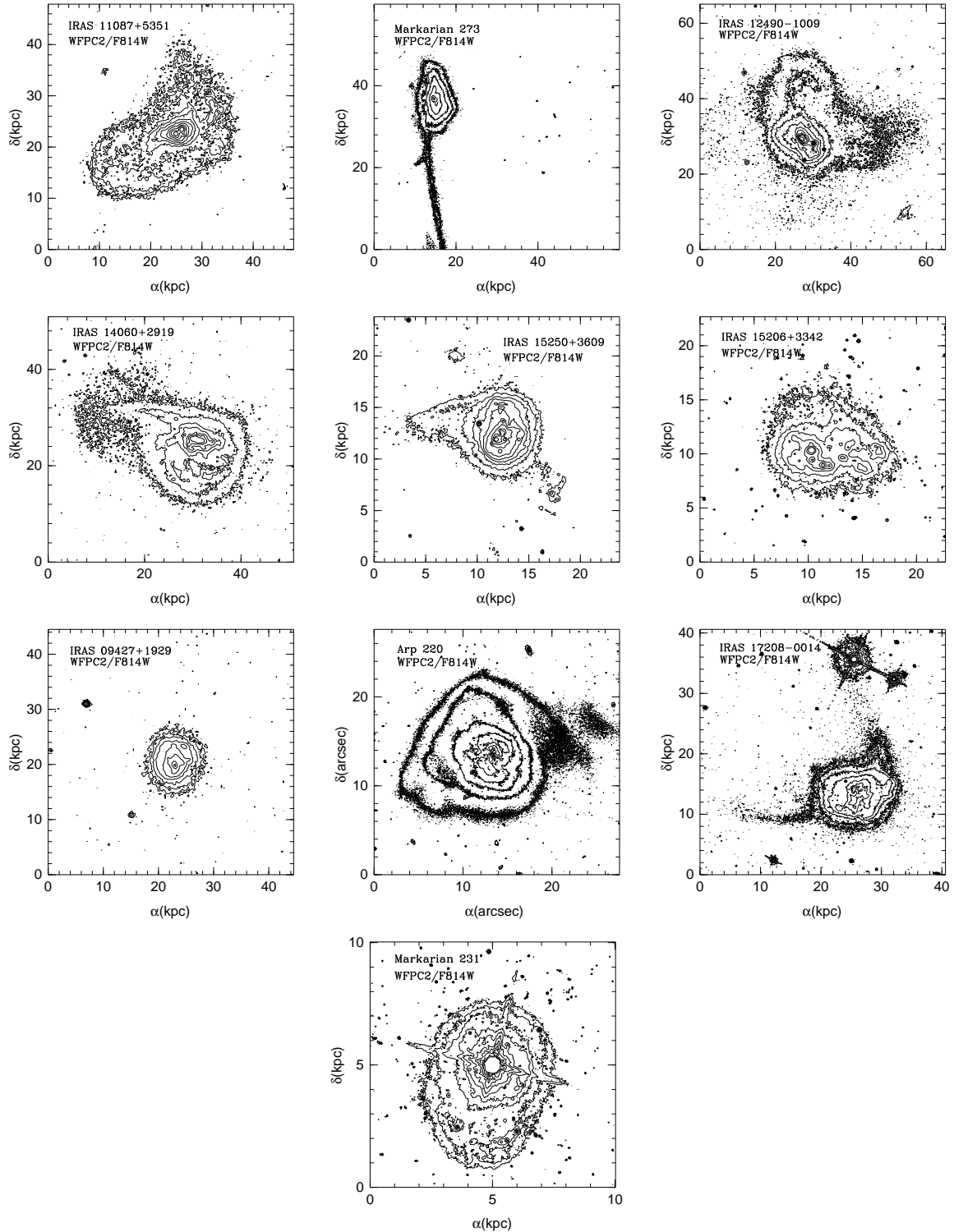


Figure A.2: Contour plot on a logarithmic scale for the WFPC2/F814W images of the ULIRGs sample (see galaxy name on labels). From top to bottom and left to right, the objects are sorted by nuclear separation. North is up, east to the left.

two galaxies with their individual structure still well-conserved. The western galaxy appears to be almost face on, and presents a mini-spiral in the nucleus. One of their original spiral arms appears to be elongated 15.5 kpc towards the north. Towards the east of the main body of the galaxy there is a plume of material of 7.1 kpc in length. The eastern galaxy appears to be almost edge-on and presents a tidal tail of 15.5 kpc. Both galaxies are connected by a bridge, and in this region there is a bright knot which is a good candidate for becoming a tidal dwarf galaxy.

- **IRAS 06268+3509**

This pre-coalescence systems covers 28.9 kpc on the sky, with two small arc-like tidal tails. One towards the North-East (17.4 kpc) and the other towards the South-West (8.7 kpc). The two nuclei are located about 9.1 kpc apart, and share a well defined bridge. The structure surrounding the nucleus of the southern galaxy is twisted and presents some bright knots.

- **IRAS 08572+3915**

The total size of this merging system is 27.1 kpc, with the nuclei separated by 6.1 kpc. Both galaxies have very well defined tidal tails, the northern one of 12.3 kpc and the southern of 10.2 kpc. The latter presents some small low-surface brightness knots, which are candidates to be tidal dwarf galaxies. The northern galaxy appears to be almost face-on, and presents an irregular structure with indications of dust. The southern galaxy is more inclined, and compact.

- **IRAS 14348–1447**

This pre-coalescence system occupies 45.1 kpc on the sky, and has the not so common characteristic of having a mini-spiral structure in the southern nucleus. The main morphological merging features are a tidal tail of about 17 kpc towards the north, and a small plume of 11.7 kpc towards the south. Moreover, there are small bright knots all over the galaxy, with the brightest one located about 13.2 kpc of the northern galaxy.

- **Arp 299**

This is a pre-coalescence system formed by two galaxies that, including the low surface brightness regions occupy about 15.4 kpc of the sky. The system is the result of the merger between two disk galaxies connected by an interface region. The extinction produced by the dust is partly responsible for the morphology of the system (i.e. dust lanes and buried nucleus). There are bright star forming regions knots located all over the galaxy, with newly formed stars that are a direct product of the merger. Two arc-like structures of about 3.0 kpc in length are present in the western galaxy.

- **IRAS 13469+5833**

This double galaxy has a size of 28.6 kpc, although taking into account the very low-surface brightness structures (almost at the sky level) there are two tails that increase the total extension of the galaxy up to 89.4 kpc. The nuclei of the galaxy are connected by a bridge of material and from both, western and eastern, there is an arc structure of about 12 kpc in size. At about 6.1 kpc towards the South of the bridge a high surface brightness knot stands out. As a reference, the low surface brightness tails towards North and South (not shown in the contour image) are 57 and 34 kpc in length respectively.

- **IRAS 12112+0305**

The total size of this morphologically exotic galaxy is about 34.6 kpc. It is composed of

two galaxies that at this merger phase form an almost unique structure, not coalesced yet, with two well separated (4.5 kpc) nuclei. The tidal tail located towards the South of the galaxy has 29.6 kpc in length, and presents several bright condensations, which could be good candidates to be tidal dwarf galaxies (TDG) once the galaxy reaches its final relaxation. In the northern region there is a plume of about 10 kpc, with very small condensations. Both nuclei are obscured by the presence of dust, but whereas the less extincted northern nucleus is barely visible, the southern is clearly visible. Finally, at about 7 kpc to the east of the North nucleus the presence of a bright knot stands out.

- **Markarian 463**

This pre-coalescence galaxy has a total size of about 26 kpc, with an external envelope surrounding the two nuclei located 4.3 kpc apart. There is an arc-like structure of 16.7 kpc that surrounds the East nucleus. There are no other remarkable morphological features such as tails or plumes. The East nucleus (that hosts an AGN) presents structure, probably caused by the presence of dust.

- **IRAS 06487+2208**

This is a post-coalescence galaxy with a double nucleus separated by 1.5 kpc. The structure is quite compact, and has 17.4 kpc in length. There are no prominent tidal tails, arcs, or any other features. The morphology is rather simple. Two nuclei separated by about 1.5 kpc surrounded by an envelope with a small plume of 3.5 kpc towards the NW.

- **IRAS 11087+5351**

This double nucleus (separated by 1.5 kpc) post-coalescence galaxy has a total size of about 36.3 kpc. There is an arc structure that starts in the W nucleus. At about 5.3 kpc from the western nucleus there is a low surface brightness region of 4.2 kpc that presents Seyfert-like ionization (see Chapter 4). The outer envelope of the galaxy bears resemblance with an elliptical structure, although towards the N its symmetry is broken.

- **Markarian 273**

Using the WFPC2 (chip3) the length of this post-coalescence galaxy is 49.4 kpc, including the tidal tail (about 30 kpc). The main body of this double-nucleus galaxy whose nuclei are separated by 0.7 kpc is elongated, with dust lanes and structures causing much of the extinction.

- **Arp 220**

In the *HST* image the size of the galaxy is about 24.6 kpc. This is a post-coalescence two nuclei galaxy with the nuclei located 0.4 kpc apart. It has no tails or arcs but a central region highly extincted by the presence of dust. The central morphology is quite round, more than the outer envelope. Nevertheless, the outer low surface brightness structure bears resemblance with an elliptical envelope.

- **IRAS 12490–1009**

Taking into account the low surface brightness regions, the size of the system is about 50 kpc. This is a single nucleus post-coalescence galaxy, with bright knots and dust structures in the central regions. Towards the N there is an arc-like tidal tail with a total length of 19.5 kpc. On EW direction there are low surface brightness structures.

- **IRAS 14060–2919**

Taking into account the low surface brightness regions towards the E, this post-coalescence galaxy has an angular size of about 38.4 kpc. Apart from the elongated nucleus, there are two structures worth mentioning: (1) an arc structure of 17 kpc surrounding the nuclear regions of the galaxy, and that is part of a bigger cocoon, and (2) a short tail (18.4 kpc) starting from the northern part of the galaxy towards the East. There are no significant dust lanes in this galaxy.

- **IRAS 15250+3609**

With a total size of about 17.7 kpc, this post-coalescence galaxy has a single nucleus and internal structures such as bright knots and presence of dust. The morphology of the galaxy is almost spherical with tidal tail towards W direction of 8.2 kpc. It is remarkable the presence of a condensation at a distance of 4.9 kpc from the main body of the galaxy. In spite of its size and low surface brightness this region is bright line emitter (see Fig. 3.5).

- **IRAS 15206+3342**

This post-coalescence galaxy has a total size of about 17.7 kpc. With a single nucleus, the morphological feature that stands out is a chain of bright condensations starting from the nucleus. The morphology is confused due to the presence of dust. There are no tails, bridges or plumes. The outer envelope of the system shows an elliptical-like morphology.

- **IRAS 09427+1929**

Compared to the other galaxies and at the present resolution, this post-coalescence galaxy has a rather ordered morphology. With a size of 12.0 kpc, the morphology is almost spherical, with no tails or secondary signs of merger. The most remarkable aspect is that the nucleus of the galaxy is off-centered with respect to the outer isophotes.

- **IRAS 17208-0014**

This single-nucleus galaxy has a size of 29.5 kpc on the sky. This post-coalescence system shows an almost spherical main body and large amounts of dust that extinguish the emission and bury the nucleus. The galaxy presents two low surface brightness plumes each one of about 15.2 kpc in length.

- **Markarian 231**

This is one of the most advanced merger of the sample; it has lost its nuclear envelopes and shows the naked QSO. It has 9.5 kpc in length and an arc-like structure of 4.6 kpc remnant of the previous merger.

Appendix B

Emission Line Maps for all the Galaxies of the Sample

In this Appendix the maps of interest for all the galaxies of the sample, as obtained with the INTEGRAL system, are presented. The emission-line free stellar continuum, along with the most relevant optical-emission line ($H\beta$, $[O\text{ III}]\lambda 5007$, $[O\text{ I}]\lambda 6300$, $H\alpha + [N\text{ II}]\lambda\lambda 6548, 6584$, $[S\text{ II}]\lambda\lambda 6716, 6731$) maps are shown. Complementary optical ($0.8\ \mu\text{m}$) *HST* images are presented too.

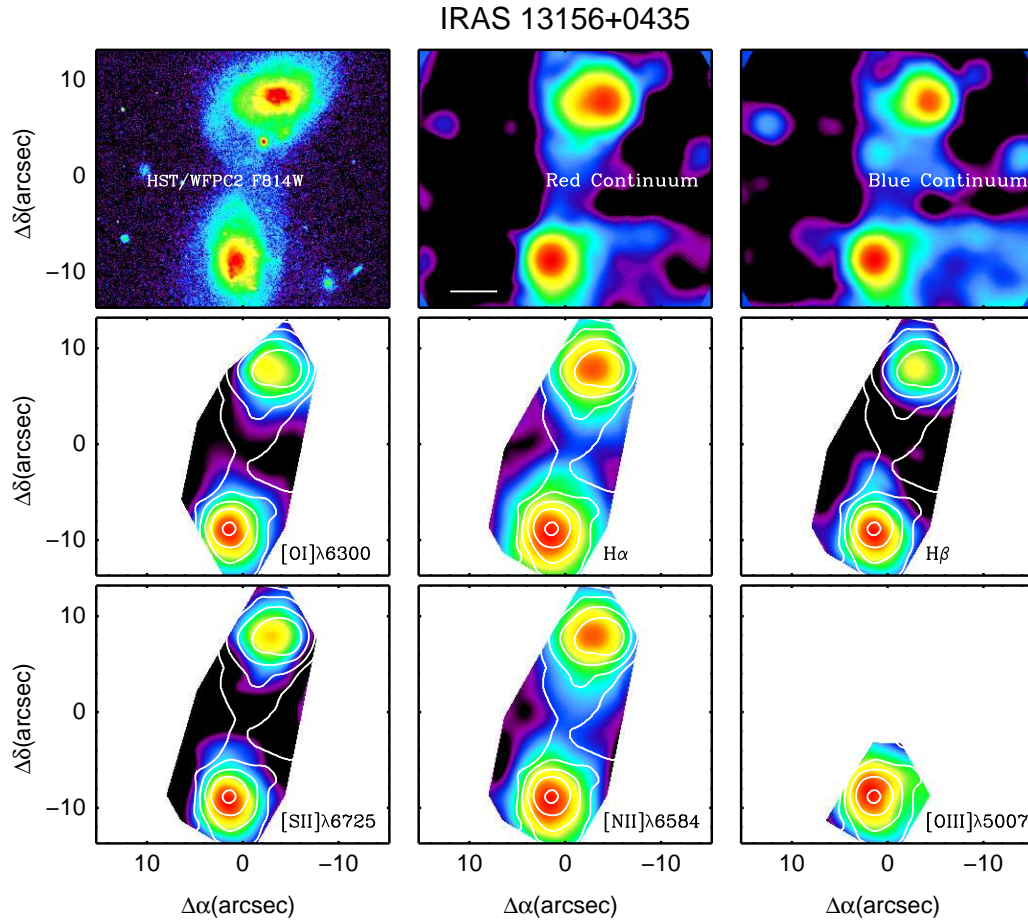


Figure B.1: Emission-line free stellar continua and emission-line images for IRAS3156+0435 obtained with the INTEGRAL SB3 bundle. Contours represent the red continuum. The *HST*-WFPC2 F814W images is shown for comparison. All the images are shown in a logarithmic scale, and the color code represent different intensity levels in each of the individual maps. North is up, east to the left. The scale represents 10 kpc.

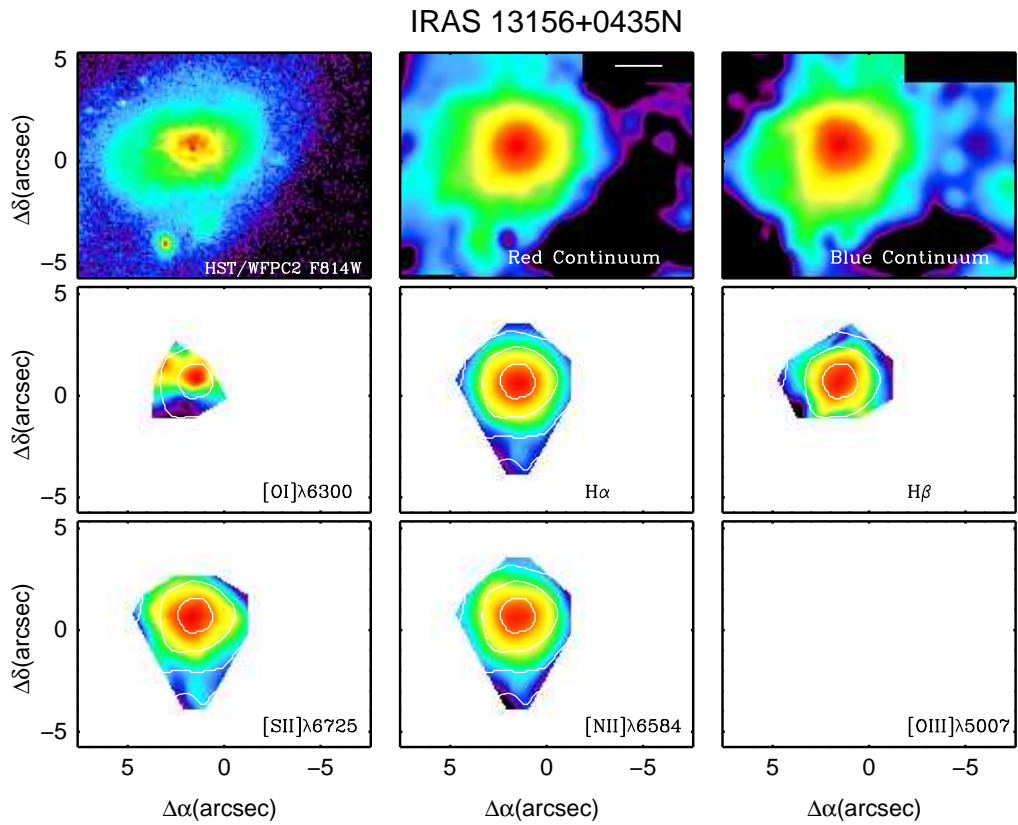


Figure B.2: Emission-line free stellar continua and emission-line images for the northern component of IRAS3156+0435 obtained with the INTEGRAL SB2 bundle. Contours represent the red continuum. The *HST*-WFPC2 F814W images is shown for comparison. All the images are shown in a logarithmic scale, and the color code represent different intensity levels in each of the individual maps. North is up, east to the left. The scale represents 5 kpc. [O III] is detected, but not with enough spatial information as to obtain a map.

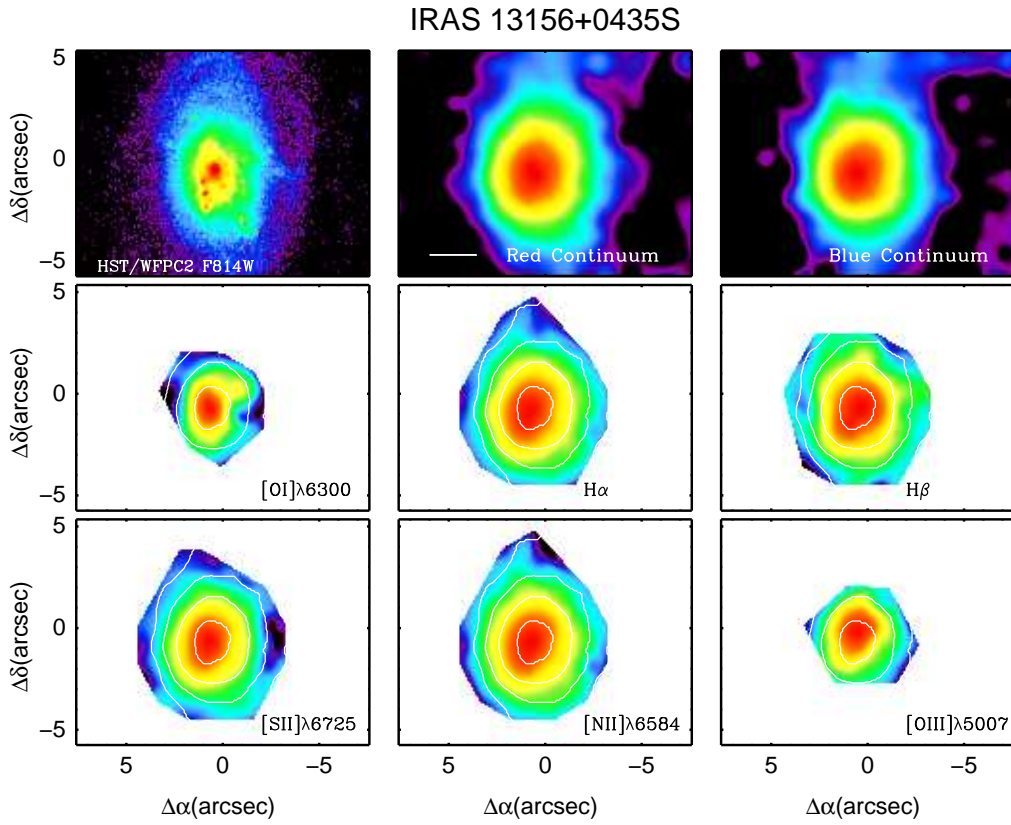


Figure B.3: Emission-line free stellar continua and emission-line images for the southern component of IRAS3156+0435 obtained with the INTEGRAL SB2 bundle. Contours represent the red continuum. The *HST*-WFPC2 F814W images is shown for comparison. All the images are shown in a logarithmic scale, and the color code represent different intensity levels in each of the individual maps. North is up, east to the left. The scale represents 5 kpc.

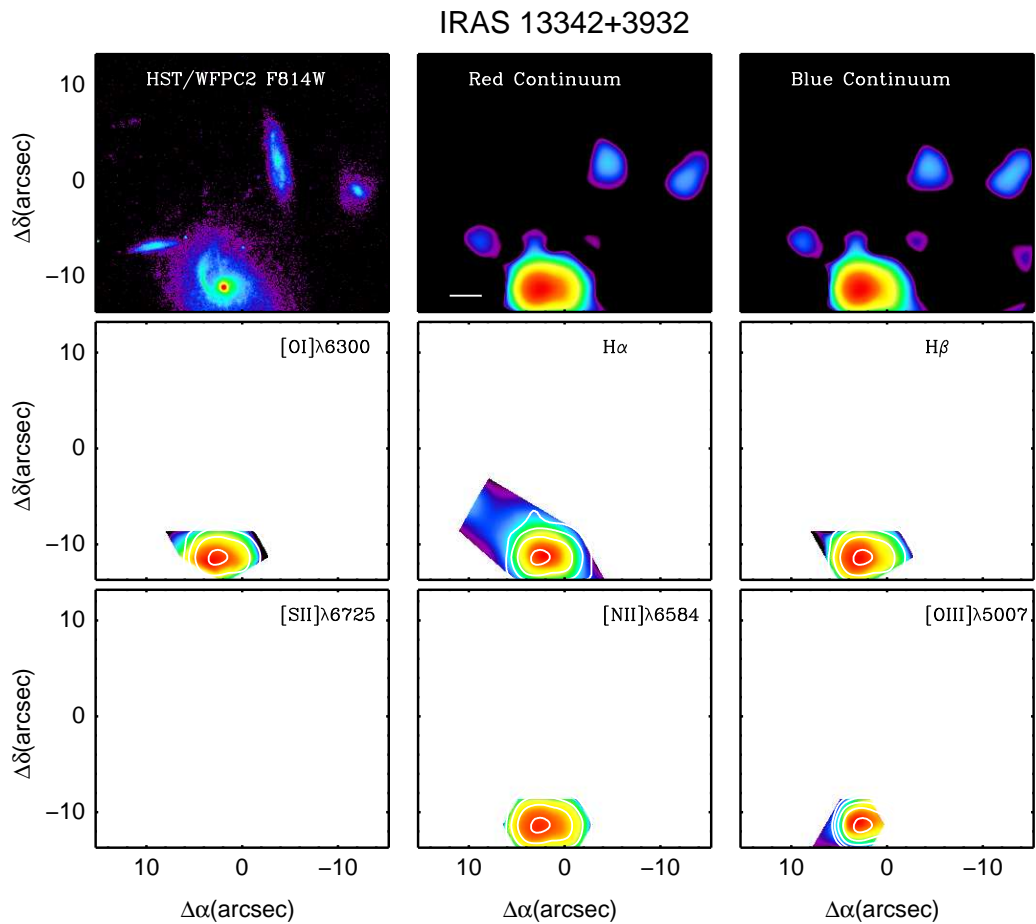


Figure B.4: Emission-line free stellar continua and emission-line images for IRAS 13342+3932 obtained with the INTEGRAL SB3 bundle. Contours represent the red continuum. The *HST*-WFPC2 F814W images is shown for comparison. All the images are shown in a logarithmic scale, and the color code represent different intensity levels in each of the individual maps. North is up, east to the left. The scale represents 5 kpc. The blank panel indicates no emission line detected.

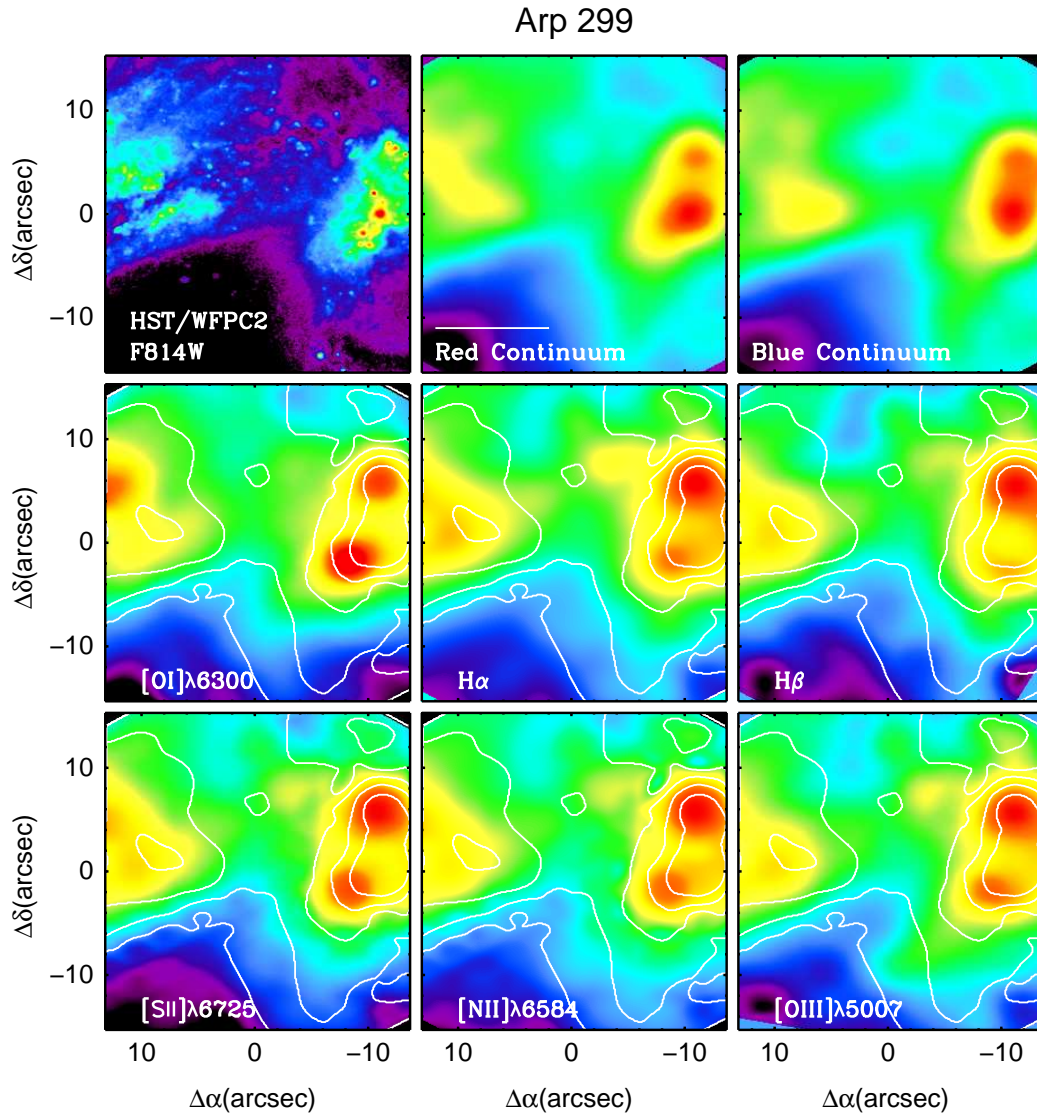


Figure B.5: Emission-line free stellar continua and emission-line images for Arp 299 obtained with the INTEGRAL SB3 bundle. NGC 3690 is located to the west, and IC 694 to the east. Contours represent the red continuum. The *HST*-WFPC2 F814W images is shown for comparison. All the images are shown in a logarithmic scale, and the color code represent different intensity levels in each of the individual maps. North is up, east to the left. The scale represents 2 kpc.

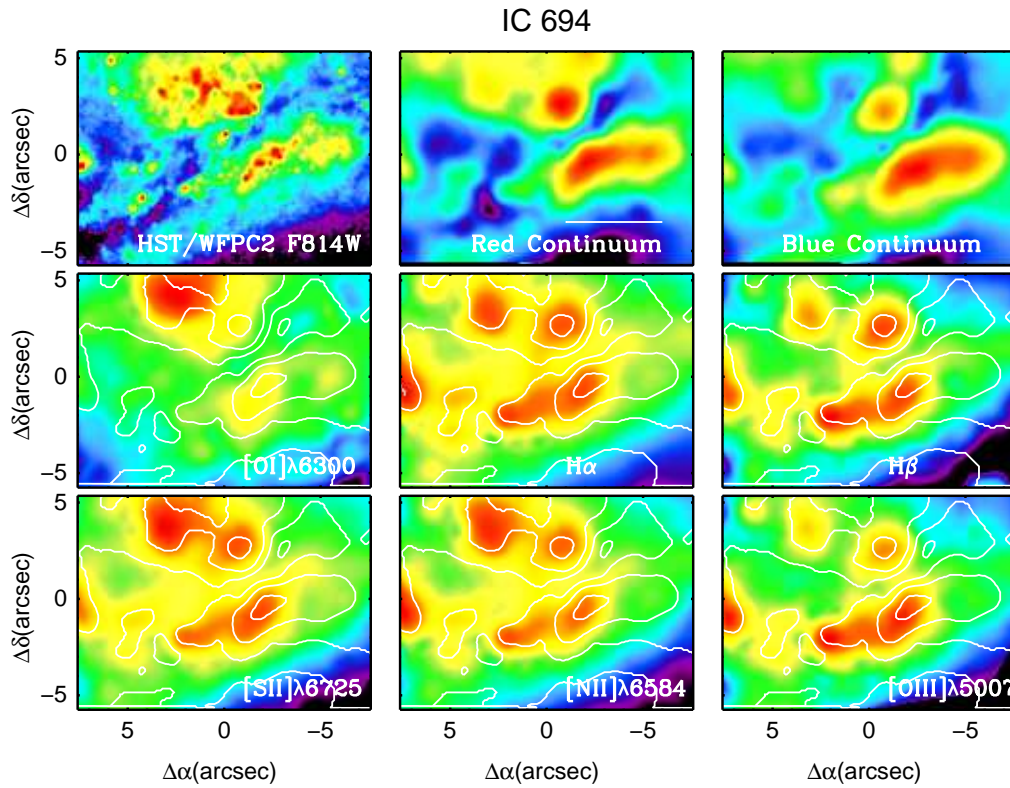


Figure B.6: Emission-line free stellar continua and emission-line images for IC 694 (eastern component of Arp 299) obtained with the INTEGRAL SB2 bundle. Contours represent the red continuum. The *HST*-WFPC2 F814W images is shown for comparison. All the images are shown in a logarithmic scale, and the color code represent different intensity levels in each of the individual maps. North is up, east to the left. The scale represents 1 kpc.

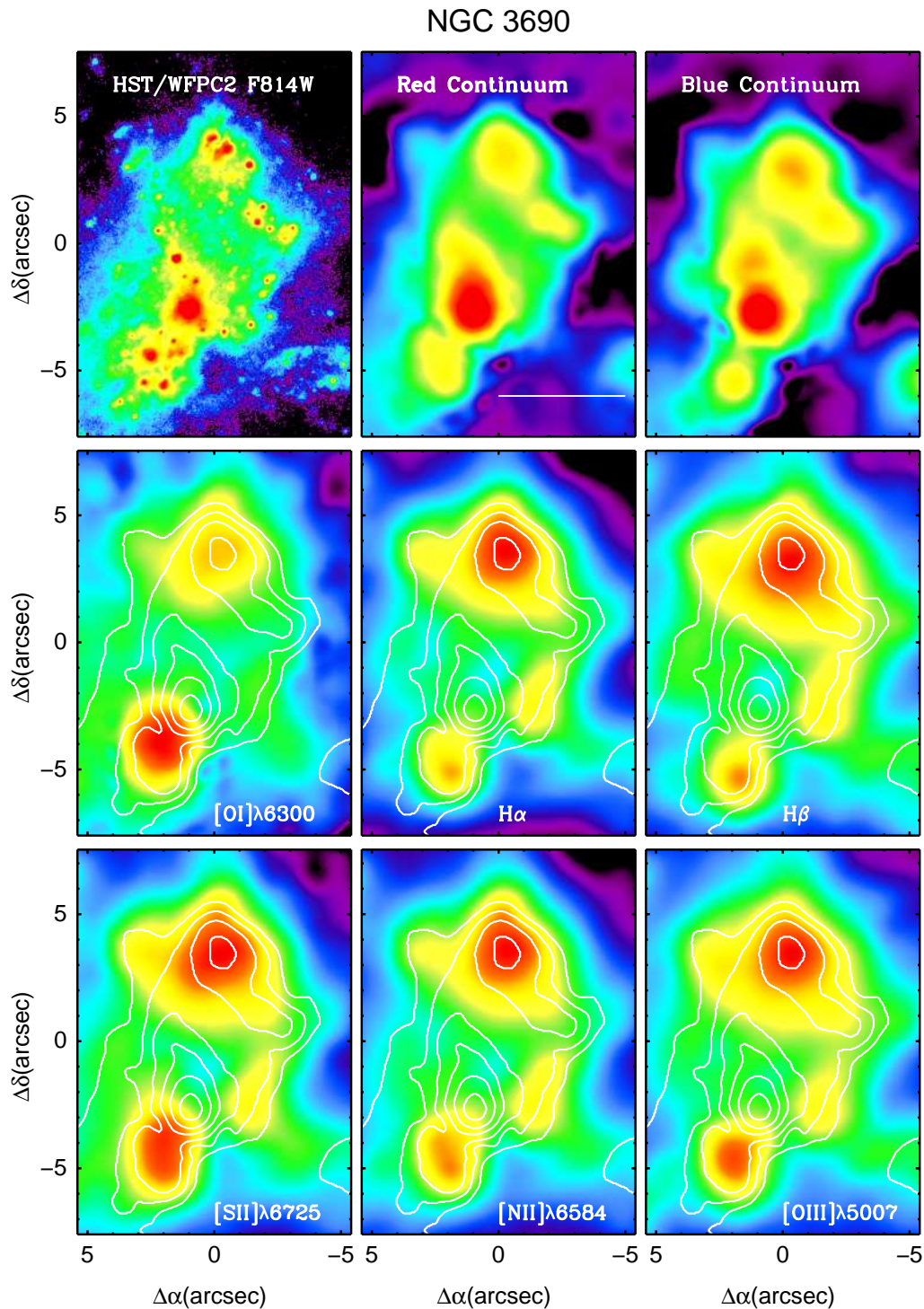


Figure B.7: Emission-line free stellar continua and emission-line images for NGC 3690 (western component of Arp 299) obtained with the INTEGRAL SB2 bundle. Contours represent the red continuum. The *HST*-WFPC2 F814W images is shown for comparison. All the images are shown in a logarithmic scale, and the color code represent different intensity levels in each of the individual maps. North is up, east to the left. The scale represents 1 kpc.

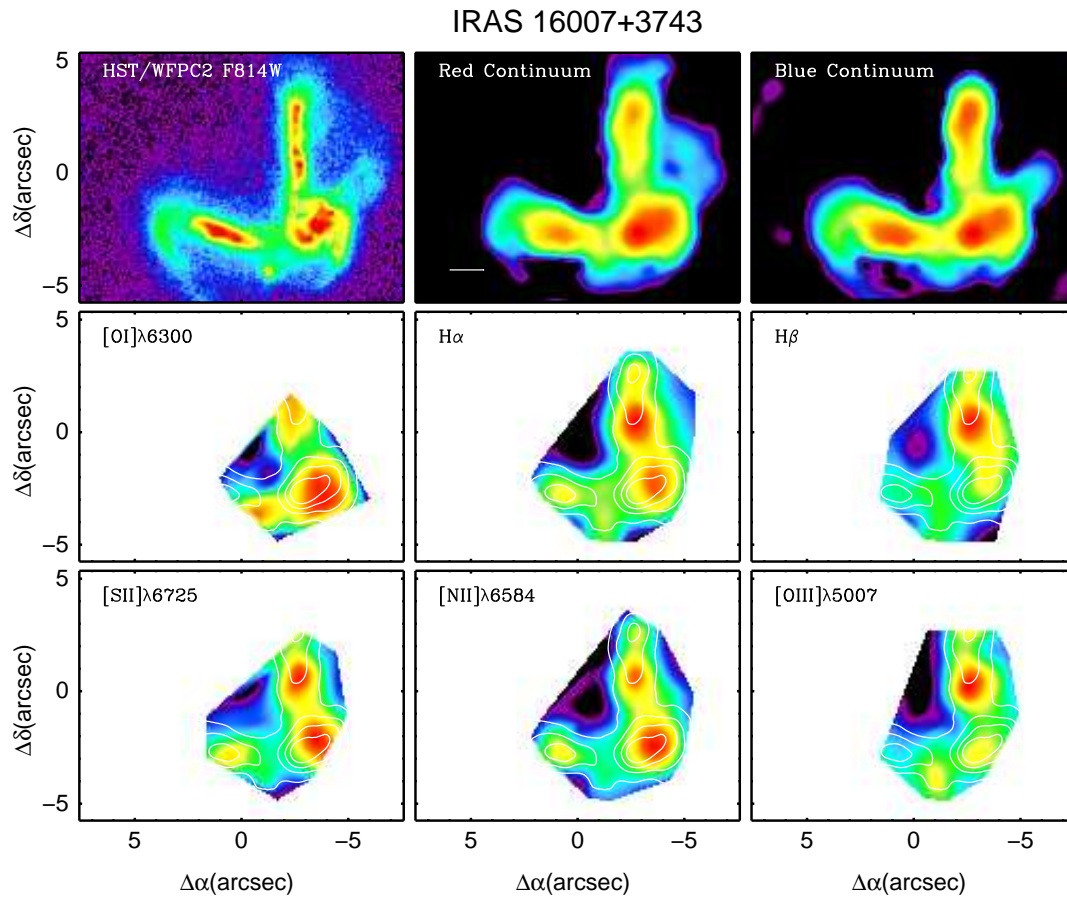


Figure B.8: Emission-line free stellar continua and emission-line images for IRAS 16007+3743 obtained with the INTEGRAL SB2 bundle. Contours represent the red continuum. The *HST*-WFPC2 F814W images is shown for comparison. All the images are shown in a logarithmic scale, and the color code represent different intensity levels in each of the individual maps. North is up, east to the left. The scale represents 5 kpc.

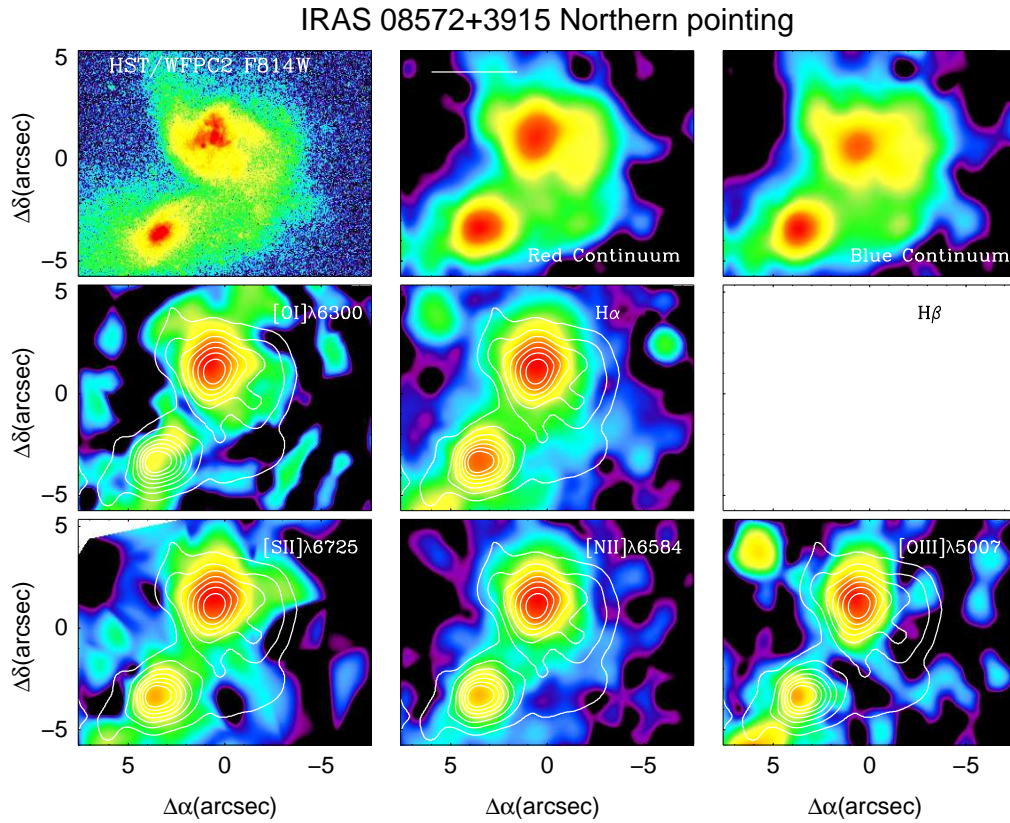


Figure B.9: Emission-line free stellar continua and emission-line images for the northern pointing of IRAS 08572+3915 obtained with the INTEGRAL SB2 bundle. Contours represent the red continuum. The *HST*-WFPC2 F814W images is shown for comparison. All the images are shown in a logarithmic scale, and the color code represent different intensity levels in each of the individual maps. North is up, east to the left. The scale represents 5 kpc. The blank panel indicates that there is no spatial information as to derive a map.

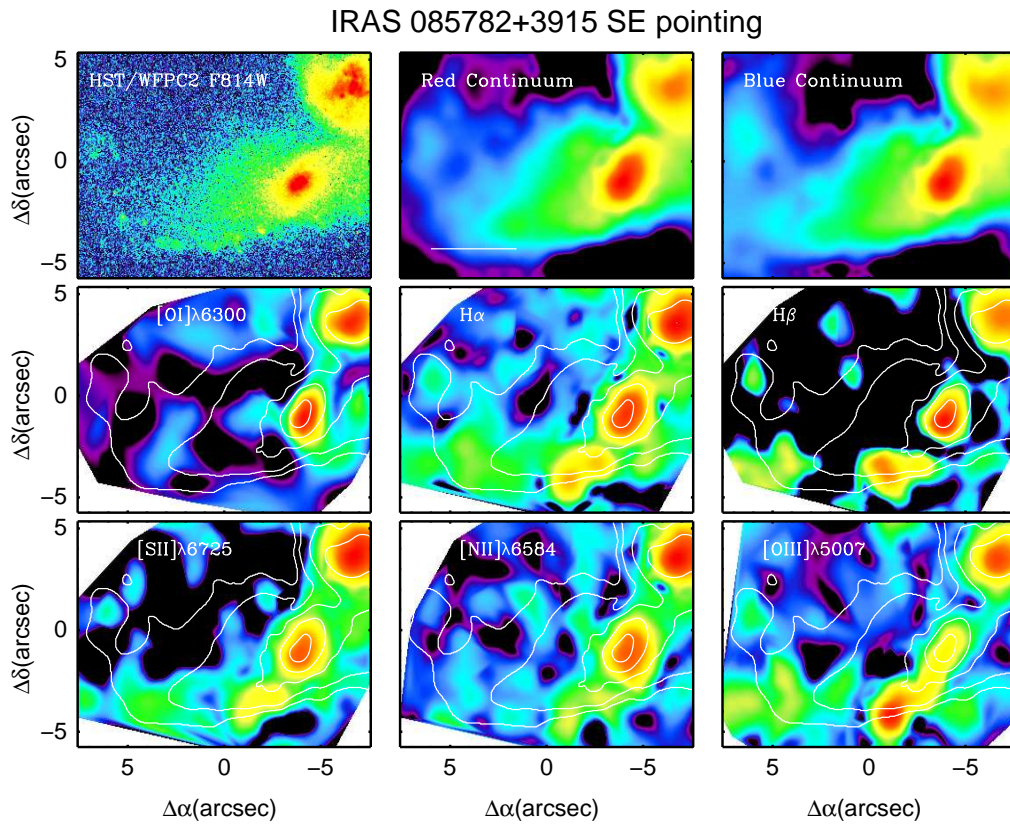


Figure B.10: Emission-line free stellar continua and emission-line images for the southern pointing of IRAS 08572+3915 obtained with the INTEGRAL SB2 bundle. Contours represent the red continuum. The *HST*-WFPC2 F814W images is shown for comparison. All the images are shown in a logarithmic scale, and the color code represent different intensity levels in each of the individual maps. North is up, east to the left. The scale represents 5 kpc.

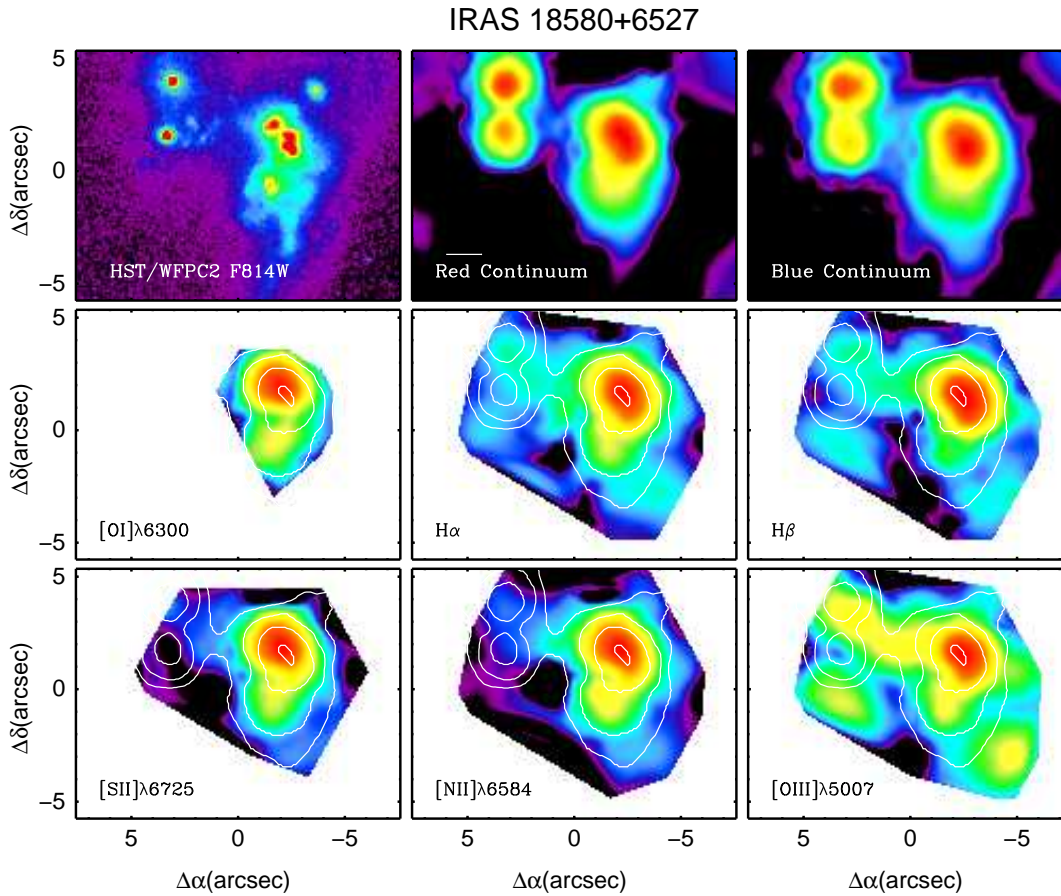


Figure B.11: Emission-line free stellar continua and emission-line images for IRAS 18580+6527 obtained with the INTEGRAL SB2 bundle. Contours represent the red continuum. The *HST*-WFPC2 F814W images is shown for comparison. All the images are shown in a logarithmic scale, and the color code represent different intensity levels in each of the individual maps. North is up, east to the left. The scale represents 5 kpc.

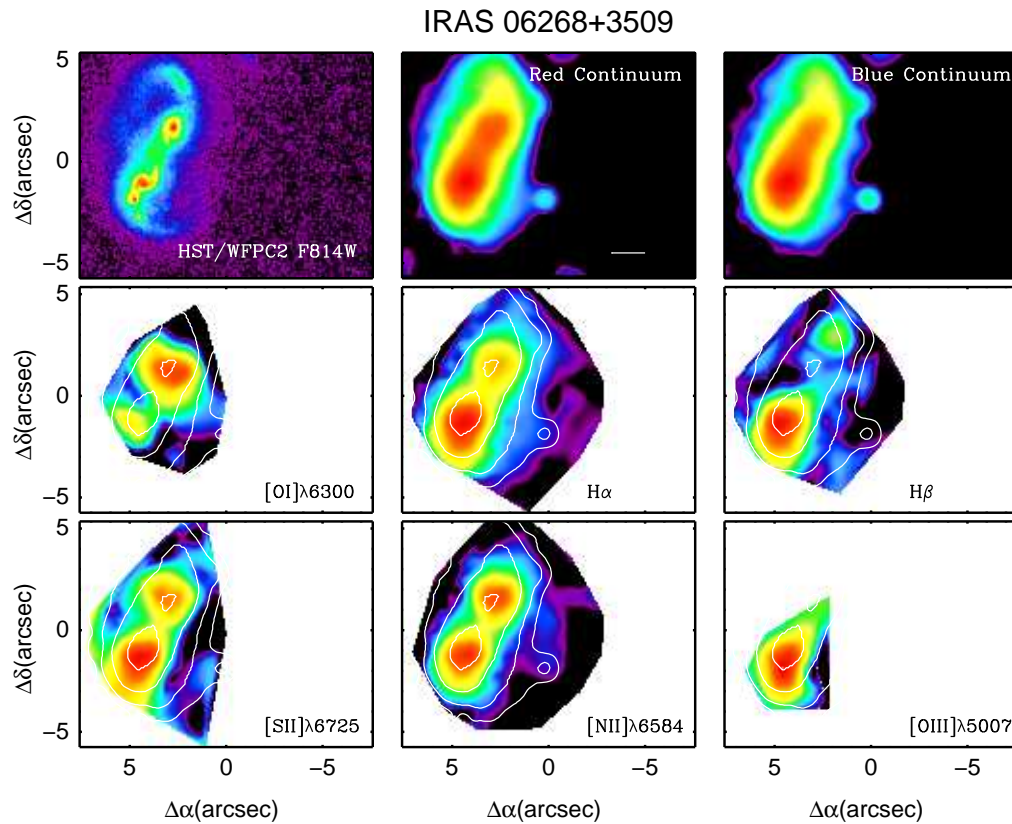


Figure B.12: Emission-line free stellar continua and emission-line images for IRAS 06268+3509 obtained with the INTEGRAL SB2 bundle. Contours represent the red continuum. The *HST*-WFPC2 F814W images is shown for comparison. All the images are shown in a logarithmic scale, and the color code represent different intensity levels in each of the individual maps. North is up, east to the left. The scale represents 5 kpc.

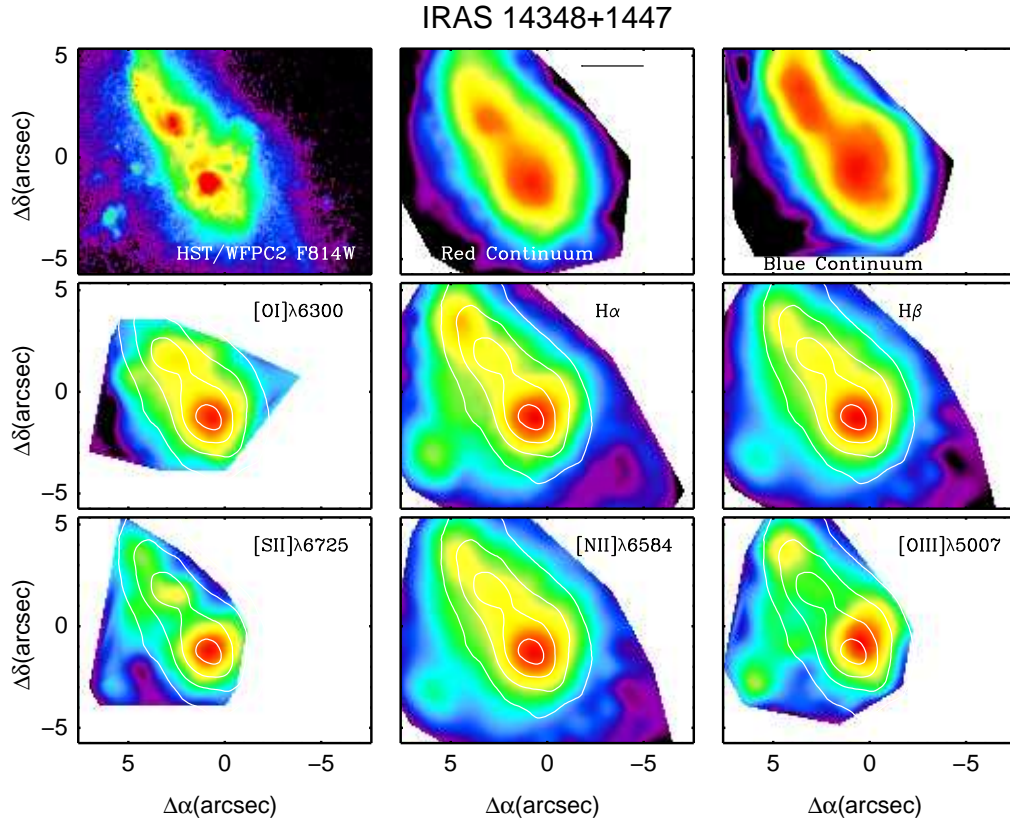


Figure B.13: Emission-line free stellar continua and emission-line images for IRAS 14348-1447 obtained with the INTEGRAL SB2 bundle. Contours represent the red continuum. The *HST*-WFPC2 F814W images is shown for comparison. All the images are shown in a logarithmic scale, and the color code represent different intensity levels in each of the individual maps. North is up, east to the left. The scale represents 5 kpc.

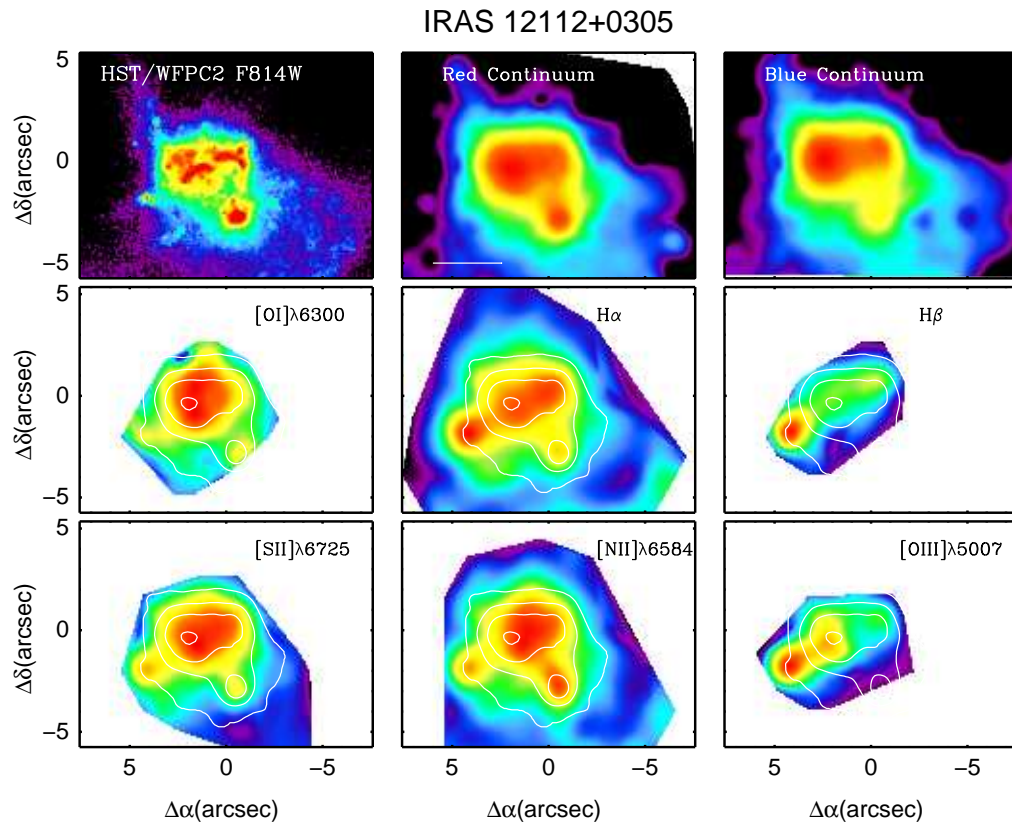


Figure B.14: Emission-line free stellar continua and emission-line images for IRAS 12112+0305 obtained with the INTEGRAL SB2 bundle. Contours represent the red continuum. The *HST*-WFPC2 F814W images is shown for comparison. All the images are shown in a logarithmic scale, and the color code represent different intensity levels in each of the individual maps. North is up, east to the left. The scale represents 5 kpc.

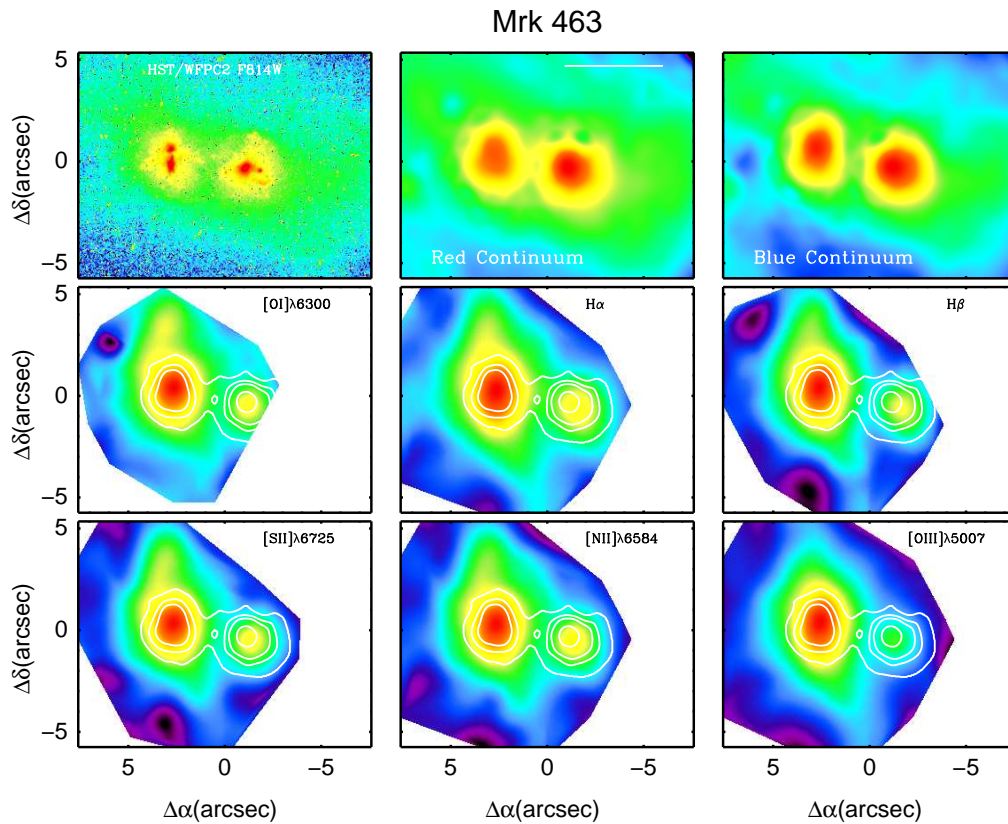


Figure B.15: Emission-line free stellar continua and emission-line images for Mrk 463 obtained with the INTEGRAL SB2 bundle. Contours represent the red continuum. The *HST*-WFPC2 F814W images is shown for comparison. All the images are shown in a logarithmic scale, and the color code represent different intensity levels in each of the individual maps. North is up, east to the left. The scale represents 5 kpc.

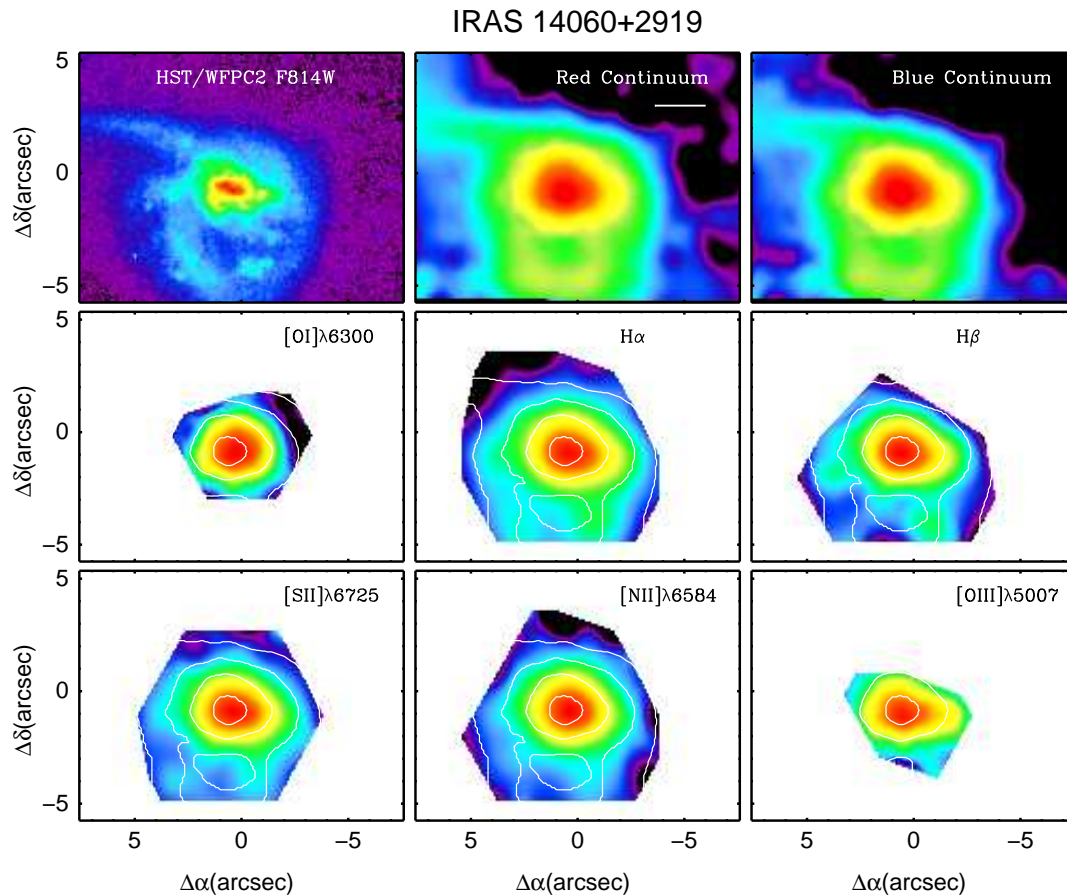


Figure B.16: Emission-line free stellar continua and emission-line images for IRAS 14060+2919 obtained with the INTEGRAL SB2 bundle. Contours represent the red continuum. The *HST*-WFPC2 F814W images is shown for comparison. All the images are shown in a logarithmic scale, and the color code represent different intensity levels in each of the individual maps. North is up, east to the left. The scale represents 5 kpc.

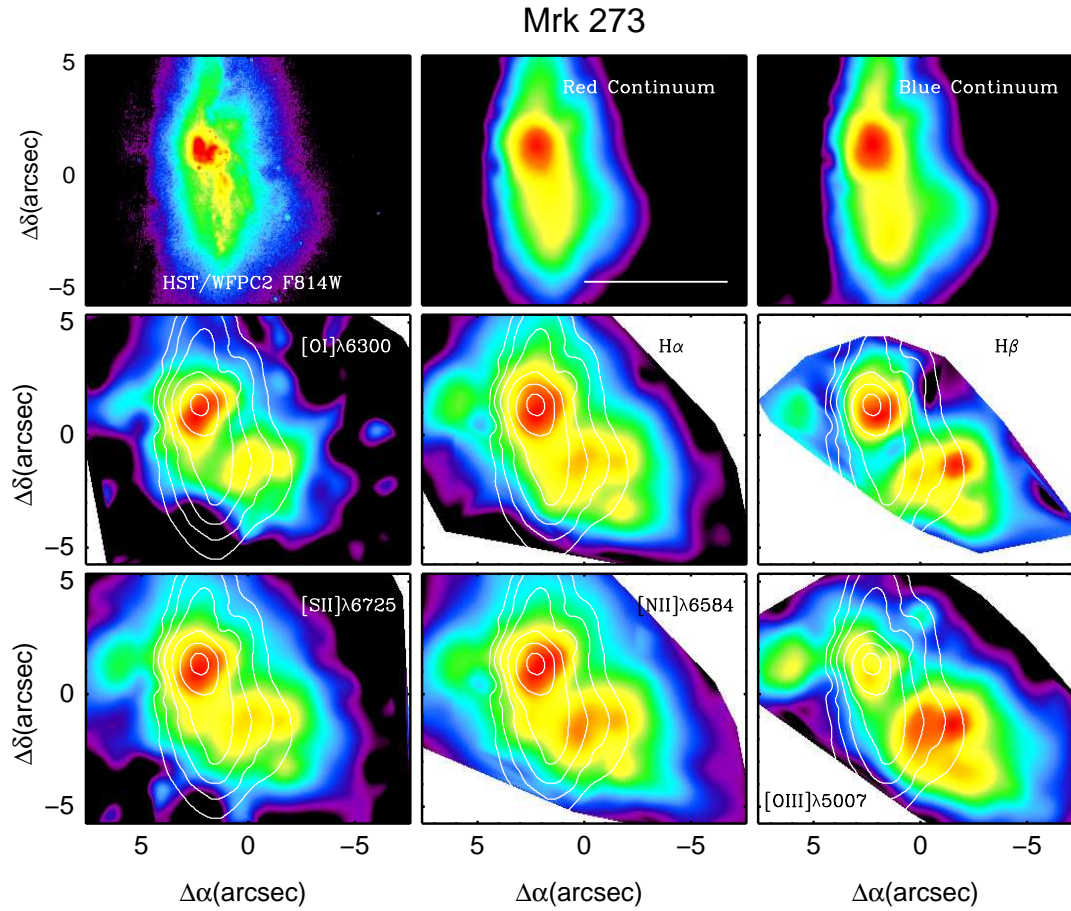


Figure B.17: Emission-line free stellar continua and emission-line images for Mrk 273 obtained with the INTEGRAL SB2 bundle. Contours represent the red continuum. The *HST*-WFPC2 F814W images is shown for comparison. All the images are shown in a logarithmic scale, and the color code represent different intensity levels in each of the individual maps. North is up, east to the left. The scale represents 5 kpc.

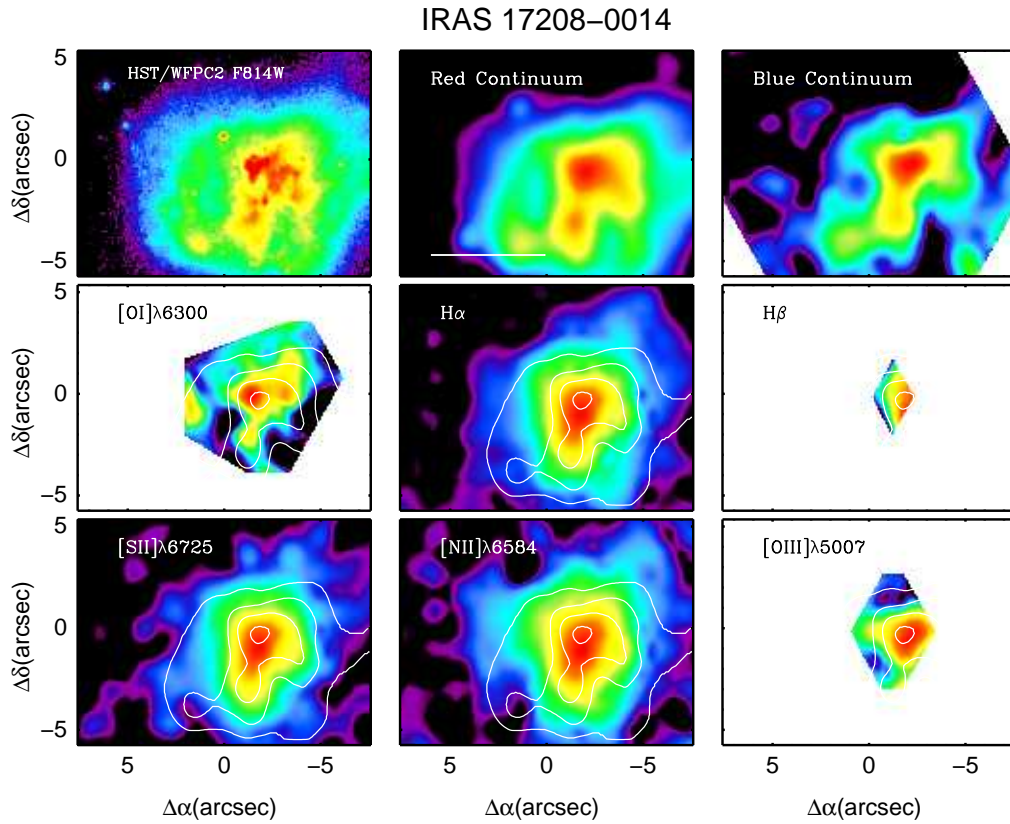


Figure B.18: Emission-line free stellar continua and emission-line images for IRAS 17208-0014 obtained with the INTEGRAL SB2 bundle. Contours represent the red continuum. The *HST*-WFPC2 F814W images is shown for comparison. All the images are shown in a logarithmic scale, and the color code represent different intensity levels in each of the individual maps. North is up, east to the left. The scale represents 5 kpc.

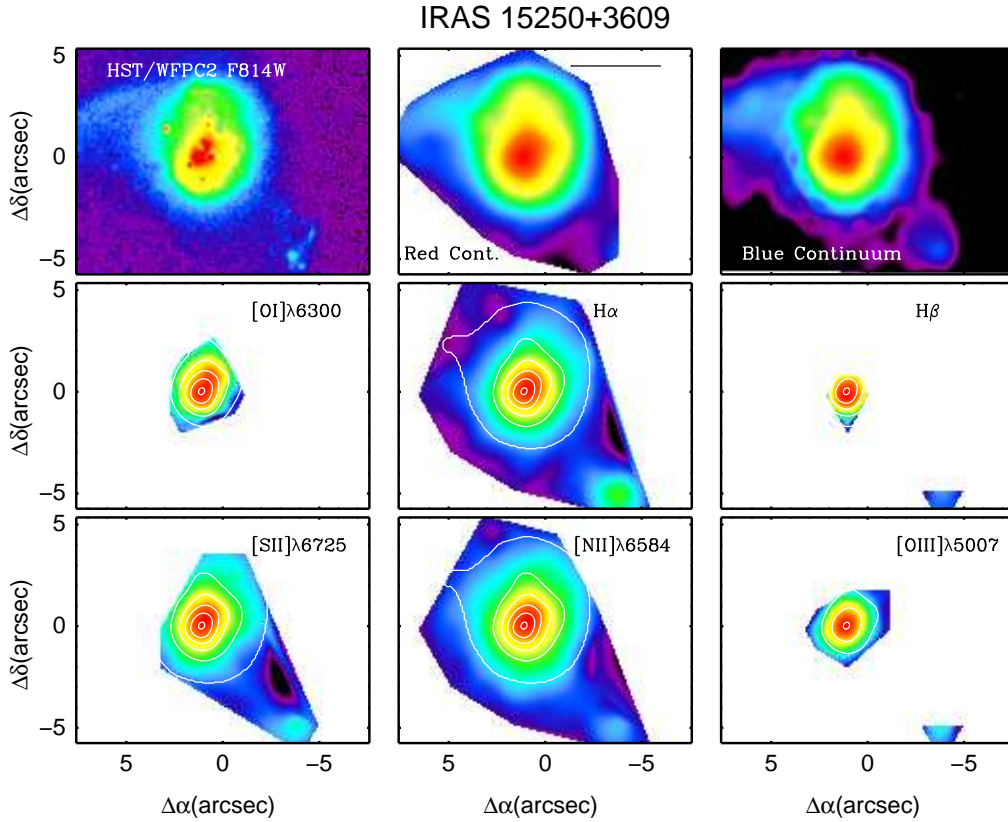


Figure B.19: Emission-line free stellar continua and emission-line images for IRAS 15250+3609 obtained with the INTEGRAL SB2 bundle. Contours represent the red continuum. The *HST*-WFPC2 F814W images is shown for comparison. All the images are shown in a logarithmic scale, and the color code represent different intensity levels in each of the individual maps. North is up, east to the left. The scale represents 5 kpc.

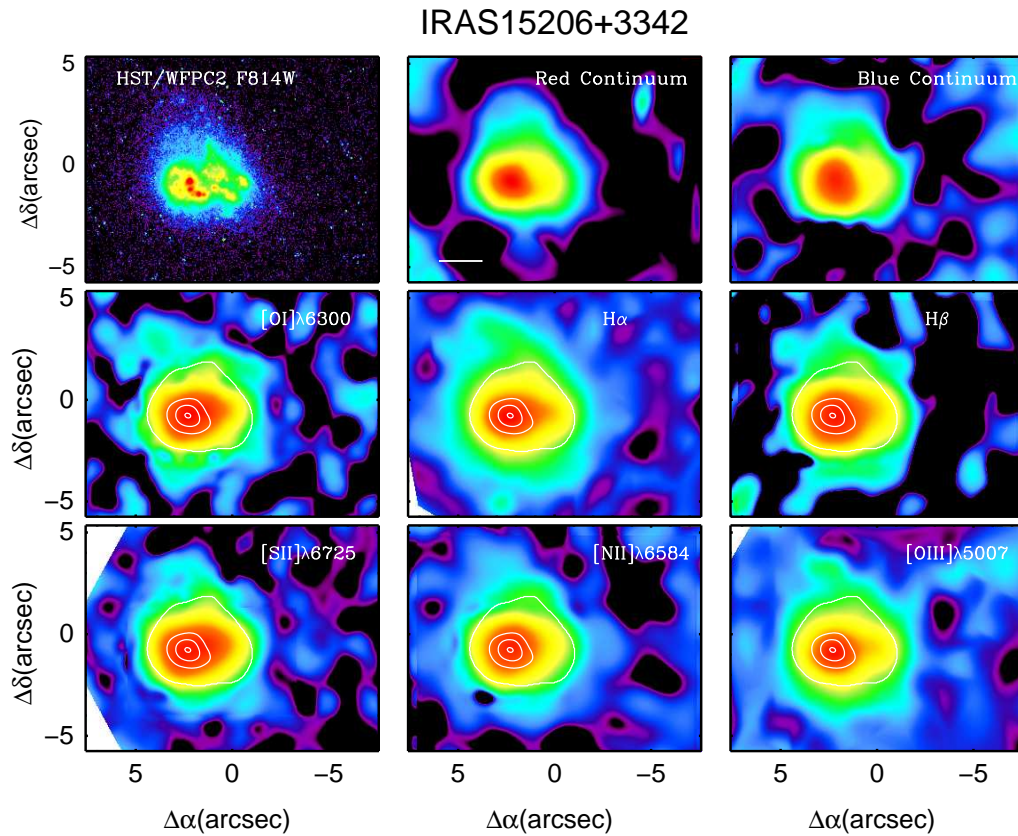


Figure B.20: Emission-line free stellar continua and emission-line images for IRAS 15206+3342 obtained with the INTEGRAL SB2 bundle. Contours represent the red continuum. The *HST*-WFPC2 F814W images is shown for comparison. All the images are shown in a logarithmic scale, and the color code represent different intensity levels in each of the individual maps. North is up, east to the left. The scale represents 5 kpc.

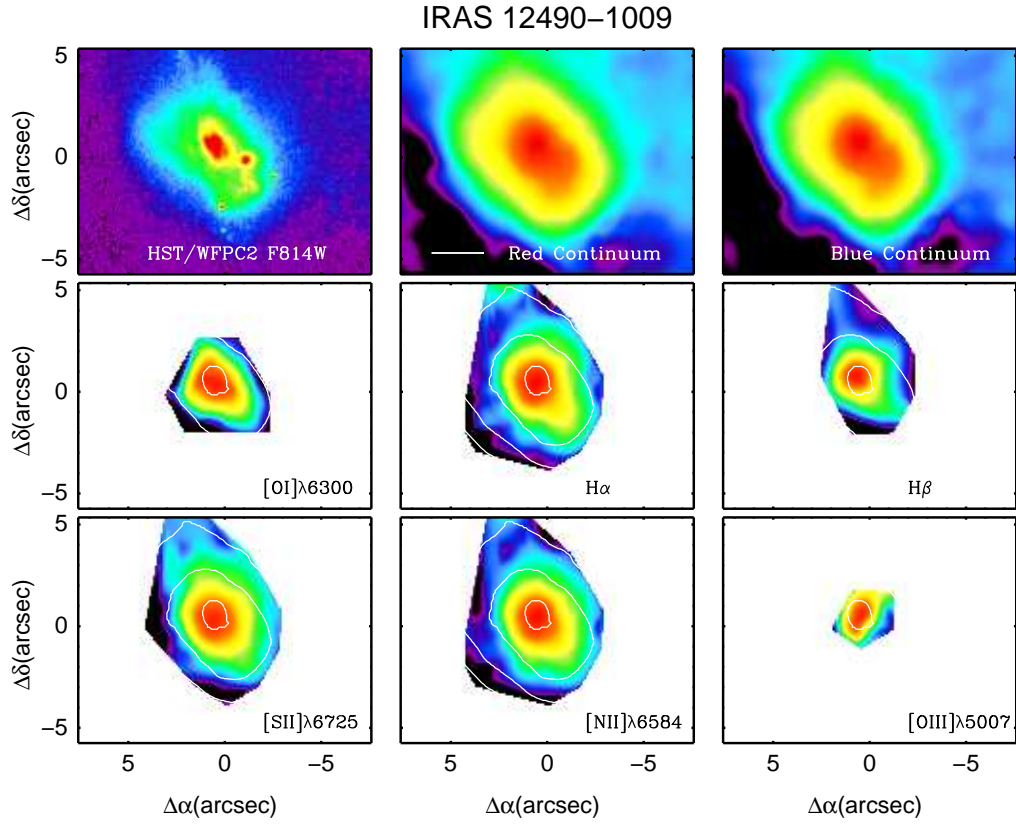


Figure B.21: Emission-line free stellar continua and emission-line images for IRAS 12490-1009 obtained with the INTEGRAL SB2 bundle. Contours represent the red continuum. The *HST*-WFPC2 F814W images is shown for comparison. All the images are shown in a logarithmic scale, and the color code represent different intensity levels in each of the individual maps. North is up, east to the left. The scale represents 5 kpc.

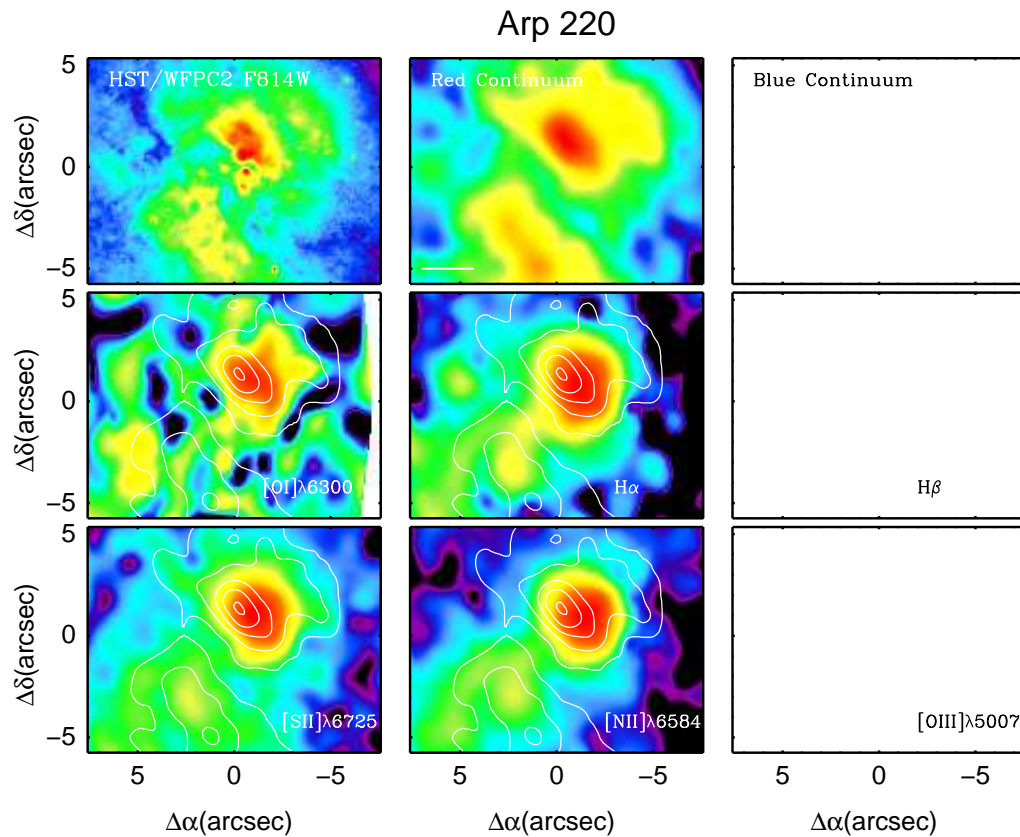


Figure B.22: Emission-line free stellar continua and emission-line images for Arp 220 obtained with the INTEGRAL SB2 bundle. Contours represent the red continuum. The *HST*-WFPC2 F814W images is shown for comparison. All the images are shown in a logarithmic scale, and the color code represent different intensity levels in each of the individual maps. North is up, east to the left. The scale represents 1 kpc. The blue region of the spectra was not covered.

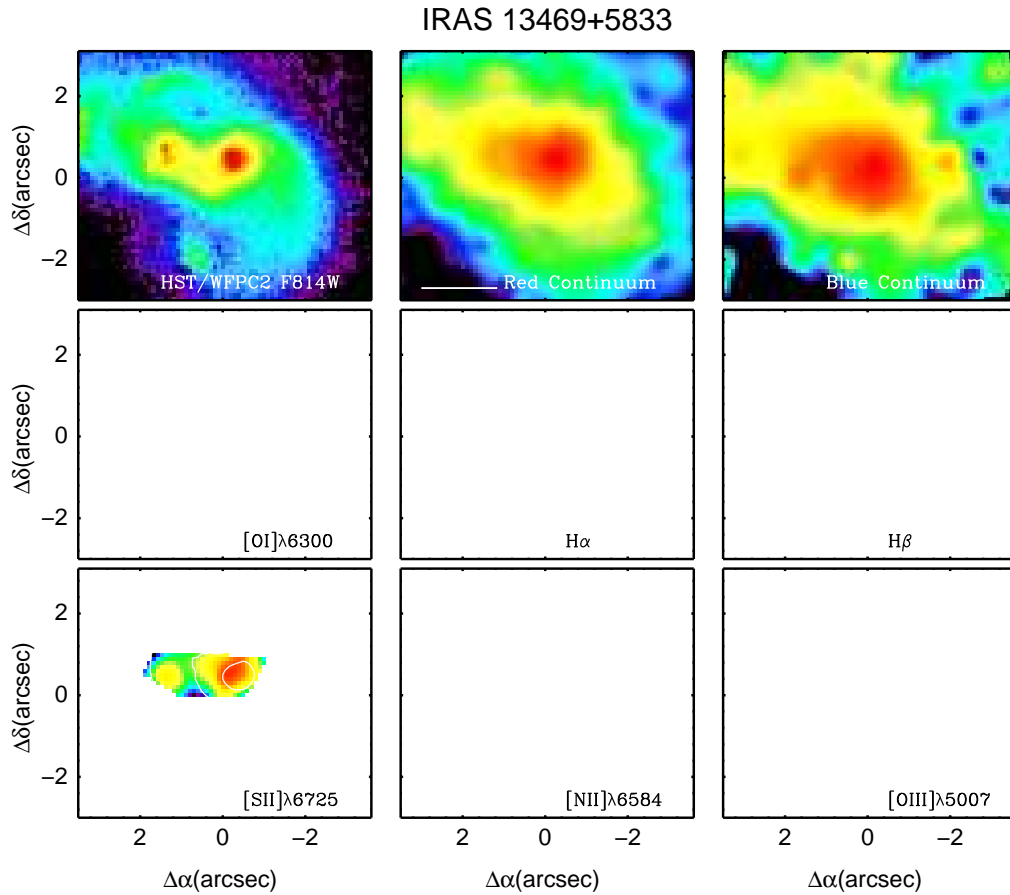


Figure B.23: Emission-line free stellar continua and emission-line images for IRAS 13469+5833 obtained with the INTEGRAL SB1 bundle. Contours represent the red continuum. The *HST*-WFPC2 F814W images is shown for comparison. All the images are shown in a logarithmic scale, and the color code represent different intensity levels in each of the individual maps. North is up, east to the left. The scale represents 5 kpc. The blank panels indicate no emission line detected.

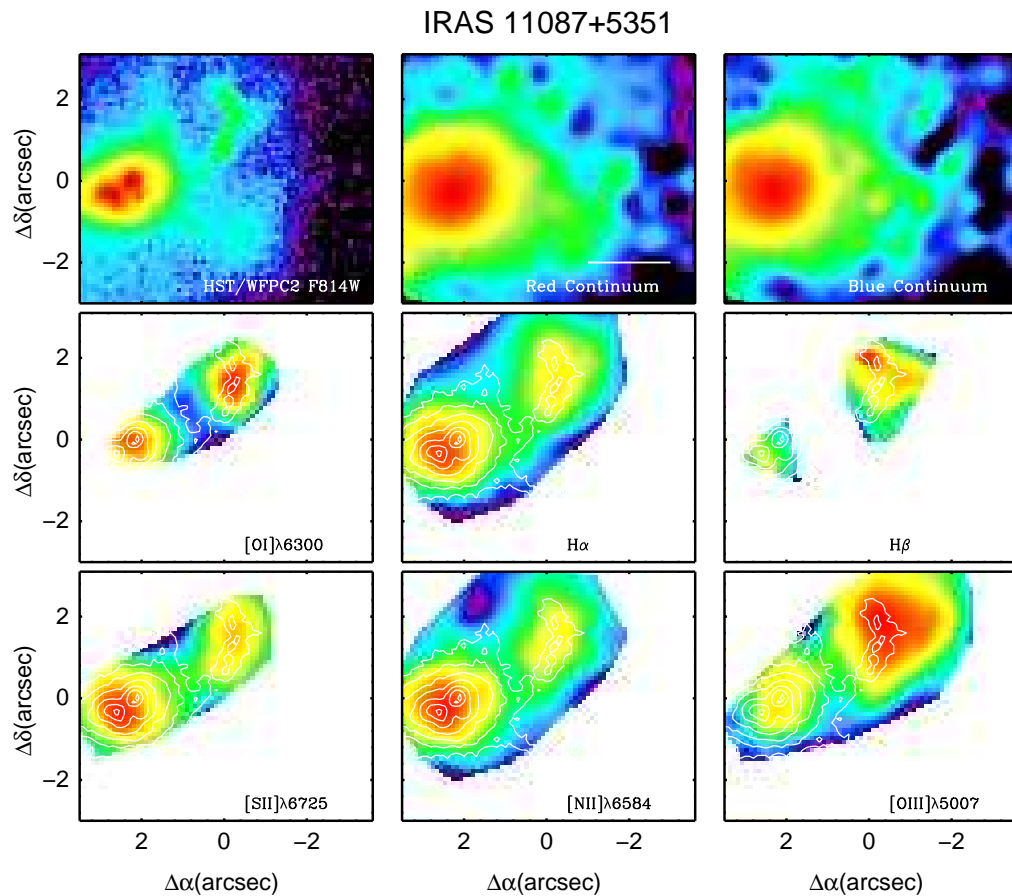


Figure B.24: Emission-line free stellar continua and emission-line images for IRAS 11087+5351 obtained with the INTEGRAL SB1 bundle. Contours represent the red continuum. The *HST*-WFPC2 F814W images is shown for comparison. All the images are shown in a logarithmic scale, and the color code represent different intensity levels in each of the individual maps. North is up, east to the left. The scale represents 5 kpc.

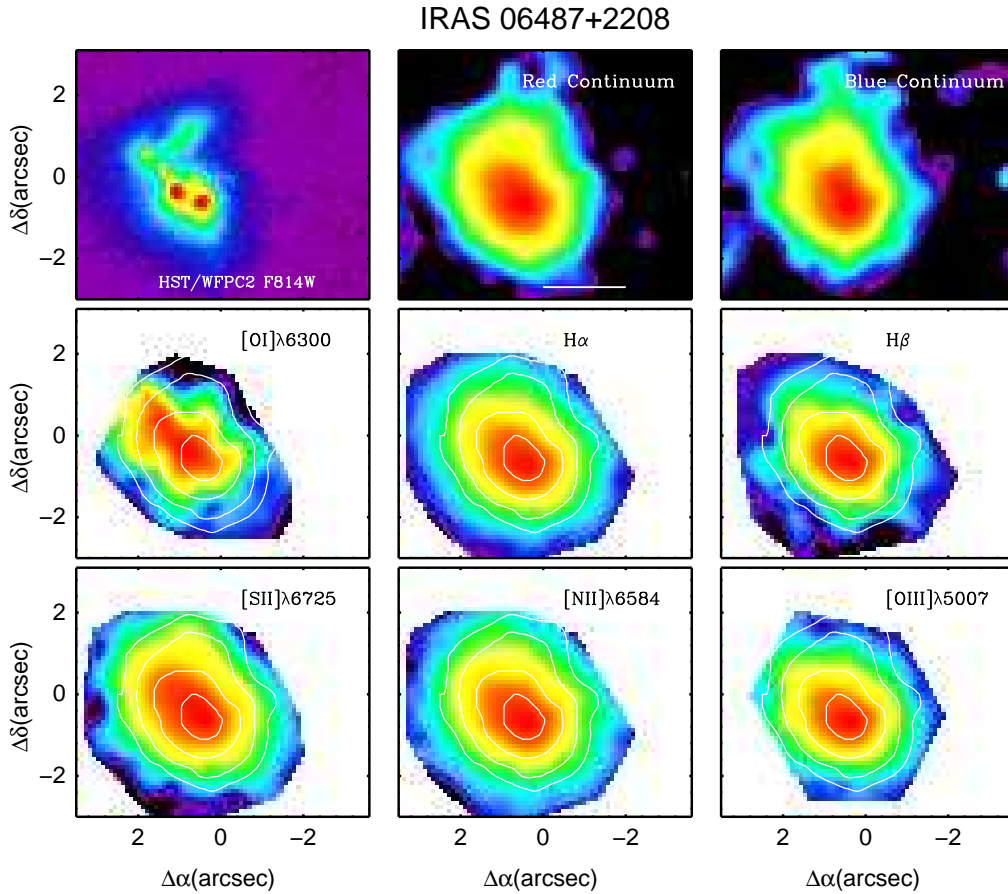


Figure B.25: Emission-line free stellar continua and emission-line images for IRAS 06487+2208 obtained with the INTEGRAL SB1 bundle. Contours represent the red continuum. The *HST*-WFPC2 F814W images is shown for comparison. All the images are shown in a logarithmic scale, and the color code represent different intensity levels in each of the individual maps. North is up, east to the left. The scale represents 5 kpc.

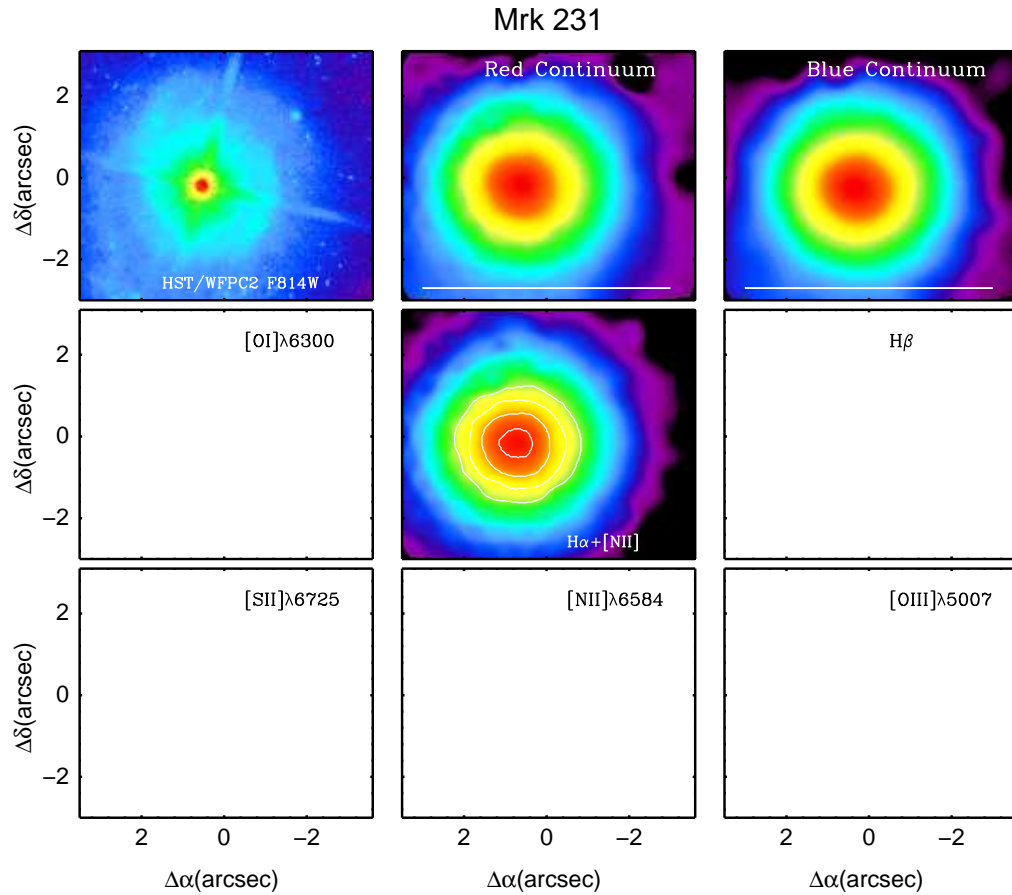


Figure B.26: Emission-line free stellar continua and emission-line images for Mrk 231 obtained with the INTEGRAL SB1 bundle. Contours represent the red continuum. The *HST*-WFPC2 F814W images is shown for comparison. All the images are shown in a logarithmic scale, and the color code represent different intensity levels in each of the individual maps. North is up, east to the left. The scale represents 5 kpc. The spectra is highly contaminated by the Seyfert, which preclude the detection of some lines.

Appendix C

Two-Dimensional Distribution of the Dust

This Appendix shows the two-dimensional distribution of the dust for the sample of ULIRGs, calculated using the Balmer decrement.

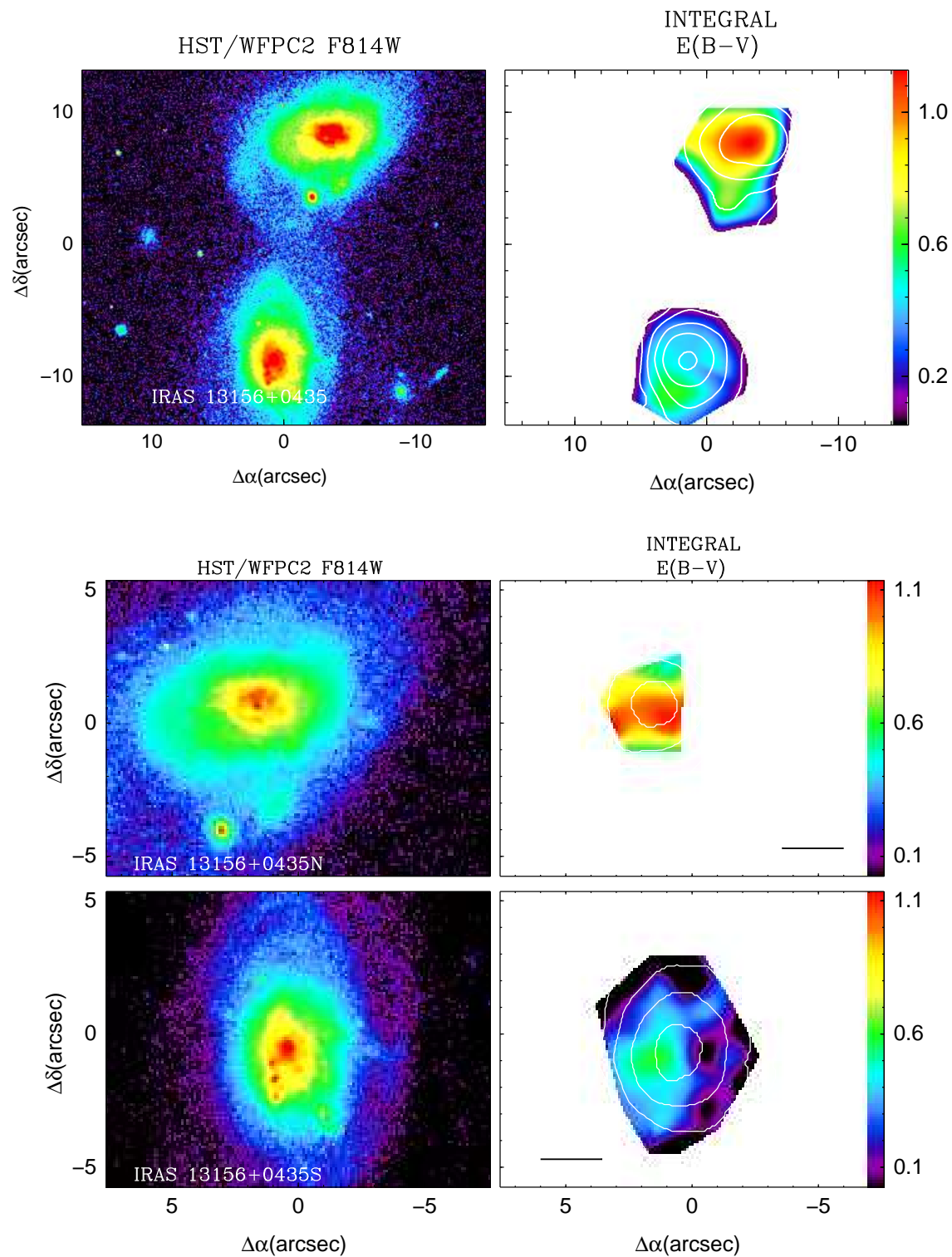


Figure C.1: Extinction maps derived for the two components of the system IRAS 13156+0435 observed with the SB3 (upper panel) and SB2 bundles (lower panels). The scale represents 10 kpc.

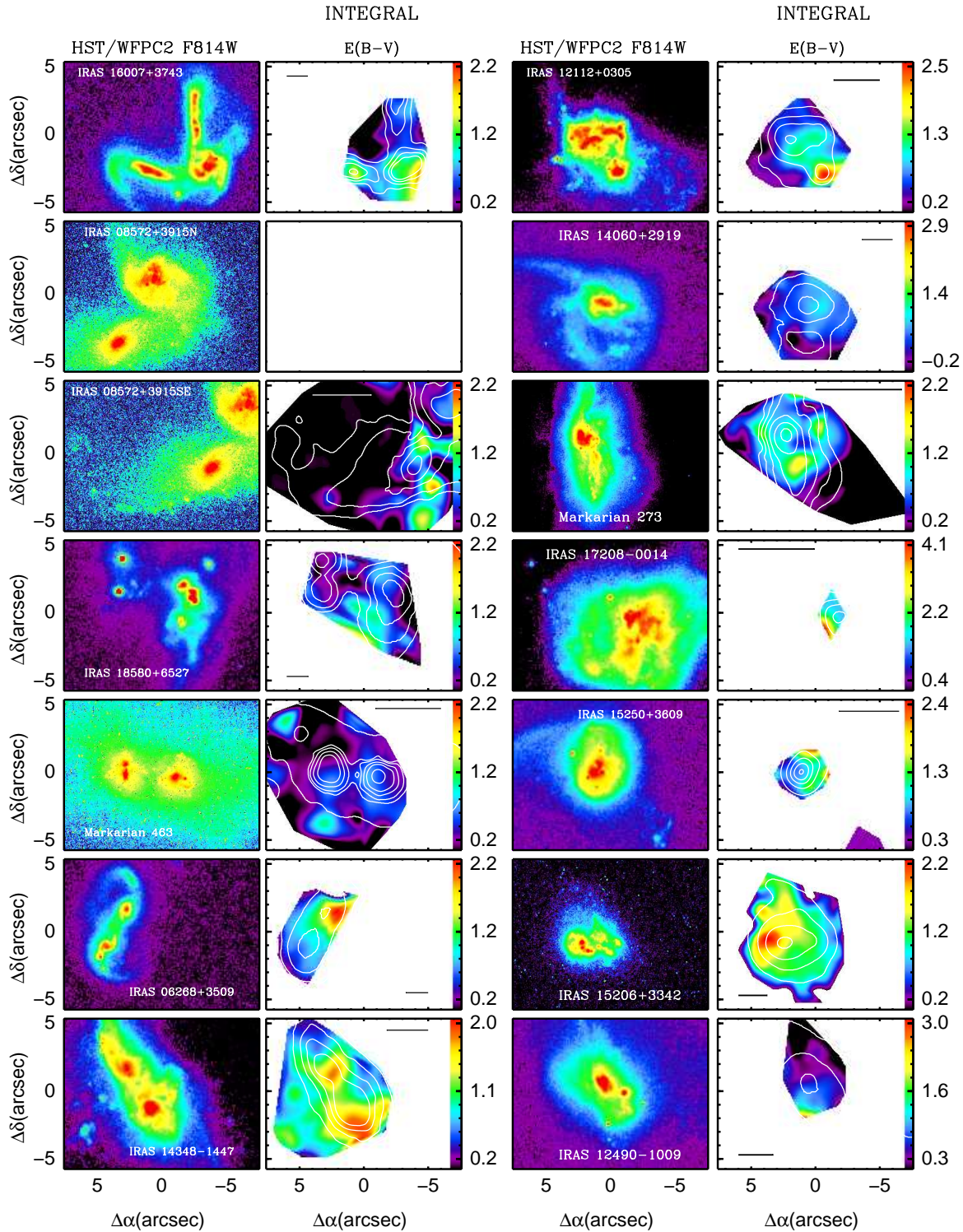


Figure C.2: Extinction maps derived for the sample of ULIRGs as observed with the SB2 bundle. The scale represents 5 kpc.

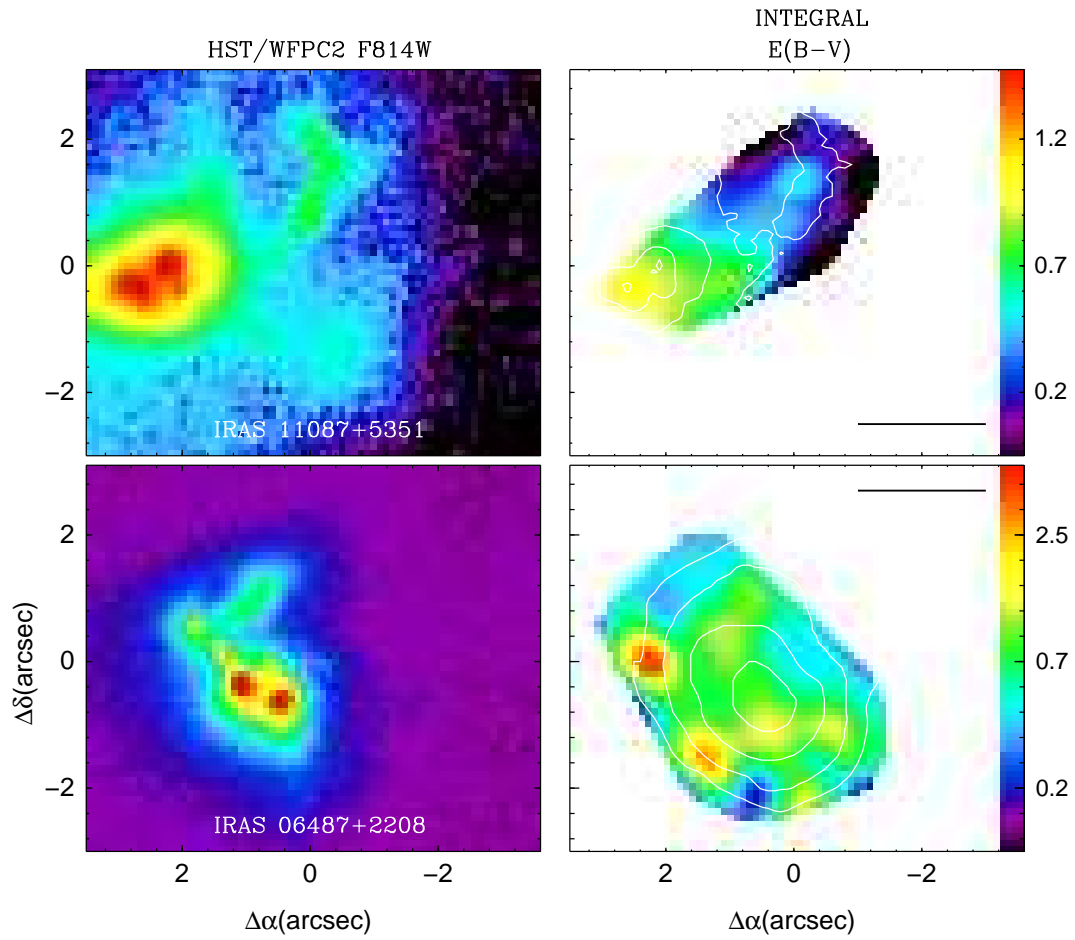


Figure C.3: Extinction maps derived for two ULIRGs of the sample observed with the SB1 bundle. The scale represents 5 kpc.

Appendix D

Reliability of the Classifications According to the BPT Diagrams

The optical BPT diagrams are one of the most extended and powerful tools for classifying the excitation state in emission line galaxies. Through the years, several working groups have derived different frontiers for separating the H II-, LINER- and Seyfert-like ionization. The most common-used classification has been that of Veilleux & Osterbrock (1987, from now on VO87), and more recently those from Kewley et al. (2001), Kauffmann et al. (2003) and Kewley et al. (2006) (from now on Ke06 see Fig. 4.1). Both classification schemes tend to be in well agreement when the galaxies under study are purely dominated by one process (e.g., star formation or AGN), but show inconsistencies for classifying galaxies with mixing processes like ULIRGs.

Through the present thesis, the Veilleux & Osterbrock (1987) classification has been applied. Nonetheless it is useful to compare the results using both sets of frontiers, testing their impact in the classification of ULIRGs. Furthermore, the classification proposed by Stasińska et al. (2006, from now on S06) using only the $[\text{N II}]/\text{H}\alpha$ lines ratio¹ is included in the comparison too (see Table D.1).

We find that galaxies with clear (i.e., agreement in two or three diagnostic) H II classification ($\sim 40\%$) show total agreement between the classifications from VO87 and Ke06. The S06 scheme assign NSF or hybrid galaxies. The same unambiguity is found among VO87 and Ke06 in found for galaxies classified as Seyfert ($\sim 20\%$). On the contrary, and because of the use of only one line ratio, S06 method is not capable of clearly separate Seyfert activity. Finally, $\sim 40\%$ are galaxies classified as LINER or close to the LINER frontier using the VO87, with no agreement with Ke06. In this case the limits established by S06 generally classify those objects Hybrid or AGN.

From this comparison we can conclude that when a galaxy is clearly dominated by star formation or AGN, the frontier selection does not lead to any difference in the classification. In the case of LINER or mixed (i.e. close to frontiers) classification, we find inconsistencies when using different frontiers. This reflects the mixed nature of LINER processes in ULIRGs, that are likely to be due to a combination of shocks and photo-ionization by star formation. The S06 classification based only on the $[\text{N II}]/\text{H}\alpha$ ratio is not adequate

¹The proposed limits are: (i) $\log([\text{N II}]/\text{H}\alpha) \leq -0.4$ NSF (Normal Star-Forming galaxies). (ii) $-0.4 < \log([\text{N II}]/\text{H}\alpha) \leq -0.2$ Hybrid. (iii) $\log([\text{N II}]/\text{H}\alpha) > -0.2$ AGN

Table D.1: Nuclear classification for the sample of ULIRGs with different classification schemes

Galaxy		[O I]/H α ^(a)	[N II]/H α ^(a)	[S II]/H α ^(a)	Classification ^(b)
IRAS 13156+0435N	Hybrid [†]	H II	H II	H II	H II
		H II	Comp	H II	H II
IRAS 13156+0435S	Hybrid [†]	H II/L	L	L	L
		H II/S	Comp	S	S:
IRAS 18580+6527E	NSF [†]	...	S	S	S
		...	S	S	S
IRAS 18580+6527W	Hybrid [†]	L	H II	H II	H II
		H II/S	Comp	H II	H II
IRAS 16007+3743E	Hybrid [†]	L	H II/L	H II/L	L
		H II/L	Comp	H II	?
IRAS 16007+3743W	Hybrid [†]	L	H II/L	H II	H II:
		S/H II	Comp	H II	H II:
IRAS 06268+3509N	Hybrid [†]	...	L	L	L
		...	S	S	S
IRAS 06268+3509S	Hybrid [†]	H II	H II	H II	H II
		H II	Comp	H II	H II
IRAS 08572+3915N	NSF [†]	H II	H II	L	H II
		H II	Comp	H II	H II
IRAS 08572+3915S	NSF [†]	H II/L	H II	H II	H II
		H II	H II	H II	H II
IRAS 14348–1447N	AGN [†]	L	L	L	L
		L	Comp	H II	Comp:
IRAS 14348–1447S	AGN [†]	L	L	L/H II	L
		L/S	Comp	H II	Comp:
Arp 299(NGC 3690)	Hybrid [†]	S	S	S	S
		S	S	S	S
Arp 299(IC 694)	Hybrid [†]	L	H II	H II/L	H II
		H II	Comp	H II	H II
IRAS 12112+0305N	NSF [†]	S/L	H II	S/L	S/L
		S	Comp	S	S
IRAS 12112+0305S		
		
Mrk 463E	Hybrid [†]	S	S	S	S
		S	S	S	S
Mrk 463W	AGN [†]	S	S	S	S
		S/L	S	S/L	S
IRAS 06487+2208	NSF [†]	H II	H II	H II	H II
		H II	Comp	H II	H II
IRAS 11087+5351E	AGN [†]	L	L	L	L
		L	S	S/L	L/S
IRAS 11087+5351W	AGN [†]	S	S	S	S
		S	S	S/L	S
IRAS 12490–1009	AGN [†]	L	H II/L	H II	H II/L
		H II	Comp	H II	H II
Mrk 273	AGN [†]	L	L	L	L
		S/L	S:	S/L	S/L
IRAS 14060+2919	Hybrid [†]	H II	H II	H II	H II
		H II	Comp	H II	H II
IRAS 15206+3342	NSF [†]	H II	H II	H II	H II
		H II	H II/Comp	H II	H II
IRAS 15250+3609	Hybrid [†]	L/H II	H II	H II	H II
		H II	H II	H II	H II
IRAS 17208–0014	Hybrid [†]	L	H II	L	L
		S/H II	H II/Comp	H II	H II:

Note: Nuclear classification for the ULIRGs of the sample. The † symbols below each galaxy identification shows the classification into NSF (Normal Star-Forming galaxies), Hybrid galaxies AGN galaxies using only the [N II]/H α line ratio (Stasińska et al. 2006). (a) Classification derived from the nuclear (observed) emission lines ration using the Veilleux & Osterbrock (1987) (first row) and the Kewley et al. (2006) (second row) frontiers. (b) Average classification. Colon indicates uncertain classification

for clearly separate ULIRGs dominated by AGN; in 50% of them S06 classify them as Hybrid objects.

Publications

Referred Publications

1. *VLT-VIMOS Integral Field Spectroscopy of Luminous and Ultraluminous Infrared Galaxies. I. The sample and first results*
Arribas, S., Colina, L., Monreal-Ibero, A., Alfonso, J., **García-Marín, M.**, & Alonso-Herrero, A. 2007, *A&A*, accepted
2. *Search for tidal dwarf galaxy candidates in a sample of ultraluminous infrared galaxies*
Monreal-Ibero, A., Colina, L., Arribas, S. & **García-Marín, M.** 2007, *A&A*, 472, 421
3. *Integral Field Spectroscopy of the Luminous Infrared Galaxy Arp 299 (IC 694 + NGC 3690)*
García-Marín, M., Colina, L., Arribas, S., Alonso-Herrero, A., & Mediavilla, E. 2006, *ApJ*, 650, 850
4. *Discovery of Blue Hook Stars in the Massive Globular Cluster M54*
Rosenberg, A., Recio-Blanco, A. & **García-Marín, M.** 2004, *ApJ*, 603, 135

Non-referred Publications

1. *Specsim: the MIRI medium resolution spectrometer simulator*
Lorente, N. P. F., Glasse, A. C. H., Wright, G. S. & **García-Marín, M.** 2006, SPIE (The International Society for Optical Engineering), 6274E
2. *Integral-field spectroscopy and HST imaging of ULIRGs at low and high redshift: IRAS 16007+3743*
García-Marín, M., Colina, L. & Arribas, S. 2005, *ASSL*, 329, 19
Proceedings of: Starbursts: From 30 Doradus to Lyman Break Galaxies, Held in Cambridge, UK, 6-10 September 2004. Edited by R. de Grijs and R.M. González Delgado. Astrophysics & Space Science Library, Vol. 329. Dordrecht: Springer, 2005, p. 19
3. *2D kinematics and mass derivations in ULIRGs*
García-Marín, M., Colina, L. Arribas, S. & Monreal-Ibero A. 2005 *ASSL*, 329, 173
Proceedings of: Starbursts: From 30 Doradus to Lyman Break Galaxies, Held in Cambridge, UK, 6-10 September 2004. Edited by R. de Grijs and R.M. González Delgado. Astrophysics & Space Science Library, Vol. 329. Dordrecht: Springer, 2005, p. 173

4. *3D spectroscopy of low-z (Ultra)Luminou Infrared Galaxies*

García-Marín, M., Colina, L. Arribas, Monreal-Ibero A., Alonso-Herrero, A., & Mediavilla, E.

To appear in the Proceeding of: ESO Workshop on Science Perspectives for 3D Spectroscopy. Edited by M. Kissler-Patig, M.M. Roth and J.R. Walsh and will be published in the Springer-Verlag series "ESO Astrophysics Symposia".

5. *Simulations of high-z starburst galaxies for the JWST-MIRI Integral Field Unit*

García-Marín, M., Lorente, N. P. F., Glasse, A., Colina L. & Wright, G.

To appear in the Proceeding of: ESO Workshop on Science Perspectives for 3D Spectroscopy. Edited by M. Kissler-Patig, M.M. Roth and J.R. Walsh, and will be published in the Springer-Verlag series "ESO Astrophysics Symposia".

6. *2D study of a Representative Sample of low-z (U)LIRGs using Integral Field Spectroscopy*

García-Marín, M., Colina, L., Arribas, S., A. Alonso-Herrero, & Monreal-Ibero, A.

To appear in the Proceeding of: At the Edge of the Universe: latest results from the deepest astronomical surveys. Edited by Afonso, J., Ferguson, H. & Norris, R., and will be published by the Astronomical Society of the Pacific Conference Series (ASPCS).

Bibliography

- Adelman-McCarthy, J. K., Agüeros, M. A., Allam, S. S., Anderson, K. S. J., Anderson, S. F., Annis, J., Bahcall, N. A., Baldry, I. K., Barentine, J. C., Berlind, A. & 131 coauthors 2006, *ApJS*, 162, 38
- Afanasyev, V. L., Vlasiouk, V. V. & Green, R. F. 1995, *ASPC*, 71, 266
- Allington-Smith, J. R. 2007, *RMxAC*, 28, 17
- Alonso-Herrero, A., Ward, M. J. & Kotilainen, J. K. 1997, *MNRAS*, 288, 977
- Alonso-Herrero, A., Simpson, C., Ward, M. J. & Wilson, A. S. 1998, *ApJ*, 495, 196
- Alonso-Herrero, A., Rieke, George H., Rieke, M. J. & Scoville, N Z. 2000, *ApJ*, 532, 845
- Alonso-Herrero, A., Rieke, M. J., Rieke, G. H. & Shields, J C. 2000b, *ApJ*, 530,688
- Alonso-Herrero, A., Rieke, G. H., Rieke, M. J., Colina, L., Pérez-González, P.G., & Ryder, S. D 2006, *ApJ*, 650, 835
- Anantharamaiah, K. R., Viallefond, F., Mohan, Niruj R., Goss, W. M. & Zhao, J. H. 2000, *ApJ*, 537, 613
- Armus, L., Heckman, T. M. & Miley, G. K. 1989, *ApJ*, 347, 727
- Armus, L., Charmandaris, V., Bernard-Salas, J., Spoon, H. W. W., Marshall, J. A., Higdon, S. J. U., Desai, V., Teplitz, H. I., Hao, L., Devost, D. & 6 coauthors 2007, *ApJ*, 656, 148
- Arribas, S., Mediavilla, E. & Rasilla, J. L. 1991, *ApJ*, 369, 260
- Arribas, S., Carter, D., Cavaller, L., del Burgo, C., Edwards, R., Fuentes, F. J., Garcia, A. A., Herreros, J. M., Jones, L. R., Mediavilla, E. & 5 coauthors *SPIE*, 3355, 821
- Arribas, S., Colina, L. & Borne, K. 1999, *Ap&SS*, 266, 143
- Arribas, S., Colina, L. & Borne, K. D. 2000, *ApJ*, 545, 228
- Arribas, S., Colina, L. & Clements, D. 2001, *ApJ*, 560, 160
- Arribas, S., & Colina, L. 2002, *ApJ*, 573, 576
- Arribas, S., Colina, L., 2003, *ASP Conference Proceedings*, 297, 24-28
- Bacon, R., Adam, G., Baranne, A., Courtes, G., Dubet, D., Dubois, J. P., Emsellem, E., Ferruit, P., Georgelin, Y., Monnet, G. & 3 coauthors, 1995, *A&AS*, 113, 347
- Barden, S. C. & Wade, R. A. 1988, *ASPC*, 3, 113
- Barth, A. J. & Shields, J. C. 2000, *PASP*, 112, 753
- Baldwin, J. A., Phillips, M. M., & Terlevich, R. 1981, *PASP*, 93, 5
- Barnes, J. E. & Hernquist, L. 1996, *ApJ*, 471, 115

- Barnes, J. E. 2002, *MNRAS*, 333, 481
- Barth, A. J. & Shields, J. C. 2000, *PASP*, 112, 753
- Beckwith, S. V. W., Stiavelli, M., Koekemoer, A. M., Caldwell, J. A. R., Ferguson, H. C., Hook, R., Lucas, R. A., Bergeron, L. E., Corbin, M., Jøgee, S. & 5 coauthors 2006, *AJ*, 132, 1729
- Bekki, K. & Shioya, Y. 1997, *ApJ*, 478L, 17
- Bekki, K., Shioya, Y. & Whiting, M. 2006, *MNRAS*, 371, 805
- Bender, R., Burstein, D. & Faber, S. M. 1992, *ApJ*, 399, 462
- Bender, R., Saglia, R. P., Ziegler, B., Belloni, P., Greggio, L., Hopp, U. & Bruzual, G. 1998, *ApJ*, 493, 529
- Bendo, G. J. & Barnes, J. E. 2000, *MNRAS*, 316, 315
- Bertoldi, F., Carilli, C. L., Menten, K. M., Owen, F., Dey, A., Gueth, F., Graham, J. R., Kreysa, E., Ledlow, M., Liu, M. C., & 4 coauthors 2000, *A&A*, 360, 92
- Binette, L., Magris, C. G., Stasińska, G. & Bruzual, A. G. 1994, *A&A*, 292, 13
- Binney, J. 1978, *MNRAS*, 183, 501
- Blain, A. W., Smail, Ian, Ivison, R. J., & Kneib, J.P. 1999, *MNRAS*, 302, 4, 632
- Blain, A. W., Smail, I., Ivison, R., Kneib, J., & Frayer, D. 2002, *PhR*, 369, 111
- Blanton, M. R. 2006, *ApJ*, 648, 268
- Boller, T., Bertoldi, F., Dennefeld, M. & Voges, W. 1998, *A&AS*, 129, 87
- Bondi, M., Pérez-Torres, M.A., Dallacasa, D. & Muxlow, T. W. B. 2005, *MNRAS*, 361, 748
- Borne, K.D., Bushouse, H., Lucas, R. A., & Colina, L. 2000, *ApJ*, 529L, 77
- Bowen, I. S. 1938, *ApJ*, 88, 113
- Braito, V., Della Ceca, R., Piconcelli, E., Severgnini, P., Bassani, L., Cappi, M., Franceschini, A., Iwasawa, K., Malaguti, G., Marziani, P. & 4 coauthors 2004, *A&A*, 420, 79
- Bruzual A. G., & Charlot, S. 1993, *ApJ*, 405, 538-553
- Bryant, P. M. & Scoville, N. Z. 1999, *AJ*, 117, 2632
- Bushouse, H. A., Borne, K. D., Colina, L., Lucas, R. A., Rowan-Robinson, M., Baker, A. C., Clements, D. L., Lawrence, A. & Oliver, S. 2002, *ApJS*, 138, 1
- Capak, P., Aussel, H., Ajiki, M., McCracken, H. J., Mobasher, B., Scoville, N., Shopbell, P., Taniguchi, Y., Thompson, D., Tribiano, S. & 48 coauthors 2007, *ApJS*, 172, 99
- Carilli, C. L., Wrobel, J. M., & Ulvestad, J. S. 1998, *AJ*, 115, 928
- Carilli, C. L. & Yun, M. S. 2000, *ApJ*, 530, 618
- Cecil, G., Bland-Hawthorn, J., Veilleux, S. & Filippenko, A. V. 2001, *ApJ*, 555, 338
- Chapman, S. C., Blain, A. W., Ivison, R. J., Smail, & Ian R. 2003, *Nature*, 422, 695
- Cimatti, A., Daddi, E., Renzini, A., Cassata, P., Vanzella, E., Pozzetti, L., Cristiani, S., Fontana, A., Rodighiero, G., Mignoli, M., & Zamorani, G. 2004, *Nature*, 430, 184
- Coccatto, L., Corsini, E. M., Pizzella, A. & Bertola, F. 2007, *A&A*, 465, 777

- Cole, S., Norberg, P., Baugh, C. M., Frenk, C. S., Bland-Hawthorn, J., Bridges, T., Cannon, R., Colless, M., Collins, C., Couch, W. & 17 coauthors 2001, *MNRAS*, 326, 255
- Colina, L., & Pérez-Olea, D. 1992, *MNRAS*, 259, 709
- Colina, L. & Pérez-Olea, D. E. 1995, *MNRAS*, 277, 845
- Colina, L. & Arribas, S. 1999, *ApJ*, 514, 637
- Colina, L., Arribas, S. & Borne, K. D. 1999, *ApJ*, 527L, 13
- Colina, L., Arribas, S., Borne, K. D. & Monreal, A. 2000, *ApJ*, 533L, 9
- Colina, L., Arribas, S. & Borne, K. D. 2001, *Ap&SSS*, 277, 413
- Colina, L., Borne, K., Bushouse, H., Lucas, R. A., Rowan-Robinson, M., Lawrence, A., Clements, D., Baker, A., & Oliver, S. 2001b, *ApJ*, 563, 546
- Colina, L., Arribas, S. & Monreal-Ibero, A. 2005, *ApJ*, 621, 725
- Colless, M., Dalton, G., Maddox, S., Sutherland, W., Norberg, P., Cole, S., Bland-Hawthorn, J., Bridges, T., Cannon, R., Collins, C. & 19 coauthors 2001, *MNRAS*, 328, 1039
- Combes, F., Rampazzo, R., Bonfanti, P. P., Pringniel, P. & Sulentic, J. W. 1995, *A&A*, 297, 37
- Condon, J. J., & Broderick, J. J. 1991, *AJ*, 102, 1663-1679
- Conselice, Christopher J. 2003, *ApJS*, 147, 1-28
- Courteau, S. 1997, *AJ*, 114, 2402
- Courtes, G. 1982, *ASSL*, 92, 123
- Croton, D. J., Springel, V., White, S. D. M., De Lucia, G., Frenk, C. S., Gao, L., Jenkins, A., Kauffmann, G., Navarro, J. F. & Yoshida, N. 2006, *MNRAS*, 365, 11
- Cui, J., Xia, X.-Y., Deng, Z.-G., Mao, S. & Zou, Z.-L. 2001, *AJ*, 122, 63
- Darling, J. & Giovanelli, R. 2006, *AJ*, 132, 2596
- Dasyra, K. M., Tacconi, L. J., Davies, R. I., Naab, T., Genzel, R., Lutz, D., Sturm, E., Baker, A. J., Veilleux, S., Sanders, D. B., & Burkert, A. 2006, *ApJ*, 651, 835
- del Burgo, C. 2000, PhD Thesis, Universidad de La Laguna
- Della Ceca, R., Ballo, L., Tavecchio, F., Maraschi, L., Petrucci, P. O., Bassani, L., Cappi, M., Dadina, M., Franceschini, A., Malaguti, G., & et al. 2002, *ApJ*, 581, 9
- Di Matteo, T., Springel, V. & Hernquist, L. 2005, *Nature*, 433, 604
- Dinh-V-Trung, Lo, K. Y., Kim, D.C., Gao, Y. & Gruendl, R. A. 2001, *ApJ*, 556, 141
- Djorgovski, S. & Davis, M. 1987, *ApJ*, 313, 59
- Dopita, M. A. & Sutherland, R. S. 1995, *ApJ*, 455, 468
- Downes, D., Solomon, P., & Radford, S. 1993, *ApJ*, 414, 13
- Downes, D. & Eckart, A. 2007, astro-ph/07062599
- Dressler, A., Lynden-Bell, D., Burstein, D., Davies, R. L., Faber, S. M., Terlevich, R. & Wegner, G. 1987, *ApJ*, 313, 42
- Duc, P., Bournaud, F., & Masset, F., 2004, *A&A*, 427, 803

- Eales, S., Bertoldi, F., Ivison, R., Carilli, C., Dunne, L., & Owen, F. 2003, *MNRAS*, 344, 169
- Elbaz, D., Arnaud, M., Casse, M., Mirabel, I. F., Prantzos, N., & Vangioni-Flam, E. 1992, *A&A*, 265L, 29
- Evans, A. S., Mazzarella, J. M., Surace, J. A., & Sanders, D. B. 2002, *ApJ*, 580, 749
- Faber, S. M., Tremaine, S., Ajhar, E. A., Byun, Y., Dressler, A., Gebhardt, K., Grillmair, C., Kormendy, J., Lauer, T. R. & Richstone, D. 1996, *AJ*, 114, 1771
- Fabian, A. C., Nulsen, P. E. J. & Canizares, C. R. 1984, *Nature*, 310, 733
- Fabian, A. C. 2003, *MNRAS*, 344L, 27
- Farrah, D., Rowan-Robinson, M., Oliver, S., Serjeant, S., Borne, K., Lawrence, A., Lucas, R. A., Bushouse, H., & Colina, L. 2001, *MNRAS*, 326, 1333
- Farrah, D., Afonso, J., Efstathiou, A., Rowan-Robinson, M., Fox, M. & Clements, D. 2003, *MNRAS*, 343, 585
- Floyd, D. J. E., Kukula, M. J., Dunlop, J. S., McLure, R. J., Miller, L., Percival, W. J., Baum, S. A. & O'Dea, C. P. 2004, *MNRAS*, 355, 196
- Franceschini, A., Braitto, V., Persic, M., Della Ceca, R., Bassani, L., Cappi, M., Malaguti, P., Palumbo, G. G. C., Risaliti, G., Salvati, M., & Severgnini, P. 2003, *MNRAS*, 343, 1181
- Gallais, P., Charmandaris, V., Le Floch, E., Mirabel, I. F., Sauvage, M., Vigroux L., & Laurent O. 2004, *A&A*, 414, 845
- Gamow, G. 1946, *Phys. Rev.* 70, 572
- García-Lorenzo, B., Acosta-Pulido, J. A., & Megias-Ferez, E. 2002, *ASP Conference Proceedings*, 282
- García-Marín, M., Colina, L., Arribas, S., Alonso-Herrero, A. & Mediavilla, E. 2006, *ApJ*, 650, 850
- Gehrz, R. D., Sramek, R. A. & Weedman, D. W. 1983, *ApJ*, 267, 551
- Genzel, R., Lutz, D., Sturm, E., Egami, E., Kunze, D., Moorwood, A. F. M., Rigopoulou, D., Spoon, H. W. W., Sternberg, A., Tacconi-Garman, L. E., & 2 coauthors 1998, *ApJ*, 498, 579
- Genzel, R., Tacconi, L. J., Rigopoulou, D., Lutz, D., & Tecza, M. 2001, *ApJ*, 563, 527
- Gialalisco, M., Steidel, C., Adelberger, K., Dickinson, Mark E., Pettini, M., & Kellogg, M. 1998, *ApJ*, 503, 543
- Gialalisco, M., Ferguson, H. C., Koekemoer, A. M., Dickinson, M., Alexander, D. M., Bauer, F. E., Bergeron, J., Biagetti, C., Brandt, W. N., Casertano, S. & 47 coauthors 2004, *ApJ*, 600L, 93
- Glass, I. S. 1999, Cambridge University Press, *Handbook of Infrared Astronomy*
- Goldader, J. D., Joseph, R. D., Doyon, R. & Sanders, D. B. 1995, *ApJ*, 444, 97
- Goldader, J. D., Joseph, R. D., Doyon, R. & Sanders, D. B. 1997, *ApJS*, 108, 449
- Graciá-Carpio, J., Planesas, P. & Colina, L. 2007, *A&A*, 468L, 67
- Greve, T. R., Ivison, R. J., Bertoldi, F., Stevens, J. A., Dunlop, J. S., Lutz, D. & Carilli, C. L. 2004, *MNRAS*, 354, 779
- Groves, B. A., Dopita, M. A. & Sutherland, R. S. 2004, *ApJS*, 153, 75
- Harper, D. A. & Low, F. J. 1973, *ApJ*, 182L, 89

- Hauser, M. G., Arendt, R. G., Kelsall, T., Dwek, E., Odegard, N., Weiland, J. L., Freudenreich, H. T., Reach, W. T., Silverberg, R. F., Moseley, S. H., & 8 coauthors 1998, *ApJ*, 508, 25
- Heckman, T. M. 1981, *ApJ*, 250L, 59
- Heckman, T., Armus, L., & Miley, G. 1990, *ApJS*, 74, 833
- Heckman, T. M., Dahlem, M., Eales, S. A., Fabbiano, G. & Weaver, K. 1996, *ApJ*, 457, 616
- Helou, G., Soifer, B. T. & Rowan-Robinson, M. 1985, *ApJ*, 298L, 7
- Hernquist, L. 1993, *ApJ*, 409, 548
- Ho, L., Filippenko, A., & Sargent, W. 1993, *ApJ*, 417, 63
- Hopkins, P. F., Hernquist, L., Martini, P., Cox, T. J., Robertson, B., Di Matteo, T. & Springel, V. 2005, *ApJ*, 625L, 71
- Hopkins, P. F., Bundy, K., Hernquist, L. & Ellis, R. S. 2007, *ApJ*, 659, 976
- Howarth, I. D., & Murray, J. 1988, DIPS0 A Friendly Spectrum Analysis Program (Starlink User Note 50; Chilton: Rutherford Appleton Lab.)
- Iglesias-Páramo J., & Vílchez J. M. 2001, *ApJ*, 550, 204
- Imanishi, M., Dudley, C. C., Maiolino, R., Maloney, P. R., Nakagawa, T. & Risaliti, G. 2007, *ApJS*, 171, 72
- Iverson, R. J., Smail, I., Le Borgne, J.-F., Blain, A. W., Kneib, J.-P., Bezecourt, J., Kerr, T. H. & Davies, J. K. 1998, *MNRAS*, 298, 583
- Iverson, R. J., Greve, T. R., Smail, I., Dunlop, J. S., Roche, N. D., Scott, S. E., Page, M. J., Stevens, J. A., Almaini, O., Blain, A. W., & 5 coauthors 2002, *MNRAS*, 337, 1
- Iverson, R. J., Greve, T. R., Serjeant, S., Bertoldi, F., Egami, E., Mortier, A. M. J., Alonso-Herrero, A., Barmby, P., Bei, L., Dole, H. & and 19 coauthors 2004, *ApJS*, 154, 124
- James, P., Bate, C., Wells, M., Wright, G. & Doyon, R. 1999, *MNRAS*, 309, 585
- Jesseit, R., Naab, T., Peletier, R. F. & Burkert, A. 2007, *MNRAS*, 376, 997
- Kapany, N. 1958, in *Concepts of Classical Optics*, Ed. Strong, Feeman publish, (San Francisco).
- Kaufmann, G. et al. 2003, *MNRAS*, 346, 1055
- Kennicutt, R. C., Chu, & You-Hua 1988, *AJ*, 95, 720
- Kewley, L. J., Dopita, M. A., Sutherland, R. S., Heisler, C. A., & Trevena, J. 2001a, *ApJ*, 556, 121
- Kewley, L. J., Groves, B., Kauffmann, G. & Heckman, T. 2006, *MNRAS*, 372, 961
- Kim, D.-C., Sanders, D. B., Veilleux, S., Mazzarella, J. M., & Soifer, B. T. 1995, *ApJS*, 98, 129
- Kim, D. C., Veilleux, S. & Sanders, D. B. 1998, *ApJ*, 508, 627
- Kormendy, J. & Illingworth, G. 1982, *ApJ*, 256, 460
- Kormendy, J. & Norman, C. A. 1979, *ApJ*, 233, 539
- Kormendy, J. & Sanders, D. B. 1992, *ApJ*, 390L, 53
- Krabbe, A., Thatte, N. A., Kroker, H., Tacconi-Garman, L. E. & Tecza, M. 1997, *SPIE*, 2871, 1179
- Krumm, N. & Salpeter, E. E. 1977, *A&A*, 56, 465

- Larson, R. B., & Tinsley, B. M. 1978, *ApJ*, 219, 46
- Lehnert, M. D. & Heckman, T. M. 1996, *ApJ*, 462, 651
- Leitherer, C., Schaerer, D., Goldader, J. D., Delgado, R. M., Robert, C., Kune, D. F., de Mello, D. F., Devost, D., & Heckman, T. M. 1999, *ApJS*, 123, 3
- Lequeux, J. 1983, *A&A*, 125, 394
- Li, A. 2005, *ApJ*, 622, 965
- Lonsdale, C. J., Lonsdale, C. J., Smith, H. E. & Diamond, P. J. 2003, *ApJ*, 592, 804
- Lonsdale, C., Farrah, D. & Smith, H. 2006, astro-ph/0603031
- Lotz, J. M., Madau, P., Giavalisco, M., Primack, J. & Ferguson, H. C. 2006, *ApJ*, 636, 592
- Low, J., Kleinmann, & D. E. 1968, *AJ*, 73, 868
- Lutz, D., Veilleux, S. & Genzel, R. 1994, *ApJ*, 517L, 13
- Lutz, D., Spoon, H. W. W., Rigopoulou, D., Moorwood, A. F. M. & Genzel, R. 1998, *ApJ*, 505L, 103
- Lutz, D., Valiante, E., Sturm, E., Genzel, R., Tacconi, L. J., Lehnert, M. D., Sternberg, A. & Baker, A. J. 2005, *ApJ*, 625L, 83
- Martin, C. L. 2005, *ApJ*, 621, 227
- McCarthy, P. J., Le Borgne, D., Crampton, D., Chen, H., Abraham, R. G., Glazebrook, K., Savaglio, S., Carlberg, R. G., Marzke, R. O., Roth, K. & 4 coauthors 2004, *ApJ*, 614L, 9
- McDowell, J. C., Clements, D. L., Lamb, S. A., Shaked, S., Hearn, N. C., Colina, L., Mundell, C., Borne, K., Baker, A. C. & Arribas, S. 2003, *ApJ*, 591, 154
- Mihalas D., & Binney J. 1981, *Galactic Astronomy: Structure and kinematics*, 2nd edition, San Francisco, CA, W. H. Freeman and Co.
- Mihos, J. C. & Hernquist, L. 1994, *ApJ*, 431L, 9
- Mihos, J. C. & Hernquist, L. 1996, *ApJ*, 464, 641
- Mihos, J. C. 1999, *Ap&SS*, 266, 195
- Miller, J. S. & Goodrich, R. W. 1990, *ApJ*, 355, 456
- Momjian, E., Romney, J. D., Carilli, C. L., Troland, T. H. & Taylor, G. B. 2003, *ApJ*, 587, 160
- Monreal-Ibero, A. 2004, PhD Thesis, Universidad de La Laguna
- Monreal-Ibero, A., Arribas, S. & Colina, L. 2006, *ApJ*, 637, 138
- Monreal-Ibero, A., Colina, L., Arribas, S. & García-Marín, M. 2007, *A&A*, 472, 421
- Moshir, M., Copan, G., Conrow, T., McCallon, H., Hacking, P., Gregorich, D., Rohrbach, G., Melnyk, M., Rice, W., & Fullmer, L. 1993, *VizieR On-line Data Catalog: II/156A*
- Moy, E., Rocca-Volmerange, B. & Fioc, M. 2001, *A&A*, 365, 347
- Mulchaey, J. S., Wilson, A. S. & Tsvetanov, Z. 1996a, *ApJ*, 467, 197
- Mulchaey, J. S., Wilson, A. S. & Tsvetanov, Z. 1996b, *ApJS*, 102, 309
- Murphy, T. W., Soifer, B. T., Matthews, K., Kiger, J. R. & Armus, L. 1999, *ApJ*, 525L, 85

- Naab, T., Burkert, A. & Hernquist, L. 1999, *ApJ*, 523L, 133
- Naab, T. & Burkert, A. 2001, *ApJ*, 555L, 91
- Naab, T. & Burkert, A. 2003, *ApJ*, 597, 893
- Naab, T., Jesseit, R. & Burkert, A. 2006, *MNRAS*, 372, 839
- Naab, T., Khochfar, S. & Burkert, A. 2006, *ApJ*, 636L, 81
- Neff, S. G., Ulvestad, J. S. & Teng, S. H. 2004, *ApJ*, 611, 186
- Neugebauer, G., Habing, H. J., van Duinen, R., Aumann, H. H., Baud, B., Beichman, C. A., Beintema, D. A., Boggess, N., Clegg, P. E., de Jong, T. & 18 coauthors 1984, *ApJ*, 278L, 1
- Nieto, J.-L., Bender, R., Arnaud, J. & Surma, P. 1991, *A&A*, 244L, 25
- Oke, J., & Gunn, E. 1983, *ApJ*, 266, 713
- Origlia L., & Leitherer C. 2000, *AJ*, 119, 2018
- Papovich, C., Dole, H., Egami, E., Le Floch, E., Pérez-González, P. G., Alonso-Herrero, A., Bai, L., Beichman, C. A., Blaylock, M., Engelbracht, C. W. & 13 coauthors, 2004, *ApJS*, 154, 70
- Papovich, C., Moustakas, L. A., Dickinson, M., Le Floch, E., Rieke, G. H., Daddi, E., Alexander, D. M., Bauer, F., Brandt, W. N., Dahlen, T., and 11 coauthors 2006, 2006, *ApJ*, 640, 92
- Penzias, A. A., & Wilson, R. W. 1964, *AJ*, 142, 419
- Pérez-González, P. G., Rieke, G. H., Egami, E., Alonso-Herrero, A., Dole, H., Papovich, C., Blaylock, M., Jones, J., Rieke, M., Rigby, J. & 4 coauthors 2005, *ApJ*, 630, 82
- Pierce, A. K. 1965, *PASP*, 77, 216
- Planesas, P., Colina, L., & Pérez-Olea, D. 1997, *A&A*, 325, 81
- Puget, J.-L., Abergel, A., Bernard, J.-P., Boulanger, F., Burton, W. B., Desert, F.-X., & Hartmann, D. 1996, *A&A*, 308L, 5
- Ren, D. & Allington-Smith, J. 2002, *PASP*, 114, 866
- Rieke, G. H. & Low, F. J. 1972, *ApJ*, 176L, 95
- Rieke, G. H. & Lebofsky M. J. 1979, *ARA&A*, 17, 477
- Rieke, G. H. 1988, *ApJ*, 331L, 5
- Rieke, G. H. 1988, *ApJ*, 331L, 5
- Rigopoulou, D., Lawrence, A. & Rowan-Robinson, M. 1996, *MNRAS*, 278, 1049
- Rigopoulou, D., Spoon, H. W. W., Genzel, R., Lutz, D., Moorwood, A. F. M. & Tran, Q. D. 1999, *AJ*, 118, 2625
- Risaliti, G., Maiolino, R., Marconi, A., Sani, E., Berta, S., Braitto, V., Ceca, R. D., Franceschini, A., & Salvati, M. 2006, *MNRAS*, 365, 303
- Rix, H.-W. Barden, M., Beckwith, S. V. W., Bell, E. F., Borch, A., Caldwell, J. A. R., Häussler, B., Jahnke, K., Jogee, S., McIntosh, D. H. & 6 coauthors 2004, *ApJS*, 152, 163
- Romanishin, W. 1986, *ApJ*, 301, 675
- Rogstad, D. H., Lockart, I. A., & Wright, M. C. H. 1974, *ApJ*, 193, 309-319

- Rothberg, B. & Joseph, R. D. 2006, *AJ*, 132, 976
- Rupke, D. S., Veilleux, S. & Sanders, D. B. 2002, *ApJ*, 570, 588
- Rupke, D. S., Veilleux, S. & Sanders, D. B. 2005, *ApJ*, 632, 751
- Rupke, D. S. & Veilleux, S. 2007, astro-ph/07081766
- Sanders, D. B., & Mirabel, I. F. 1985, *ApJ*, 298L, 31
- Sanders, D. B., Soifer, B. T., Elias, J. H., Madore, B. F., Matthews, K., Neugebauer, G. & Scoville, N. Z. 1988, *ApJ*, 325, 74
- Sanders, D. B., Soifer, B. T., Elias, J. H., Neugebauer, G., & Matthews, K. 1988b, *ApJ*, 328L, 35
- Sanders, D. B., Scoville, N. Z. & Soifer, B. T. 1991, *ApJ*, 370, 158
- Sanders, D. B. & Mirabel, I. F. 1996a, *ARA&A*, 34, 749
- Savage, B. D., & Mathis, J. S. 1979, *ARA&A*, 17, 73
- Schweizer, F. 1982, *ApJ*, 252, 455
- Scott, S. E., Fox, M. J., Dunlop, J. S., Serjeant, S., Peacock, J. A., Ivison, R. J., Oliver, S., Mann, R. G., Lawrence, A., Efstathiou, A., & 5 coauthors 2002, *MNRAS*, 331, 817
- Scoville, N. Z., Evans, A. S., Thompson, R., Rieke, M., Hines, D. C., Low, F. J., Dinshaw, N., Surace, J. A. & Armus, L. 2000, *AJ*, 119, 991
- Shier, L. M., Rieke, M. J., & Rieke, G. H. 1996, *ApJ*, 470, 222
- Shier, L. M. & Fischer, J., 1998, *ApJ*, 497, 163
- Skrutskie, M. F., Cutri, R. M., Stiening, R., Weinberg, M. D., Schneider, S., Carpenter, J. M., Beichman, C., Capps, R., Chester, T., Elias, J. & 21 coauthors 2006, *AJ*, 131, 1163
- Slipher, V. M. 1914, *PA*, 22, 19
- Smail, Ian, Ivison, R. J., & Blain, A. W. 1997, *ApJ*, 490L, 5
- Smail, I., Ivison, R., Owen, F., Blain, A., & Kneib, J. 2000, *ApJ*, 528, 612
- Smail, I., Ivison, R. J., Blain, A. W. & Kneib, J.P. 2002, *MNRAS*, 331, 495
- Smith, H. E., Lonsdale, C. J. & Lonsdale, C. J. 1998, *ApJ*, 492, 137
- Smith, H. E., Lonsdale, C. J., Lonsdale, C. J. & Diamond, P. J. 1998, *ApJ*, 493L, 17
- Sofue, Y. & Rubin, V. 2001, *ARA&A*, 39, 137
- Soifer, B. T., Rowan-Robinson, M., Houck, J. R., de Jong, T., Neugebauer, G., Aumann, H. H., Beichman, C. A., Boggess, N., Clegg, P. E., Emerson, J. P. & 6 coauthors 1984, *ApJ*, 278L, 71
- Solomon, P. M., Downes, D., Radford, S., & Barrett, J. 1997, *ApJ*, 478, 144
- Sommerville, J. 2001, *IPNPR*, 145, 1
- Spitzer, L. 1987, Dynamical evolution of Globular Clusters, Princeton Series in Astrophysics
- Spoon, H. W. W., Tielens, A. G. G. M., Armus, L., Sloan, G. C., Sargent, B., Cami, J., Charmandaris, V., Houck, J. R. & Soifer, B. T. 2006, *ApJ*, 638, 759
- Springel, V., Di Matteo, T. & Hernquist, L. 2005, *MNRAS*, 361, 776

- Stasińska, G. & Izotov, Y. 2003, *A&A*, 397, 71
- Stasińska, G., Cid Fernandes, R., Mateus, A., Sodrá, L. & Asari, N. V. 2006, *MNRAS*, 371, 972
- Surace, J. A., Sanders, D. B., Vacca, W. D., Veilleux, S. & Mazzarella, J. M. 1998, *ApJ*, 492, 116
- Surace, J. A. & Sanders, D. B. 2000, *AJ*, 120, 604
- Surace, J. A., Wang, Z., Willner, S., Smith, H., Pipher, J., Forrest, W., Fazio, G., Howell, J., Evans, A., Hibbard, J. & 2 coauthors 2006, astro-ph/0601066
- Tacconi, L., Genzel, R., Tecza, M., Gallimore, J., Downes, D., & Scoville, N. 1999, *ApJ*, 524, 732
- Tacconi, L. J., Genzel, R., Lutz, D., Rigopoulou, D., Baker, A. J., Iserlohe, C., & Tecza, M. 2002, *ApJ*, 580, 73
- Telesco, C. M., & Harper, D. A. 1980, *ApJ*, 235, 392
- Terlevich, R., & Melnick, J. 2005, *MNRAS*, 195, 839
- Toomre, A., & Toomre, J. 1972, *ApJ*, 178, 623
- van der Kruit, P. C. & Allen, R. J. 1978, *ARA&A*, 16, 103
- Vanderriest, C. 1980, *PASP*, 92, 858
- Vanderriest, C. & Lemonier, J. P. 1988, in *Instrumentation for Ground-based Astronomy*, Ed. L. Robinson, New York, Springer-Verlag, p. 304
- van der Kruit, P. C. 1971, *A&A*, 15, 110
- van Dokkum, P. G., Franx, M., Förster Schreiber, N. M., Illingworth, G. D., Daddi, E., Knudsen, K. K., Labbé, I., Moorwood, A., Rix, H., Röttgering, H. & 6 coauthors 2004, *ApJ*, 611, 703
- Veilleux, S., & Osterbrock, D. E. 1987, *ApJS*, 63, 295
- Veilleux, S., Goodrich, R. W., & Hill, G. J. 1994, *ASP Conference Series*, 54, 273
- Veilleux, S., Kim, D.C., Sanders, D. B., Mazzarella, J. M., & Soifer, B. T. 1995, *ApJS*, 98, 171
- Veilleux, S., Kim, D.C., & Sanders, D. B. 1999, *ApJ*, 522, 113
- Veilleux, S., Kim, D.C., & Sanders, D. B. 2002, *ApJS*, 143, 315
- Veilleux, S., Cecil, G. & Bland-Hawthorn, J. 2005, *ARA&A*, 43, 769
- Weedman, D. W., Hao, L., Higdon, S. J. U., Devost, D., Wu, Y., Charmandaris, V., Brandl, B., Bass, E. & Houck, J. R. 2005, *ApJ*, 633, 706
- Weitzel, L., Krabbe, A., Kroker, H., Thatte, N., Tacconi-Garman, L. E., Cameron, M. & Genzel, R. 1996, *A&AS*, 119, 531
- Wolf, M. 1912, *AN*, 190, 229
- Wright, G. S., James, P. A., Joseph, R. D. & McLean, I. S. 1990, *Nature*, 344, 417
- Wright 2006, *PASP*, 118, 1711
- Yun, Min S., Reddy, N. A. & Condon, J. J. 2001, *ApJ*, 554, 803
- Zheng, Z., Wu, H., Mao, S., Xia, X.-Y., Deng, Z.-G., & Zou, Z.-L. 1999, *A&A*, 349, 735
- Zibetti, S., Gavazzi, G., Scodreggio, M., Franzetti, P. & Boselli, A. 2002, *ApJ*, 579, 261
- Zwicky F., 1956, "Ergrb.Exakt.Naturwiss", 29, 344

List of figures

1.1	Atmospheric windows	8
1.2	Luminosity function and spectral energy distribution for ULIRGs	9
1.3	Spectral classification of infrared galaxies	10
1.4	Near-IR diagnostic diagram.	12
1.5	ISO diagnostic diagram	12
1.6	Influence of black holes in simulations of galaxy mergers	15
1.7	Merger simulation between two disk galaxies	17
1.8	Location of ULIRGs in the fundamental plane	18
1.9	Evolution of the global SFR	19
1.10	Cumulative redshift distribution of the 8-mJy SCUBA survey	21
1.11	Selection effect on IR luminosity for galaxies up to redshift 3	22
1.12	SDSS predicted and observed distribution of color and absolute magnitude	23
2.1	Advantages of IFS vs. longslit spectroscopy	28
2.2	IR luminosity distribution for our sample of ULIRGs	30
2.3	<i>HST</i> images of the sample of galaxies with the F814W filter	31
2.4	<i>HST</i> images of the sample of galaxies with the F814W filter	32
2.5	<i>HST</i> images of the sample of galaxies with the F160W filter	33
2.6	<i>HST</i> image of the galaxy Mrk 231 with the F160W filter	34
2.7	IFS techniques	38
2.8	Layout of INTEGRAL	40
2.9	INTEGRAL fiber bundles	41
2.10	INTEGRAL IFS concept and raw spectra.	42
2.11	INTEGRAL data reduction	46
2.12	Full nuclear spectra for the sample of galaxies	48
2.13	Full nuclear spectra for the sample of galaxies	49
2.14	Two-dimensional spectra and reconstructed map for IRAS 16007+3743	50
2.15	Two-dimensional spectra and derived velocity field	51
2.16	Alignment between the <i>HST</i> images and INTEGRAL data	52
3.1	Continuum and ionized gas maps for the galaxies IRAS 13156+0435 and IRAS 13342+3932	59
3.2	Continuum and ionized gas maps for the system Arp 299	60
3.3	Continuum and ionized gas maps for several ULIRGs	61
3.4	Continuum and ionized gas maps for several ULIRGs	62
3.5	Continuum and ionized gas maps for several ULIRGs	63

3.6	Continuum and ionized gas maps for Arp 220	64
3.7	INTEGRAL pointings for the Arp 299 system	65
3.8	Extinction map for the entire Arp 299 system	66
3.9	Extinction map for the galaxy IC 694, member of the Arp 299 system	66
3.10	Extinction map for the galaxy NGC 3690, member of the Arp 299W system	67
3.11	Azimuthal profiles for the galaxy sample	71
3.12	F814W-F160W color for the galaxy sample	74
3.13	Parameter a4 vs. ellipticity for the galaxies of the sample	78
3.14	Comparison of parameters a4 and ellipticity as measured in the F160W-band with models	79
3.15	Isophotal twist $\Delta\phi$ vs. ellipticity	80
3.16	Observed isophotal twist $\Delta\phi$ vs. ellipticity compared with models	82
3.17	Ratio of the observed velocity and velocity dispersion vs. ellipticity	83
3.18	Ratio of the observed velocity and velocity dispersion vs. ellipticity compared with models	84
4.1	BPT diagnostic diagrams	88
4.2	Definition of regions under study	89
4.3	Diagnostic diagrams for the system Arp 299	90
4.4	Diagnostic (BPT) diagrams for the galaxy IC 694	92
4.5	Diagnostic (BPT) diagrams for the galaxy NGC 3690	93
4.6	Diagnostic (BPT) diagrams for all the galaxies of the sample	94
4.7	Average line ratios for the different regions of the individual pre-coalescence galaxies.	96
4.8	Average line ratios for the different regions of the individual post-coalescence galaxies.	97
4.9	Optical line ratios compared to models.	101
4.10	Velocity dispersion-ionization state relation.	102
4.11	Averaged velocity dispersion-ionization state relation.	104
4.12	Integrated values of ULIRGs compared with SDSS galaxies and with nuclear values	105
5.1	Geometric relationships of the coordinates in the galaxy	111
5.2	Rotation curve model for a disk galaxy, and spider diagram	111
5.3	Symmetric distortions in galaxy velocity fields	112
5.4	Model for galaxy superwinds	113
5.5	Kinematic maps for the galaxy IRAS 13156+0435	117
5.6	Kinematic maps for the galaxy Arp 299	118
5.7	Kinematic maps for the sample of ULIRGs	119
5.8	Kinematic maps for the sample of ULIRGs	120
5.9	Kinematic maps for the sample of ULIRGs	121
5.10	Kinematic maps for the galaxy Arp 220	122
5.11	Comparison between parameters of the observed and modeled velocity fields	126
5.12	Observed and predicted velocity fields for Arp 299	127
5.13	Observed and predicted velocity fields for the sample of ULIRGs	128
5.14	Observed and predicted velocity fields for the sample of ULIRGs	129

5.15	Observed and predicted velocity fields for IRAS 06487+2208	130
5.16	Kinematic model residuals	130
5.17	Dynamical mass histogram for ULIRGs	132
5.18	Location of the sample of ULIRGs in the fundamental plane.	134
5.19	Location of the sample of ULIRGs in the fundamental plane compared with elliptical galaxies and other ULIRGs	135
A.1	Contour plot for the WFPC2/F814W ULIRGs sample	148
A.2	Contour plot for the WFPC2/F814W ULIRGs sample	149
B.1	Continuum and emission line maps for IRAS 13156+0435	154
B.2	Continuum and emission line maps for IRAS 13156+0435 North	155
B.3	Continuum and emission line maps for IRAS 13156+0435 South	156
B.4	Continuum and emission line maps for IRAS 13342+3932	157
B.5	Continuum and emission line maps for Arp 229	158
B.6	Continuum and emission line maps for IC 694	159
B.7	Continuum and emission line maps for NGC 3690	160
B.8	Continuum and emission line maps for IRAS 16007+3743	161
B.9	Continuum and emission line maps for IRAS 08572+3915 (northern pointing)	162
B.10	Continuum and emission line maps for IRAS 08572+3915 (southern pointing)	163
B.11	Continuum and emission line maps for IRAS 18580+6527	164
B.12	Continuum and emission line maps for IRAS 06268+3509	165
B.13	Continuum and emission line maps for IRAS 14348-1447	166
B.14	Continuum and emission line maps for IRAS 12112+0305	167
B.15	Continuum and emission line maps for Markarian 463	168
B.16	Continuum and emission line maps for IRAS 14060+2919	169
B.17	Continuum and emission line maps for Markarian 273	170
B.18	Continuum and emission line maps for IRAS 17208-0014	171
B.19	Continuum and emission line maps for IRAS 15250+3609	172
B.20	Continuum and emission line maps for IRAS 15206+3342	173
B.21	Continuum and emission line maps for IRAS 12490-1009	174
B.22	Continuum and emission line maps for Arp 220	175
B.23	Continuum and emission line maps for IRAS 13469+5833	176
B.24	Continuum and emission line maps for IRAS 11087+5351	177
B.25	Continuum and emission line maps for IRAS 06487+2208	178
B.26	Continuum and emission line maps for Mrk 231	179
C.1	Two-dimensional extinction map derived for the galaxy IRAS 13156+0435	182
C.2	Two-Dimensional extinction maps for the sample of ULIRGs	183
C.3	Two-Dimensional extinction maps for the sample of ULIRGs	184

List of tables

1.1	Acronyms and definitions used by the <i>IRAS</i> catalog	9
2.1	Properties of the Ultra-luminous Infrared Galaxies sample	29
2.2	Available data: <i>HST</i> archive data and INTEGRAL observing logs details . .	35
2.3	Characteristics of NICMOS cameras	35
2.4	IFUs on 8-10 m telescopes	40
2.5	Characteristics of the INTEGRAL fiber bundles	41
2.6	WYFFOS spectral Characteristics (old camera)	41
3.1	Characteristics of the sample of galaxies	55
3.2	Separation between the red continuum and the emission-line gas peaks. . . .	57
3.3	Extinction information for the sample of galaxies	69
3.4	Variation in magnitudes for the light profiles, and departures form the $r^{1/4}$ law	73
3.5	Comparison of R_{eff} values	76
3.6	Comparison of velocity dispersion values	77
4.1	Average emission line ratios for the galaxies	95
5.1	Kinematic results for the sample of ULIRGs	123
5.2	Parameters derived from the velocity field model	125
5.3	Mass calculations for the sample of ULIRGs	133
D.1	Nuclear classification for the sample of ULIRGs with different classification schemes	186

